BRNO UNIVERSITY OF TECHNOLOGY

VYSOKÉ UČENÍ TECHNICKÉ V BRNĚ

CENTRAL EUROPEAN INSTITUTE OF TECHNOLOGY BUT

STŘEDOEVROPSKÝ TECHNOLOGICKÝ INSTITUT VUT

ELECTROCHEMICAL STUDY OF NOVEL MATERIALS FOR ENERGY CONVERSION APPLICATION

ELEKTROCHEMICKÉ STUDIUM NOVÝCH MATERIÁLŮ PRO APLIKACE PŘEMĚNY ENERGIE

DOCTORAL THESIS TOPIC

POJEDNÁNÍ

AUTHOR

AUTOR PRÁCE

Ing. Katarina Novčić, M.Sc.

SUPERVISOR

ŠKOLITEL

prof. RNDr. Martin Pumera, Ph.D.

BRNO 2024

This page is intentionally left empty.

Acknowledgement

This amazing journey resulted in a doctoral thesis that would not be possible without the enormous support of certain people I would like to acknowledge.

Firstly, I would like to thank my supervisor Prof. Dr. Martin Pumera for the opportunity to carry out my research and be part of the Future Energy and Innovation Group at CEITEC BUT. I very much appreciate his help, enormous support and guidance, and always positive attitude, which helped me to grow as a scientist and person.

I would also like to thank Dr. Christian Iffelsberger, who mentored me during the first half of my PhD studies and introduced me to the field of SECM. Special thanks to all current and former members of the Future Energy and Innovation Group for an enjoyable working environment; Dr. Siow Woon Ng, Dr. Kalyan Gosh, for very much delightful scientific discussions and support during my PhD journey; Dr. Mario Palacios-Corella, Dr. Jose Munos and Dr. Anna Jančík Prochásková for their help and support; Katka for her help with paperwork and always being there for us. Special thanks to Michela and Cagatay who were there through the most challenging times and were always full of advice. Thank you for your help and inspirational chats over a lunch break in Bistro.

Additionally, I am very thankful to Prof. Dr. Babak Anasori for the opportunity to conduct my internship in his group and for his enormous help and support during my stay in the USA. It was an incredible experience to meet and work with all group members from the Layered Materials and Structures Lab at Purdue University, Indianapolis, especially Dr. Anupma Thakur and Nithin Chandran, B.S.

Also, I would like to thank my friends Andjela, Sunčica, Ivana, Goran, Milica, David, Dragana, Todora, Natalija, Saška, Tijana, Stevan and Nevena for their enormous emotional support, and

fun and amazing time we spent together which gave me strength to refresh my mind and do my best at work.

I would like to sincerely acknowledge the CEITEC Nano core facilities and the financial support from CEITEC Junior Projects (CEITEC VUT-J-23-8341) and (CEITEC VUT-J-21-7535) and Quolity Internal Grants of BUT (Reg. No. CZ.02.2.69 / 0.0 / 0.0 19_073 / 0016948).

Finally, this Thesis would not be possible without massive support, unwavering love, patience, and encouragement from my family. Their positivity and backing were immeasurably important for me, especially during Covid time. Dear dad Aleksandar, mom Ljiljana and sister Marija, thank you for being there for me! ХВАЛА!

I would like to thank everyone who contributed to this Thesis, directly or indirectly for your cooperation and support during my PhD journey.

Bibliographic citation

NOVCIC, Katarina. *Electrochemical study of novel materials for energy conversion application.* Brno, 2024. Available also at: https://www.vut.cz/studenti/zav-prace/detail/158803. Doctoral Thesis. Vysoké učení technické v Brně, Středoevropský technologický institut VUT, Central European Institute of Technology BUT. Supervisor Martin Pumera.

Declaration

I declare that I have conducted this doctoral thesis titled “Electrochemical study of novel materials for energy conversion application”, independently, under the supervision of Prof. Dr. Martin Pumera. The work includes proper citations and references from relevant literature and professional sources.

Brno

MSc. Katarina Novčić

Author Publications and Academic Outputs

List of published articles:

1. **K. A. Novčić**, C. Iffelesberger, M. Palacios Corella, and M. Pumera, *Solvents dramatically influence the atomic composition and catalytic properties of $Ti_3C_2T_x$ MXenes*, **Journal of Material Chemistry A (2023)**, DOI: 10.1039/D3TA01441J.
2. M. Sanna, **K. A. Novčić**, S. Ng, M. Černý, and M. Pumera, *The unexpected photoelectrochemical activity of MAX phases: the role of oxide impurities,* **Journal of Material Chemistry A (2023)**, DOI: 10.1039/d2ta06929f.
3. S. Wert, C. Iffelesberger, **K. A. Novčić**, and M. Pumera, *Corrosion of Catalyst in High Resolution: Layered Transition Metal Dichalcogenides Electrocatalyse Water Splitting and Corrode During the Process*, **Journal of Catalysis (2022)**, 416, 85-91, doi.org/10.1016/j.jcat.2022.10.023.
4. **K. A. Novčić**, C. Iffelesberger, and M. Pumera, *Layered MAX phase electrocatalyst activity is driven by only a few hot spots*, **Journal of Material Chemistry A (2022)**, 10, 3206-3215, doi.org/10.1039/D1TA06419C.
5. S. Wert, C. Iffelesberger, **K. A. Novčić**, F-M Matysik, and M. Pumera, *Edges are more active than basal planes in synthetic bulk crystals of TiS_2 and $TiSe_2$,* **Applied Materials Today (2022)**, 26, 101309, doi.org/10.1016/j.apmt.2021.101309.
6. **K. A. Novčić**, C. Iffelesberger, S. Ng and, M. Pumera, *Local Electrochemical Activity of Transition Metal Dichalcogenides and their Heterojunctions on 3D-Printed Nanocarbon Surfaces*, **Nanoscale (2021)**, 13, 5324-5332, DOI: 10.1039/D0NR06679F.

Projects as Principal Investigator:

1. ***Specific Junior Project***, Central European Institute of Technology (CEITEC), Brno University of Technology (BUT), Brno, Czech Republic (2023), project no. CEITEC VUT-J-23-8341.
2. ***Quality Internal Grand Competition***, Brno University of Technology (KinG BUT), Brno, Czech Republic (2021-2022), Reg. No. CZ.02.2.69 / 0.0 / 0.0 19_073 / 0016948.
3. ***Specific Junior Project***, Central European Institute of Technology (CEITEC), Brno University of Technology (BUT), Brno, Czech Republic (2021), project no. CEITEC VUT-J-21-7535.

List of International Conferences:

1. **International Congress on Analytical Nanoscience and Nanotechnology (X NyNA 2022), Ciudad Real, Spain, 5th-8th September 2022**

   Poster pesentation: *Layered MAX phase electrocatalyst activity is driven by a few hot spots.*

2. **18th International Conference on Electroanalysis (ESEAC 2022), 5th-9th June 2022, Vilnius, Lithuania**.

   Oral Presentation: *Microscopic activity for the hydrogen evolution reaction of the layered MAX phase electrocatalyst.*
   Award: The Analytical and Bioanalytical Chemistry Award for the best student oral presentation.

3. **Falling Walls Lab, Sep 2021, national level, Prague, Czech Republic**.

   Flash Talk: *Breaking the wall of the increased fossil fuel consumption*.

4. **3rd Cross-Border Seminar on Electroanalytical Chemistry (CBSEC), Virtual Seminar, April 2021, Regensburg, Germany**.

   Oral Presentation: *Local electrochemical activity of TMD heterojunctions on 3D-printed nanocarbon surfaces*.

List of Seminars:

1. **Ceitec PhD Retreat, Virtual Seminar, Sep 2021, Brno, Czech Republic**.

   Flash Talk: *Local electrochemical activity of 3D-printed nanocarbon surfaces*.
   Award: The best flash talk on the seminar

2. **Ceitec PhD Retreat 2022, Telč, Czech Republic**

3. **Ceitec PhD Retreat 2023, Milovy, Czech Republic**

Student Internship:

May-Aug 2023: Layered Structures and Materials Lab, Purdue University, Indianapolis, USA

Abstract

A promising alternative to resolve the current energy and environmental crisis lies in the utilization of electrochemical water splitting via hydrogen evolution reaction (HER). Therefore, there is urgency for investigation and development of new electrocatalysts for the energy conversion application. Different novel materials have been promising electrocatalysts for the HER. Among them, two-dimensional (2D) materials such as transition metal dichalcogenides (TMDs), MAX phases and MXenes have drawn much attention due to their distinctive electrochemical properties. Even though 3D-printing opened the way for the fast prototyping and manufacturing of electrode devices, their merging with different 2D materials still remains challenging.

This Thesis deals with the electrochemical study of different novel materials for energy conversion applications and clean hydrogen production. It represents a study on the macroscopic and microscopic electrochemical performance of modified 3D-printed nanocarbon electrodes and TMDs, MAX phase, and MXene electrocatalysts. The macroscopic electrochemical activity is examined by traditional techniques such as voltammetry, providing information about the average electrochemical performance of the materials. Additionally, their microscopic electrochemical activity is performed by scanning electrochemical microscopy (SECM), which gives an insight into the local differences in the materials' electrochemical activity and provides information about the distribution and uniformity of the HER active sites on the material surfaces. This Thesis has broad implications for the general understanding of the electrocatalytic performance of novel 2D materials, which is important for their future development as electrocatalysts.

Keywords: 2D materials, TMDs, MAX phases, MXenes, 3D-printing, energy conversion, hydrogen evolution reaction, scanning electrochemical microscopy

Abstrakt:

Slibnou alternativou k řešení současné energetické a environmentální krize spočívá v využití elektrochemického rozkladu vody pomocí reakce na vývoj vodíku (HER). Proto existuje naléhavá potřeba zkoumat a vyvíjet nové elektrokatalyzátory pro aplikaci přeměny energie a HER jako součást tohoto procesu. Různé nové materiály se ukázaly jako slibní elektrokatalyzátory pro HER. Mezi nimi mají dvourozměrné (2D) materiály, jako jsou dichalkogenidy přechodových kovů (TMD), MAX fáze a MXeny, velkou pozornost díky svým slibným elektrochemickým vlastnostem. Navíc tisk ve 3D otevřel cestu k rychlému prototypování a výrobě elektrodových zařízení, a jejich kombinace s různými 2D materiály zůstává výzvou.

Tato práce se zabývá elektrochemickým studiem různých nových materiálů pro aplikace přeměny energie a čisté výroby vodíku. Představuje studium makroskopické a mikroskopické elektrochemické výkonnosti upravených 3D-tisknutých nanouhlíkových elektrod a elektrokatalyzátorů TMD, MAX fáze a MXen. Makroskopická elektrochemická aktivita je studována tradičními technikami, jako je voltametrie, poskytující informace o průměrném elektrochemickém výkonu materiálů. Kromě toho je jejich mikroskopická elektrochemická aktivita prováděna skenovací elektrochemickou mikroskopií (SECM), která poskytuje vhled do místních rozdílů v elektrochemické aktivitě materiálů a informace o distribuci a rovnoměrnosti HER aktivních míst na površích materiálů. Tato práce má široké důsledky pro obecné porozumění elektrokatalytickému výkonu nových 2D materiálů, což je důležité pro jejich budoucí vývoj jako elektrokatalyzátorů.

Klíčová slova: 2D materiály, 3D tisk, TMD, MAX fáze, **MXeny, přeměna energie, reakce vývoje vodíku**, **skenovací elektrochemická mikroskopie**

Table of Content:

i. Thesis Organization

This thesis is paper-based, containing results from five published papers and it consists of eleven Chapters. It begins with **Chapter 1**, which sets the main aims and objectives of the Thesis. **Chapter 2** provides an overview of the topic and its significance, while **Chapter 3** reviews literature and state-of-the-art research on novel two-dimensional materials. **Chapters 4** and **5** give the theoretical background and an overview of and methods used in this Thesis, respectively. List of references can be found at the end of each chapter. Following that, the main results are presented as published articles (in the Appendix to each Chapter) in the sections from **Chapter 6** to **Chapter 10**. The results obtained from the research on the local electrochemical activity of transition metal dichalcogenides on 3D-printed nanocarbon electrodes are presented in **Chapter 6**. Following that, **Chapter 7** and **Chapter 8** provide the results of the local electrochemical activity of the edges of transition metal dichalcogenide crystals and the corrosion study of their bulk crystals**,** respectively. Subsequently, the main results from the research on the double transition metal MAX phase electrocatalysts and their microscopic electrochemical activity for hydrogen evolution reaction are shown in **Chapter 9**. **Chapter 10** presents the study of the solvent effects on the electrochemical activity of MXene electrocatalysts. Finally, this work is concluded in **Chapter 11** with a summary and the future perspective of the field. Additional work on MAX phase photoelectrocatalysts can be found in the **Appendix** to this Thesis.

Chapter 1. Aims and Goals of Thesis

This Thesis aims to gain profound knowledge about the macroscopic and microscopic electrochemical properties of layered two-dimensional (2D) materials and their application as catalysts in clean hydrogen production via electrochemical water splitting reactions such as hydrogen evolution reaction (HER). The materials studied in this Thesis are transition metal dichalcogenides (TMDs), 3D-printed nanocarbon electrodes, MAX phases, and MXenes. This aim is achieved by detailed electrochemical and physicochemical investigations of these materials, and it is divided into four objectives:

Objective 1. Microscopic electrochemical study of the 3D-printed nanocarbon electrodes modified transition metal dichalcogenides

- Fabricating and characterizing thermally activated 3D-printed nanocarbon electrodes modified with layers of TMDs;
- Investigating the local electrochemical activity and distribution of electrochemical HER active sites of the fabricated TMD-modified 3D-printed nanocarbon electrodes;
- Providing the detailed study of the penetration depth of the deposited materials inside the porous 3D-printed nanocarbon structure.

Objective 2. Local electrochemical performance of the bulk crystals of transition metal dichalcogenides

- Investigating the microscopic electrochemical activity of the edges and basal planes of the TMDs bulk crystals;
- Monitoring the microscopic changes in the surface morphology, elemental composition, and electrochemical activity of the bulk TMDs crystals during the HER.

<u>Objective 3.</u> Microscopic electrochemical performance of the double transition metal MAX phase electrocatalysts

- Investigating the uniformity and distribution of the catalytically active sites for the HER on the double transition metal MAX phase electrocatalysts;
- Providing a detailed physicochemical characterization of the studied MAX phase.

<u>Objective 4.</u> Electrochemical performance of the MXene electrocatalysts

- Examining the effects of solvent media used in the sample preparation of MXenes and their influence on the MXene electrocatalytic activity for the HER;
- Investigating the solvent influence on the MXene long-term electrocatalytic performance and material storage.

Chapter 2. Overview of the Research Topic

The constant rise in the global population, the increasing energy demands, and climate change represent the paramount concerns that have been raised over the security of our energy future. Nowadays, the vast majority of worldwide energy consumption is derived from fossil fuels (coal, oil and gas), according to the International Energy Agency [1]. As a result, significant concerns have been raised over the energy supply due to many downsides of the widely used non-renewable energy sources, such as fossil fuels. Therefore, there is a strong tendency to diversify the global-scale energy system by reducing the reliance on fossil fuels while preserving our environment by switching to renewable energy sources.

Developing a green hydrogen economy with no emission of harmful gasses is becoming a great challenge. Hydrogen has gained great attention as an energy carrier and it is considered to be the key player in the battle against climate change [2-4]. Thus, its production is key as well. Namely, the Earth's atmosphere provides a universal feedstock of water (71%), which can be converted into hydrogen gas and oxygen gas via an electrochemical water-splitting process coupled with renewable energy [5]. As a one-half reaction in the water splitting, the hydrogen evolution reaction (HER) represents a way toward clean hydrogen production.

However, this reaction does not occur spontaneously, and it requires the electrocatalytic material to minimize the potential barrier necessary to drive HER reaction [6-8]. Additionally, the platinum (Pt) based materials have been demonstrated to be highly efficient electrocatalysts for the HER [9-12]. Due to scarcity and high cost of these materials, their wide-scale application is limited. Thus, there is an urgent need to investigate new electrocatalytic materials for clean hydrogen production via HER.

Two-dimensional (2D) materials have received significant attention as promising electrocatalysts for clean hydrogen production [13]. This is evidenced by the increased number of articles published on this topic, as shown in **Figure 2.1**.

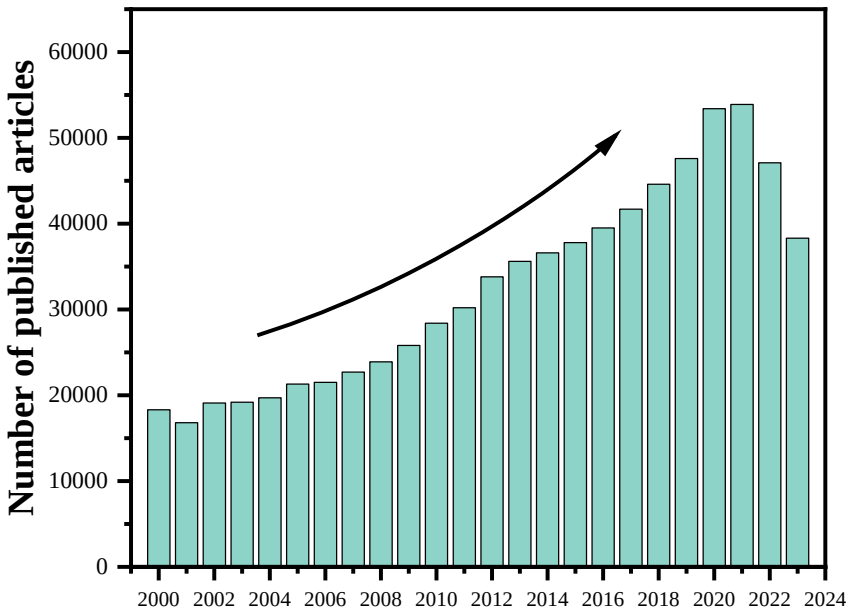

Figure 2.1. Graphical illustration showing the rise of the number of published articles from the period from 2000 until 2023. The data source: *Google scholar*, key words: *2D materials for HER*.

Among them, the group of transition metal dichalcogenides (TMDs) and the group of ternary metal carbides and nitrides (MXenes) have attracted notable interest due to their excellent properties and electrochemical activity towards HER [14-20]. In addition, MAX phases, known as precursors that are used for the MXene synthesis, have been demonstrated as good electrocatalysts for this reaction [21-22].

On the other hand, the development of new technologies brought 3D-printing. This technique enables manufacturing of conductive devices with a specific shape and composition used in electrochemical applications [23]. The 3D-printed nanocarbon devices were used as electrodes in energy conversion and clean hydrogen production [24]. However, the electrode activation

and surface modification of the 3D-printed electrodes are required to enhance their electrochemical performance towards HER.

Understanding the electrochemical reactions on the microscopic level and the distribution of the electroactive sites over the catalytic surfaces are the keys to designing materials with improved catalytic performance. The activity of the electrocatalytic surfaces is usually studied by traditional electrochemical techniques, such as voltammetry, providing information about the materials' average or macroscopic electrochemical activity. However, a more profound understanding of the microscopic electrochemical performance of the electrocatalytic surfaces, such as distribution and location of the electrocatalytic active sites, uniformity of the HER active sites, etc., cannot be provided by traditional techniques, which limits the current knowledge of the field of electrocatalysts. This Thesis deals with the electrochemical activity (both macroscopic and microscopic) of different materials, such as modified 3D-printed nanocarbon electrodes, TMDs, MAX phases, and MXenes. It uses an advanced electrochemical tool, scanning electrochemical microscopy (SECM), to provide more profound knowledge about the location and distribution of the active sites for hydrogen production on the electrocatalytic surfaces.

The obtained results about the microscopic electrochemical activity of the electrocatalysts have a broad impact on our knowledge and understanding of electrocatalytic performance in general, as well as on the systematic improvement of the electrocatalysts for electrochemical applications and green hydrogen production.

2.1. References

[1] International Energy Agency, "Net Zero by 2050: A Roadmap for the Global Energy Sector," *Int. Energy Agency* **2021**, 224, https://www.iea.org/reports/net-zero-by-2050.

[2] M. A. Rosen and S. Koohi-Fayegh, "The prospects for hydrogen as an energy carrier: an overview of hydrogen energy and hydrogen energy systems," *Energ. Ecol. Environ.* **2016**, 1, 10–29. https://doi.org/10.1007/s40974-016-0005-z

[3] M. P. Society, "Hydrogen: An Overview," *Chem. Rev.* **2007**, 107, 10, 3900–3903,

doi.org/10.1021/cr050200z.

[4] K. T. Møller, T. R. Jensen, E. Akiba, and H. Wen Li, "Hydrogen - A sustainable energy carrier," *Prog. Nat. Sci. Mater. Int.*, **2017**, 27, 1, 34–40, doi: 10.1016/j.pnsc.2016.12.014.

[5] S. Y. Tee *et al.*, "Recent Progress in Energy-Driven Water Splitting," *Adv. Sci.* **2017**, 4, 5, doi: 10.1002/advs.201600337.

[6] S. J. Gutić, A. S. Dobrota, E. Fako, N. V. Skorodumova, N. López, and I. A. Pašti, "Hydrogen evolution reaction-from single crystal to single atom catalysts," *Catalysts* **2020**, 10, 3, doi: 10.3390/catal10030290.

[7] A. Eftekhari, "Electrocatalysts for hydrogen evolution reaction," *Int. J. Hydrogen Energy* **2017**, 42, 16, 11053–11077, doi: 10.1016/j.ijhydene.2017.02.125.

[8] W. Yang and S. Chen, "Recent progress in electrode fabrication for electrocatalytic hydrogen evolution reaction: A mini review," *J. Chem. Eng.* **2020**, 393, 124726, doi: 10.1016/j.cej.2020.124726.

[9] J. Zhang, Y. Zhao, X. Guo, C. Chen, C-L. Dong, R-S. Liu, C-P. Han, Y. Li, Y. Gogotsi, G. Wang, "Single platinum atoms immobilized on an MXene as an efficient catalyst for the hydrogen evolution reaction," *Nat. Catal.* **2018**, 1, 985-992, doi: 10.1038/s41929-018-0195-1.

[10] F. Li., X. V. Medvedeva, J. J. Medvedev, E. Khairullina, H. Engelhardt, S. Chandrasekar, Y. Guo, J. Jin, A. Lee, H. Thérien-Aubin, A. Ahmed, Y. Pamg, A. Klinova, "Interplay of electrochemical and electrical effects induces structural transformations in electrocatalysts," *Nat. Catal.* **2021**, 4, 479-487, doi: 10.1038/s41929-021-00624-y.

[11] J. Li, J. Hu, M. Zhang, W. Gou, S. Zhang, Z. Chen, Y. Qu, Y. Ma, "A fundamental viewpoint on the hydrogen spillover phenomenon of electrocatalytic hydrogen evolution," *Nat. Commun.*, **2021**, 12, 3502, doi: 10.1038/s41467-021-23750-4.

[12] Y. Jiao, Y. Zheng, K. Davey, and S. Z. Qiao, "Activity origin and catalyst design principles for electrocatalytic hydrogen evolution on heteroatom-doped graphene," *Nat. Energy*, **2016**, 1, 16130, doi.org/10.1038/nenergy.2016.130.

[13] L. Tang, X. Meng, D. Deng, and X. Bao, "Confinement Catalysis with 2D Materials for Energy Conversion," *Adv. Mater.* **2019**, 31, 50, doi: 10.1002/adma.201901996.

[14] X. Chia and M. Pumera, "Layered transition metal dichalcogenide electrochemistry: journey across the periodic table," *Chem. Soc. Rev.* **2018**, 47, 15, 5602–5613, doi: 10.1039/c7cs00846e.

[15] Q. Lu, Y. Yu, Q. Ma, B. Chen, and H. Zhang, "2D Transition-Metal-Dichalcogenide-Nanosheet-Based Composites for Photocatalytic and Electrocatalytic Hydrogen Evolution Reactions," *Adv. Mater*. **2016**, 28, 10, 1917-1933, doi: 10.1002/adma.201503270.

[16] C. C. Mayorga-Martinez, A. Ambrosi, A. Y. S. Eng, Z. Sofer, and M. Pumera, "Transition metal dichalcogenides (MoS_2, $MoSe_2$, WS_2 and WSe_2) exfoliation technique has strong influence upon their capacitance," *Electrochem. Commun.* **2015**, 56, 24–28, doi: 10.1016/j.elecom.2015.03.017.

[17] X. Chia and M. Pumera, "Characteristics and performance of two-dimensional materials for

electrocatalysis," *Nat. Catal*. **2018**, 1, 909-921, doi: 10.1038/s41929-018-0181-7.

[18] Z. W. Seh *et al.*, "Two-Dimensional Molybdenum Carbide (MXene) as an Efficient Electrocatalyst for Hydrogen Evolution," *ACS Energy Lett.*, **2016**, 1, 3, 589-594, doi: 10.1021/acsenergylett.6b00247.

[19] Y. Wei, R. A. Soomro, X. Xie, and B. Xu, "Design of efficient electrocatalysts for hydrogen evolution reaction based on 2D MXenes," *J. Energy Chem.* **2021**, 55, 244-255, doi: 10.1016/j.jechem.2020.06.069.

[20] G. Gao, A. P. O'Mullane, and A. Du, "2D MXenes: A New Family of Promising Catalysts for the Hydrogen Evolution Reaction," *ACS Catal.*, **2017**, 7, 1, 494–500, doi: 10.1021/acscatal.6b02754.

[21] M. Sokol, V. Natu, S. Kota, and M. W. Barsoum, "On the Chemical Diversity of the MAX Phases," *Trends in Chemistry*. **2019**, 1, 2, 210-223, doi: 10.1016/j.trechm.2019.02.016.

[22] N. F. Rosli *et al.*, "MAX and MAB Phases: Two-Dimensional Layered Carbide and Boride Nanomaterials for Electrochemical Applications," *ACS Appl. Nano Mater.* **2019**, 2, 9, 6010-6021, doi: 10.1021/acsanm.9b01526.

[23] X. Tian and K. Zhou, "3D printing of cellular materials for advanced electrochemical energy storage and conversion," *Nanoscale* **2020**, 12, 7416-7432, doi: 10.1039/d0nr00291g.

[24] M. P. Browne, E. Redondo, and M. Pumera, "3D Printing for Electrochemical Energy Applications," *Chem. Rev.* **2020**, 120, 5, 2783-2810, doi: 10.1021/acs.chemrev.9b00783.

Chapter 3. Literature Review

This Chapter summarizes the state-of-the-art related to the two-dimensional (2D) layered materials such as transition metal dichalcogenides (TMDs), MAX phases and MXenes and challenges in their development as electrocatalysts. Additionally, a literature review of the 3D-printed nanocarbon-based electrodes as electrocatalysts for the hydrogen evolution reaction (HER) is presented. This chapter also shows the applicability of scanning electrochemical microscopy (SECM) in the study of the microscopic properties of these materials.

3.1. Two-Dimensional materials

The two-dimensional materials exhibit properties that differ from those of their three-dimensional (3D) counterparts. With the rediscovery of graphene by Andre Geim and Konstantin Novoselov (The Nobel Prize in Physics in 2010) [1], the class of 2D materials has expanded and attracted much attention due to its properties and wide applications. Outstanding electrocatalytic activity, high surface area, and semiconductive nature render them attractive for energy conversion applications and electrochemical water splitting [2-4]. Among various 2D materials, layered materials such as TMDs, MAX phases and MXenes have drawn significant attention as promising catalysts for clean hydrogen production.

3.2. Transition Metal Dichalcogenides

Transition metal dichalcogenides (TMDs) are an emerging class of materials with properties that make them highly attractive for various applications ranging from energy conversion to optoelectronics [5-8]. After the first determination of their structure by Linus Pauling in 1923 [9], the research of TMDs was highly expanded, and around 40 new TMDs with layered structures were found by the late 1960s [10]. This was followed by the first report by Robert Frindt on the use of adhesive tapes for producing ultrathin MoS_2 layers [11]. The fast-growing

research on graphene materials encouraged the development of new technologies suitable for the investigation of layered materials, which enabled further studies of TMDs.

3.2.1. Structure and Properties

This group of 2D layered materials has a general formula of MX_2, which is composed of a transition metal plane (*M*) sandwiched between two hexagonal planes of chalcogen atoms (*X*), as *X-M-X*. **Figure 3.1** illustrates the structure of TMDs. The *M* represents an element from the group IV B (Ti, Zr, Hf), V B (V, Nb, Ta), VI B (Mo, W), or VII B (Tc, Re) and X is a chalcogen atom from VI A group (S, Se, Te). The layered structure is formed by strong in-plane covalent bonding and weak out-plane *Van-der Waals* bonding. In terms of different stacking order between the three atomic planes, the TMDs can be divided into several structural phases, such as 2H and 1T [12], [13].

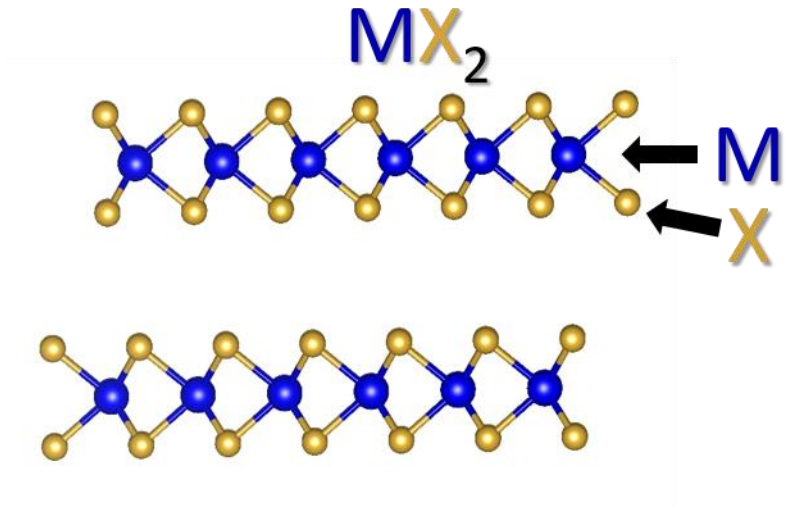

Figure 3.1. Illustration of the general structure of transition metal dichalcogenides with a general formula MX_2. The structure was created in *VESTA*, the program for structure visualization [14].

The diversity of the chemical composition and structural phases of TMDs results in their broad range of electronic properties and band structure character (from metallic to insulating nature). Unlike graphene, a semimetal with a zero band gap, the TMDs possess the tunable band gap that is indirect in multi-layer form and direct in monolayer form [15-18]. Therefore, in order to

tune their electronic properties and electrocatalytic activity, a lot of attention has been given to the exfoliation of TMDs to single-layer materials [19-22]. Among the big library of TMDs, group VI B has attracted significant attention due to the stability and tunable electronic properties of molybdenum disulfide (MoS_2) and tungsten disulfide (WS_2). They occur on the Earth's crust as mineral ores (MoS_2 as the mineral molybdenite and WS_2 as tungstenite). However, only molybdenum in the form of molybdenite can be found in nature in large quantities. Additionally, group IV B, with the leading representatives TiS_2 and $TiSe_2$, has advantages over group VI B due to high conductivity and theoretical capacity, which makes them attractive in energy conversion and storage applications [23-24].

The TMDs are immensely popular as electrocatalysts in electrochemical reactions, such as HER [5-7], [25-28]. The electrochemical investigation performed on the MoS_2 demonstrates the catalytically active edges to be highly responsible for their electrochemical HER activity [29-34]. Additionally, their HER activity was found to be strongly dependent on the density of the vacancies and defects on the electrocatalytic surfaces [35]. Changing the crystals' dimensions from bulk to single-layer structure enhances the HER performance. For instance, the single layer 1T-MoS_2 showed enhanced HER performance compared to the bulk form [36]. Many efforts have been made in the field to improve the HER performance of TMDs by exposing their edge sides and thus increasing the surface area and number of their catalytically active HER sites [28], [37], [38].

In general, the widely used approach for improving the HER activity of TMDs is using a substrate that can facilitate electron injection and improve the chemical properties of the catalysts. Much attention is given to the carbon-based materials such as graphene and carbon nanomaterials as conductive substrates [39]. It is reported that non-stoichiometric MoS_2 and WS_2 electrodeposited on the current collector surfaces have similar or even enhanced electrocatalytic activity compared to 2D MoS_2 and WS_2 [40-42]. Therefore, the

electrodeposition technique opened the way for modifying arbitrary complex current collector surfaces, including 3D-printed surfaces [43-47].

3.2.2. Challenges

1. The electrochemical activity of the edges of the MoS_2 crystals has been widely studied. The critical question is whether such a trend of increased electrocatalytic edges is a phenomenon that generally occurs in the group of 2D materials. Additionally, it is interesting to explore if this trend occurs in the bulk crystals of TMDs.

2. More knowledge about the stability of the bulk TMD crystals during the HER is needed, which is very important for their future application as electrocatalysts.

3. The great challenge in the field lies in combining the TMDs with the 3D-printed nanocarbon electrodes (described later in this *Chapter*) to improve their activity towards HER. In addition, more knowledge is needed about the distribution of the TMD-deposited materials in the porous 3D-printed nanocarbon structure and the distribution of the HER active sites on the TMD-modified 3D-printed nanocarbon electrodes.

3.3. MAX phases and MXenes

Around 50 years ago, Nowotny and co-workers published a review article about their work on synthesizing a large number of layered ternary transition metal carbides and nitrides, which represented an impressive accomplishment for that time [48], [49]. However, it took over 30 years to develop new MAX phases and research their properties when Prof. Barsoum's group published the first detailed study of the oxidation of the Ti_3SiC_2 MAX phase [50]. The breakthrough in the field happened in 2011 with the discovery of the first MXene ($Ti_3C_2T_x$) [51]. Since then, MXenes have become a large and fast-growing family of 2D materials.

3.3.1. Structure and Properties

A family of layered transition metal carbides and nitrides, MAX phases, has attracted great attention due to a unique combination of their metallic and ceramic properties [52], [53]. The general formula of MAX phases can be defined as $M_{n+1}AX_n$, where *M* stands for an early transition metal, *A* is the element from III_A and IV_A group (usually Al), *X* is C or N and $n = 1$, 2, or 3. In general, MAX phases have a hexagonal crystal structure where the *M* and *X* layers are closely packed and interleaved by *A* atoms. The *M-X* bonds are strong and have a mixed covalent/metallic/ionic character. The wide range of elements that can be involved in the MAX phase structure produces a vast number of combinations of theoretically calculated and experimentally synthesized MAX phases [54], [55]. The MAX phases themselves have been reported to possess excellent properties, i.e., good thermal and electrical conductivity, oxidation resistance, damage tolerance, and low toxicity [56], [57]. The rapid development of MAX phase chemistry led to the discovery of new subfamilies of MAX phases, known as double transition metal carbides [58-60]. The relevance of *double transition metal MAX phases*, such as Mo_2TiAlC_2, is in the unique combination of the transition metals and improved electronic and electrochemical properties [61-64].

Unlike graphene and TMDs with layers bonded by weak *Van-der Waals* forces, the *M-A* bond in MAX phases is metallic and cannot be broken by shearing or any other similar mechanical means. Therefore, the strong treatments of MAX phases, such as selective etching of the *A* element with hydrofluoric acid (HF), result in the formation of another group of 2D layered materials, known as MXenes [51], [65]. The MXenes are ternary transition metal carbides and nitrides with the general formula of $M_{n+1}X_nT_x$, where *M* represents an early transition metal (such as Sc, Ti, Zr, V, Nb, Mo or Cr), *X* is the carbon and/or nitrogen and T_x stands for the surface termination (e.g., oxygen, hydroxyl, fluorine, or chlorine). *Van-der Waals* forces bond the MXene sheets, and they can be easily broken into monolayers during the delamination

process [66], [67]. The optimized process for the successful synthesis of $Ti_3C_2T_x$ flakes is described in the recently published paper by Prof. Anasori's group [68]. **Figure 3.2** illustrates the etching (**B**) and delamination (**C**) processes in the MXenes' synthesis from their counterpart MAX phase (**A**). The distinguishing properties of MXenes, including high electronic conductivity [69], electrochemical activity [70], [71], high-temperature stability [72], hydrophilic nature [73], chemical stability [74], optical properties [75], and unique layered structure with rich chemistry have rendered them attractive as the catalysts in energy storage and conversion [76-79], as well as in the applications such as chemical sensors, electromagnetic interference shielding and biomedicine [80-85].

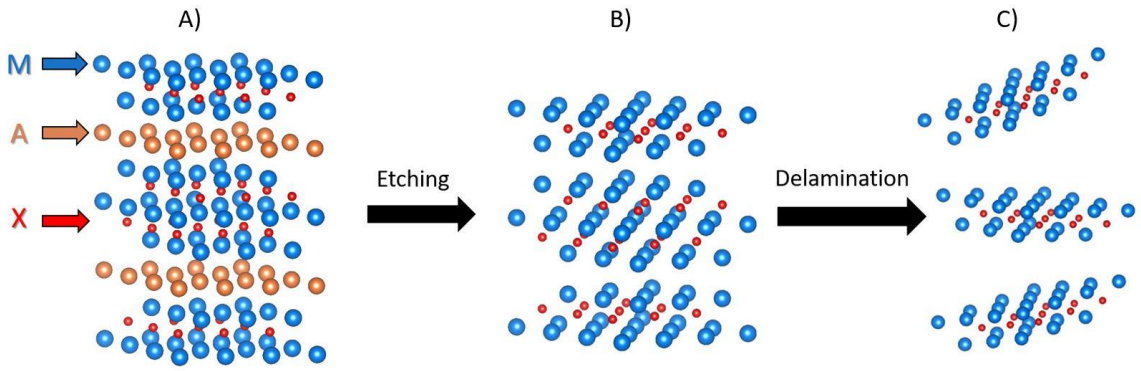

Figure 3.2. Schematic illustration of the MXene synthesis. (**A**) Structure of the MAX phase precursor, (**B**) MXene structure obtained after selective etching of *A* element from the MAX phase and (**C**) delaminated MXene layers. The MAX phase and MXene structures are created in *VESTA*, the program for structure visualization [14].

Similarly to the double transition metal MAX phases, MXenes with two transition metals, known as *double transition metal MXenes*, have attracted significant attention in this 2D family. This breakthrough opened a door for the synthesis of a *sandwiched* structure, where the M sites are occupied by two different transition metals, improving their electrical properties. Additionally, recent developments in the MXene family brought *high-entropy 2D carbides*, which are considered promising materials with outstanding properties [86-88]. Unlike the

traditional mono- and double-transition metal MXenes having the single 2D sheets composed of one type of element, a single sheet of the high-entropy MXenes is built up from several elements (five or more) in high and near equiatomic concentrations. An increase of transition metal elements in the atomic layer minimizes *Gibbs* free energy, forming *stable single-phase high entropy MXenes*. The entropy-stabilization concept offers high durability of high-entropy MXenes, even under harsh thermal and corrosive conditions, which is extremely important for their application in aqueous solutions [89-91].

As a result of the exciting properties of MAX phases and MXenes, they are highly desirable as electrocatalysts. Moreover, their electrocatalytic properties have been investigated recently, and thus, the interest in their application as electrocatalysts has been growing. So far, several review papers about MAX phases and MXene-based materials have summarized their (electro)chemical properties and potential applications [92-95].

Moreover, recent electrochemical studies of different MAX phases have demonstrated their electrochemical performance for energy-related applications such as HER, oxygen reduction reaction (ORR), and oxygen evolution reaction (OER).

In contrast to other widely studied 2D materials, such as TMDs (e.g., MoS_2 and WS_2), featuring catalytically active edges for the HER, the MXenes are reported to have a catalytically active basal plane. The experimental evidence of the catalytic activity of MXene basal plane is provided by *Djire et al.*, who performed the microscopic electrochemical study on the M-$Ti_4N_3T_x$ MXene nanoflakes and demonstrated the basal plane of the MXene nanoflakes to be highly active compared to the edge sides due to the primarily exposed metallic sites for the proton adsorption [96].

Recent studies focusing on the MXene surface chemistry have shown the surface termination (T_x) and type of the *M* element in the MXene structure to be highly important for tuning their properties for HER performance [97]. In addition, the density functional theory (DFT)

calculations of the $Ti_3C_2T_x$ MXenes predicted a strong influence of the surface termination type on MXenes' work function and electronic band [98]. Furthermore, the etching and delamination conditions used in the MXene synthesis and the post-synthesis treatments were found to have a strong influence on the MXene surface termination and oxidation stability of MXenes [99].

3.3.2. Challenges

1. More knowledge about microscopic HER activity of MAX phases is needed, since it is crucial for understanding of their electrocatalytic properties and their further improvements as electrocatalysts.

2. Electrochemical studies of powder-based materials, such as MXenes, need a special electrode preparation that requires solvent media. The influence of the solvent used in the preparation of the particle-based samples can alter the distribution and elemental composition of the drop-casted particles and, therefore, affect the electrochemical activity of the particle-based samples. Since the polar surface of MXenes allows their dispersion in different solvent media [100], it is of the utmost importance to investigate the influence of the MXene surface chemistry on their electrochemical activity.

3.4. 3D-printed Nanocarbon Electrodes

The development of new technologies has brought 3D-printing, the additive manufacturing technique that enables the fast production of simple and complex devices with a specific shape and composition [101], [102]. Its involvement in electrochemistry is growing, especially in the fabrication of conductive devices for energy conversion and storage applications [103-105]. In the last few years, it has been considered as an eco-friendly technology for the large-scale and low-cost production of electrochemical devices.

Among various 3D-printing methods, Fused Deposition Modelling (FDM) is one of the most widely used for the fabrication of 3D-devices [106], [107]. The main principle of this technique is based on the filament extrusion through a heated nozzle to build the printed objects layer-by-

layer [108], [109]. It involves the use of thermoplastic materials such as polylactic acid (PLA), acrylonitrile butadiene styrene (ABS), polycarbonate (PC), polyamide (PA) etc. [104]. These materials are usually provided in a filament form as feeding spools. Additionally, different polymer-nanocarbon blends were tested for 3D-printing application, while polystyrene was identified as the best-performing matrix material for application in aqueous media [110]. The active 2D materials (such as MoS_2) are blended with the nanocarbon-based polymer to form the conductive filament that is afterwards used to fabricate the electrochemical devices [111]. Furthermore, the utilization of the nanocarbon-based materials is extended with the nanocarbon/polymer filaments. The commercially available nanocarbon/PLA filament (Black Magic ®) has emerged as the most commonly used 3D-printing material for electrochemical applications such as energy conversion and storage [112]. Due to the insulating issues of the commercially available filaments, the 3D-printed structures are reported to be low electrochemically active [113]. In order to solve this drawback and improve the performance and applicability of the 3D-printed devices, post-printing treatments such as thermal annealing, chemical activation, or additional surface modifications are applied [46], [103], [114]. **Figure 3.3** illustrates the post-printing treatments of the 3D-printed electrodes. Thermal annealing, chemical and electrochemical activation are used to remove insulating PLA from nanocarbon/PLA filament and thus make the 3D-printed devices conductive. Moreover, the electrochemical activity of the thermally activated electrodes is found to be higher compared to the chemically activated electrodes when solvents such as NaOH, DMF and $NaBH_4$, etc., are used for the electrode activation [115], [116]. Interestingly, the treated electrodes made from the commercial Black Magic are found to have a high surface area. They also contain metal-oxide impurities, including Fe_3O_4 and TiO_2, which are reported to be responsible for their improved catalytic activity [117], [118]. Namely, the change in the electrochemical response before and after treatment was related to the increase in the amount of these impurities on the

surface, thus leading to an improved catalytic performance. Furthermore, the porous surface of the activated 3D-printed electrodes makes them highly attractive for energy conversion applications.

The main advantage of 3D-printing is its versatility, which opens endless possibilities associated with the geometry, porosity, size, and mechanical properties of 3D-printed devices by tuning their catalytic activity. Recently, metal-based filaments (such as Cu-based) have been used for the fabrication of 3D-printed electrodes to improve their electrochemical performance [119-122].

Regardless of the route taken to tackle the problem with the low conductivity and electrochemical limitations of the as-printed electrodes, additional modification of the activated 3D-printed surfaces is needed to enhance their electrochemical performance for specific applications, such as HER. There are various ways to modify 3D-printed electrodes, such as electrodeposition, atomic layer deposition (ALD) and anodization [46], [105], [122-124], as illustrated in **Figure 3.3**. Among them, electrodeposition has been used extensively to grow the layer(s) of the active material on the 3D-printed electrode surfaces. Furthermore, the electrochemical activity for the HER of the modified electrodes varies depending on the material used for the electrode modification.

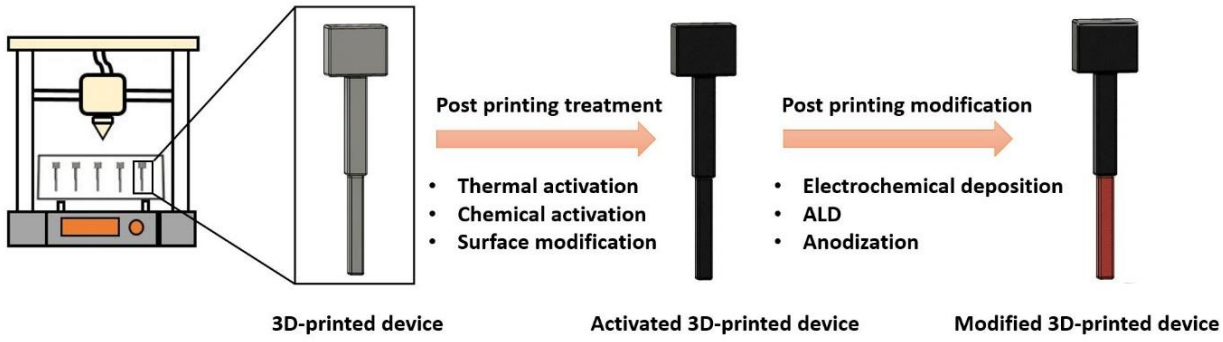

Figure 3.3. Schematic illustration of the post-printing treatments of 3D-printed electrodes.

Table 3.1. summarizes the HER overpotential measured at the current density of -10 mA cm^{-2} and Tafel slope values of different catalysts supported on the 3D-printed electrode surfaces.

Table 3.1. Table showing the comparison of the active catalysts supported on the 3D-printed platform for hydrogen evolution reaction.

Catalyst	Electrolyte	HER overpotential at -10 mA cm^{-2} (V vs RHE)	Tafel slope / mV dec^{1}	Ref.
Ni-modified 3D*-steel	1M KOH	- 0.40	131	[53]
MoS_2-modified-3D-steel	1M KOH	- 0.35	120	[53]
Ni-MoS_2-modified-3D-steel	1M KOH	- 0.30	106	[53]
$NiCo_2S_4$-spray coated 3D	0.5M H_2SO_4	- 0.226	38.7	[130]
ReS_2@3D	0.5 M H_2SO_4	- 0.28	147	[52]
MoS_2 spray coated 3D	0.5 M H_2SO_4	~- 0.55	N/A**	[46]
$MoS_{3-\delta}$@3D	0.5 M H_2SO_4	- 0.298	119	[50]
MoS_2@3D	0.5 M H_2SO_4	- 0.28	220	[125]***
WS_2@3D	0.5 M H_2SO_4	- 0.53	168	[125]***
MoS_2@WS_2@3D	0.5 M H_2SO_4	- 0.32	152	[125]***
WS_2@MoS_2@3D	0.5 M H_2SO_4	- 0.43	190	[125]***
Cu-3D electrodes	0.5 M H_2SO_4	- 0.523	147	[126]
Pd@Cu-3D	0.5 M H_2SO_4	- 0.435	188	[127]

*3D - 3D printed electrode; ** N/A – not available, *** work presented in this Thesis

3.4.1. Challenges

The biggest challenge in this field lies in a deeper understanding of the surface chemistry and electrochemical performance of activated and modified 3D-printed electrodes. This is of crucial importance for the further development of the 3D-printing technology in the electrochemical-related applications.

3.5. SECM in the Study of Electrocatalytic Materials

The fast-growing role of layered 2D materials in energy conversion applications makes understanding their electrocatalytic properties and applicability vital. The electrochemical activity of 2D materials is studied by traditional techniques, such as cyclic voltammetry (CV) and linear sweep voltammetry (LSV), where the potential is cycled or swapped linearly (**Chapter 5.1**). At the same time, the measured current allows the determination of the averaged macroscopic electrochemical performance of the catalytic material. In addition, the essential properties of 2D materials, such as catalytic activity, conductivity, and electrochemical activity, can differ along their edges, at defect sites, or upon folding and stacking. However, the variations in the electrocatalytic activity of these imperfections on the material surface cannot be measured by traditional techniques, which limits the knowledge of the local activity of catalysts. This is notably the case for the HER, where the homogeneity/heterogeneity over the catalytic surface plays a crucial role in the electrocatalytic performance of materials [128]. In order to gain a profound knowledge of the localized electrochemistry on the material surfaces, the scanning probe technique, such as scanning electrochemical microscopy (SECM), has been used to study the electrochemical activity of different electrocatalytic materials. A detailed explanation of the SECM principles is shown in **Chapter 5.2**. The SECM combines a standard three-electrode setup with a micro- to nano-sized probe whose movement across the substrate is controlled by a 3D-positioning system. Since it was first presented by *Bard and co-workers* as an electrochemical tool analyzing catalysts in 1980' [129], SECM has been widely applied in electrocatalyst research. It is used for scanning the catalytic surfaces by reflecting the surface morphology, conductivity, and electrochemical activity, as well as mapping the location and distribution of the HER active sites with the resolution determined by the probe size [130-132]. This technique is employed to address the microscopic electrochemical activity of different materials ranging from crystals to nanoparticles. Due to the fact that the individual particles'

size, geometry and orientation strongly influence the catalytic activity, the SECM is used for the microscopic study of the particles at the level of a single particle [133-136]. For instance, it was employed in the study of different individual metal nanoparticles such as Au [137], [138], Ag [139], [140], Pd [141], Pt [142], Ni-ZrO_2 [143] and IrO_x [144], to investigate their microscopic catalytic activity. In addition, it was used in the study of Pt nanoparticle catalysts, which had a differently controlled shape to spot the differences in their catalytic activity [145]. The SECM was also applied in the differential analysis of the catalytic activity of the edge and basal plane of nickel oxide (NiO) nanosheets, reflecting the morphology and activity of their basal planes [146].

The versatility of SECM matches the diversity of 2D materials. Thus, it was performed in the study of the electrochemical activity of different TMDs and MXenes. The SECM revealed the differences in HER performance of the basal plane and edge site on the MoS_2 crystal [147-151]. Apart from the SECM micrographs, *Unwin et al*. used SECM to electrochemically scan the surface of MoS_2 nanoflakes, providing information about the real-time changes in their HER performance [152]. Furthermore, it was used for localized deposition and microstructuring of MoS_x electrocatalysts [153]. Additionally, it was performed in the study of MXenes, providing experimental evidence of the electrochemical activity of the MXenes' basal plane [96].

Subsequently, the SECM found its application in the research of 3D-printed electrodes. For instance, the SECM study of the 3D-printed electrodes showed how printing conditions affect the dispersion of graphite particles in the PLA matrix [154]. The SECM was used in the research of the electrocatalysts deposited on the 3D-printed current collectors. For example, the microscopic analysis of the HER activity of MoS_2, ReS_2, and Al_2O_3 coatings on the 3D-printed electrodes was performed to spot the local differences in their topography and HER performance [43], [45].

The SECM studies of different 2D materials provide relevant knowledge about the microscopic electrochemical characterization of the catalytic surfaces and offer insight into the imaging of electrocatalytically active sites. Therefore, its use in the study of layered 2D materials is of the utmost importance since it would lead to the systematic improvement of these catalytic materials for their applications in energy conversion and clean hydrogen production.

3.6. References

[1] A. K. Geim and K. S. Novoselov, "The rise of graphene," in *Nanoscience and Technology: A Collection of Reviews from Nature Journals*, **2009**, 11-19.

[2] A. J. Mannix, B. Kiraly, M. C. Hersam, and N. P. Guisinger, "Synthesis and chemistry of elemental 2D materials," *Nat. Rev. Chem.* **2017**, l, 1–15, doi: 10.1038/s41570-016-0014.

[3] D. Akinwande, C. J. Brennan, J. S. Bunch, P. Egberts, J. R. Felts, H. Gao, R. Huang, J-S. Kim, T. Li, Y. Li, K. M. Liechti, N. Lu, H. S. Park, E. J. Reed, P. Wang, B. I. Yakobson, T. Zhang, Y-W. Zhang, Y. Zhou, Y. Zhu, "A review on mechanics and mechanical properties of 2D Materials-Graphene and beyond," *Extrem. Mech. Lett.* **2017**, 13, 42–77, doi: 10.1016/j.eml.2017.01.008.

[4] R. Mas-Ballesté, C. Gómez-Navarro, J. Gómez-Herrero, and F. Zamora, "2D materials: To graphene and beyond," *Nanoscale* **2011**, 3, 1, 20–30, doi: 10.1039/c0nr00323a.

[5] M. Pumera, Z. Sofer, and A. Ambrosi, "Layered transition metal dichalcogenides for electrochemical energy generation and storage," *J. Mater. Chem. A* **2014**, 2, 8981-8987, doi: 10.1039/c4ta00652f.

[6] J. Yang and H. S. Shin, "Recent advances in layered transition metal dichalcogenides for hydrogen evolution reaction," *J. Mater. Chem. A* **2014**, 2, 5979-5985, doi: 10.1039/c3ta14151a.

[7] Q. Fu, J. Han, X. Wang, P. Xu, T. Yao, J. Zhong, W. Zhong, S. Liu, T. Gao, Z. Zhang, L. Xu, B. Song., "2D Transition Metal Dichalcogenides: Design, Modulation, and Challenges in Electrocatalysis," *Adv. Mater.* **2020**, 33, 6, 1907818, doi: 10.1002/adma.201907818.

[8] K. F. Mak and J. Shan, "Photonics and optoelectronics of 2D semiconductor transition metal dichalcogenides," *Nat. Photonics* **2016**, 10, 4, 216–226, doi: 10.1038/nphoton.2015.282.

[9] K. Waltersson, "The crystal structure of $Cs[VOF_3]\cdot 12\ H_2O$," *J. Solid State Chem.* **1979**, 28, 1, 121–131, doi: 10.1016/0022-4596(79)90064-1.

[10] J. A. Wilson and A. D. Yoffe, "The transition metal dichalcogenides discussion and interpretation of the observed optical, electrical and structural properties," *Adv. Phys.* **1969**, 18, 73, 193–335, doi: 10.1080/00018736900101307.

[11] R. F. Frindt and A. D. Yoffe, "Physical properties of layer structures: optical properties and photoconductivity of thin crystals of molybdenum disulphide," *Proc. R. Soc. London. Ser. A. Math. Phys. Sci.* **1963**, 273, 1352, 69–83, doi: 10.1098/rspa.1963.0075.

[12] S. Manzeli, D. Ovchinnikov, D. Pasquier, O. V. Yazyev, and A. Kis, "2D transition metal dichalcogenides," *Nat. Rev. Mater.* **2017**, 2, doi: 10.1038/natrevmats.2017.33.

[13] D. Voiry, A. Mohite, and M. Chhowalla, "Phase engineering of transition metal dichalcogenides," *Chem. Soc. Rev.* **2015**, 44, 9, 2702–2712, doi: 10.1039/c5cs00151j.

[14] K. Momma and F. Izumi, "VESTA: A three-dimensional visualization system for electronic and structural analysis," *J. Appl. Crystallogr.* **2008**, 41, 653-658, doi: 10.1107/S0021889808012016.

[15] Q. H. Wang, K. Kalantar-Zadeh, A. Kis, J. N. Coleman, and M. S. Strano, "Electronics and optoelectronics of two-dimensional transition metal dichalcogenides," *Nat. Nanotechnol.* **2012**, 7, 11, 699–712, doi: 10.1038/nnano.2012.193.

[16] A. Splendiani, L. Sun, Y. Zhang, T. Li, J. Kim, C-Y. Chim, G. Galli, F. Wang, "Emerging photoluminescence in monolayer MoS_2," *Nano Lett.* **2010**, 10, 4, 1271–1275, doi: 10.1021/nl903868w.

[17] L. Pi, L. Li, K. Liu, Q. Zhang, H. Li, and T. Zhai, "Recent Progress on 2D Noble-Transition-Metal Dichalcogenides," *Adv. Funct. Mater.* **2019**, 29, 51, doi: 10.1002/adfm.201904932.

[18] X. Lin, W. Li, Y. Dong, C. Wang, Q. Chen, and H. Zhang, "Two-dimensional metallic MoS_2: A DFT study," *Comput. Mater. Sci.* **2016**, 124, 49–53, doi: 10.1016/j.commatsci.2016.07.020.

[19] A. Anto Jeffery, C. Nethravathi, and M. Rajamathi, "Two-dimensional nanosheets and layered hybrids of MoS_2 and WS_2 through exfoliation of ammoniated MS_2 (M = Mo, W)," *J. Phys. Chem. C* **2014**, 118, 2, 1386–1396, doi: 10.1021/jp410918c.

[20] A. Jawaid, D. Nepal, K. Park, M. Jespersen, A. Qualley, P. Mirau, L. F. Drummy, R. A. Vaia, Mechanism for Liquid Phase Exfoliation of MoS_2," *Chem. Mater.* **2016**, 28, 1, 337–348doi: 10.1021/acs.chemmater.5b04224.

[21] D. Xu, P. Xu, Y. Zhu, W. Peng, Y. Li, G. Zhang, F. Zhang, T. E. Mallouk, X. Fan, "High Yield Exfoliation of WS_2 Crystals into 1-2 Layer Semiconducting Nanosheets and Efficient Photocatalytic Hydrogen Evolution from WS_2/CdS Nanorod Composites," *ACS Appl. Mater. Interfaces* **2018**, 10, 3, 2810–2818, doi: 10.1021/acsami.7b15614.

[22] X. Hai, K. Chang, H. Pang, M. Li, P. Li, H. Liu, L. Shi, J. Ye, "Engineering the Edges of MoS_2 (WS_2) Crystals for Direct Exfoliation into Monolayers in Polar Micromolecular Solvents," *J. Am. Chem. Soc.* **2016**, 138, 45, 14962–14969 doi: 10.1021/jacs.6b08096.

[23] H. Tao, M. Zhou, R. Wang, K. Wang, S. Cheng, K. Jiang, "TiS_2 as an advanced con- version electrode for sodium-ion batteries with ultra-high capacity and long- cycle life," *Adv. Sci.* **2018**, 5 (11), 1801021, doi: 10.1002/advs.201801021.

[24] P. Li, X. Zheng, H. Yu, G. Zhao, J. Shu, X. Xu, W. Sun, S.X. Dou, "Electrochemical potassium/lithium-ion intercalation into $TiSe_2$: kinetics and mechanism," *Energy Stor. Mater.* **2019**, 16, 512–518, doi: 10.1016/j.ensm.2018.09.014.

[25] X. Chia and M. Pumera, "Layered transition metal dichalcogenide electrochemistry: journey across the periodic table," *Chem. Soc. Rev.* **2018**, 47, 15, 5602–5613, doi: 10.1039/c7cs00846e.

[26] Q. Lu, Y. Yu, Q. Ma, B. Chen, and H. Zhang, "2D Transition-Metal-Dichalcogenide-Nanosheet-Based Composites for Photocatalytic and Electrocatalytic Hydrogen Evolution Reactions," *Advanc. Mater*. **2016**, 28, 10, 1917-1933, doi: 10.1002/adma.201503270.

[27] F. Wang, T. A. Shifa, X. Zhan, Y. Huang, K. Liu, Z. Cheng, C. Jiang, J. He, "Recent advances in transition-metal dichalcogenide based nanomaterials for water splitting," *Nanoscale* **2015**, 7, 19764-19788, doi: 10.1039/c5nr06718a.

[28] X. Chia, Z. Sofer, J. Luxa, and M. Pumera, "Layered Noble Metal Dichalcogenides: Tailoring Electrochemical and Catalytic Properties," *ACS Appl. Mater. Interfaces* **2017**, 9, 30, 25587–25599, doi: 10.1021/acsami.7b05083.

[29] Y. Yan, B. Xia, X. Ge, Z. Liu, J. Y. Wang, and X. Wang, "Ultrathin MoS_2 nanoplates with rich active sites as highly efficient catalyst for hydrogen evolution," *ACS Appl. Mater. Interfaces* **2013**, 5, 24, 12794–12798, doi: 10.1021/am404843b.

[30] T. F. Jaramillo, K. P. Jørgensen, J. Bonde, J. H. Nielsen, S. Horch, and I. Chorkendorff, "Identification of active edge sites for electrochemical H_2 evolution from MoS_2 nanocatalysts," *Science (80-.)* **2007**, 317, 5834, 100–102, doi: 10.1126/science.1141483.

[31] G. Li, D. Zhang, Q. Qiao, Y. Yu, D. Peterson, A. Zafar, R. Kumar, S. Curtarolo, F. Hunte, S. Shannon, Y. Zhu, W. Yang, L. Cao, "All the Catalytic Active Sites of MoS_2 for Hydrogen Evolution," *J. Am. Chem. Soc.*, **2016**, 138, 51, 16632–16638, doi: 10.1021/jacs.6b05940.

[32] J. Xie, H. Zhang, S. Li, R. Wang, X. Sun, M. Zhou, J. Zhou, X. Wen (David) Lou, Y. Xie, "Defect-rich MoS_2 ultrathin nanosheets with additional active edge sites for enhanced electrocatalytic hydrogen evolution," *Adv. Mater*. **2013**, 25, 40, 5807-5813, doi: 10.1002/adma.201302685.

[33] J. Zhang, J. Wu, H. Guo, W. Chen, J. Yuan, U. Martinez, G. Gupta, A. Mohite, P. M. Ajayan, J. Lou, "Unveiling Active Sites for the Hydrogen Evolution Reaction on Monolayer MoS_2," *Adv. Mater*. **2017**, 29, 42, 1701955, doi: 10.1002/adma.201701955.

[34] L. Li, Z. Qin, L. Ries, S. Hong, T. Michel, J. Yang, C. Salameh, M. Bechelany, P. Miele, D. Kaplan, M. Chhowalla, D. Voiry, "Role of sulfur vacancies and undercoordinated Mo regions in MoS_2 nanosheets toward the evolution of hydrogen," *ACS Nano* **2019**, 13, 6, 6824–6834, doi: 10.1021/acsnano.9b01583.

[35] A. Y. S. Eng, A. Ambrosi, Z. Sofer, P. Šimek, and M. Pumera, "Electrochemistry of transition metal dichalcogenides: Strong dependence on the metal-to-chalcogen composition and exfoliation method," *ACS Nano* **2014**, 8, 12, 12185–12198, doi: 10.1021/nn503832j.

[36] M. A. Lukowski, A. S. Daniel, F. Meng, A. Forticaux, L. Li, and S. Jin, "Enhanced hydrogen evolution catalysis from chemically exfoliated metallic MoS_2 nanosheets," *J. Am. Chem. Soc.* **2013**, 135, 28, 10274–10277, doi: 10.1021/ja404523s.

[37] X. Chia, A. Y. S. Eng, A. Ambrosi, S. M. Tan, and M. Pumera, "Electrochemistry of Nanostructured Layered Transition-Metal Dichalcogenides," *Chem. Rev.* **2015**, 115, 21, 11941–

11966 doi: 10.1021/acs.chemrev.5b00287.

[38] L. Cheng, W. Huang, Q. Gong, C. Liu, Z. Liu, Y. Li, H. Dai, "Ultrathin WS_2 nanoflakes as a high-performance electrocatalyst for the hydrogen evolution reaction," *Angew. Chemie - Int. Ed.* **2014**, 53, 30, 7860–7863, doi: 10.1002/anie.201402315.

[39] Z. Pu, Q. Liu, A. M. Asiri, A. Y. Obaid, and X. Sun, "One-step electrodeposition fabrication of graphene film confined WS_2 nanoparticles with enhanced electrochemical catalytic activity for hydrogen evolution," *Electrochim. Acta* **2014**, 134, 8–12, doi: 10.1016/j.electacta.2014.04.092.

[40] X. Chia, N. A. A. Sutrisnoh, and M. Pumera, "Tunable Pt-MoS_x Hybrid Catalysts for Hydrogen Evolution," *ACS Appl. Mater. Interfaces* **2018**, 10, 10, 8702–8711, doi: 10.1021/acsami.7b19346.

[41] S. M. Tan, Z. Sofer, J. Luxa, and M. Pumera, "Aromatic-Exfoliated Transition Metal Dichalcogenides: Implications for Inherent Electrochemistry and Hydrogen Evolution," *ACS Catal.* **2016**, 6, 7, 4594–4607, doi: 10.1021/acscatal.6b00761.

[42] X. J. Chua, J. Luxa, A. Y. S. Eng, S. M. Tan, Z. Sofer, and M. Pumera, "Negative Electrocatalytic Effects of p-Doping Niobium and Tantalum on MoS_2 and WS_2 for the Hydrogen Evolution Reaction and Oxygen Reduction Reaction," *ACS Catal.* **2016**, 6, 9, 5724–5734, doi: 10.1021/acscatal.6b01593.

[43] C. Iffelsberger, S. Ng, and M. Pumera, "Catalyst coating of 3D printed structures via electrochemical deposition: Case of the transition metal chalcogenide MoS_x for hydrogen evolution reaction," *Appl. Mater. Today* **2020**, 20, 100654, doi: 10.1016/j.apmt.2020.100654.

[44] K. Ghosh, S. Ng, C. Iffelsberger, and M. Pumera, "ReS_2: A high-rate pseudocapacitive energy storage material," *ACS Appl. Energy Mater.* **2020**, 3, 10, 10261–10269, doi: 10.1021/acsaem.0c02187.

[45] S. Ng, C. Iffelsberger, Z. Sofer, and M. Pumera, "Tunable Room-Temperature Synthesis of ReS_2 Bicatalyst on 3D- and 2D-Printed Electrodes for Photo- and Electrochemical Energy Applications," *Adv. Funct. Mater.* **2020**, 30, 19, 191019, doi: 10.1002/adfm.201910193.

[46] A. Ambrosi and M. Pumera, "Multimaterial 3D-Printed Water Electrolyzer with Earth-Abundant Electrodeposited Catalysts," *ACS Sustain. Chem. Eng.* **2018**, 6, 12, 16968–16975, doi: 10.1021/acssuschemeng.8b04327.

[47] C. Zhu, T. Liu, F. Qian, W. Chen, S. Chandrasekaran, B. Yao, Y. Song, E. B. Duoss, J. D. Kuntz, C. M. Spadaccini, M. A. Worsley, Y. Li, "3D printed functional nanomaterials for electrochemical energy storage," *Nano Today* **2017**, 15, 107-120, doi: 10.1016/j.nantod.2017.06.007.

[48] V. H. Nowotny, "Strukturchemie einiger Verbindungen der Übergangsmetalle mit den elementen C, Si, Ge, Sn," *Prog. Solid State Chem.* **1971**, 5, C, 27–70, doi: 10.1016/0079-6786(71)90016-1.

[49] H. Nowotny, P. Rogl, and J. C. Schuster, "Structural chemistry of complex carbides and related

compounds," *J. Solid State Chem.* **1982**, 44, 1, 126–133, doi: 10.1016/0022-4596(82)90409-1.

[50] M. Barsoum, "Synthesis and Characterization of a Remarkable Ceramic Ti_3SiC_2", *J. Am. Ceram. Soc.* **1996**, 79, 7, 1953-1956, doi.org/10.1111/j.1151-2916.1996.tb08018.x.

[51] M. Naguib *et al.*, "Two-dimensional nanocrystals produced by exfoliation of Ti_3AlC_2," *Adv. Mater*. **2011**, 23, 37, 4248–4253, doi: 10.1002/adma.201102306.

[52] M. Radovic and M. W. Barsoum, "MAX phases: Bridging the gap between metals and ceramics," *Am. Ceram. Soc. Bull.* **2013.**

[53] M. Barsoum and T. El-Raghy, "The MAX Phases: Unique New Carbide and Nitride Materials," *Am. Sci.* **2001**, 89, 4, 334-343, doi: 10.1511/2001.4.334.

[54] M. Sokol, V. Natu, S. Kota, and M. W. Barsoum, "On the Chemical Diversity of the MAX Phases," *Trends Chem*. **2019**, 1, 2, 210-223, doi: 10.1016/j.trechm.2019.02.016.

[55] M. Benchakar, L. Loupias, C. Garnero, T. Bilyk, C. Morais, C. Canaff, N. Guignard, S. Morisset, H. Pazniak, S. Hurand, P. Chartier, J. Pacaud, V. Mauchamp, M. W. Barsoum, A. Habrioux, S. Célérier, "One MAX phase, different MXenes: A guideline to understand the crucial role of etching conditions on $Ti_3C_2T_x$ surface chemistry," *Appl. Surf. Sci.* **2020**, 530, doi: 10.1016/j.apsusc.2020.147209.

[56] Z. M. Sun, "Progress in research and development on MAX phases: A family of layered ternary compounds," *Int. Mater. Rev.* **2011**, 56, 3, 143-166, doi: 10.1179/1743280410Y.0000000001.

[57] D. Sauceda, P. Singh, A. R. Falkowski, Y. Chen, T. Doung, G. Vazquez, M. Radovic, R. Arroyave, "High-throughput reaction engineering to assess the oxidation stability of MAX phases," *npj Comput. Mater.* **2021**, 7, 6, doi: 10.1038/s41524-020-00464-7.

[58] E. Drouelle, V. Brunet, J. Cormier, P. Villechaise, P. Sallot, F. Naimi, F. Bernard, S. Dubois, "Oxidation resistance of Ti_3AlC_2 and $Ti_3Al_{0.8}Sn_{0.2}C_2$ MAX phases: A comparison," *J. Am. Ceram. Soc.* **2020**, 103, 2, 1270-1280, doi: 10.1111/jace.16780.

[59] B. Anasori, C. Shi, E. J. Moon, Y. Xie, C. A. Voigt, P. R. C. Kent, S. J. May, S. J. L. Billinge, M. W. Barsoum, Y. Gogosi, "Control of electronic properties of 2D carbides (MXenes) by manipulating their transition metal layers," *Nanoscale Horiz.* **2016**, 1, 227-234, doi: 10.1039/c5nh00125k.

[60] M. Khazaei, A. Ranjbar, K. Esfarjani, D. Bogdanovski, R. Dronskowski, and S. Yunoki, "Insights into exfoliation possibility of MAX phases to MXenes," *Phys. Chem. Chem. Phys.* **2018**, 20, 13, 8579–8592, doi: 10.1039/c7cp08645h.

[61] Y. F. Li, Y. C. Ding, B. Xiao, and Y. H. Cheng, "Anisotropic electrical and lattice transport properties of ordered quaternary phases Cr_2TiAlC_2 and Mo_2TiAlC_2: A first principles study," *Phys. Lett. Sect. A Gen. At. Solid State Phys.* **2016**, 380, 44, 3748-3755, doi: 10.1016/j.physleta.2016.09.015.

[62] B. Anasori, M. Dahlqvist, J. Lu, L. Hultman, P. Eklund, J. Rosén, J. Halim, J. E. Moon, C. B. Hosler, J. S. May, N. E. Caspi, "Experimental and theoretical characterization of ordered MAX

phases Mo_2TiAlC_2 and $Mo_2Ti_2AlC_3$," *J. Appl. Phys.* **2015**, 118, 094304, doi: 10.1063/1.4929640.

[63] B. Anasori, J. Halim, J. Lu, C. A. Voigt, L. Hultman, and M. W. Barsoum, "Mo_2TiAlC_2: A new ordered layered ternary carbide," *Scr. Mater.* **2015**, 101, 5–7, doi: 10.1016/j.scriptamat.2014.12.024.

[64] K. P. Akshay Kumar, O. Alduhaish, and M. Pumera, "Electrocatalytic activity of layered MAX phases for the hydrogen evolution reaction," *Electrochem. Commun.* **2021**, 125, 106977, doi: 10.1016/j.elecom.2021.106977.

[65] Y. Gogotsi and B. Anasori, "The Rise of MXenes," *ACS Nano* **2019**, 13, 8, 8491–8494, doi: 10.1021/acsnano.9b06394.

[66] M. Naguib, O. Mashtalir, J. Carle, V. Presser, J. Lu, L. Hultman, Y. Gogotsi, M. W. Barsoum, "Two-dimensional transition metal carbides," *ACS Nano* **2012**, 2, 1322–1331, doi: 10.1021/nn204153h.

[67] B. Anasori, M. R. Lukatskaya, and Y. Gogotsi, "2D metal carbides and nitrides (MXenes) for energy storage," *Nat. Rev. Mater.* **2017**, 2, 16098, doi: 10.1038/natrevmats.2016.98.

[68] A. Thakur, N. Chandran B. S., K. Davison, A. Bedford, H. Fang, Y. Im, V. Kanduri, B. C. Wyatt, S. K. Nemani, V. Poliukhova, R. Kumar, Z. Fakhraai, B. Anasori, "Step-by-Step Guide for Synthesis and Delamination of $Ti_3C_2T_x$ MXene," *Small Methods* **2023**, 2300030, doi: 10.1002/smtd.202300030.

[69] J. L. Hart, K. Hantanasirisakul, A. C. Lang, N. Anasori, D. Pinto, Y. Pivak, J. Tijin van Omme, S. J. May, Y. Gogotsi, M. L. Taheri, "Control of MXenes' electronic properties through termination and intercalation," *Nat. Commun.* **2019**, 10, 522, doi: 10.1038/s41467-018-08169-8.

[70] Z. W. She, K. D. Fredrickson, B. Anasori, J. Kibsgaard, A. L. Strickler, M. R. Lukatskaya, Y. Gogotsi, T. F. Jaramillo, A. Vojvodic, "Two-Dimensional Molybdenum Carbide (MXene) as an Efficient Electrocatalyst for Hydrogen Evolution," *ACS Energy Lett.* **2016**, 1, 3, 589-594, doi: 10.1021/acsenergylett.6b00247.

[71] H. Wang and J. M. Lee, "Recent advances in structural engineering of MXene electrocatalysts," *J. Mater. Chem. A.* **2020**, 8, 10604-10624, doi: 10.1039/d0ta03271a.

[72] M. Seredych, C. Eugene Shuck, D. Pinto, M. Alhabeb, E. Precetti, G. Deysher, B. Anasori, N. Kurra, Y. Gogotsi, "High-Temperature Behavior and Surface Chemistry of Carbide MXenes Studied by Thermal Analysis," *Chem. Mater.* **2019**, 31, 9, 3324–3332, doi: 10.1021/acs.chemmater.9b00397.

[73] Y. Zhang, L. Wang, N. Zhang, and Z. Zhou, "Adsorptive environmental applications of MXene nanomaterials: A review," *RSC Adv.* **2018**, 8, 19895-19905, doi: 10.1039/c8ra03077d.

[74] Y.-J. Wan, K. Rajavel, X.-M. Li, X.-Y. Wang, S.-Y. Liao, Z.-Q. Lin, P.-L. Zhu, R. Sun, C.-P. Wong, "Electromagnetic interference shielding of $Ti_3C_2T_x$ MXene modified by ionic liquid for high chemical stability and excellent mechanical strength," *Chem. Eng. J.* **2021**, 408, 15, 127303, doi: 10.1016/j.cej.2020.127303.

[75] L. Gao, H. Chen, A. V. Kuklin, S. Wageh, A. A. Al-Ghamdi, H. Agren, H. Zhang, "Optical Properties of Few-Layer Ti_3CN MXene: From Experimental Observations to Theoretical Calculations," *ACS Nano* **2022**, 16, 2, 3059–3069, doi: 10.1021/acsnano.1c10577.

[76] Y. Wei, R. A. Soomro, X. Xie, and B. Xu, "Design of efficient electrocatalysts for hydrogen evolution reaction based on 2D MXenes," *J. Energy Chem.* **2021**, 55, 244-255, doi: 10.1016/j.jechem.2020.06.069.

[77] M. R. Lukatskaya, O. Mashtalir, C. E. Ren, Y. Dall`Agnese, P. Rozier, P. L. Taberna, M. Naguib, P. Simon, M. W. Barsoum, Y. Gogotsi, "Cation intercalation and high volumetric capacitance of two-dimensional titanium carbide," *Science (80-.)* **2013**, doi: 10.1126/science.1241488.

[78] Y. Xia, T. S. Mathis, M.-Q. Zhao, B. Anasori, A. Dang, Z. Zhou, H. Cho, Y. Gogotsi, S. Yang, "Thickness-independent capacitance of vertically aligned liquid-crystalline MXenes," *Nature* **2018**, 557, 409-412, doi: 10.1038/s41586-018-0109-z.

[79] E. Redondo and M. Pumera, "MXene-functionalised 3D-printed electrodes for electrochemical capacitors," *Electrochem. Commun.* **2021**, 124, 106920, doi: 10.1016/j.elecom.2021.106920.

[80] Y. Z. Zhang, K. H. Lee, D. H. Anjum, R. Sougrat, Q. Jiang, H. Kim, H. N. Alshareef, "MXenes stretch hydrogel sensor performance to new limits," *Sci. Adv.*, **2018**, 4, 6, doi: 10.1126/sciadv. aat0098.

[81] P. Mayorga-Burrezo, J. Muñoz, D. Zaoralová, M. Otyepka, and M. Pumera, "Multiresponsive 2D $Ti_3C_2T_x$ MXene via Implanting Molecular Properties," *ACS Nano* **2021**, 15, 6, 10067–10075, doi: 10.1021/acsnano.1c01742.

[82] J. Liu, L. Mckeon, J. Garcia, S. Pinilla, S. Barwich, M. Mobius, P. Stamenov, J. N. Coleman, V. Nicolosi, "Additive Manufacturing of Ti_3C_2-MXene-Functionalized Conductive Polymer Hydrogels for Electromagnetic-Interference Shielding," *Adv. Mater.* **2022**, 34, 5, 2106253, doi: 10.1002/adma.202106253.

[83] C. Zhang, L. McKeon, M. P. Kremer, S.-H. Park, O. Ronan, A. Seral-Ascaso, S. Barwich, C. O. Coileain, N. McEvoy, H. C. Nerl, B. Anasori, J. N. Coleman, Y. Gogotsi, V. Nicolosi, "Additive-free MXene inks and direct printing of micro-supercapacitors," *Nat. Commun.* **2019**, 10, 1795, doi: 10.1038/s41467-019-09398-1.

[84] M. Soleymaniha, M. A. Shahbazi, A. R. Rafieerad, A. Maleki, and A. Amiri, "Promoting Role of MXene Nanosheets in Biomedical Sciences: Therapeutic and Biosensing Innovations," *Adv. Healthc. Mater.* **2019**, 8, 1, 1801137, doi: 10.1002/adhm.201801137.

[85] L. Li, X. Fu, S. Chen, S. Uzun, A. S. Levitt, C. E. Shuck, W. Han, Y. Gogotsi, "Hydrophobic and Stable MXene-Polymer Pressure Sensors for Wearable Electronics," *ACS Appl. Mater. Interfaces* **2020**, 12, 13, 15362–15369, doi: 10.1021/acsami.0c00255.

[86] A. K. Nemani, B. Zhang, B. C. Wyatt, Z. D. Hood, S. Manna, R. Khaledialidusti, W. Hong, M. G. Sternberg, S. K. R. S. Sankaranarayanan, B. Anasori, "High-Entropy 2D Carbide MXenes: $TiVNbMoC_3$ and $TiVCrMoC_3$," *ACS Nano* **2021**, 15, 8, 12815-12825,

doi.org/10.1021/acsnano.1c02775.

[87] Z. Du, C. Wu, Y. Chen, Z. Cao, R. Hu, Y. Zhang, J. Gu, Y. Cui, H. Chen, Y. Shi, J. Shang, B. Li, S. Yang, "High-Entropy Atomic Layers of Transition-Metal Carbides (MXenes)," *Adv. Mater*. **2021**, 33, 39, 2101473, doi.org/10.1002/adma.202101473.

[88] J. Zhou, Q. Tao, B. Ahmed, J. Palisaitis, I. Persson, J. Halim, M. W. Barsoum, P. O. A. Persson, J. Rosen, "High-Entropy Laminate Metal Carbide (MAX Phase) and Its Two-Dimensional Derivate MXene," *Chem. Mater*. **2022**, 34, 2098-2106, doi.org/10.1021/acs.chemmater.1c03348.

[89] Z. Leong, H. Jin, Z. Marvin Wong, K. Nemani, B. Anasori, T. Leong Tan, "Elucidating the Chemical Order and Disorder in High-Entropy MXenes: A High-Throughput Survey of the Atomic Configurations in $TiVNbMoC_3$ and $TiVCrMoC_3$," *Chem. Mater*. **2022**, 34, 20, 9062-9071, doi.org/10.1021/acs.chemmater.2c01673.

[90] S. K. Nemani, M. Torkamanzadeh, B. C. Wyatt, V. Presser, B. Anasori, "Functional two-dimensional high-entropy materials," *Comm. Mater.* **2023**, 4, doi.org/10.1038/s43246-023-00341-y.

[91] B. C. Wyatt, A. Thakur, K. Nykiel, Z. D. Hood, S. P. Adhikari, K. K. Pulley, W. J. Highland, A. Strachan, B. Anasori, "Design of Atomic Ordering in $Mo_2Nb_2C_3T_x$ MXenes for Hydrogen Evolution Electrocatalysis," *Nano Lett*. **2023**, 23, 3, 931-938, doi.org/10.1021/acs.nanolett.2c04287.

[92] Z. Kang, M. A. Khan, Y. Gong, R. Javed, Y. Xu, D. Ye, H. Zhao, J. Zhang, "Recent progress of MXenes and MXene-based nanomaterials for the electrocatalytic hydrogen evolution reaction," *J. Mater. Chem. A* **2021**, 9, 10, 6089–6108, doi: 10.1039/d0ta11735h.

[93] B. M. Jun, S. Kim, J. Heo, C. M. Park, N. Her, M. Jang, Y. Huang, J. Han, Y. Yoon, "Review of MXenes as new nanomaterials for energy storage/delivery and selected environmental applications," *Nano Res.* **2019**, 12, 3, 471–487, doi: 10.1007/s12274-018-2225-3.

[94] M. Naguib, V. N. Mochalin, M. W. Barsoum, and Y. Gogotsi, "25th anniversary article: MXenes: A new family of two-dimensional materials," *Adv. Mater.* **2014**, 26, 7, 992–1005, doi: 10.1002/adma.201304138.

[95] S. Bai, M. Yang, J. Jiang, X. He, J. Zou, Z. Xiong, G. Liao, S. Liu, "Recent advances of MXenes as electrocatalysts for hydrogen evolution reaction," *npj 2D Mater. Appl.* **2021**, 5, 1, doi: 10.1038/s41699-021-00259-4.

[96] A. Djire, X. Wang, C. Xiao, O. C. Nwamba, M. V. Mirkin, and N. R. Neale, "Basal Plane Hydrogen Evolution Activity from Mixed Metal Nitride MXenes Measured by Scanning Electrochemical Microscopy," *Adv. Funct. Mater*. **2020**, 33, 47, 2001136, doi: 10.1002/adfm.202001136.

[97] A. D. Handoko, K. D. Fredrickson, B. Anasori, K. W. Convey, L. R. Johnson, Y. Gogotsi, A. Vojvodic, Z. W. She, "Tuning the Basal Plane Functionalization of Two-Dimensional Metal

Carbides (MXenes) to Control Hydrogen Evolution Activity," *ACS Appl. Energy Mater.* **2018**, 1, 1, 173–180, doi: 10.1021/acsaem.7b00054.

[98] T. Schultz, N. C. Frey, K. Hantanasirisakul, S. Park, S. J. May, V. B. Shenoy, Y. Gogotsi, N. Koch, "Surface Termination Dependent Work Function and Electronic Properties of $Ti_3C_2T_x$ MXene," *Chem. Mater.* **2019**, 31, 17, 6590–6597, doi: 10.1021/acs.chemmater.9b00414.

[99] M. Malaki, A. Maleki, and R. S. Varma, "MXenes and ultrasonication," *J. Mater. Chem. A.* **2019**, 7, 10843-10857, doi: 10.1039/c9ta01850f.

[100] K. Maleski, V. N. Mochalin, and Y. Gogotsi, "Dispersions of Two-Dimensional Titanium Carbide MXene in Organic Solvents," *Chem. Mater.* **2017**, 29, 4, 1632–1640, doi: 10.1021/acs.chemmater.6b04830.

[101] X. Tian and K. Zhou, "3D printing of cellular materials for advanced electrochemical energy storage and conversion," *Nanoscale*. **2020**, 12, 7416-7432, doi: 10.1039/d0nr00291g.

[102] J. Li and M. Pumera, "3D printing of functional microrobots," *Chem. Soc. Rev.* **2021**, 50, 4, 2794–2838, doi: 10.1039/d0cs01062f.

[103] A. Ambrosi and M. Pumera, "3D-printing technologies for electrochemical applications," *Chem Soc Rev* **2016**, 45, 2740-2755, doi: 10.1039/c5cs00714c.

[104] M. P. Browne, V. Urbanova, J. Plutnar, F. Novotný, and M. Pumera, "Inherent impurities in 3D-printed electrodes are responsible for catalysis towards water splitting," *J. Mater. Chem. A* **2020**, 8, 1120-1126, doi: 10.1039/c9ta11949c.

[105] M. P. Browne, E. Redondo, and M. Pumera, "3D Printing for Electrochemical Energy Applications," *Chem. Rev.* **2020**, 120, 5, 2783-2810, doi: 10.1021/acs.chemrev.9b00783.

[106] C. W. Foster, M. P. Down, Y. Zhang, X. Ji, S. J. Rowley-Neale, G. C. Smith, P. J. Kelly, C. E. Banks, "3D Printed Graphene Based Energy Storage Devices," *Sci. Rep.* **2017**, 7, 42233, doi: 10.1038/srep42233.

[107] X. Wei, D. Li, W. Jiang, Z. Gu, X. Wang, Z. Zhang, Z. Sun, "3D Printable Graphene Composite," *Sci. Rep.* **2015**, 5, 11181, doi: 10.1038/srep11181.

[108] S. A. M. Tofail, E. P. Koumoulos, A. Bandyopadhyay, S. Bose, L. O'Donoghue, and C. Charitidis, "Additive manufacturing: scientific and technological challenges, market uptake and opportunities," *Mater. Today* **2018**, 21, 1, 22-37, doi: 10.1016/j.mattod.2017.07.001.

[109] F. Zhang, M. Wei, V. V. Viswanathan, B. Swart, Y. Shao, G. Wu, C. Zhou, "3D printing technologies for electrochemical energy storage," *Nano Energy* **2017**, 40, 418-431, doi: 10.1016/j.nanoen.2017.08.037.

[110] Z. Rymansaib *et al.*, "All-Polystyrene 3D-Printed Electrochemical Device with Embedded Carbon Nanofiber-Graphite-Polystyrene Composite Conductor," *Electroanalysis* **2016**, 28, 7, 1517-1523, doi: 10.1002/elan.201600017.

[111] K. Ghosh, S. Ng, C. Iffelsberger, and M. Pumera, "2D MoS_2/carbon/polylactic acid filament for 3D printing: Photo and electrochemical energy conversion and storage," *Appl. Mater. Today*

2022, 26, doi: 10.1016/j.apmt.2021.101301.

[112] C. Y. Foo, H. N. Lim, M. A. Mahdi, M. H. Wahid, and N. M. Huang, "Three-Dimensional Printed Electrode and Its Novel Applications in Electronic Devices," *Sci. Rep.* **2018**, 8, 7399, doi: 10.1038/s41598-018-25861-3.

[113] M. P. Browne, F. Novotný, Z. Sofer, and M. Pumera, "3D Printed Graphene Electrodes' Electrochemical Activation," *ACS Appl. Mater. Interfaces* **2018**, 10, 46, 40294–40301, doi: 10.1021/acsami.8b14701.

[114] J. Muñoz and M. Pumera, "Accounts in 3D-Printed Electrochemical Sensors: Towards Monitoring of Environmental Pollutants," *ChemElectroChem* **2020**, 7, 16, 3404–3413, doi: 10.1002/celc.202000601.

[115] F. Novotný, V. Urbanová, J. Plutnar, and M. Pumera, "Preserving Fine Structure Details and Dramatically Enhancing Electron Transfer Rates in Graphene 3D-Printed Electrodes via Thermal Annealing: Toward Nitroaromatic Explosives Sensing," *ACS Appl. Mater. and Interfaces* **2019**, 11, 38, 35371–35375, doi: 10.1021/acsami.9b06683.

[116] K. Ghosh, S. Ng, C. Iffelsberger, and M. Pumera, "Inherent Impurities in Graphene/Polylactic Acid Filament Strongly Influence on the Capacitive Performance of 3D-Printed Electrode," *Chem. - A Eur. J.* **2020**, 26, 67, 15746-15753, doi: 10.1002/chem.202004250.

[117] M. P. Browne and M. Pumera, "Impurities in graphene/PLA 3D-printing filaments dramatically influence the electrochemical properties of the devices," *Chem. Commun.* **2019**, 55, 8374-8377, doi: 10.1039/c9cc03774h.

[118] E. Redondo and M. Pumera, "Fully metallic copper 3D-printed electrodes via sintering for electrocatalytic biosensing," *Appl. Mater. Today* **2021**, 25, 101253, doi: 10.1016/j.apmt.2021.101253.

[119] J. Muñoz, C. Iffelsberger, E. Redondo, and M. Pumera, "Design of bimetallic 3D-printed electrocatalysts via galvanic replacement to enhance energy conversion systems," *Appl. Catal. B Environ.* **2022**, 316, doi: 10.1016/j.apcatb.2022.121609.

[120] C. Iffelsberger, D. Rojas, and M. Pumera, "Photo-Responsive Doped 3D-Printed Copper Electrodes for Water Splitting: Refractory One-Pot Doping Dramatically Enhances the Performance," *J. Phys. Chem. C* **2021**, 126, 21, 9016–9026 doi: 10.1021/acs.jpcc.1c10686.

[121] V. Urbanová, J. Plutnar, and M. Pumera, "Atomic layer deposition of electrocatalytic layer of MoS_2 onto metal-based 3D-printed electrode toward tailoring hydrogen evolution efficiency," *Appl. Mater. Today* **2021**, 24, doi: 10.1016/j.apmt.2021.101131.

[122] S. Ng, C. Iffelsberger, J. Michalička, and M. Pumera, "Atomic Layer Deposition of Electrocatalytic Insulator Al_2O_3 on Three-Dimensional Printed Nanocarbons," *ACS Nano* **2021**, 15, 1, 686–697, doi: 10.1021/acsnano.0c06961.

[123] J. Muñoz, D. Rojas, and M. Pumera, "Faceted Crystal Nanoarchitectonics of Organic-Inorganic 3D-Printed Visible-Light Photocatalysts," *ACS Appl. Energy Mater.* **2022**, 5, 3, 3252–3258, doi:

10.1021/acsaem.1c03863.

[124] S. Chang, X. Huang, C. Y. Aaron. Ong, L. Zhao, L. Li, X. Wang, J. Ding, "High loading accessible active sites: Via designable 3D-printed metal architecture towards promoting electrocatalytic performance," *J. Mater. Chem. A* **2019**, 7, 18338-18347, doi: 10.1039/c9ta05161a.

[125] K. A. Novčić, C. Iffelsberger, S. Ng, and M. Pumera, "Local electrochemical activity of transition metal dichalcogenides and their heterojunctions on 3D-printed nanocarbon surfaces," *Nanoscale* **2021**, 13, 5324-5332, doi: 10.1039/d0nr06679f.

[126] J. Muñoz, C. Iffelsberger, E. Redondo, and M. Pumera, "Design of bimetallic 3D-printed electrocatalysts via galvanic replacement to enhance energy conversion systems," *Appl. Catal. B Environ.* **2022**, 316, doi: 10.1016/j.apcatb.2022.121609.

[127] B. Tao, P. R. Unwin, and C. L. Bentley, "Nanoscale Variations in the Electrocatalytic Activity of Layered Transition-Metal Dichalcogenides," *J. Phys. Chem. C* **2020**, 124, 1, 789–798, doi: 10.1021/acs.jpcc.9b10279.

[128] A. J. Bard and M. V. Mirkin, *Scanning electrochemical microscopy, second edition*. **2012**.

[129] J. Kwak and A. J. Bard, "Scanning Electrochemical Microscopy. Apparatus and Two-Dimensional Scans of Conductive and Insulating Substrates", *Anal. Chem* **1989**, 61, 1794-1799.

[130] M. A. Edwards, S. Martin, A. L. Whitworth, J. V. Macpherson, and P. R. Unwin, "Scanning electrochemical microscopy: Principles and applications to biophysical systems," *Physiol. Meas.* **2006**, 27, 12, doi: 10.1088/0967-3334/27/12/R01.

[131] D. Polcari, P. Dauphin-Ducharme, and J. Mauzeroll, "Scanning Electrochemical Microscopy: A Comprehensive Review of Experimental Parameters from 1989 to 2015," *Chem. Rev.* **2016**, 116, 22, 13234–13278, doi: 10.1021/acs.chemrev.6b00067.

[132] P. Bertoncello, "Advances on scanning electrochemical microscopy (SECM) for energy," *Energy Environ. Sci.* **2010**, 3, 11, 1620–1633, doi: 10.1039/c0ee00046a.

[133] A. Preet and T. E. Lin, "A review: Scanning electrochemical microscopy (SECM) for visualizing the real-time local catalytic activity," *Catalysts* **2021**, 11, 5, 1–15, doi: 10.3390/catal11050594.

[134] R. Tel-Vered and A. J. Bard, "Generation and detection of single metal nanoparticles using scanning electrochemical microscopy techniques," *J. Phys. Chem. B* **2006**, 110, 50, 25279–25287, doi: 10.1021/jp064434d.

[135] C. L. Bentley, "Scanning electrochemical cell microscopy for the study of (nano)particle electrochemistry: From the sub-particle to ensemble level," *Electrochem. Sci. Adv.* **2022**, 2, 3, 1–18, doi: 10.1002/elsa.202100081.

[136] E. Oswald, K. Palanisamy, and C. Kranz, "Nanoscale surface modification via scanning electrochemical probe microscopy," *Curr. Opin. Electrochem* **2022**, 34, 100965, doi: 10.1016/j.coelec.2022.100965.

[137] D. G. Georganopoulou, M. V. Mirkin, and R. W. Murray, "SECM measurement of the fast

electron transfer dynamics between Au^+ nanoparticles and aqueous redox species at a liquid/liquid interface," *Nano Lett.* **2004**, 4, 9, 1763–1767, doi: 10.1021/nl049196h.

[138] Y. Yu, T. Sun, and M. V. Mirkin, "Scanning Electrochemical Microscopy of Single Spherical Nanoparticles: Theory and Particle Size Evaluation," *Anal. Chem.* **2015**, 87, 14, 7446–7453, doi: 10.1021/acs.analchem.5b01690.

[139] T. Sun, Y. Yu, B. J. Zacher, and M. V. Mirkin, "Scanning Electrochemical Microscopy of Individual Catalytic Nanoparticles," *Angew. Chemie* **2014**, 126, 51, 14344–14347, doi: 10.1002/ange.201408408.

[140] E. Malel, J. Colleran, and D. Mandler, "Studying the localized deposition of Ag nanoparticles on self-assembled monolayers by scanning electrochemical microscopy (SECM)," *Electrochim. Acta* **2011**, 56, 20, 6954–6961, doi: 10.1016/j.electacta.2011.06.017.

[141] F. Li, I. Ciani, P. Bertoncello, P. R. Unwin, J. Zhao, C. R. Bradbury, D. Fermin, "Scanning electrochemical microscopy of redox-mediated hydrogen evolution catalyzed by two-dimensional assemblies of palladium nanoparticles," *J. Phys. Chem. C* **2008**, 112, 26, 9686–9694, doi.org/10.1021/jp8001228.

[142] J. Kim, C. Renault, N. Nioradze, N. Arroyo-Currás, K. C. Leonard, and A. J. Bard, "Electrocatalytic Activity of Individual Pt Nanoparticles Studied by Nanoscale Scanning Electrochemical Microscopy," *J. Am. Chem. Soc.* **2016**, 138, 27, 8560–8568, doi: 10.1021/jacs.6b03980.

[143] J. R. Xavier, "Electrochemical and Mechanical Investigation of Newly Synthesized NiO-ZrO_2 Nanoparticle–Grafted Polyurethane Nanocomposite Coating on Mild Steel in Chloride Media," *J. Mater. Eng. Perform.* **2021**, 30, 2, 1554–1566, doi: 10.1007/s11665-020-05448-8.

[144] S. J. Kwon and A. J. Bard, "Analysis of diffusion-controlled stochastic events of iridium oxide single nanoparticle collisions by scanning electrochemical microscopy," *J. Am. Chem. Soc.* **2012**, 134, 16, 7102–7108, doi: 10.1021/ja300894f.

[145] C. M. Sánchez-Sánchez, J. Solla-Gullón, F. J. Vidal-Iglesias, A. Aldaz, V. Montiel, and E. Herrero, "Imaging structure sensitive catalysis on different shape-controlled platinum nanoparticles," *J. Am. Chem. Soc.* **2010**, 132, 16, 5622–5624, doi: 10.1021/ja100922h.

[146] T. Sun, D. Wang, M. V. Mirkin, H. L. Xin, "Direct high-resolution mapping of electrocatalytic activity of semi-two-dimensional catalysts with single-edge sensitivity," *Proc. Natl. Acad. Sci. U. S. A.* **2019**, 116, 24, 11618–11623, doi: 10.1073/pnas.1821091116.

[147] H. Li, M. Du, M. J. Mleczko, A. L. Koh, Y. Nishi, E. Pop, A. J. Bard, X. Zheng, "Kinetic Study of Hydrogen Evolution Reaction over Strained MoS_2 with Sulfur Vacancies Using Scanning Electrochemical Microscopy," *J. Am. Chem. Soc.* **2016**, 138, 15, 5123–5129, doi: 10.1021/jacs.6b01377.

[148] T. Sun, H. Zhang, X. Wang, J. Liu, C. Xiao, S. U. Nanayakkara, J. L. Blackburn, M. V. Mirkin, E. M. Miller, "Nanoscale mapping of hydrogen evolution on metallic and semiconducting MoS_2

nanosheets," *Nanoscale Horizons* **2019**, **4**, 619-624, doi: 10.1039/c8nh00346g.

[149] N. L. Ritzert, V. A. Szalai, and T. P. Moffat, "Mapping Electron Transfer at MoS_2 Using Scanning Electrochemical Microscopy," *Langmuir* **2018**, 34, 46, 13864–13870, doi: 10.1021/acs.langmuir.8b02731.

[150] J. W. Hill and C. M. Hill, "Directly Mapping Photoelectrochemical Behavior within Individual Transition Metal Dichalcogenide Nanosheets," *Nano Lett.* **2019**, 19, 8, 5710–5716, doi: 10.1021/acs.nanolett.9b02336.

[151] H. Y. Du, Y.-F. Huang, D. Wong, M.-F. Tseng, Y.-H. Lee, C.-H. Wang, C.-L. Lin, G. Hoffmann, K.-H. Chen, L.-C. Chen, "Nanoscale redox mapping at the MoS_2-liquid interface," *Nat. Commun.* **2021**, 12, 1, 1–10, doi: 10.1038/s41467-021-21660-z.

[152] C. L. Bentley, M. Kang, F. M. Maddar, F. Li, M. Walker, J. Zhang, P. R. Unwin, "Electrochemical maps and movies of the hydrogen evolution reaction on natural crystals of molybdenite (MoS_2): Basal: vs. edge plane activity," *Chem. Sci.* **2017**, 8, 9, 6583–6593, doi: 10.1039/c7sc02545a.

[153] C. Iffelsberger and M. Pumera, "High resolution electrochemical additive manufacturing of microstructured active materials: case study of MoS_x as a catalyst for the hydrogen evolution reaction," *J. Mater. Chem. A* **2021**, 9, 38, 22072–22081, doi: 10.1039/d1ta05581j.

[154] C. Iffelsberger, C. W. Jellett, M. Pumera, "3D Printing Temperature Tailors Electrical and Electrochemical Properties Through Changing Inner Distribution of Graphite/Polymer", *Small* **2021**, 17, 24, 2101233, doi.org/10.1002/smll.202101233.

Chapter 4. Theoretical Background

This Chapter gives an overview of the theoretical background of the electrochemical reactions. It provides insight into the main principles and mechanisms of the hydrogen evolution reaction (HER).

4.1. Theoretical Background of Electrochemical Reactions

Electrochemistry, as a branch of physical chemistry, deals with phenomena related to the mutual conversion of chemical and electrical energy. It describes the processes located at the electrode/electrolyte interface. An electrochemical reaction between two chemical species can be defined as:

$$O + ne^- \rightleftharpoons R \quad (1)$$

Where (O) stands for the electron-accepting species and (R) represents the electron-donating species, while n is the number of electrons (e^-) transferred between those two chemical species during an electrochemical reaction. These types of reactions are also called oxidation/reduction (*O/R*) reactions because the oxidation of one chemical species (R) is followed by reduction of the other species (O). Therefore, the electrode on which an oxidation process occurs is called an anode, while the electrode on which reduction takes place is a cathode.

The relationship between the potential (E) of a O/R process and the activities of the electroactive species (a_o and a_R) is given by Nernst equation (2) [1]:

$$E = E^0_{O/R} + \frac{RT}{nF} ln \frac{a_o}{a_R} \quad [V] \quad (2)$$

The $E^0_{O/R}$ [V] refers to the standard electrode potential of an electrochemical reaction, R is the ideal gas constant (R = 8.3145 J mol^{-1} K^{-1}), T is temperature [K] and F is the Faraday constant (which is given as the amount of charge (e) carried by one mole (Na), as: $F = e \cdot Na$ = 96485.3 C mol^{-1}). The $E^0_{O/R}$ represents an electrode potential with the unit activities of the electroactive species *O* and *R*.

The activity of an electroactive species (a_i) can be described as (3):

$$a_i = \gamma_i \cdot [\mathrm{i}] \quad (3)$$

Where γ_i is the activity coefficient and [i] is the molar concentration of the species *i*. Therefore, the Nernst equation is written as:

$$E = E^0_{O/R} + \frac{RT}{nF} ln \frac{\gamma_O \cdot [O]}{\gamma_R \cdot [R]} = E^0_{O/R} + \frac{RT}{nF} ln \frac{\gamma_O}{\gamma_R} + \frac{RT}{nF} ln \frac{[O]}{[R]} \quad [V] \quad (4)$$

Since the activity coefficients and, thus activities of the electroactive species are often unknown, a formal standard potential $E^{0`}$ is introduced as (5):

$$E^{0`} = E^0_{O/R} + \frac{RT}{nF} ln \frac{\gamma_O}{\gamma_R} \quad [V] \quad (5)$$

Therefore, the Nernst equation (6) gives the linear dependence between the electrode potential and the logarithm of molar bulk concentrations of the electroactive species [O] and [R], and it is transformed into [1]:

$$E = E^{0`} + \frac{RT}{nF} ln \frac{[O]}{[R]} \quad [V] \quad (6)$$

An individual electrode potential cannot be experimentally measured. However, the potential difference between two electrodes can be measured. Thus, a reference electrode, which is the electrode that has a defined standard electrode potential, is introduced into the system. The electrode potential is usually measured against silver/silver chloride reference electrode (Ag/1M KCl/AgCl), which has a defined standard potential of $E^0_{Ag/AgCl}$ = 0.235 V (at the temperature of 25 ^{0}C). The electrochemical investigation is experimentally carried out in a three-electrode system with the working electrode (WE), reference electrode (RE), and counter electrode (CE). **Figure 4.1** illustrates the three-electrode system.

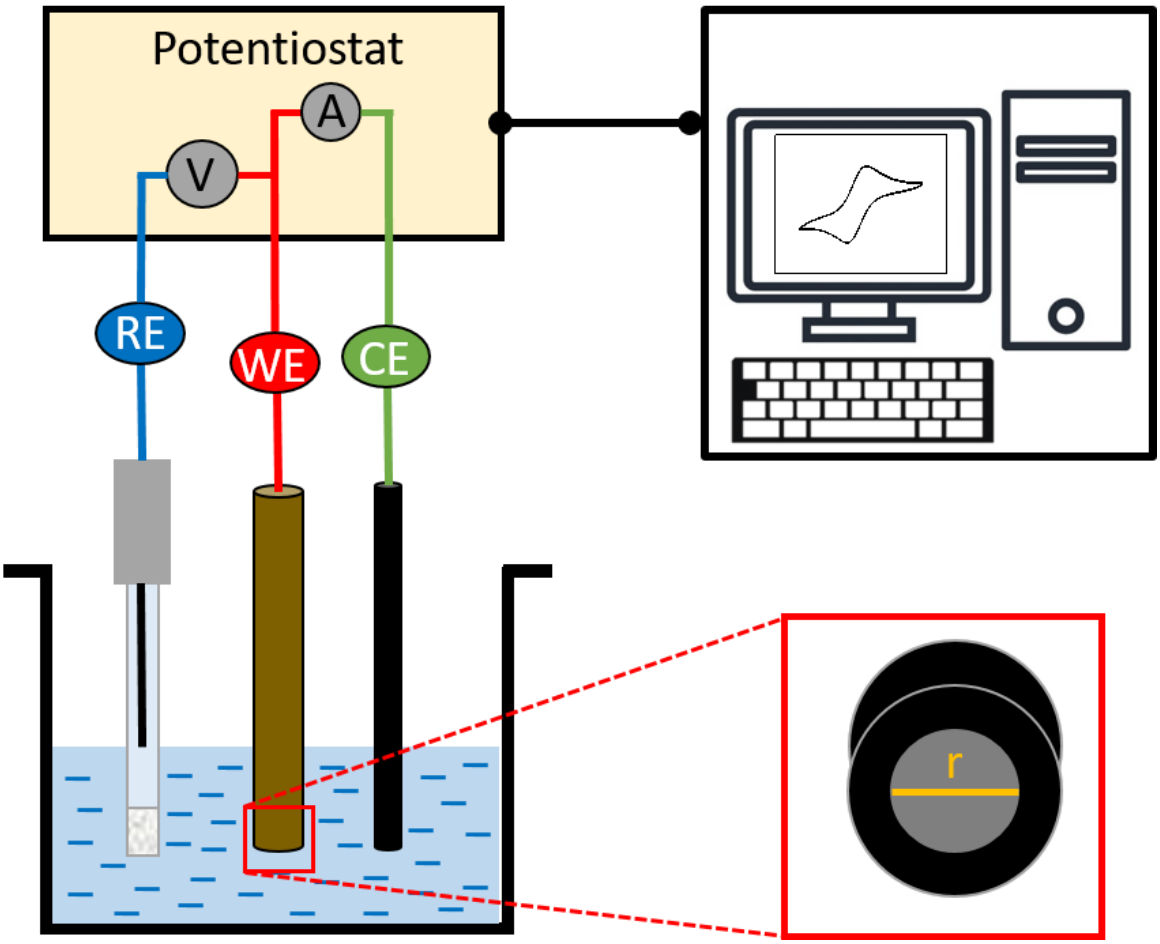

Figure 4.1. Schematic illustration of a three-electrode system with reference (RE), working (WE) and counter (CE) electrodes. Inset shows the electroactive area of the working electrode with an electrode radius (*r*).

The WE is the electrode of interest with a defined electrode active area with radius (*r*), where the reaction takes place and whose potential is measured with respect to the RE. The CE is introduced in the system to prevent the *IR* drops through the electrolyte (*I* is current and *R* is resistance) and maintain a constant potential at the RE.

4.1.1. Faradaic and Non-Faradaic Processes

An electrochemical process that can be described by Faradaic law is called the Faradaic process. The Faradaic law defines the charge transfer processes in which the charge (*Q*) which passes through the electrochemical cell during an electrochemical reaction is proportional to the amount of product (*n*) and the number of transferred electrons (*z*):

$$Q = nFz \qquad (7)$$

The Faradaic law cannot describe the Non-Faradaic processes, which include all non-charge-transfer processes that occur on the electrode/electrolyte interface, such as adsorption and desorption. These processes can be described by Ohm`s law due to the fact that the change in the electrode potential causes the change in the electrode/electrolyte interface and results in the formation of the electrical double layer. The double layer consists of the oppositely charged ions, and the charging of the double layer can be described as the charging of a capacitor. The capacitive current (I_C) is defined as [1]:

$$I_c = \frac{E}{R_s}\exp(\frac{t}{R_s C_{dl}}) \quad (8)$$

Where E is applied potential [V], R_s is the Ohmic resistance [Ω], t is time [s], and C_{dl} is double layer capacity [Farad-F].

The total current measured during the electrochemical process is the sum of the current flow from both Faradaic (I_F) and non-Faradaic processes:

$$I = I_F + I_C \qquad (9)$$

4.1.2. Diffusion

Mass transport in the electrolyte can be quantitatively described as the flux of species i (J_i), which represents the amount of product n [mol] per surface A [m^{-2}] during time t [s^{-1}].

$$J_i = \frac{dn}{A\,dt} \qquad [mol\,m^{-2}\,s^{-1}] \quad (10)$$

The mass transport is forced by the three main gradients: concentration ($^{\delta c}/_{\delta x}$), electric field ($^{\delta \phi}/_{\delta x}$), and speed ($^{\delta v}/_{\delta x}$), which results in three factors: diffusion, migration, and convection, respectively. The total flux of species i can be presented as the sum of all of these factors:

$$J_i = -D\,\frac{\delta_c\,(x)}{\delta_x} - \frac{zF}{RT} D_c \frac{\delta_\phi(x)}{\delta_x} + vc(x) \qquad (11)$$

Where D stands for the diffusion coefficient [$m^2\ s^{-1}$], x is the distance [m], R is the ideal gas constant (R = 8.3145 J $mol^{-1}\ K^{-1}$), T is temperature [K], F is the Faraday constant ($F = 96485.3$ C mol^{-1}), and z is a charge.

The first part of the equation (11) stands for the mass transport caused by diffusion, given by the first Fick`s law [1], [2]:

$$J_x = -D\ \frac{d_c\ (x)}{d_x} \quad (12)$$

The minus in the first part of the equation (12) defines the direction of the diffusion. The second part in equation (11) corresponds to the mass transport caused by migration, while the third part stands for the flux caused by forced convection. Without an externally forced convection, the third part of this equation can be neglected. Also, the mass transport caused by migration is minimized by the addition of highly concentrated supporting electrolyte that contains the non-electroactive species. Therefore, the total mass transport becomes diffusion-limited.

The diffusion is a consequence of the differences in the concentration (dC_i) of the bulk species (C_i^*) and species near the electrode/electrolyte interface (C_i for x=0), and it causes a certain distance in the bulk, which results in the formation of the diffusion layer:

$$\frac{dC_i}{dx} = \frac{(C_i^* - C_i(x=0))}{dx} \quad (13)$$

The thickness of the diffusion layer (δ_i) increases with time (t), and it is proportional to the diffusion coefficient (D_i) as:

$$\delta_i = 2\sqrt{D_i t} \quad (14)$$

Following, the flux in the diffusion-limited reactions is described as:

$$J_i(x) = -D_i\ \frac{d_c\ (x)}{d_x} = \ D_i \frac{(C_i^* - C_i(x=0))}{\delta x} = \ m_i\ \left(C_i - C(x=0)\right) \quad (15)$$

The m_i [ms^{-1}] is the mass transport coefficient and it is defined as D_i/δ_i.

Additionally, the concentration gradient that changes during time is defined by the second Fick`s law, as:

$$\frac{\delta C_i}{\delta t} = D\frac{\delta^2 C_i}{\delta x^2} \qquad (16)$$

Depending on the thickness of the diffusion layer, diffusion can be planar or spherical. The planar diffusion is dominant on the disc macroelectrode since its electrode radius is larger than the diffusion layer thickness [2], [3]. The current resulting only from the planar diffusion is derived by combining the equation (12) and (16) and it is defined as:

$$I = nFAC^* \sqrt{\frac{D_i}{\pi t}} \qquad (17)$$

This equation is also known as the Cottrell equation. On the other hand, the spherical diffusion dominates on the electrodes with a smaller electrode radius, such as dick ultramicroelectrode (UME), since the electrode radius is smaller than the diffusion layer thickness [4]. **Figure 4.2** illustrates the lateral (**A**) and spherical (**B**) diffusion on the disk macroelectrode and UME, respectively [5].

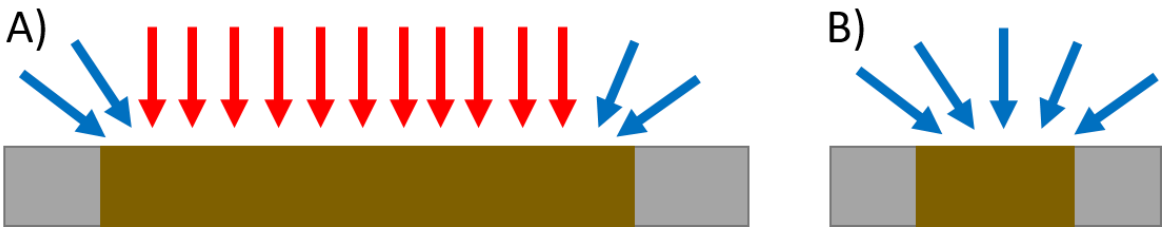

Figure 4.2. Diffusion on the electrode surfaces of (**A**) macroelectrode and (**B**) UME.

4.2. Hydrogen Evolution Reaction

The electrochemical water splitting reaction is considered a promising clean hydrogen production approach. Namely, in this process, green electricity breaks down the water molecules into hydrogen and oxygen. The total equation of this process can be described as:

$$2H_2O \rightarrow 2H_2 + O_2 \qquad (18)$$

The electrochemical water splitting involves two separate reactions: hydrogen evolution reaction (HER) and oxygen evolution reaction (OER). The HER is a one-half reaction in the electrochemical water splitting and it depends on the pH of the used electrolyte. In the acid solution it can be described as (19):

$$2H^+(aq) + 2e^- \rightarrow H_2\,(g) \qquad (19)$$

The two hydrogen ions ($2H^+$) are reduced on the electrode surface and released as hydrogen gas (H_2). The mechanism (20) – (22) of this reaction is widely investigated and it can be described as [6], [7]:

$$H^+ + e^- + (*) \rightarrow H_{ads} \qquad (20)$$

$$H_{ads} + H_{ads} \rightarrow H_2 + 2(*) \qquad (21)$$

$$H^+ + H_{ads} + e^- \rightarrow H_2 + (*) \qquad (22)$$

The (*) refers to the active site on the catalytic surface, (H_{ads}) is the intermediate, representing the H adsorbed on the electrode surface.

The reaction starts with the *Volmer step* (20) or hydrogen adsorption, which is followed by recombination of the adsorbed hydrogen atoms, *Tafel step*, (21) or by electrochemical hydrogen desorption, *Heyrovský step* (22) [8]. The reaction rate is greatly affected by how H_{ads} interacts with the surface and the number of available active sites on the surface. According to the *Sabatier* principle, the reaction between the intermediate and surface should be neither too strong nor too weak. The strong reaction results in intermediate bonding, which lowers the

removal of the intermediate from the surface. On the other hand, a weak reaction leads to low interaction between the intermediate and the surface.

There are various catalysts used as the electrode material in the HER. The catalytic performance of different catalysts can be quantified with two main parameters. One is the overpotential value, calculated from the linear sweep voltammogram at the current density of -10 mA cm^{-2}. The second is the *Tafel slope*, an inherent property of the reaction's kinetic that gives a sign of the energy needed to cause the significant increase in the current density. By plotting the overpotential values as a function of the logarithm of the absolute values of current density ($E = f$ (*log* (*abs* (*current density*))), the Tafel value is defined as the slope of this plot. The obtained Tafel slope value provides more information about the slow-rate step in the HER mechanism (20) – (22). In theory, the Tafel value of – 120 mV dec^{-1} indicates the *Volmer step* (20) as a rate-determining step, while the values of - 30 and – 40 mV dec^{-1} indicate the slow-rate steps of *Tafel* (21) and *Heyrovský* (22), respectively, calculated for the Pt electrode. However, most of the reported Tafel slope values for different catalysts fall outside of the theoretical range. Thus, the detailed determination of the HER mechanism cannot be done only by the Tafel slope analysis.

4.3. References

[1] A. J. Bard, L. R. Faulkner, H. S. White, *Electrochemical Methods-Fundamentals and Applications*, Third Edition, Wiley **2022**.

[2] R. G. Compton and C. E. Banks, *Cyclic Voltammetry at Macroelectrodes*. **2007**.

[3] N. Elgrishi, K. J. Rountree, B. D. McCarthy, E. S. Rountree, T. T. Eisenhart, and J. L. Dempsey, "A Practical Beginner's Guide to Cyclic Voltammetry," *J. Chem. Educ.* **2018**, 95, 2, 197–206, doi: 10.1021/acs.jchemed.7b00361.

[4] D. A. Walsh, K. R. J. Lovelock, and P. Licence, "Ultramicroelectrode voltammetry and scanning electrochemical microscopy in room-temperature ionic liquid electrolytes," *Chem. Soc. Rev.* **2010**, 39, 11, 4185–4194, doi: 10.1039/b822846a.

[5] A. L. Whitworth, D. Mandler, and P. R. Unwin, "Theory of scanning electrochemical microscopy (SECM) as a probe of surface conductivity," *Phys. Chem. Chem. Phys.* **2005**, 384–393, doi: 10.1039/b407397e.

[6] R. Van de Krol and M. Gratzel, “Electronic materials: Science & Technology,” in *Photoelectrochemical Hydrogen Production*, **2012**.

[7] S. M. Tan and M. Pumera, “Bottom-up Electrosynthesis of Highly Active Tungsten Sulfide (WS_{3-x}) Films for Hydrogen Evolution,” *ACS Appl. Mater. Interfaces* **2016**, 8, 6, 3948–3957, doi: 10.1021/acsami.5b11109.

[8] T. Shinagawa, A. T. Garcia-Esparza, and K. Takanabe, “Insight on Tafel slopes from a microkinetic analysis of aqueous electrocatalysis for energy conversion,” *Sci. Rep.* **2015**, 5, 1–21, doi: 10.1038/srep13801.

Chapter 5. Methods

This Chapter gives an overview of the methods used for the electrochemical and physicochemical characterization of the layered two-dimensional (2D) materials studied in this Thesis. The electrochemical characterization includes macroscopic and microscopic electrochemical examination of these materials, while their physicochemical characterization considers optical and elemental composition analysis.

5.1. Macroscopic Electrochemical Methods

Macroscopic electrochemical techniques provide information about the average electrochemical activity of the catalytic surfaces. The most commonly used macroscopic methods are cyclic voltammetry and linear sweep voltammetry.

5.1.1. Voltammetry

Traditional techniques, such as cyclic voltammetry (CV) and linear sweep voltammetry (LSV) are often used in the electrochemical study of the O/R processes on the macroscopic level. In the CV, the potential is swept linearly from the starting potential (E_1) to the final potential (E_2), while the current is measured, as shown in **Figure 5.1 A**. No reaction occurs when the potential E_1 is applied, thus the current flow is negligible. Once the E_2 is reached, the potential is swept back to the E_1. The obtained potential-current (E-I) plot is called a *voltammogram* [1-3]. The typical CV voltammogram of the Pt-disk electrode is shown in **Figure 5.1 B**. Similarly, in the LSV, the potential is swept linearly in a fixed potential range, but the voltage is scanned from a lower (E_1) to an upper (E_2) value, while the current is measured (as shown in **Figure 5.1 C**) [1], [2]. The typical LSV of a Pt-disk electrode is shown in **Figure 5.1 D**.

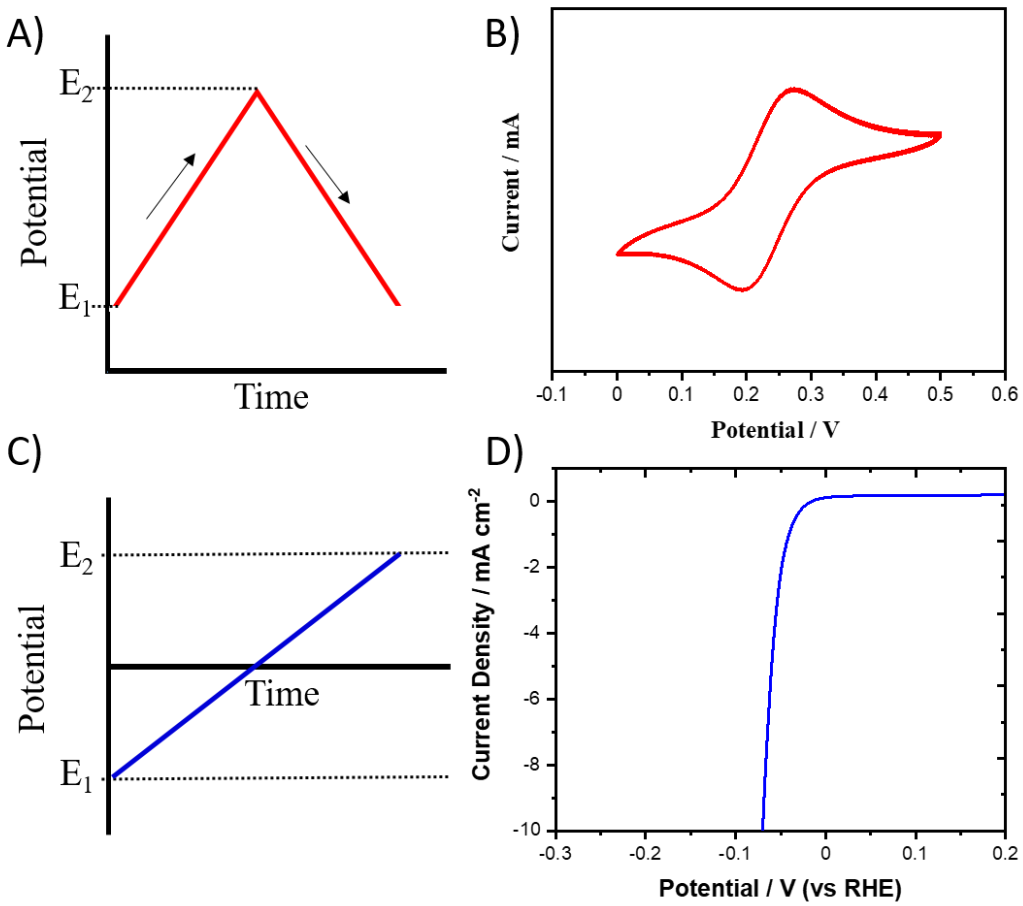

Figure 5.1. Electrochemical analysis performed by cyclic voltammetry (**A**-**B**) and linear sweep voltammetry (**C**-**D**). (**A**) Schematic illustration of the CV experiment, (**B**) CV voltammogram of a 1 mm Pt disk macroelectrode. (**C**) Schematic illustration of the LSV experiment, (**B**) LSV voltammogram of a 1 mm Pt disk macroelectrode. The measurements were obtained in (**B**) 1.5 mM FcMeOH in 0.2 M KNO_3 electrolyte with the scan rate of 50 mV s^{-1} and in (**D**) 0.5 M H_2SO_4 solution with a scan rate of 5 mVs^{-1}.

5.2. Microscopic Electrochemical Methods

Microscopic electrochemical methods enable studying materials` electrochemical processes at micro- to nano-scale. These methods are valuable for studying the electrochemical properties of the materials on a tiny scale, such as the level of individual particles or single molecules. They require a probe with small dimensions to scan the surface of interest. The most common microscopic electrochemical probe techniques are atomic force microscopy (AFM), scanning tunneling microscopy (STM), and scanning electrochemical microscopy (SECM).

5.2.1. Ultramicroelectrode

The ultramicroelectrode (UME) is a disc-shaped electrode with a radius of 25 μm or less [4]. As previously discussed in **Chapter 4.1.2**, the radius of a UME is smaller than the thickness of the diffusion layer, making the spherical diffusion dominant. A typical 25 μm diameter UME is shown in the optical image in **Figure 5.2 A**. The most crucial parameters of the UME are the active electrode area (red line) and the r_g value (the insulating part with the active area, yellow line), as presented in the optical image in **Figure 5.2 B**. The widely used and commercially available probes are platinum (Pt)-based that have specific electrode radius ranging from micrometer to nanometer. A typical CV of a Pt UME is shown in **Figure 5.2 C**.

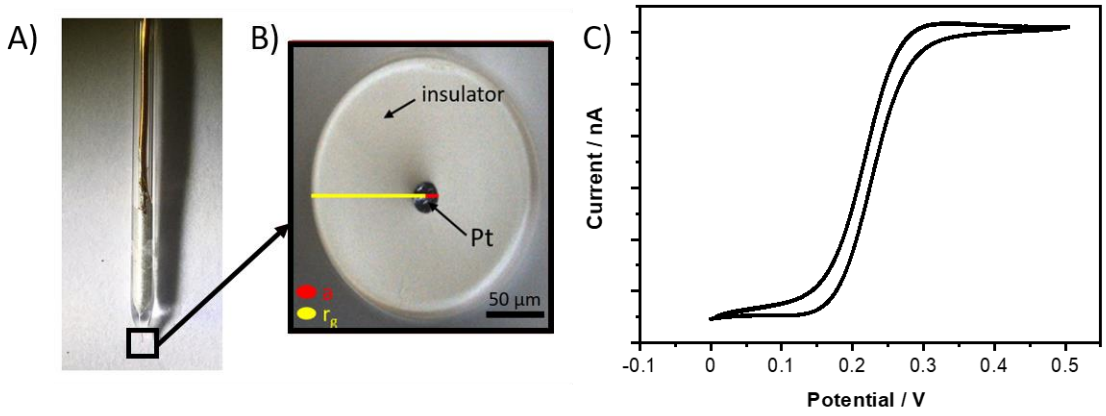

Figure 5.2. Illustration and electrochemical characterization of the 25 μm Pt disk UME electrode. (**A**) Optical images of the UME, (**B**) the active area (*a*) with the surrounding insulating part of the UME tip and (**C**) a typical CV of the 25 μm Pt disk UME electrode**.** The measurement was obtained in 1.5 mM FcMeOH in 0.2 M KNO_3 electrolyte with the scan rate of 50 mV s^{-1}.

The importance of the thickness of the insulating part is considered within the RG value which is defined as:

$$RG = \frac{a}{r_g} \qquad (23)$$

For the UME with RG $>$ 10 the diffusion-limited current is defined by the equation:

$$I = 4nFC_i^* D_i a \quad (24)$$

Where n is the number of electrons, F is the Faraday constant, and C_i^* and D_i are bulk concentration and diffusion coefficient of electrochemically active species i, respectively [5]. In general, the RG value strongly influences the electrochemical contrast, which is why it has to be determined.

5.2.2. Scanning Electrochemical Microscopy

Scanning electrochemical microscopy (SECM) is an advanced electrochemical tool used for the microscopic electrochemical investigation of electrode surfaces. The main principle of its operation is based on scanning the UME tip across the surface of interest [4]. **Figure 5.3** illustrates the typical SECM setup. It consists of an electrochemical cell used for measurements and electrodes: a reference electrode, a counter electrode, and a UME disc probe as a working electrode. The instrument is equipped with a step motor used for accurate 3D-positioning of the UME tip with the step width in the nanometer to micrometer range. The movement of the UME is controlled by a PC connected to the potentiostat that requires measurements in an amperometric regime. The electrochemical reaction occurring on the UME requires the electrochemically active species from the mediator solution (such as ferrocene methanol, FcMeOH), and the measured signal is represented on the SECM image processed on the PC. SECM can work in the three-electrode system, with the potential applied to the UME tip, and in the four-electrode system, when the potential is also applied to the substrate which, in this case, acts as the second working electrode.

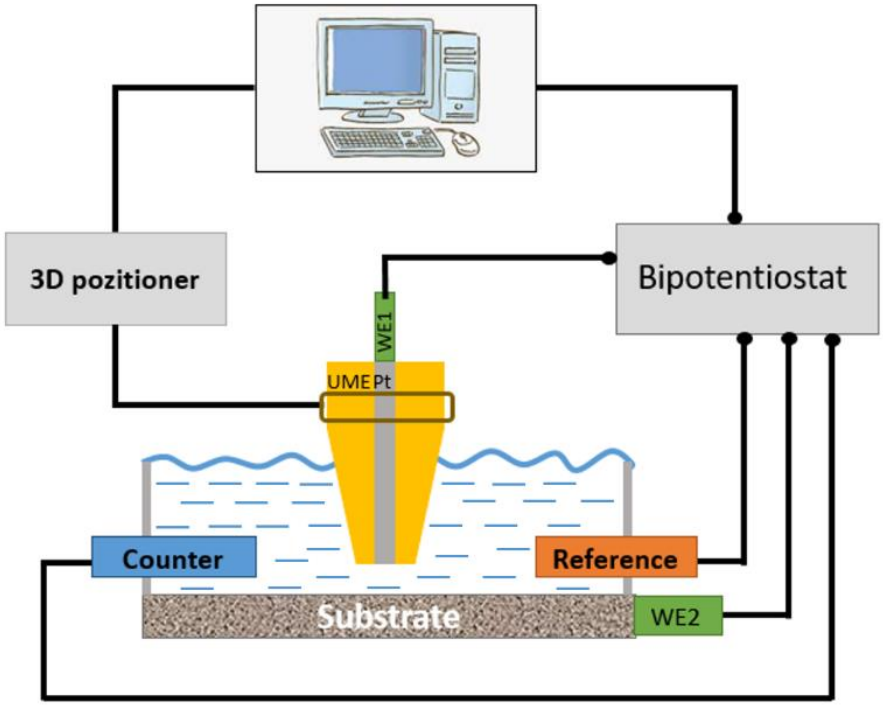

Figure 5.3. Schematic illustration of the SECM setup.

5.2.3. Operational Modes of SECM

The most widely used SECM mode is the feedback mode. In this mode, the UME probe is scanned across the substrate of interest in a three-electrode system with a reference electrode, counter electrode, and UME as a working electrode (**Figure 5.4 A**).

The feedback mode is used for the microscopic investigation of the surface topography and conductivity [4], [6]. The current measured at the UME by scanning in this mode is Faraday current (**Chapter 4.1.1.**), and it depends on the tip-to-substrate distance, substrate topography, and substrate kinetics. The substrate kinetics is determined by the kinetic reaction constant, which depends on the conductive/insulating behavior of the substrate. By tip approaching an insulator (e.g., glass), the substrate hinders the diffusion of the electroactive species on the tip, resulting in a decrease in the tip current, i.e., *negative feedback* [7].

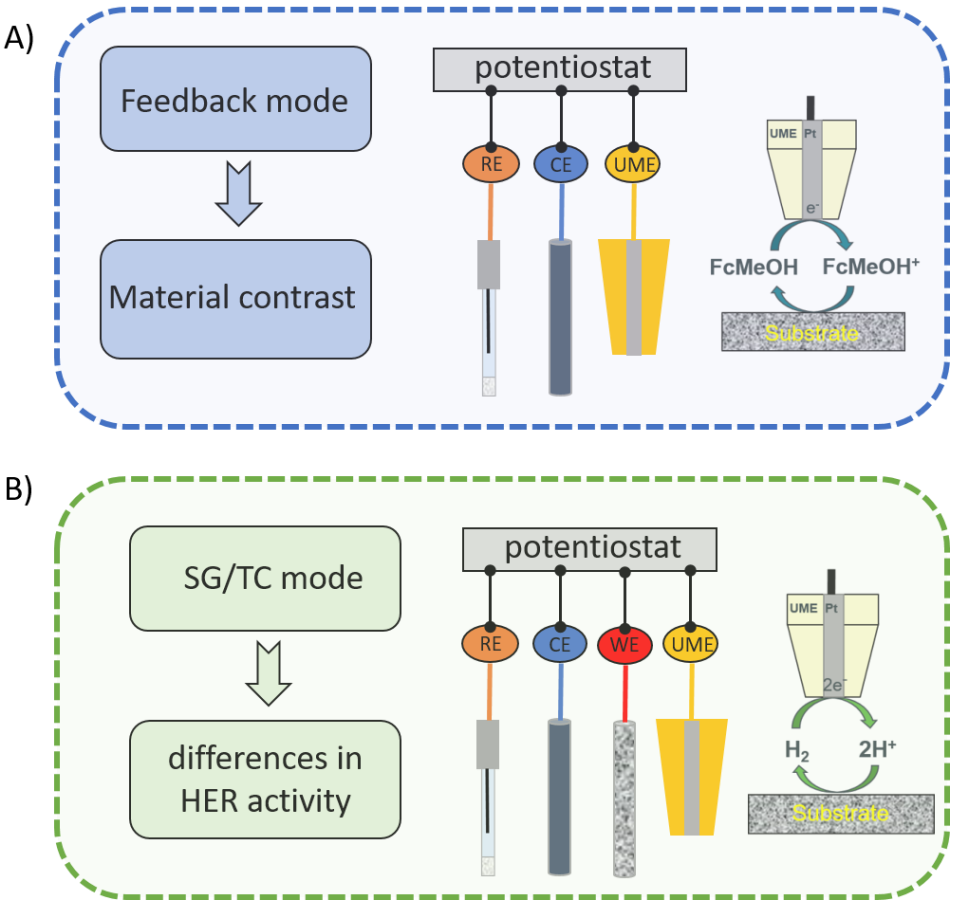

Figure 5.4. Schematic illustration of the SECM operational modes (**A**) feedback and (**B**) substrate generation/ tip collection (SG/TC) mode.

However, by tip approaching the conductive substrate (i.e., Au), the electrochemical regeneration of the active species on the conductive electrode surface is followed by fast kinetic, resulting in so-called *positive feedback* [8]. The plot showing the change in current with the tip-to-substrate distance (*d*) is called the probe approach curve (PAC). The PAC plots measured on the glass and gold substrates are shown in **Figure 5.5 A**. Moreover, it is usually presented as the change of the normalized current (I_{nor}) versus the normalized distance (L), where the L is:

$$L = \frac{d}{a} \qquad (25)$$

The normalized current is defined as:

$$I_{nor} = \frac{I_M}{I_\infty} \quad (26)$$

Where I_M is the measured current and I_∞ is the current measured in the bulk.

The normalized current measured during the UME approaching negative substrate is mathematically given by *Lefrou et al* [6]:

$$N_I(L, RG) = \frac{\frac{2.08}{RG^{0.358}}\left(L - \frac{0.145}{RG}\right) + 1.585}{\frac{2.08}{RG^{0.358}}(L + 0.0023\,RG) + 1.57 + \frac{\ln(RG)}{L} + \frac{2}{\pi RG}\ln\left(1 + \frac{\pi RG}{2L}\right)} \quad (27)$$

It strongly depends on the RG value of the UME probe.

Subsequently, the normalized current measured during positive PAC given by the approximation reported by *Shao et al.* [9] is defined as:

$$I\,(L) = B + \frac{C}{L} + Dexp\left(\frac{E}{L}\right) \quad (28)$$

The B, C and D are the parameters which can have different values [10].

However, the RG value does not strongly influence the normalized positive feedback current. The theoretically predicted plots for the pure positive and negative feedback are plotted with the experimentally obtained curves on the glass and gold in **Figure 5.5 A**. As can be seen from this Figure, the experimentally obtained plots follow the theoretically predicted plots.

Subsequently, the substrate generation/tip collection (SG/TC) SECM mode is used to investigate the local differences in the electrochemical activity of the electrocatalytic surfaces. In this mode, a sufficient potential is applied to the substrate to initiate the reaction and an adequate potential is applied to the UME tip to collect the generated species. The SG/TC mode is used for the electrochemical investigation of the microscopic differences in the HER activity of the electrocatalysts, as illustrated in **Figure 5.4 B**. Because a locally higher hydrogen concentration results in a higher anodic current response, locating the active sites for HER on the electrocatalytic surfaces is possible, as shown in **Figure 5.4 B**. The SECM micrograph obtained in SG/TC mode provides information about the local differences in the HER activity as well as the location and distribution of the HER active sites on the electrocatalytic surfaces.

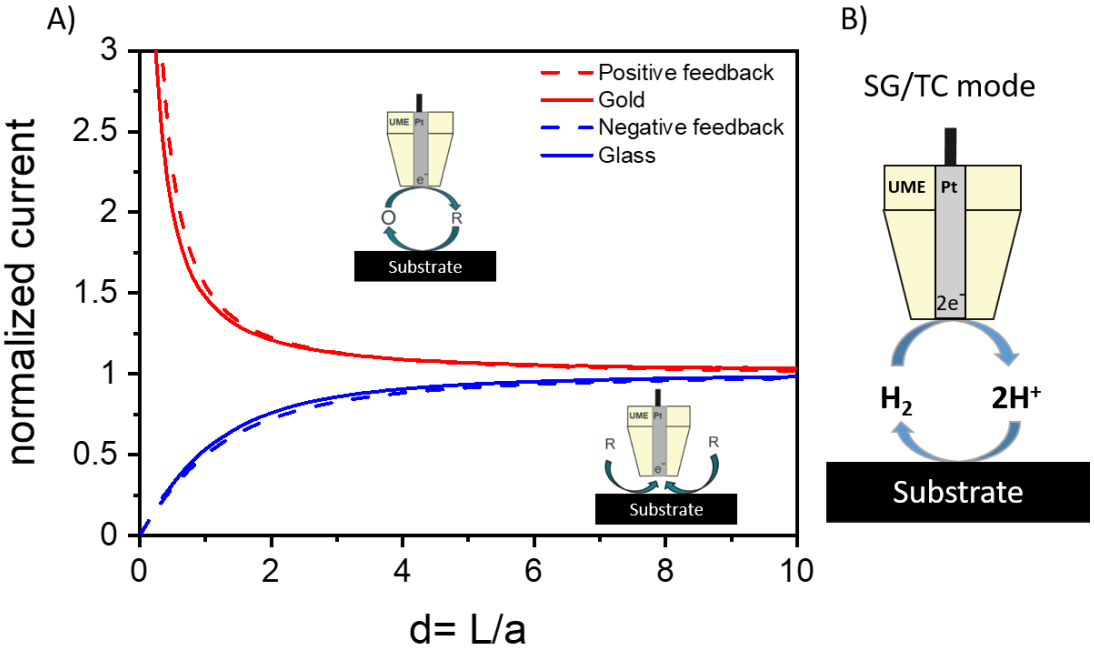

Figure 5.5. (**A**) Probe approach curves for the positive (red) and negative (blue) feedback. The experimentally obtained plots for the glass (blue) and gold-sputtered on the glass slide (red) are compared with the theoretically predicted plots for the pure positive and negative feedback (dashed lines). (**B**) Schematic illustration of the substrate generation/tip collection (SG/TC) SECM mode. The probe approach curve measurements were performed with a 25 µm Pt UME probe, in the 1.5 mM FcMeOH in 0.2 M KNO_3 electrolyte solution with a UME potential of 0.4 V (vs. Ag/AgCl), a max. approach speed of 1 µm s^{-1}, step width of 1 µm and waiting time of 0 ms. The PACs for theoretically positive and negative feedback were calculated according to the literature [5], [6], [7]. The glass slide coated with the 30 nm thick gold film was used for the measurement of the positive feedback.

5.3. Characterization Techniques

Material characterization includes the analysis of the surface morphology and topography as well as the samples' chemical and elemental composition.

5.3.1. Optical Characterization

The optical characterization considers the analysis of the surface morphology and topography. The optical or light microscope is often used to make the magnified image of the investigated sample. In contrast to conventional light microscopy, confocal laser scanning microscopy (CLSM) provides relevant information about the surface topography and roughness. A light source in the CLSM comprises a laser beam and the sample's surface is scanned layer-by-layer. The layers are composed into a 3D microscopic image of the sample. The optical characterization of the investigated samples in this Thesis was carried out by CLSM Olympus Lext OLS4100 instrument with a 20 x and 100 x lenses as well as a stereomicroscope (Zeiss Stemi 508) with a color camera (Axiocam 105) and Axio Vision Software. A detailed analysis of the surface morphology is provided by scanning electron microscopy (SEM). Namely, the interaction between an electron beam and a sample is followed by different scattering and emissions of the electrons. The secondary and backscattered electrons are used to record an image of the sample in SEM. The surface morphology analysis in this Thesis was done by Myra 3 XMU SEM (Tescan) and TESCAN Lyra 3 SEM instruments. For SEM imaging, an accelerating voltage of 5 kV was used.

5.3.2. Elemental and Chemical Composition Analysis

The elemental composition analysis of the investigated samples is performed by energy-dispersive X-ray spectroscopy (EDS). The main principle of EDS operation is based on the excitation of the sample when exposed to a focused electron beam. The emitted X-rays from

the sample are afterwards collected by the EDS detector and converted into proportional electrical voltages. The produced signals act like a fingerprint of the element and allow the elemental composition analysis. The EDS detectors (Oxford Instruments X-MAX^{20} and BRUKER XFlash 5010), as a part of Myra 3 XMU SEM and TESCAN Lyra 3, respectively, were used in this Thesis. The EDS measurements require an accelerating voltage of 20 kV. A more detailed analysis of the chemical composition of the sample surface was done by surface sensitive technique, X-ray Photoelectron Spectroscopy (XPS). The X-rays with a specific energy are used to bombard a solid sample in a vacuum system, which results in the excitation of the electronic states of the atoms. The energy and the number of the electrons ejected from the surface carry the information about the atoms on the surface. They are used to identify and quantify the elemental composition of the specific elements as well as their nearest neighbor chemical bonding or valence state. A chemical composition analysis in this Thesis was performed by an XPS instrument, Kratos AXIS Supra using monochromatic Al Kα (1486.7 eV) excitation source. The spectra were calibrated against the carbon 1s signal at 284.8 eV and were fitted using Casa XPS software. X-Ray Diffraction (XRD) is a widely used technique to assess the crystallinity and structure of the solid samples. The XRD pattern of the investigated samples in this Thesis was obtained by an X-ray diffractometer (Rigaku SmartLab, 9kW) using Cu $K_{\alpha 1}$ radiation. All the equipment mentioned is available at CETEC Nano Facilities.

5.4. References

[1] A. J. Bard, L. R. Faulkner, H. S. White, *Electrochemical Methods-Fundamentals and Applications*, Third Edition, Wiley **2022**.

[2] R. G. Compton and C. E. Banks, *Cyclic Voltammetry at Macroelectrodes*. **2007**.

[3] N. Elgrishi, K. J. Rountree, B. D. McCarthy, E. S. Rountree, T. T. Eisenhart, and J. L. Dempsey, "A Practical Beginner's Guide to Cyclic Voltammetry," *J. Chem. Educ.* **2018**, 95, 2, 197–206, doi: 10.1021/acs.jchemed.7b00361.

[4] A. J. Bard and M. V. Mirkin, *Scanning electrochemical microscopy, second edition*. **2012**.

[5] C. Lefrou and R. Cornut, "Analytical expressions for quantitative scanning electrochemical microscopy (SECM)," *ChemPhysChem* **2010**, 11, 3, 547–556, doi: 10.1002/cphc.200900600.

[6] R. Cornut and C. Lefrou, “A unified new analytical approximation for negative feedback currents with a microdisk SECM tip,” *J. Electroanal. Chem.* **2007**, 608, 1, 58-66, doi:10.1016/j.jelechem.2007.05.007.

[7] J. L. Amphlett and G. Denuault, “Scanning Electrochemical Microscopy (SECM): An investigation of the effects of tip geometry on amperometric tip response,” *J. Phys. Chem. B*, **1998**, 102, 49, 9946–9951, doi: 10.1021/jp982829u.

[8] T. Shinagawa, A. T. Garcia-Esparza, and K. Takanabe, “Insight on Tafel slopes from a microkinetic analysis of aqueous electrocatalysis for energy conversion,” *Sci. Rep.* **2015**, 5, 1–21, doi: 10.1038/srep13801.

[9] Y. Y. Shao and M. V. Mirkin, “Probing Ion Transfer at the Liquid/Liquid Interface by Scanning Electrochemical Microscopy (SECM),” *J. Phys. Chem. B* **1998**, 102, 49, 9915–9921, doi: 10.1021/jp9828282.

[10] A. L. Whitworth, D. Mandler, and P. R. Unwin, “Theory of scanning electrochemical microscopy (SECM) as a probe of surface conductivity,” *Phys. Chem. Chem. Phys.* **2005**, 384–393, doi: 10.1039/b407397e.

Chapter 6. Local Electrochemical Activity of Transition Metal Dichalcogenides on 3D-Printed Nanocarbon Surfaces

Published paper included in this chapter:

K. A. Novčić, C. Iffelesberger, S. Ng and, M. Pumera, *Local Electrochemical Activity of Transition Metal Dichalcogenides and their Heterojunctions on 3D-Printed Nanocarbon Surfaces*, **Nanoscale (2021)**, 13, 5324-5332, DOI: 10.1039/D0NR06679F.

The results were presented at the conference: **3rd Cross-Border Seminar on Electroanalytical Chemistry (CBSEC), Virtual Seminar, April 2021, Regensburg, Germany**.

6.1. Motivation for the Study

The main motivation for the work on TMD-modified 3D-printed nanocarbon electrodes lies in the porous structure of 3D-printed nanocarbon electrodes when thermally activated, which leads to increased surface area and improved electrochemical properties. In order to enhance their electrocatalytic activity for the energy conversion application, the thermally activated 3D-printed electrodes are modified with electroactive materials such as MoS_2 and WS_2, as well as their heterojunctions. The main scientific questions to be addressed in this study are the penetration depth of the deposited electroactive materials and their heterojunctions into the 3D-printed porous structure and the distribution as well as the location of the HER active sites on the material surfaces.

6.2. Paper Conclusion

This paper provides a detailed study of the catalytic activity of the unmodified and modified thermally activated 3D-printed nanocarbon electrodes. In this study, successful fabrication of the thermally activated 3D-printed nanocarbon electrodes modified with the layers of MoS_2, WS_2 as well as MoS_2@WS_2 and WS_2@MoS_2 heterojunctions is achieved. The macroscopic electrochemical performance of the produced electrodes studied by linear sweep voltammetry shows the MoS_2-modified thermally activated 3D-printed electrode to be highly active for the

hydrogen evolution reaction. The microscopic electrochemical performance studied by SECM demonstrates different penetration depths of the deposited materials inside the porous structure and non-uniform distribution of electrochemically active sites for the HER over the investigated electrode surfaces. This study shows that the electrodeposition of the electroactive material on the 3D-printed electrodes results in the HER active sites that are not solely located at the outer surface, but also in the interior of the nanocarbon structure. As a result, it provides valuable information for a deeper understanding and systemic improvement of these materials in energy conversion applications.

6.3. Student Contribution

The student is the first author of this paper who contributed to the study by organizing figures, plotting data and drafting the manuscript. The student`s work consisted of the preparation, activation and modification of the 3D-printed nanocarbon electrodes, and microscopic electrochemical measurements of the fabricated electrodes as well as their detailed physicochemical characterization.

Nanoscale

PAPER

View Article Online
View Journal | View Issue

Cite this: *Nanoscale*, 2021, **13**, 5324

Local electrochemical activity of transition metal dichalcogenides and their heterojunctions on 3D-printed nanocarbon surfaces†

Katarina A. Novčić, [a] Christian Iffelsberger, [a] Siowwoon Ng [a] and Martin Pumera *[a,b,c,d]

Received 16th September 2020,
Accepted 22nd January 2021

DOI: 10.1039/d0nr06679f

rsc.li/nanoscale

Transition metal dichalcogenides (TMDs) have shown to be promising catalysts for the electrochemical hydrogen evolution reaction (HER) and 3D-printing enables fast prototyping and manufacturing of water splitting devices. However, the merging of TMDs with complex 3D-printed surfaces and nanostructures as well as their localized characterization remains challenging. In this work, electrodeposition of MoS_2 and WS_2 and their heterojunctions are used to modify thermally activated 3D-printed nanocarbon structures. Their electrochemical performance for the HER is investigated macroscopically by linear sweep voltammetry and microscopically by scanning electrochemical microscopy. This study demonstrates different local HER active sites of MoS_2 and WS_2 within the 3D-printed nanocarbon structure that are not solely located at the outer surface, but also in the interior up to ~150 μm for MoS_2 and ~300 μm for WS_2.

Introduction

Generation of hydrogen for clean energy application poses a great challenge. Electrochemistry is one of the main and the simplest method to produce pure hydrogen *via* the hydrogen evolution reaction (HER) and thus this reaction has been highly investigated in recent research.[1–3] Transition metal dichalcogenides (such as MoS_2 and WS_2) have attracted significant attention as they show great promise to replace precious metal electrocatalysts for the HER.[4–6] A lot of attention was given to the exfoliation of MoS_2 and WS_2 to single layer 2D materials[7–10] to tune their electrocatalytic activity. These 2D materials are difficult to deposit on the surfaces of the current collectors[11] and for practical purposes, they need to be blended with polymer composites which may decrease their efficiency. Recently, it has been shown that non-stoichiometric MoS_2 and WS_2 electrodeposited on the current collector surfaces[6,12] have similar or even enhanced electrocatalytic activity compared to 2D MoS_2 and WS_2.

Also, TMD composites with MoS_2/WS_2 hybrids have attracted much interest due to their great mechanical, thermal and optical properties with tunable bandgaps.[13–15] The synthesis of two or more layered materials relies on complicated procedures that include high temperature environment and special preparation conditions.[16,17] However, the electrodeposition technique opens the way for the modification of arbitrary complex current collector surfaces, including 3D-printed surfaces.[18,19]

The development of 3D-printing enables the manufacturing of conductive devices with a specific shape and composition.[20,21] Moreover, the involvement of 3D-printing technology in electrochemistry is growing, especially in the aspect of fabrication of electrodes, electrochemical cells or supercapacitors.[22–25] Among the 3D-printing techniques, Fused Deposition Modelling (FDM) is one of the most widely used technique for the fabrication of 3D devices.[20,26] The principle of this technique is based on filament extrusion through a heated nozzle to build printed objects layer-by-layer.[27,28] Additionally, different polymer–nanocarbon blends were tested for 3D-printing application, while polystyrene was identified as the best performing matrix material for applications in aqueous media.[29] However, the utilization of nanocarbon-based materials is extended with the nanocarbon/

[a]*Future Energy and Innovation Laboratory, Central European Institute of Technology, Brno University of Technology, Purkyňova 123, 61200 Brno, Czech Republic. E-mail: pumera.research@gmail.com*
[b]*Department of Chemistry and Biochemistry, Mendel University in Brno, Zemedelska 1, CZ-613 00 Brno, Czech Republic*
[c]*Department of Chemical and Biomolecular Engineering, Yonsei University, 50 Yonsei-ro, Seodaemun-gu, Seoul 03722, Korea*
[d]*Department of Medical Research, China Medical University Hospital, China Medical University, No. 91 Hsueh-Shih Road, Taichung 40402, Taiwan*

†Electronic supplementary information (ESI) available: Details about the cross section sample, cyclic voltammogram of the UME, cyclic voltammogram for the TMD electrodeposition, SEM micrograph of the thermally activated 3D-printed electrode, XPS study of thermally activated and TMDs modified 3D-printed electrodes, schematic energy band diagrams for TMDs, Tafel plots and table for comparison of the current literature reports. See DOI: 10.1039/d0nr06679f

polymer filaments. The commercially available nanocarbon/polylactic acid (PLA) filament has emerged as the most commonly used 3D-printing material for electrochemical applications such as energy conversion[30] and energy storage.[31] Since the filament contains insulating PLA, the 3D-printed structures are found to have low electrochemical activity and thus post-printing treatments such as thermal annealing,[32] chemical activation[31,33] and further surface modifications[18] have to be applied to improve their performance and applicability. Thermal annealing and chemical activation are used to remove PLA from the nanocarbon/PLA filament and thus make the 3D-printed devices conductive. However, compared to chemical activation, thermal activation is found to create more electrochemically active electrodes, but these are also less mechanically stable.[18,32] Moreover, thermal activation results in an increased active surface area that can be modified in order to additionally enhance electrochemical performance for energy conversion applications.

In this work, macroscopic and microscopic electrocatalytic activity of the electrodeposited MoS_2 and WS_2, as well as the combination of MoS_2 and WS_2 as two-layered heterojunctions on thermally activated 3D-printed nanocarbon electrodes were investigated. The characterization of the macroscopic electrochemical activity for the HER was carried out *via* linear sweep voltammetry (LSV). The local highly resolved electrochemical activity of the electrodeposited TMDs was investigated on the cross sections of the electrodeposited thermally activated 3D-printed electrodes using scanning electrochemical microscopy (SECM). The microscopic electrochemical performance was investigated in order to gain insight into the position of the electrochemically active sites of electrodeposited TMDs within the 3D-printed nanocarbon structure.

Experimental

Chemicals & materials

All electrodes were printed from conductive nanocarbon/PLA filament (3D Black Magic®, Graphene Laboratories Ink., New York, USA). For electrochemical deposition, 10 mM $(NH_4)_2MoS_4$ (99.97%, Sigma-Aldrich) and 10 mM $(NH_4)_2WS_4$ (99.9%, Sigma-Aldrich) with 0.1 M KCl (analytical grade, Merck KGaA, Germany) as supporting electrolyte were used. For SECM mediator, a 1.5 mM FcMeOH solution (99%, ABCR GmbH Germany) with 0.2 M KNO_3 (analytical grade, Merck KGaA, Germany) as the supporting electrolyte was used. 0.5 M H_2SO_4 (96%, analytical grade, Penta, Czech Republic) was used for hydrogen evolution reaction measurements. All solutions were prepared in deionized water with a resistivity greater than 18 MΩ cm.

Material characterization

The morphology and chemical composition of the 3D-printed electrodes were characterized using a scanning electron microscope (SEM, TESCAN Lyra 3 and Mira 3 XMU) equipped with an energy dispersive X-ray (EDX) detector (Bruker XFlash 5010 and Oxford Instruments X-MAX EDS, respectively). An accelerating voltage of 20 kV was used. In addition, chemical composition analysis was performed by X-ray photoelectron spectroscopy (XPS, Kratos AXIS Supra) using a monochromatic Al Kα (1486.7 eV) excitation source. The spectra were calibrated against the carbon 1s signal at 284.8 eV and were fitted using Casa XPS software.

3D-printing of electrodes

The electrode, as shown in Scheme 1A, was designed using Fusion 360 (Autodesk, USA) software. The corresponding .stl file was sliced using open source Slicer software (Prusa Research, Czech Republic). Electrodes were printed using a Prusa 3D printer (Prusa i3 MK3, Czech Republic) with a 0.6 mm nozzle (Olsson Ruby, 3DVerkstan, Sweden). The printing conditions were temperatures of 220 °C for the nozzle and 60 °C for the bed with 90% filament infill. After printing, the 3D-printed electrodes were thermally activated for 3 h at 350 °C in a furnace (Electrické Pece, Svoboda, Czech Republic) with a heating rate of 5 °C min^{-1}. After naturally cooling down to room temperature, the thermally activated 3D-printed electrodes were fixed on a copper tape with a nitrocellulose film (Nail polish, Flormar-Kosan Kozmetik, Turkey). For the electrical contact between the electrode and the copper tape, silver conductive ink (ELCHEMCo spol. s.r.o., Czech Republic) was used. After drying, the electrodes were ready for electrodeposition.

Electrochemical deposition of TMDs on 3D-printed electrodes

The electrochemical deposition on the 3D-printed nanocarbon electrode was performed with a potentiostat (Autolab, Metrohm, Netherlands) controlled by Nova 2.1 software. The potentials were measured relative to the Ag/AgCl reference electrode and a graphite electrode served as the counter electrode.

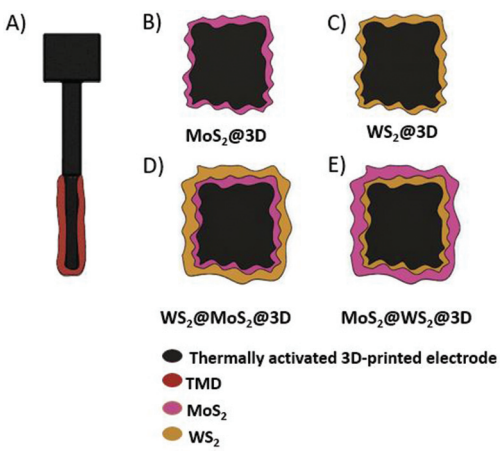

Scheme 1 Schematic illustration of the TMD modified thermally activated 3D-printed nanocarbon electrode (A), and the corresponding cross sections (B–E) showing the single layer modification with MoS_2 (MoS_2@3D) (B), WS_2 (WS_2@3D) (C) as well as the modification with WS_2 on MoS_2 (WS_2@MoS_2@3D) (D) and MoS_2 on WS_2 (MoS_2@WS_2@3D) (E) to create two-layered heterojunction.

Unless stated otherwise, all potentials were converted and reported *versus* the reference hydrogen electrode (RHE), according to the literature.[34] A schematic representation of the deposited materials is shown in Scheme 1(B–E). Electrochemical deposition of MoS_2 [12] (Scheme 1B) and WS_2 [6] (Scheme 1C) was performed in 10 mM $(NH_4)_2MoS_4$ precursor solution and 10 mM $(NH_4)_2WS_4$ precursor solution, respectively, with 0.1 M KCl as the supporting electrolyte using cyclic voltammetry (CV). The potential was cycled between −1.3 V and 0.6 V (*vs.* Ag/AgCl) for MoS_2 and between −1.3 V and 1.1 V (*vs.* Ag/AgCl) for WS_2, separately for 20 cycles. The deposition started from 0 V in the cathodic direction with a scan rate of 50 mV s^{-1}. Two consecutive electrochemical depositions of heterojunctions were performed. First, MoS_2 (or WS_2) was deposited and dried overnight, then the second layer, WS_2 (or MoS_2) was deposited, the procedures described above resulted in heterojunctions, as shown in Scheme 1(D and E). All depositions were carried out in a three electrode system with Ag/AgCl and glassy carbon as reference and counter electrodes, respectively.

Sample preparation for scanning electrochemical microscopy

After electrodeposition, the modified electrodes were encapsulated in an epoxy resin mixture (12.5 g of EpoFix Resin and 1.5 g of EpoFix Hardener, Struers Aps, Denmark) in a vacuum impregnation chamber (CitoVac). Scheme 2A shows the illustration of the sample preparation process. A plastic holder (MultiClips, Struers, Denmark) was used for the fixation of the electrode. The curing took place overnight at room temperature and after this, mechanical grinding and polishing were performed with a grinder/polisher (Tegramin 30) until the cross sections of the electrodes were exposed. Sample grinding was performed with a series of SiC foils (180, 500, 1200 and 4000 grit sizes). Final polishing was performed with the diamond suspension polishing fluids (DP-Suspension P, 9 μm, 3 μm and 1 μm) and an MD Nap-T polishing cloth until a mirror-like surface was achieved. A typical cross section sample is depicted in Fig. S1 in the ESI.† The prepared samples were fixed on copper tape which was supported on a glass slide. For electrical contact between the sample and the copper tape, a silver conductive epoxy adhesive (MG Chemicals, Canada) was used. After drying the silver epoxy adhesive at room temperature, SECM measurements were performed. The optical images of the electrode cross sections were taken with a stereo microscope (Zeiss Stemi 508) with a color camera (Axiocam 105) connected to Axio Vision Software.

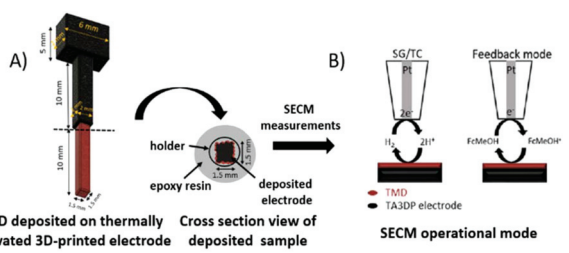

Scheme 2 Illustration of the cross section sample preparation process for SECM measurement (A) and feedback and substrate generation/tip collection (SG/TC) operational modes in SECM (B).

Electrochemical characterization of electrocatalytic hydrogen evolution reaction performance

The macroscopic HER performance was characterized by LSV on the modified thermally activated 3D-printed electrode by immersing only the modified part in 0.5 M H_2SO_4. The dimensions of the immersed section were 1.5 mm × 1.5 mm × 10 mm as shown in Scheme 2A. LSV measurement started at a potential of 0.2 V with a scan rate of 5 mV s^{-1}. Tafel slopes were calculated from the obtained LSV measurements.

The localized microscopic HER performance was characterized by SECM (Sensolytics, Germany) performed on the cross sections of the modified electrodes. The investigated surfaces are represented in Scheme 1(B–E). For SECM imaging in constant height (tip-to-substrate distance of ~17 μm), a 25 μm diameter Pt ultra-microelectrode (UME) (Sensolytics, Germany) was used as the tip. Before the measurement, the UME was polished with 0.05 μm Al_2O_3 particles on a polishing pad and rinsed with ultrapure water. The characterization of UME was performed by CV in 1.5 mM FcMeOH with 0.2 M KNO_3 mediator solution starting from an open circuit potential with a potential range from 0 V to 0.5 V and a scan rate of 50 mV s^{-1} (Fig. S2 in the ESI†). All SECM measurements were performed with Ag/AgCl 3 M KCl as reference and Pt as counter electrodes, respectively. The cross sections were investigated in the feedback and substrate generation/tip collection (SG/TC) mode. Scheme 2B shows the schematic illustration of these operational modes. The SECM measurements in the feedback mode were performed in mediator solution with an applied potential of E_{UME} = 0.64 V. The HER activity of the deposited TMDs was mapped in the SG/TC mode in 0.5 M H_2SO_4 with potential applied to the UME of E_{UME} = 0.34 V, while potentials to the substrate were set at $E_{substrate1}$ = −0.28 V and $E_{substrate2}$ = −0.53 V. For imaging in the feedback mode, a maximum scan rate of 100 μm s^{-1} and a pixel size of 10 × 10 μm were used. Whereas for the imaging in the SG/TC mode, a maximum scan rate of 300 μm s^{-1}, and a pixel size of 20 × 20 μm were used. For all images, the waiting time was 4 ms. For the estimation of the thickness of HER active sites, the distribution of HER activity is considered as a peak-shaped curve. The maximum of the peak is the active site with the highest activity on the surface (red color), shown in the SECM image. The thickness of the active site is calculated as the width of the peak at ~2/3 of the peak height. For data processing and analysis, Gwyddion 2.55 and OriginPro 2019 software were used.

Results and discussion

The 3D-printed electrodes were fabricated *via* fused deposition modeling. Due to the insulating nature of the PLA which results in poor electrochemical activity, thermal treatment was used to remove PLA. The temperature was set above the degra-

dation temperature of PLA at 350 °C for 3 hours.[35] After heating, the mechanical stability of the electrode was decreased and the residual mass of the thermally activated bare electrode was found to be ~14% of the as-printed electrode. The electrochemical deposition of two different TMDs, MoS_2 (MoS_2@3D) and WS_2 (WS_2@3D) and heterojunctions were carried out at the activated electrodes. To create two-layer heterojunctions, WS_2 was electrodeposited on the MoS_2 modified electrode (WS_2@MoS_2@3D), and MoS_2 was electrodeposited on the WS_2 modified electrode (MoS_2@WS_2@3D). In the corresponding cyclic voltammograms shown in Fig. S3 in the ESI,† an increase in anodic and cathodic currents with increasing deposition cycles indicates the growth of the deposited material.

The SEM micrograph of the unmodified thermally activated electrode is presented in Fig. S4 (in the ESI†). The fiber-like morphology is in line with other works using the same type of filament to prepare 3D-printed electrodes.[20,35] Electrodeposition of the TMDs resulted in agglomerated nanostructures along the surface of the electrode, as shown in Fig. 1A–D. The elemental compositions of the TMDs on 3D-printed electrodes were characterized by EDX mapping (Fig. 1). From the presented EDX maps, the presence of Mo, S, and W, on the nanocarbon fibres is visible. Fig. 1(A and B) show a uniform elemental distribution for Mo (red) and S (green) on MoS_2@3D and W (yellow) and S (green) on WS_2@3D electrodes. However, in the case of the two-layer combinations WS_2@MoS_2@3D and MoS_2@WS_2@3D, the distribution of Mo, S and W is dominated by the top layer deposition (Fig. 1C and D). Additional analyses of the unmodified and TMDs modified thermally activated 3D-printed electrodes were carried out by XPS, as shown in Fig. S5–S7 (in the ESI†). The XPS survey spectrum of the thermally activated electrode (Fig. S5A in ESI†) confirms the presence of C, O, Ti and Fe on the electrode surface. The deconvolution of the C 1s and Ti 2p spectrum is shown in Fig. S5B and C (in ESI†), respectively, and shows the presence of sp^2 carbon from the carbon nanostructure and Ti (IV) from TiO_2, which are present as impurities. The XPS survey spectra of the TMD modified samples confirm the deposition of TMDs on the 3D-printed electrode surfaces (Fig. S6 in ESI†). The deconvolution spectra of Mo 3d, W 4f and S 2p are shown in Fig. S7A–D (in the ESI†). In general, the deconvolution spectra of Mo 3d and W 4f show two doublets for Mo(IV) and Mo(VI) and two doubles for W(IV) and W(VI) oxidation states. Subsequently, when S 2p spectra were deconvoluted, two doublets for terminal S^{2-} and bridging S_2^{2-} peaks were observed. These analyses confirm the presence of mixed MoS_2/MoS_3 and WS_2/WS_3 materials on the electrode surfaces.[18,36–38]

The overall hydrogen evolution activity of all the TMDs deposited electrodes was evaluated using LSV in 0.5 M H_2SO_4 solution. Fig. 2 shows the obtained polarization curves. Comparing as-printed and thermally activated 3D-printed electrodes, a significantly lower overpotential of −0.56 V at a current density of −10 mA cm^{-2} is observed. For the thermally activated electrode, this enhancement can be related to the more conductive electrode after thermal activation and the contribution of metal-based impurities such as TiO_2 and Fe_3O_4 in the bare filament.[32] However, the MoS_2@3D electrode reaches a current density of −10 mA cm^{-2} at the lowest overpotential of −0.28 V which is in good agreement with the reported values for MoS_x at the same current density.[12,18,39–41] The WS_2@3D electrode requires an overpotential of −0.53 V which is slightly lower than the overpotential of the thermally treated electrode. Also, compared to the overpotential values ranging from 0.72 V to 0.74 V (*vs.* RHE) obtained for WS_2 on the reduced graphene oxide composites reported in the litera-

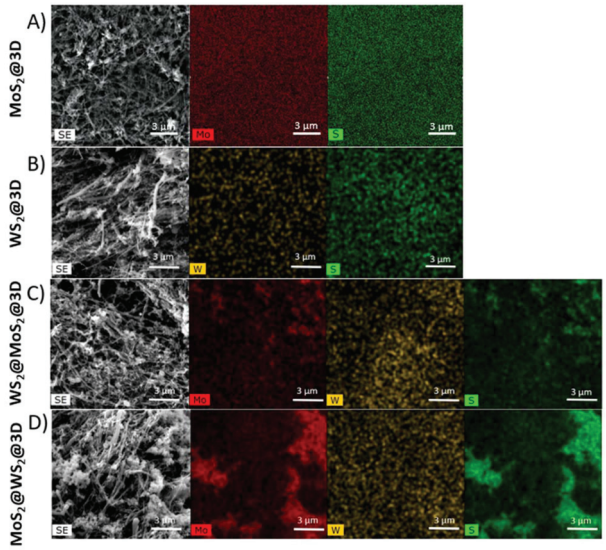

Fig. 1 Scanning electron micrographs (black & white) and energy dispersive X-ray maps of the elemental distribution of Mo (red), W (yellow) and S (green) for the electrodeposited TMDs and their heterojunctions on thermally activated 3D-printed electrodes. The investigated TMDs were MoS_2@3D (A), WS_2@3D (B), WS_2@MoS_2@3D (C) and MoS_2@WS_2@3D (D).

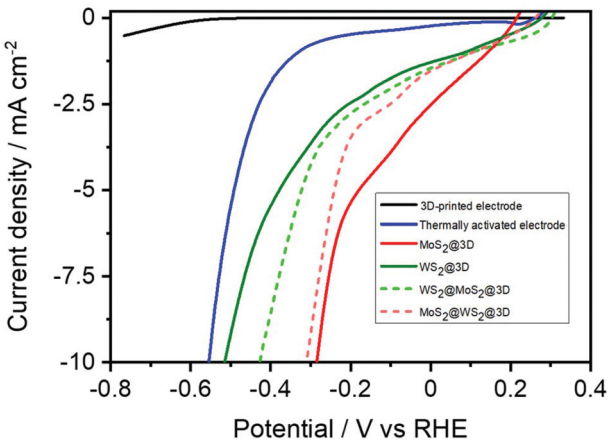

Fig. 2 Linear sweep voltammograms for the HER on the 3D-printed electrode, thermally activated 3D-printed electrode, MoS_2@3D, WS_2@3D, WS_2@MoS_2@3D, and MoS_2@WS_2@3D. Measurements were performed in 0.5 M H_2SO_4 with a scan rate of 5 mV s^{-1}.

ture,[38] the WS_2@3D electrode in this work shows higher catalytic activity. The overpotentials of the two-layer deposited electrodes are between the values for single TMDs, while the MoS_2@WS_2@3D electrode is shown to have a lower overpotential of −0.31 V. Based on the energy band diagrams of MoS_2 and WS_2 heterojunctions reported in the literature,[42–44] both the valence band and the conduction band of the WS_2 are found to be higher than those of MoS_2, as shown in Scheme S1 (in the ESI†). Considering the case of the MoS_2@WS_2@3D electrode, where the inner deposited layer is WS_2, the favourable electron transport from the conduction band of WS_2 to MoS_2 requires a lower applied potential (−0.31 V at −10 mA cm^{-2}) for the HER, as shown in Fig. 2. However, the reversed heterojunction with MoS_2 as the inner layer causes slow electron transport between layers and requires a higher applied potential (−0.42 V at −10 mA cm^{-2}) in order to drive the HER. This leads to the overpotential difference between the two heterojunctions of ≈0.11 V at −10 mA cm^{-2}, which corresponds to the difference in energy levels for the conduction bands of WS_2 and MoS_2, reportedly in a range of 0.1–0.2 V.[42–44] Thus, comparing the 3D electrodes composed of different heterojunctions, the MoS_2@WS_2@3D electrode is more electrochemically active and presented higher HER activity. Compared to the overpotential of MoS_2/WS_2 heterostructures in the range between −0.25 V and −0.45 V (*vs.* RHE) measured at a current density of −10 mA cm^{-2}, the obtained results are in good agreement with the literature.[45,46] The Tafel slopes are calculated by LSV measurements and shown in Fig. S8A (in ESI†). The Tafel slope of the MoS_2@3D electrode and WS_2@3D electrode was found to be −219 mV dec^{-1} and −168 mV dec^{-1}, respectively, which is in agreement with the reported values.[6,18,38,40] The calculated Tafel slopes of −252 mV dec^{-1} and −190 mV dec^{-1} correspond to MoS_2@WS_2@3D and WS_2@MoS_2@3D electrodes, respectively. Additionally, the Tafel slope of the thermally activated 3D-printed electrode is found to be −223 mV dec^{-1}. The comparison of the calculated Tafel slopes is presented in the bar chart in Fig. S7B (in the ESI†). The obtained overpotentials and Tafel slopes in this work are compared with the recently reported values for similar promising HER catalysts for 3D-printing and presented in Table S1 (in the ESI†).

In fact, the mechanical stability of the thermally activated bare electrode has decreased compared to the as-printed electrode, where the removal of PLA resulted in a porous electrode structure. The porosity is clearly observable in the optical image of the cross section of the thermally activated bare electrode surface (Fig. 3A). Since the electrochemical deposition of TMDs was performed on the porous thermally activated 3D-printed electrode, the question about local active sites for the HER of the deposited material in the 3D nanostructure and the electrochemical activity on the interior arises. To address this question, the cross sections of the modified electrodes were investigated by microscopic electrochemical characterization *via* SECM. In order to provide information about the electrochemical activity of TMDs, the UME is scanned across the sample cross section in feedback and substrate generation/tip collection (SG/TC) operational modes. By scanning in the feedback mode, local differences in conductivity can be recorded.[47] The HER activity of the TMDs is investigated in the SG/TC mode in a four-electrode system, where the substrate acts as a second working electrode. In this mode, a sufficient potential is applied to the substrate to initiate the reaction and an adequate potential is applied to the UME tip to collect the generated species.[48,49] This type of measurement is used for the investigation of local differences in HER activity due to the fact that a locally higher hydrogen concentration results in a higher anodic current response.[50,51]

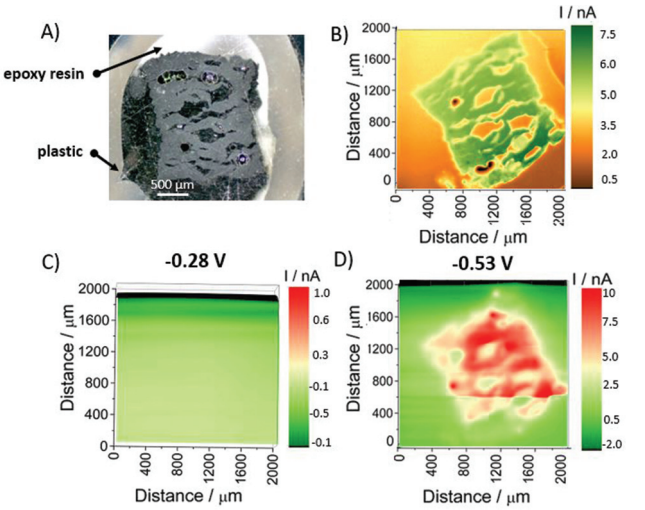

Fig. 3 Scanning electrochemical micrographs of the thermally activated bare electrode with the optical image of the sample (A). SECM image recorded in the feedback mode in 1.5 mM FcMeOH with 0.2 M KNO_3 mediator solution with a tip potential of E_{UME} = 0.64 V, a maximum scan rate of 100 µm s^{-1}, pixel size of 10 × 10 µm and a waiting time of 4 ms (B), SECM images recorded in 0.5 M H_2SO_4 solution with a hydrogen generation potential of $E_{substrate1}$ = −0.28 V (C) and $E_{substrate2}$ = −0.53 V (D) and a detection tip potential of E_{UME} = 0.34 V. For imaging a maximum scan rate of 300 µm s^{-1}, a pixel size of 20 × 20 µm, a waiting time of 4 ms and for all SECM images a 25 µm diameter Pt disc UME was used.

Firstly, the cross section of the thermally activated electrode without the deposited material is examined in both feedback and SG/TC modes and the obtained scanning electrochemical micrographs are presented in Fig. 3(B–D). The SECM image in the feedback mode (Fig. 3B) shows uniform conductivity of the activated bare electrode with insulating areas from the epoxy resin around the electrode and in the holes. Also, the structure of the electrode is comparable to the shape of the electrode in the optical image (Fig. 3A). Different generated potentials are applied to the cross section according to the LSV data (Fig. 2). Applying a potential of $E_{substrate1}$ = −0.28 V to the substrate in 0.5 M H_2SO_4 solution and scanning in the SG/TC mode (Fig. 3C), the sample is found to be inactive for the HER, which is consistent with the LSV data (Fig. 2). Setting the applied potential to $E_{substrate2}$ = −0.53 V, which corresponds to a current density of −10 mA cm^{-2}, the SECM image (Fig. 3D) shows a high HER activity (red color) of the thermally activated

bare electrode with inactive areas corresponding to the epoxy resin. According to the literature,[32] metal-based impurities present in the filament are responsible for this high HER activity. As shown in the SECM image (Fig. 3D), even the distribution of the metal-based impurities in the 3D-printed electrode is visible. The electrode structure visible in this figure is comparable with the shape of the electrode obtained in the feedback mode (Fig. 3B). The missing electrode part on the top and bottom indicates the loss of electrical contact with the potentiostat.

In the following, the cross section of the MoS_2@3D and WS_2@3D electrodes in the feedback and SG/TC modes was investigated. Different generated potentials are applied to the deposited surfaces according to the LSV data (Fig. 2). Fig. 4 shows the SECM images of the cross sections of the 3D-printed electrodes with MoS_2 and WS_2 electrodeposited layers (Fig. 4A and B, respectively). The feedback mode micrograph of MoS_2@3D (Fig. 4C) shows the difference between highly conductive edge sites and the interior zones with slightly lower conductivity. The shape of the electrode corresponds to the optical image and it is observable with interior holes filled with epoxy resin. Scanning in the SG/TC mode (Fig. 4E), shows

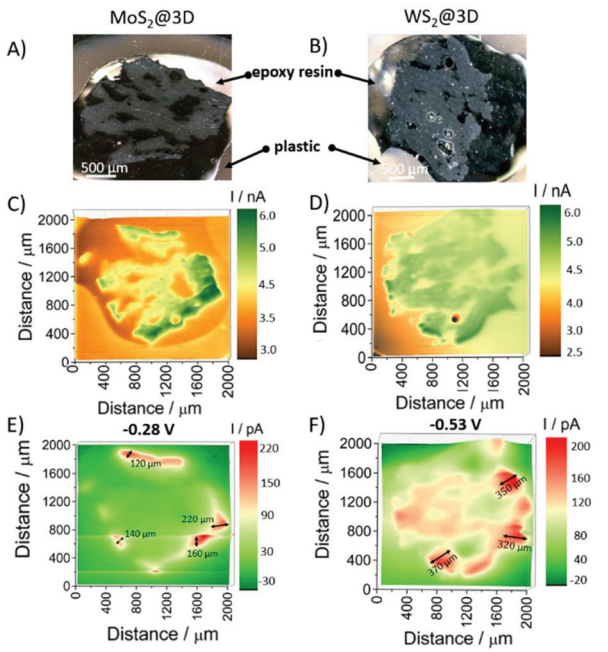

Fig. 4 Scanning electrochemical micrographs of the MoS_2@3D and WS_2@3D electrodes with optical images of the investigated MoS_2@3D (A) and WS_2@3D (B) electrode surfaces. SECM images recorded in the feedback mode in FcMeOH mediator solution for MoS_2@3D (C) and WS_2@3D (D) with a tip potential of E_{UME} = 0.64 V, a maximum scan rate of 100 µm s^{-1}, a pixel size of 10 × 10 µm and a waiting time of 4 ms. SECM images recorded in the SG/TC mode in 0.5 M H_2SO_4 solution for MoS_2@3D (E) and WS_2@3D (F) with a generation potential of $E_{substrate1}$ = −0.28 V (E) and $E_{substrate2}$ = −0.53 V (F) and a detection tip potential of E_{UME} = 0.34 V, a maximum scan rate of 300 µm s^{-1}, a pixel size of 20 × 20 µm and a waiting time of 4 ms. SECM images were recorded with a 25 µm diameter Pt UME.

that applying a potential of $E_{substrate1}$ = −0.28 V to the substrate was sufficient to initiate the HER only in the MoS_2 layer, according to Fig. 2. The highest HER activity was found on the edge sites (red color) and less activity in the interior part of MoS_2@3D. The calculated thickness of highly active sites is found to be in the range between ~120 µm and ~240 µm, as visible in Fig. 4E.

The SECM image of WS_2@3D in the feedback mode (Fig. 4D) shows negligible differences between the edge and interior sites of the electrode. The shape of the electrode with interior holes can be observed in the optical image (Fig. 4B). Consecutive, SECM images in the SG/TC mode (Fig. 4F) with a generation potential of $E_{substrate2}$ = −0.53 V revealed highly HER active edges with a slightly lower active interior electrode area. From the LSV (Fig. 2) it is observed that the applied potential is sufficient to initiate the HER on WS_2 and with small contributions to the unmodified nanostructure in the interior part of the electrode cross section. The high activity of sites corresponds to the WS_2 deposited layer and the calculated thicknesses were found to be in a range from ~320 µm to ~370 µm, as presented in Fig. 4F. The calculated thickness for the WS_2@3D electrode is larger compared to the MoS_2@3D electrode (Fig. 4E), since the used deposition procedures have different optimized potential windows, (as shown in Fig. S3 in the ESI†).

The MoS_2@WS_2@3D and WS_2@MoS_2@3D heterojunctions were investigated in order to show differences in the local HER activity. SECM images in the feedback and SG/TC mode with optical images of the investigated two-layer deposited electrodes cross sections are presented in Fig. 5. It can be observed that in the feedback mode the shape of the exposed electrode of WS_2@MoS_2@3D and MoS_2@WS_2@3D surfaces correspond to the optical images (Fig. 5A and D, respectively). In order to investigate the activity of different TMDs, different potentials were applied to the surfaces according to the potentials observed in Fig. 2. The SECM image in the SG/TC mode of the WS_2@MoS_2@3D surface with a hydrogen generation potential of $E_{substrate1}$ = −0.28 V shows that the electrode is already slightly active for the HER with visible edge sites with higher activity (red color). The active sites are mainly associated with MoS_2, based on the results in Fig. 2, and WS_2 is less active at this potential. The calculated thicknesses of ~110 µm and ~170 µm of active edges (Fig. 5E) are comparable with the values for MoS_2@3D (Fig. 4E). When the generation potential is set to $E_{substrate2}$ = −0.53 V, the HER is additionally initiated at WS_2 and the thickness of the HER active area (visible on Fig. 5F) is substantially increased due to the electrochemical activation of the WS_2 deposited layer. The calculated thicknesses of the active area (Fig. 5F) are ~385 µm and ~485 µm which are comparable to the calculated values for the WS_2@3D surface (Fig. 4F).

The MoS_2@WS_2@3D investigated in the SG/TC mode with a generated potential of $E_{substrate1}$ = −0.28 V (Fig. 5G) shows a high HER active area that covers most of the edge sites. The calculated thicknesses of active sites were found to be in a range from ~170 µm to ~220 µm and compared to the active

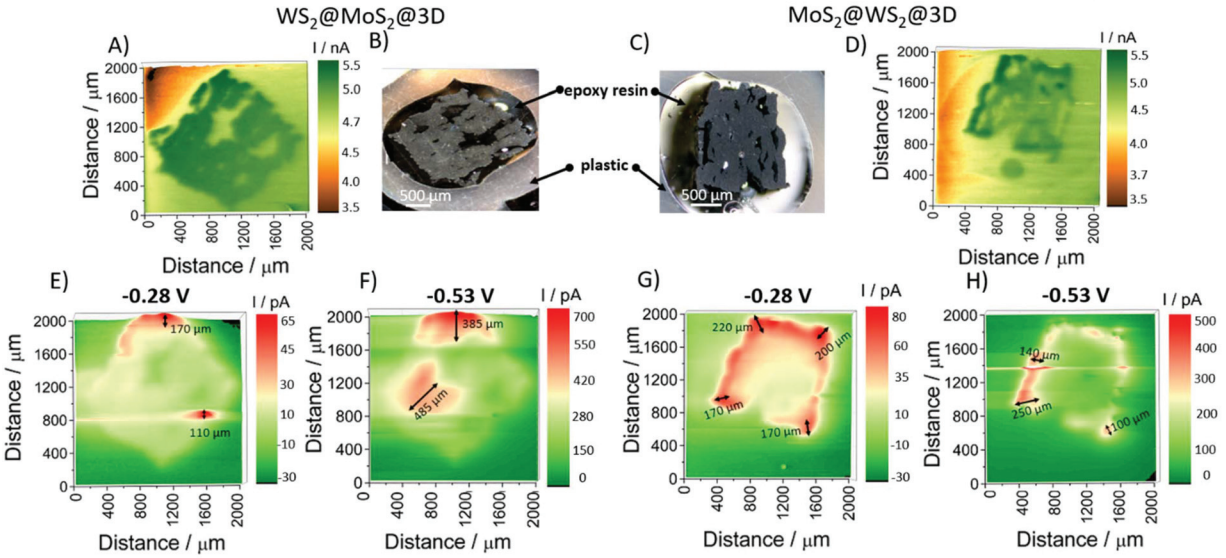

Fig. 5 Scanning electrochemical micrographs of the two-layer deposited electrodes with optical images of the investigated WS_2@MoS_2@3D (B) and MoS_2@WS_2@3D (C) electrode surfaces. SECM images of WS_2@MoS_2@3D (A) and MoS_2@WS_2@3D (D) were recorded in 1.5 mM FcMeOH mediator solution with E_{UME} = 0.64 V. A maximum scan rate of 100 µm s^{-1}, a pixel size of 10 × 10 µm and a waiting time of 4 ms was used. SECM images in the SG/TC mode of WS_2@MoS_2@3D (E and F) and MoS_2@WS_2@3D (G and H) were recorded in 0.5 M H_2SO_4 solution with a hydrogen generation potential of $E_{substrate1}$ = −0.28 V (E and G) and $E_{substrate2}$ = −0.53 V (F and H). The detection potential was E_{UME} = 0.34 V, a maximum scan rate of 300 µm s^{-1}, a pixel size of 20 × 20 µm and a waiting time of 4 ms. SECM images were recorded with a 25 µm diameter Pt disc UME.

area visible on the WS_2@MoS_2@3D surface (Fig. 5E), and with the values for MoS_2@3D (Fig. 4E) this is in good agreement and shows the activity of the MoS_2 layer. The SECM micrograph of the MoS_2@WS_2@3D surface obtained with the generated potential of $E_{substrate2}$ = −0.53 V (Fig. 5H) shows a decrease in HER activity of the edge sites with the thickness in the range from ~100 µm to ~250 µm. It is observable that the distribution of activity is better for MoS_2@WS_2@3D (Fig. 5G) compared to other deposited samples. The distribution of the activity depends on the amount and activity of the deposited material of the top layer (Fig. 2). Since the top layer of the MoS_2@WS_2@3D electrode is highly active MoS_2, a more even activity compared to the WS_2@MoS_2@3D electrode was found. Also, as previously discussed for the macroscopic HER in Fig. 2, the favourable electron transport from the WS_2 to MoS_2 layer due to the band positions of both TMDs (Scheme S1, in the ESI†), explains the activity of the MoS_2@WS_2@3D electrode. Furthermore, compared to the single TMD depositions (Fig. 4), it is observable that the distribution of the activity of the MoS_2@WS_2@3D electrode is more even because the heterojunctions are built from two layers. This indicates that the second deposited layer has a dominant influence on the local activity of the heterojunctions deposited on the activated 3D-printed electrode. Even the overpotential values of both heterojunctions are found to be intermediate compared to the obtained values for single TMDs (Fig. 2), the SECM images of heterojunctions (Fig. 5) show that the distribution of activity varies for different heterojunctions. This is essential for the MoS_2@WS_2@3D electrode (Fig. 5G), which is more even in comparison with other deposited samples and thus this study provides relevant information about 3D-printed electrodes modified with two-layer TMDs and their characterizations.

Conclusion

In summary, 3D-printed nanocarbon/polylactic acid electrodes were thermally activated and the resulting porous 3D-printed structure was modified with MoS_2 and WS_2 as well as with their heterojunctions *via* electrodeposition. The macroscopic electrochemical performance of the fabricated electrodes for the hydrogen evolution reaction (HER) was studied *via* linear sweep voltammetry and it was found that the MoS_2 modified electrode shows a significantly higher catalytic activity in comparison with the WS_2 modified electrode, while the activity of their heterojunctions is comparable to that of the outermost layer deposit. Microscopic examination of the local electrochemical activity of the deposits into the porous nanocarbon structure were investigated on cross sections through the nanocarbon electrodes using scanning electrochemical microscopy. The HER active sites for MoS_2 were found to be located on the surface with a thickness of ~150 µm in the 3D nanostructure while the thickness of active sites for the WS_2 were found to be ~300 µm. This shows that the electrodeposition and the subsequent heterojunctions of different TMDs *via* electrodeposition on 3D nanocarbon electrodes results in HER active sites that are not solely located at the outer surface, but also in the interior of the nanocarbon structure, where considerable HER activity could be detected. Furthermore, the presented methodology demonstrates a detailed study of the catalytic activity

on modified and unmodified 3D-printed nanostructures. Additionally, this study provides relevant information about the electrochemical characterization of TMD modified 3D-printed nanocarbon electrodes and offers insight into the imaging of material contrasts based on their activity for the HER, which provides valuable information for a deeper understanding and their systematical improvement for electrochemical applications.

Conflicts of interest

There are no conflicts to declare.

Acknowledgements

M. P. acknowledges the financial support from the Grand Agency of Czech Republic (GACR EXPO: 19-26896X). K. A. N., C. I. and S. N. acknowledge the support from the CzechNanoLab Research Infrastructure (ID LM2018110, MEYS CR) for providing the sample preparation and material characterization facilities.

Notes and references

1 S. J. Gutić, A. S. Dobrota, E. Fako, N. V. Skorodumova, N. López and I. A. Pašti, *Catalysts*, 2020, **10**(3), 290.
2 W. Yang and S. Chen, *Chem. Eng. J.*, 2020, **393**(1), 124726.
3 A. Eftekhari, *Int. J. Hydrogen Energy*, 2017, **42**(16), 11053–11077.
4 Q. Fu, J. Han, X. Wang, P. Xu, T. Yao, J. Zhong, W. Zhong, S. Liu, T. Gao, Z. Zhang, L. Xu and B. Song, *Adv. Mater.*, 2021, **33**(6), 1907818.
5 M. Zeng and Y. Li, *J. Mater. Chem. A*, 2015, **3**(29), 14942–14962.
6 S. M. Tan, Z. Sofer, J. Luxa and M. Pumera, *ACS Catal.*, 2016, **6**(7), 4594–4607.
7 A. A. Jeffery, C. Nethravathi and M. Rajamathi, *J. Phys. Chem. C*, 2014, **118**(2), 1386–1396.
8 X. Hai, K. Chang, H. Pang, M. Li, P. Li, H. Liu, L. Shi and J. Ye, *J. Am. Chem. Soc.*, 2016, **138**(45), 14962–14969.
9 A. Jawaid, D. Nepal, K. Park, M. Jespersen, A. Qualley, P. Mirau, L. F. Drummy and R. A. Vaia, *Chem. Mater.*, 2016, **28**(1), 337–348.
10 D. Xu, P. Xu, Y. Zhu, W. Peng, Y. Li, G. Zhang, F. Zhang, T. Mallouk and X. Fan, *ACS Appl. Mater. Interfaces*, 2018, **10**(3), 2810–2818.
11 R. Gusmão, Z. Sofer, P. Marvan and M. Pumera, *Nanoscale*, 2019, **11**, 9888–9895.
12 X. Chia, N. A. A. Sutrisnoh and M. Pumera, *ACS Appl. Mater. Interfaces*, 2018, **10**(10), 8702–8711.
13 K. Liu, Q. Yan, M. Chen, W. Fan, Y. Sun, J. Suh, *et al.*, *Nano Lett.*, 2014, **14**(9), 5097–5103.
14 W. Zhang, X. Li, T. Jiang, J. Song, Y. Lin, L. Zhu and X. Xu, *Nanoscale*, 2015, **7**, 13554–13560.
15 A. F. Rigosi, H. M. Hill, Y. Li, A. Chernikov and T. F. Heinz, *Nano Lett.*, 2015, **15**(8), 5033–5038.
16 H. Li, K. Yu, Z. Tang and Z. Zhu, *ACS Appl. Mater. Interfaces*, 2016, **8**(43), 29442–29451.
17 F. Wang, T. A. Shifa, X. Zhan, Y. Huang, K. Liu, Z. Cheng, C. Jiang and J. He, *Nanoscale*, 2015, **7**, 19764–19788.
18 C. Iffelsberger, S. Ng and M. Pumera, *Appl. Mater. Today*, 2020, **20**, 100654.
19 S. Ng, C. Iffelsberger, Z. Sofer and M. Pumera, *Adv. Funct. Mater.*, 2020, **30**(19), 1910193.
20 C. W. Foster, M. P. Down, Y. Zhang, X. Ji, S. J. Rowley-Neale, G. C. Smith, P. J. Kelly and C. E. Banks, *Sci. Rep.*, 2017, **7**, 42233.
21 K. Fu, Y. Wang, C. Yan, Y. Yao, Y. Chen, J. Dai, S. Lacey, Y. Wang, J. Wan, T. Li, Z. Wang, Y. Xu and L. Hu, *Adv. Mater.*, 2016, **28**, 2587–2594.
22 X. Tian and K. Zhou, *Nanoscale*, 2020, **12**, 7416–7432.
23 K. Fu, Y. Yao, J. Dai and L. Hu, *Adv. Mater.*, 2017, **7**, 1603486.
24 C. Zhu, Z. Qi, V. A. Beck, M. Luneau, J. Lattimer, W. Chen, *et al.*, *Sci. Adv.*, 2018, **4**, 8.
25 V. Egorov, U. Gulzar, Y. Zhang, S. Breen and C. O'Dwyer, *Adv. Mater.*, 2020, **32**(29), 2000556.
26 X. Wei, D. Li, W. Jiang, Z. Gu, X. Wang, Z. Zhang and Z. Sun, *Sci. Rep.*, 2015, **5**, 11181.
27 F. Zhang, M. Wei, V. V. Viswanathan, B. Swart, Y. Shao, G. Wu and C. Zhou, *Nano Energy*, 2017, **40**, 418–431.
28 S. A. M. Tofail, E. P. Koumoulos, A. Bandyopadhyay, S. Bose, *et al.*, *Mater. Today*, 2018, **21**(1), 22–37.
29 Z. Rymansaib, P. Iravani, E. Emslie, M. Medvidović-Kosanović, M. Sak-Bosnar, R. Verdejo and F. Marken, *Electroanalysis*, 2016, **28**(7), 1517–1523.
30 M. P. Browne, E. Redondo and M. Pumera, *Chem. Rev.*, 2020, **120**(5), 2783–2810.
31 C. Y. Foo, H. N. Lim, M. A. Mahdi, M. H. Wahid and N. M. Huang, *Sci. Rep.*, 2018, **8**, 7399.
32 M. P. Browne, V. Urbanova, J. Plutnar, F. Novotný and M. Pumera, *J. Mater. Chem. A*, 2020, **8**, 1120–1126.
33 D. M. Wirth, M. J. Sheaff, J. V. Waldman, M. P. Symcox, H. D. Whitehead, J. D. Sharp, J. R. Doerfler, A. A. Lamar, G. LeBlanc, *et al.*, *Anal. Chem.*, 2019, **91**(9), 5553–5557.
34 R. Van de Krol and M. Gratzel, Electronic materials: Science & Technology, in *Photoelectrochemical Hydrogen Production*, 2012.
35 J. P. Mofokeng, A. S. Luyt, T. Tábi and J. Kovács, *J. Thermoplast. Compos. Mater.*, 2012, **25**, 8.
36 C. H. Lee, S. Lee, G. S. Kang, Y. L. Lee, G. G. Park, D. C. Lee and H. I. Joh, *Appl. Catal., B*, 2019, **258**(5), 117995.
37 T. Y. Chen, Y. H. Chang, C. L. Hsu, K. H. Wei, C. Y. Chiang and L. J. Li, *Int. J. Hydrogen Energy*, 2013, **38**(28), 12302–12309.
38 N. M. Latiff, L. Wang, C. C. Mayorga-Martinez, Z. Sofer, A. C. Fisher and M. Pumera, *Nanoscale*, 2016, **8**, 16752–16760.
39 T. W. Lin, C. J. Liu and J. Y. Lin, *Appl. Catal., B*, 2013, **134–135**, 75–82.

40 H. Vrubel, T. Moehl, M. Grätzel and X. Hu, *Chem. Commun.*, 2013, **49**, 8985–8987.
41 X. Ge, L. Chen, L. Zhang, Y. Wen, A. Hirata and M. Chen, *Adv. Mater.*, 2014, **26**(19), 3100–3104.
42 V. Kaushik, M. Ahmad, K. Agarwal, D. Varandani, B. D. Belle, P. Das and B. R. Mehta, *J. Phys. Chem. C*, 2020, **124**(42), 23368–23379.
43 Y. Liang, S. Huang, R. Soklaski and L. Yang, *Appl. Phys. Lett.*, 2013, **103**, 042106.
44 L. Li, R. Long and O. V. Prezhdo, *Chem. Mater.*, 2017, **29**(6), 2466–2473.
45 J. Shi, R. Tong, X. Zhou, Y. Gong, Z. Zhang, Q. Ji, Y. Zhang, Q. Fang, L. Gu, X. Wang, Z. Liu and Y. Zhang, *Adv. Mater.*, 2016, **28**(48), 10664–10672.
46 D. Vikraman, S. Hussain, K. Akbar, L. Truong, A. Kathalingam, S. H. Chun, J. Jung, H. J. Park and H. S. Kim, *ACS Sustainable Chem. Eng.*, 2018, **6**(7), 8400–8409.
47 D. Polcari, P. Dauphin-Ducharme and J. Mauzeroll, *Chem. Rev.*, 2016, **116**(22), 13234–13278.
48 J. Molina, J. Fernández and F. Cases, *Synth. Met.*, 2016, **222**, 145–161.
49 R. D. Martin and P. R. Unwin, *Anal. Chem.*, 1998, **70**(2), 276–284.
50 U. M. Tefashe, M. E. Snowden, P. D. Ducharme, M. Danaie, G. A. Botton and J. Mauzeroll, *J. Electroanal. Chem.*, 2014, **720–721**, 121–127.
51 P. Hanekamp, T. Raith, C. Iffelsberger, T. Zankl, W. Robl and F. M. Matysik, *J. Appl. Electrochem.*, 2019, **49**, 455–463.

Chapter 7. Electrochemical Activity of the Transition Metal Dichalcogenide Crystals

Published paper included in this chapter:

S. Wert, C. Iffelesberger, **K. A. Novčić**, F-M Matysik, and M. Pumera, *Edges are more active than basal planes in the synthetic bulk crystals of TiS_2 and $TiSe_2$,* **Applied Materials Today (2022)**, 26, 101309, doi.org/10.1016/j.apmt.2021.101309.

7.1. Motivation for the Study

Layered transition metal dichalcogenides as two-dimensional materials have attracted much attention due to their excellent electrochemical properties. The leading representative from this group is MoS_2 whose activity comes from the catalytically active edges. However, the electrochemical activity of other transition metal dichalcogenides remains highly unexplored. This paper investigates whether the catalytically active edges are a general trend within bulk transition metal dichalcogenide crystals. Therefore, the study of TiS_2 and $TiSe_2$ was performed.

7.2. Paper Conclusion

This paper demonstrates the systematic study of the TiS_2 and $TiSe_2$ bulk crystals, their preparation and detailed physicochemical and electrochemical characterization. The microscopic electrochemical activity of the edges and basal planes of bulk crystals is examined by SECM. The results show the electrochemically active edges of the TiS_2 and $TiSe_2$ bulk crystals and confirm the general trend of the catalytically active edges in layered materials. This is important for the future development of electrocatalysts based on the IV group TMDs as electrocatalysts in energy conversion applications.

7.3. Student Contribution

The student is the third author of this paper who contributed to the study by optimizing the conductive epoxy resin used in the preparation of the crystals and providing formal analysis of the prepared samples. The student was also involved in writing the manuscript and preparing figures.

Applied Materials Today 26 (2022) 101309

Contents lists available at ScienceDirect

Applied Materials Today

journal homepage: www.elsevier.com/locate/apmt

Edges are more electroactive than basal planes in synthetic bulk crystals of TiS_2 and $TiSe_2$

Stefan Wert[a,b], Christian Iffelsberger[a], Katarina A. Novčić[a], Frank-Michael Matysik[b], Martin Pumera[a,c,d,e,*]

[a] Future Energy and Innovation Laboratory, Central European Institute of Technology, Brno University of Technology, Purkyňova 123, Brno 61200, Czech Republic
[b] Institute of Analytical Chemistry, Chemo- and Biosensors, University of Regensburg, Regensburg 93053, Germany
[c] 3D Printing and Innovation Hub, Department of Food Technology, Mendel University in Brno, Zemedelska 1, Brno CZ-613 00, Czech Republic
[d] Department of Chemical and Biomolecular Engineering, Yonsei University, 50 Yonsei-ro, Seodaemun-gu, Seoul 03722, Korea
[e] Department of Medical Research, China Medical University Hospital, China Medical University, No. 91 Hsueh-Shih Road, Taichung 40402, Taiwan

ARTICLE INFO

Article history:
Received 21 August 2021
Revised 25 November 2021
Accepted 4 December 2021

Keywords:
Transition metal dichalcogenides
Scanning electrochemical microscopy
2D materials
Titanium disulfide
Titanium diselenide
Anisotropy

ABSTRACT

Layered materials and derived 2D material couples such as graphite/graphene, layered and single layer pnictogens (i.e., black phosphorus and phosphorene) and transition metal dichalcogenides (TMDs) have gained a lot of attention due to their electrocatalytic properties and as potential materials for energy storage. Previous studies have shown that electrochemical reactions at graphite, MoS_2 and pnictogens mainly occur at the edges and steps of crystals rather than on the basal plane. The persisting question is if this is a general trend in nature within bulk crystals of 2D materials. To come closer to the answer to this question, we studied the surface of artificially grown TiS_2 and $TiSe_2$ crystals regarding their local electrochemical activity via scanning electrochemical microscopy (SECM). Both TMDs have shown increased electrochemical activity near crystal steps/edges. For correlation, optical and topographical analysis were performed via scanning electron microscopy (SEM) and atomic force microscopy (AFM). We show that the increased electrochemical activity at edges is persistent for these layered crystalline materials, thus expanding the knowledge their properties, which is important for future application in the energy sector.

1. Introduction

In the search for earth-abundant and environmental-friendly materials for energy storage, 2D materials such as graphite,[1–4] graphene [5,6], and layered pnictogens [6,7–11] (e.g., black phosphorous) [6,8–10] were found to be powerful candidates. Layered transition metal dichalcogenides (TMDs) are another large group of potential materials for energy-related applications [12–19]. With their chemical composition of MX_2, where M is a transition metal from groups IV to VII B (like Mo, W, Ti) and X is a chalcogenide (S, Se, Te), numerous elemental combinations can be realized. Due to their layered structure and strong covalent bonding within single layers, but weak interaction between layers because of van der Waals forces, these materials show anisotropy with respect to their electrical, mechanical, and electrochemical properties. Single or few layers can be prepared easily via exfoliation [20–22] and the resulting 2D materials show promising properties for a wide range of potential applications such as for energy storage [23,24], sensing [25], and solar cells.[26] Among TMDs, group VI members have been studied extensively so far, with MoS_2 being the most popular as it is a promising catalyst for the hydrogen evolution reaction [27,28].

Most notably, graphene [5,6,29], layered pnictogens [6,7–11] (e.g., black phosphorous) [6,8–10], and group VI TMDs [12–15,30–33] show increased electron transfer rates and increased electrocatalytic and electrochemical activity at the edges compared to basal planes (illustrated in Fig. 1A, with crystal structure in Fig. 1B). It is an important question whether the increased electrochemical activity at edges is a phenomenon generally occurring in 2D materials and if this property persists in bulk crystals. For group IV TMDs, studies regarding their local electrochemical activity are scarce. However, knowledge about this property is needed to expand the range of potential electrocatalysts and energy stor-

Abbreviations: AFM, atomic force microscope; EDS, energy dispersive X-ray spectroscopy; PAC, probe approach curve; PDMS, polydimethylsiloxane; SECM, scanning electrochemical microscopy; SEM, scanning electron microscope; SG/TC, substrate generation/tip collection; TMD, transition metal dichalcogenide.

* Corresponding author at: Future Energy and Innovation Laboratory, Central European Institute of Technology, Brno University of Technology, Purkyňova 123, Brno 61200, Czech Republic.
E-mail address: pumera.research@gmail.com (M. Pumera).

https://doi.org/10.1016/j.apmt.2021.101309
2352-9407/

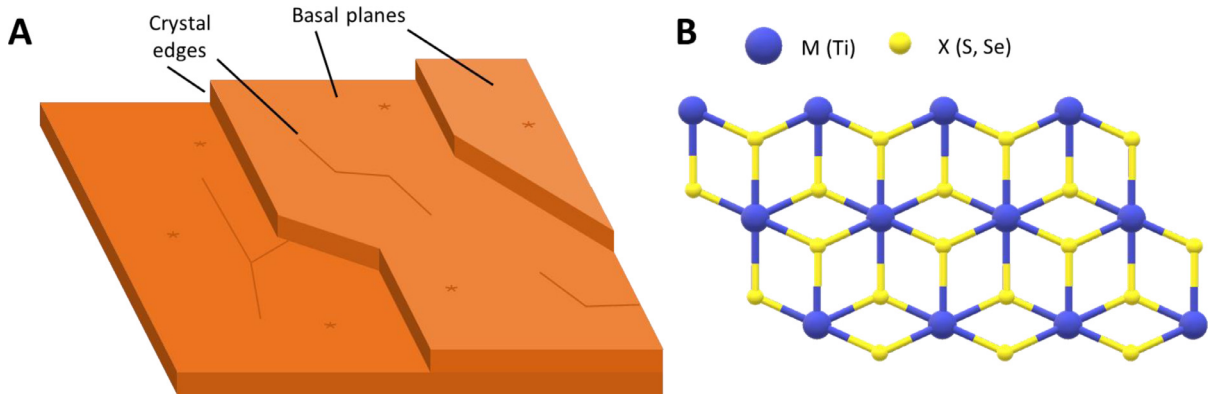

Fig. 1(. (A) Schematic view of the surface structure of layered 2D-materials like graphite, layered pnictogens and TMDs. (B) Crystal structure of group IV B TMDs, with M being coordinated octahedrally (1T phase).

age materials in the future. Therefore, we decided to study the local electrochemical activity of TiS_2 and $TiSe_2$ as representatives of group IV TMDs, which have not been investigated in this regard so far.

Generally, due to different coordination in the individual layers, group IV (octahedral 1T-phase) and VI TMDs (prismatic 2H phase) show different properties [34,35]. Group IV TMDs have attracted attention as they provide advantages over group VI TMDs like enhanced thermoelectric performance [36], high room-temperature mobility [37], ability to exhibit charge density wave [38], and high conductivity and theoretical capacity when used as anode material in sodium ion batteries [39,40]. Furthermore, they are considered as storage material in potassium ion batteries as alternative to lithium ion batteries [41].

To investigate if group IV TMDs crystals exhibit differences in the electrochemical activity between basal plane and edges, we used scanning electrochemical microscopy (SECM) over pristine TiS_2 and $TiSe_2$ surfaces for the localized imaging of the electrochemical activity. The obtained recordings were compared to scanning electron microscope (SEM), energy dispersive X-ray spectroscopy (EDS), atomic force microscope (AFM) images and X-ray photoelectron spectra (XPS) for correlating the electrochemical response with surface morphology and elemental composition.

2. Experimental

2.1. Materials and methods

TMD crystals (TiS_2, $TiSe_2$) were obtained from 2d-age.com. Two-component epoxy resin was purchased from Struers Aps, Denmark. Graphite powder (< 20 µm, synthetic) was bought from Sigma-Aldrich. Carbon SEM stubs were purchased from Micro to Nano, Netherlands. Polydimethylsiloxane (PDMS, SYLGARD^{TM} 184) was obtained from Dow Inc., Michigan, USA. Potassium ferricyanide ($K_3Fe(CN)_6$) and potassium chloride (KCl) were purchased from Merck, Germany. Solutions were prepared with deionized water with a resistivity > 18.2 MΩ cm (Milli-Q Advantage A10 system, Merck Millipore, Germany). All chemicals were of analytical grade and used as bought.

2.2. Crystal preparation

The sample preparation process is schematically shown in Fig. 2. For the fabrication of flat samples, the TMD crystals were embedded in an electrically conductive blend of graphite powder and epoxy resin with a mass ratio of 1:1 on carbon SEM stubs. About 250 mg of the mixture were spread on the stub surface and pressed on a TMD crystal placed on a flat PDMS layer in a petri dish. After 24 h, the graphite/epoxy blend hardened, and the sample was carefully removed from the PDMS. Furthermore, as the crystal was embedded within a conductive matrix, electrical contact was established at the upper layers of the crystal. Eventually, a clean sample with a pristine crystal surface was ensured by removal of the upper crystal layers according to the “scotch tape” method [42]. To introduce well-designed edges in the crystal surface, the upper layers of the TiS_2 crystal were cut with a scalpel, and the surface was rinsed to remove any residues.

2.3. Characterization

Electrochemical experiments were carried out with a commercial SECM (Sensolytics, Germany) and connected to a bipotentiostat (PGSTAT302N, Autolab, Netherlands). All potentials refer to a Ag/AgCl (3 M KCl) reference electrode. A Pt wire served as counter electrode. Electrical contact to sample stubs was established with conductive copper tape. The electrochemical cell consisted of two parts screwed together, with the sample placed in between. Images of the assembly are shown in Fig. S1.

SECM imaging was conducted with 10 and 25 µm diameter Pt disk ultramicroelectrodes (UMEs, RG > 10, Sensolytics, Germany) in a solution of $K_3Fe(CN)_6$ (10 mM in 0.1 M KCl). Prior to imaging, the probe was positioned by performing probe approach curves (PACs) above the respective crystal surface (shown in Fig. S2). The probe was approached until the probe made contact to the sample, yielding a reference PAC for estimating the substrate-to-tip distance. Prior to SECM imaging, the probe was then polished and reapproached until a well-established feedback response was obtained. Fitting this PAC to the reference PAC, an estimation about the substrate-to-tip distance at the beginning of the SECM images was possible. For images of TiS_2, the initial distance was 18 µm; for $TiSe_2$ it was 6 µm. SECM images were recorded with a pixel size of 10 µm and a maximum probe velocity of 300 µm s^{-1}. Feedback mode images were obtained with a probe potential of $E_{UME} = -0.2$ V applied and the substrate remaining at open circuit potential, while substrate generation/ tip collection (SG/TC) images were recorded with substrate and probe potentials of $E_{Substrate} = -0.5$ and $E_{UME} = 0.4$ V, respectively. The potential values were set to ensure steady current responses and were derived from cyclic voltammograms recorded with probes and samples (Fig. S3). Data processing of SECM images was done with Gwyddion 2.55 and Origin 2020 software.

Correlation of the AFM positions was achieved via optical images recorded prior to performing AFM (Dimension Icon with Airasyst cantilever, Bruker, USA). SEM and EDS images were obtained with a MIRA 3 SEM (Tescan, Czech Republic) and a Bruker XFlash 5010 EDS with an accelerating voltage of 20 kV used. Ele-

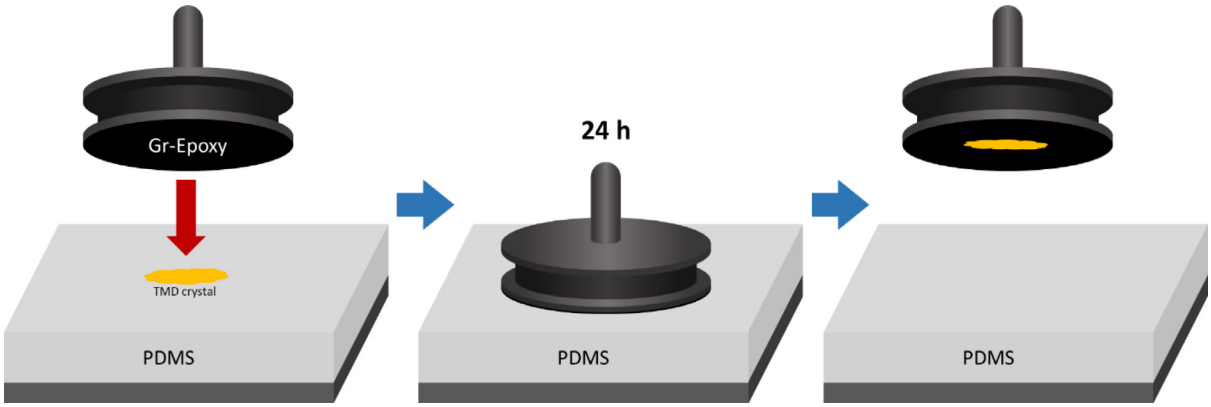

Fig. 2. Preparation of crystal samples. A sample holder covered with graphite epoxy mixture (Gr-Epoxy) was pressed onto a crystal placed on a thin layer of PDMS. After 24 h, the sample holder with the crystal was removed as the epoxy resin had hardened.

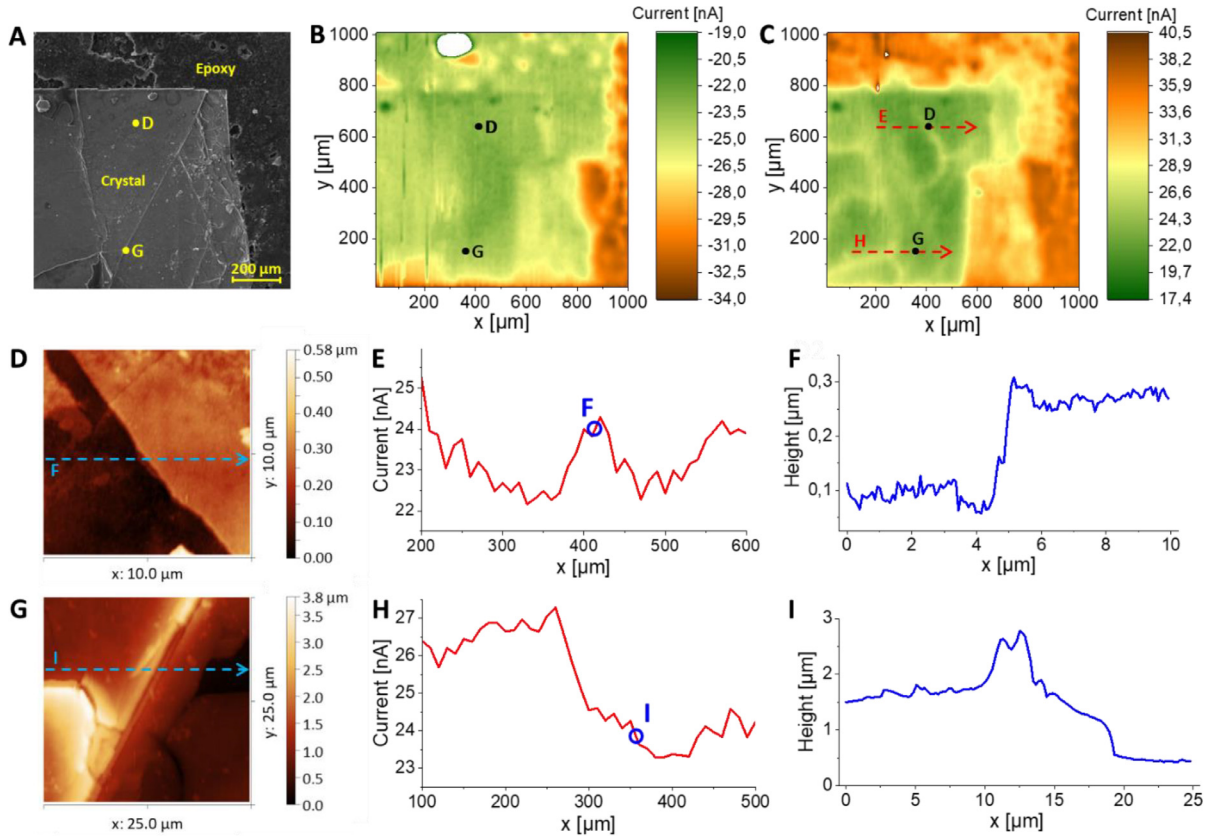

Fig. 3. Characterization of the TiS_2 crystal. (A) Scanning electron micrograph including indicators for the imaging locations of AFM images D/G (dots). (B/C) SECM images of the crystal recorded in feedback (B) and SG/TC (C) mode in 10 mM $K_3Fe(CN)_6$ as mediator. Probe diameter: 25 µm; Pixel size: 10 µm; Substrate-to-tip distance: 18 µm. E_{UME} = −0.2 V (B), 0.4 V (C). $E_{Substrate}$ = −0.5 V (C) (D/G) AFM images of crystal edges at the positions indicated in A–C. (E/H) Current profiles extracted from C, crossing spots D and G, respectively. (F/I) Line profiles extracted from D/ G.

mental composition of the samples was further confirmed by XPS (AXIS SupraTM, Kratos, United Kingdom). Spectra were recorded using a monochromatic Al Ka (1486.7 eV) excitation source and calibrated against the carbon 1 s signal at 284.8 eV. Evaluation was performed with Casa XPS software.

3. Results and discussion

Images of TiS_2 obtained via SEM (Fig. 3A) revealed a flat crystal structure surrounded by highly conductive graphite/epoxy resin blend. Multiple edges and cracks within the crystal were visible. EDS (Fig. S4) showed the presence of mainly Ti and S in the crystal. A homogeneous oxygen distribution was indicated with slight deviations at the cracks in the surface. XPS analysis indicated the presence of sulfides and oxides on the crystal surface (Fig. S5). In Table S1, the measured atomic percentages are listed. A ratio between Ti and S of ca. 1.45 is observable, which is explainable by the formation of oxides, also indicated by the EDS analysis. Generally, high C and O content was measured from the graphite-epoxy mixture surrounding the crystal.

The local electrochemical activity was analyzed (yellow box in Fig. 3A) via SECM performed in feedback and SG/TC mode (Fig. 3B and C, respectively). The processes occurring in the respective SECM measurement modes are illustrated in Fig. S6. The feedback

mode imaging, where the mediator species is converted at the probe in dependence of the sample conductivity, revealed a uniform conductivity over the entire crystal area. The orange-colored area corresponds to the highly conductive carbon surface of the graphite-epoxy mixture, which was surrounding the crystal. On the crystal itself, small deviations correlate with material grains visible in the SEM image (Fig. 3A). Due to the large probe diameter of 25 µm, small topographical variations remain undetected in the feedback mode SECM image. The white hole in the top part of the image corresponds to a rough portion within the epoxy resin. Fig. S7 shows the image in full current scale. In contrast, the SG/TC mode indicated differences in the local electrochemical activity as the mediator is reduced at the sample and the generated species is subsequently collected at the probe. The comparison with the SEM image shows that some of the poorly visible edges exhibit a high activity, while other more visible edges did not appear to be considerably electrochemically active. In addition, the bottom right area of the crystal, showing a high density of cracks in the SEM image, appears highly active in the SG/TC image while a low current was measured in feedback mode. Both observations are indicating a high electrochemical activity of crystal edges. To further analyze size and morphology of the edges at which the increased activity occurred, AFM was conducted at two different locations of the crystal to cover regions of high (position D) and low (position G) electrochemical activity. Their positions relative to SEM and SECM images are indicated in Fig. 3A–C. From the optical overview image recorded prior to AFM (Fig. S8), the edge at spot D can be localized. In Fig. 3D, an AFM image of a highly electrochemically active edge is shown. It appeared as a sharp step of 200 nm height difference. Comparing the extracted lines from the SECM (Fig. 3E) and AFM (Fig. 3F) images, the sharp step appeared considerably broader in the SECM image due to the probe size of 25 µm. In contrast, another AFM image of an edge exhibiting no noticeable increase of activity was obtained at position G (Fig. 3G). The edge appeared convoluted and considerably rougher than the edge investigated in Fig. 3D. The extracted AFM line in Fig. 3I shows that the edge consisted of a convolution of about 1 µm thickness followed by another step of 800 nm height. The extracted line from the SG/TC SECM image in Fig. 3H which covers the edge does not indicate noticeable activity differences. In contrast, at the 200 nm edge in Fig. 3D, a current increase of about 2 nA was detected. This nm-sized edge is visible in the µm-scaled SECM image due to two reasons. (1) The diffusion layer at the active sites was growing for several minutes before the SG/TC SECM image was recorded. (2) Due to its electroactive diameter of 25 µm, the SECM is in contact with this diffusion layer over a long lateral distance, which eventually leads to the active edge appearing more than 50 µm wide in the SG/TC SECM image.

To confirm the increased activity observed at the TiS_2 crystal edges, we additionally investigated the electrochemical activity at well-designed crystal edges. Therefore, a second TiS_2 crystal was studied, which contained artificially created edges (introduced by cutting the top layers of the TiS_2 crystal with a scalpel). Fig. S9A and B show the crystal before and after cutting, respectively. SG/TC mode SECM imaging (Fig. S9C) shows that both edges naturally occurring in the crystal, as well as artificially created edges exhibit increased electrochemical activity. The presence of the natural edge was confirmed by AFM (Fig. S9D-F), while the artificial edge was too rough to be measured.

Since previous localized studies with MoS_2 and WS_2 have shown increased electrochemical activity at edges compared to basal planes [30,32,33], and considering the obtained results we conclude that the same occurs in case of TiS_2. However, not in any case did the edge size correlate with activity, which could be due inconsistent electrical connections inside the crystal.

As second representative of group IV TMDs, a $TiSe_2$ crystal was investigated. The SEM micrograph of the crystal (Fig. 4A) shows a very rough surface at the crystal borders and in the top left region. However, the crystal appears predominantly flat, especially in the top right region. Notably, a slightly brighter appearing area can be seen in the bulk crystal (red boxes in Fig. 4A–D), where a lower amount of oxygen compared to the other parts of the crystal was determined via EDS (Fig. 4B) which might indicate a local difference in surface composition. EDS maps of other elements are presented in Fig. S10, showing a homogeneous distribution along the crystal surface. XPS analysis (Fig. S11) of the sample showed presence of Ti and Se. Atomic percentages in Table S2 show 1.75% Ti vs 0.86% Se. The area highlighted by a yellow box in the SEM image was studied via SECM in feedback and SG/TC mode (Fig. 4C and D). The feedback image shows a low but uniform conductivity in the parts of the crystal that appear smooth in the SEM image. At the crystal border, higher current deviations were measured due to more pronounced height differences stemming from larger cracks in the crystal. The orange areas in Fig. 4C correlate with the rough and dark areas visible in the SEM image showing the graphite-epoxy resin. In SG/TC mode, the crystal surface shows apparent differences in the electrochemical activity. Especially within the regions of the crystal with a rough topography small, remarkably active spots appear (predominantly in the dark green area in Fig. 4C), which are caused by edges being exposed due to cracks in the crystal surface. In addition, protrusions from the crystal surface that are associated with the cracks result in a lower substrate-to-tip distance, increasing the measured current even further. Smaller differences in electrochemical activity can be linked to cracks revealing active edges, which are visible in the SEM image, for example at the spots marked with “x” in SEM and SECM images.

Furthermore, the region corresponding to a decreased oxygen content visible in the EDS image exhibited an increased electrochemical activity. This observation is in line with activity differences occurring at group VI TMDs due to the formation of surface oxides [43]. In this region, the surface topography at the transition from high to low oxygen content was investigated via AFM imaging. For comparison, a second edge within the low oxygen area was imaged. The exact locations are indicated in Fig. 4A–D. Fig. 4E shows the AFM image obtained at the transition from low to high oxygen content showing a straight and clear edge. The bright part below the edge corresponds to the area of high oxygen content, while low amounts of oxygen were determined to be on the other side. The extracted line in Fig. 4F shows a sharp edge with a height difference of 300 nm and a higher surface roughness in the low oxygen area. The increased roughness (and thus surface area) and the decreased oxygen content, both might contribute to the increased electrochemical activity [43]. However, we assume that the oxygen content only has a minor effect on electrochemical activity since no conductivity difference was observed in the feedback mode SECM image. Similar to TiS_2, not all edges were observed to be electrochemically active. Spot G did not show any activity in the SG/TC image despite an edge being present (see AFM in Fig. 4G and the extracted line profile in Fig. 4H), which might be due to differences in electrical connection inside the crystal (Note that these crystals are multi-layered structures). However, the exact impact of the crystallographic structure of the edges on the electrochemical activity of the investigated crystals could not be resolved because of their multilayered and randomized structure and technical limitations. Nevertheless, the observations above show that microscopic cracks and edges can induce increased electrochemical activity. Furthermore, local differences in oxygen content on the surface might contributed to inhomogeneities in activity, as areas of higher oxygen concentration (shown by EDS in Fig. 4B) showed a reduced electrochemical activity of $TiSe_2$. Our experiments with

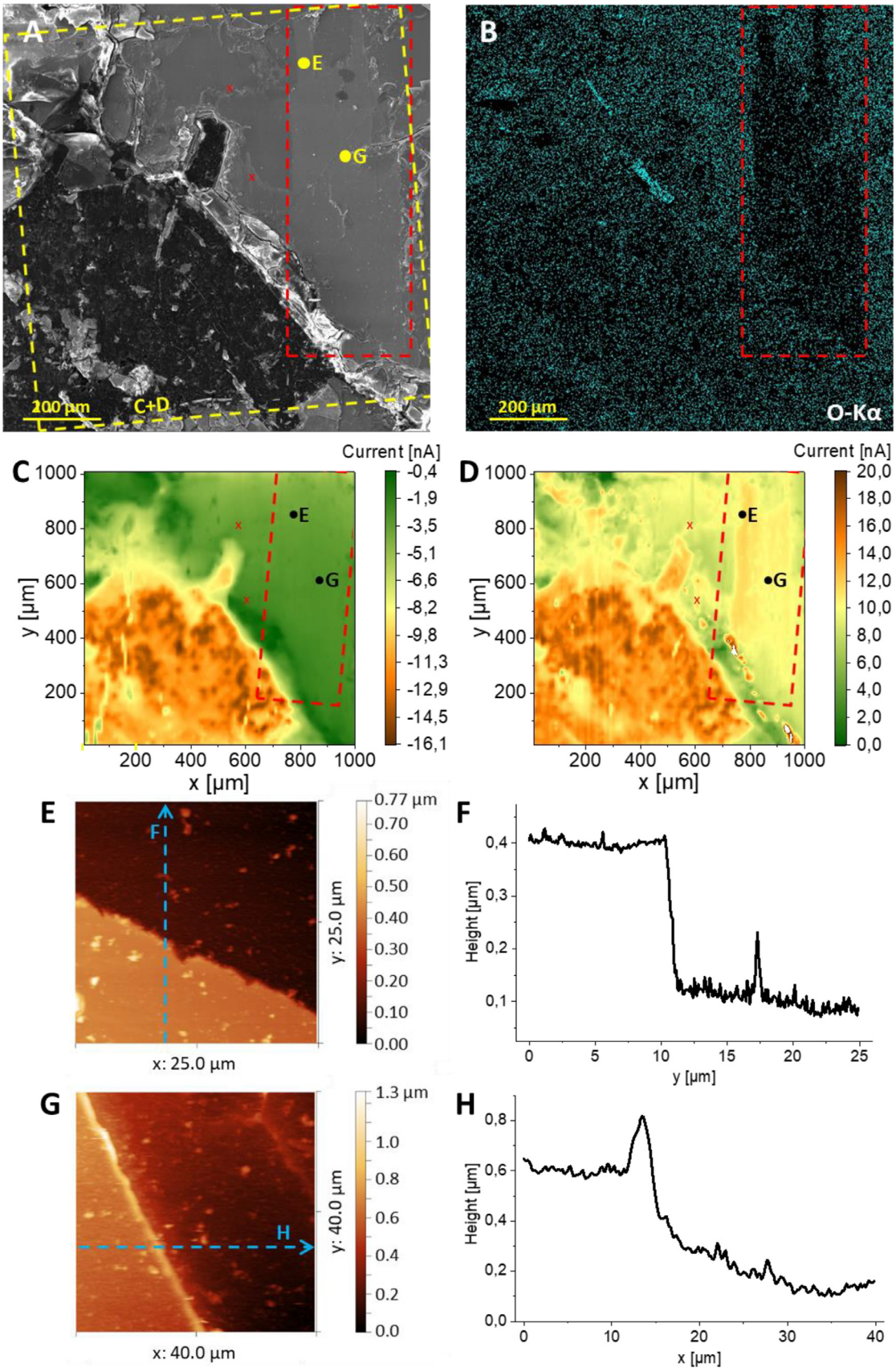

Fig. 4. Characterization of the $TiSe_2$ crystal. (A) Scanning electron micrograph of the $TiSe_2$ crystal. Imaging locations of SECM recordings C/D (yellow box) and AFM images E/G (dots) are highlighted. (B) EDS map showing the oxygen distribution in the area covered by A. The red boxes in A–D highlight the location of low oxygen content. (C/D) SECM images of the crystal recorded in feedback (C) and SG/TC (D) mode recorded in 10 mM $K_3Fe(CN)_6$. Probe diameter: 10 µm. Pixel size: 10 µm. Substrate-to-tip distance: 15 µm. $E_{UME} = -0.2$ V (C), 0.4 V (D). $E_{Substrate} = -0.5$ V (D) (E/G) AFM images of different crystal edges. (F/H) Line profiles extracted from E/G. "x" in A, C and D mark exemplary locations of active crystal edges.

TiS_2 and $TiSe_2$ so far show that electrochemical model reactions occur predominantly at crystal edges.

4. Conclusions

In this work, we tackled the persisting question if a higher electrochemical activity at the edges of crystals is a general trend in nature for layered materials. Localized electrochemical investigations performed via SECM over crystalline TiS_2 and $TiSe_2$ have shown an increased electrochemical activity at crystal edges and microscopic cracks compared to basal planes. With these results, we showed that differences in electrochemical activity between basal planes and crystal edges exist within the group IV TMDs TiS_2 and $TiSe_2$ – in analogy to other 2D materials like graphite, layered pnictogens and group VI TMDs. Further analysis utilizing SEM, EDS and AFM were employed to support these findings. Nevertheless, basal planes did not appear completely electrochemically inactive. As bulk TMD crystals were studied herein, the observed edges were mostly multi-layered, and consequently of mixed crystallographic structure. Since crystallographic structure of single edges could impact their electrochemical activity, future studies on single layer TMDs could help to answer this question. Nevertheless, these results are important for the future development of alternative energy storage materials and electrocatalysts based on group IV TMDs and beyond [44].

Supporting Information

The supporting information contains optical images of a typical TMD single crystal sample and the measurement cell, scanning electron micrographs, EDS elemental maps and XPS wide scan spectra of the investigated samples. An optical image for AFM position correlation of the TiS_2 sample is included as well. In addition, the experimental data of a second TiS_2 crystal is included.

Declaration of Competing Interest

The authors declare no conflict of interest.

CRediT authorship contribution statement

Stefan Wert: Methodology, Writing – original draft. **Christian Iffelsberger:** Visualization, Writing – original draft. **Katarina A. Novčić:** Formal analysis, Writing – original draft. **Frank-Michael Matysik:** Supervision, Writing – original draft. **Martin Pumera:** Supervision, Conceptualization, Writing – original draft.

Acknowledgment

M.P. acknowledges the financial support of Grant Agency of the Czech Republic (EXPRO: 19-26896X). S.W. would like to thank the Bayerisch-Tschechische Hochschulagentur for financial support (Project: BTHA-MOB-2020-10). C.I. acknowledges the financial support by the European Union's Horizon 2020 research and innovation program under the Marie Skłodowska-Curie grant agreement No. 888797. K.A.N. acknowledge the financial support from Quality Internal Grants of BUT (KInG BUT) (Reg.No. CZ.02.2.69/0.0/0.0/19_073/0016948), financed from the OP RDE. The authors gratefully acknowledge the CzechNanoLab project LM2018110 funded by MEYS CR for the financial support of the measurements/sample fabrication at CEITEC Nano Research Infrastructure.

References

[1] C.E. Banks, T.J. Davies, G.G. Wildgoose, R.G. Compton, Electrocatalysis at graphite and carbon nanotube modified electrodes: edge-plane sites and tube ends are the reactive sites, Chem. Commun. (7) (2005) 829–841, doi:10.1039/b413177k.
[2] T.J. Davies, M.E. Hyde, R.G. Compton, Nanotrench arrays reveal insight into graphite electrochemistry, Angew. Chem. Int. Ed. 44 (32) (2005) 5121–5126, doi:10.1002/anie.200462750.
[3] C.C.M. Neumann, C. Batchelor-McAuley, C. Downing, R.G. Compton, Anthraquinone monosulfonate adsorbed on graphite shows two very different rates of electron transfer: surface heterogeneity due to basal and edge plane sites, Chem. Eur. J. 17 (26) (2011) 7320–7326, doi:10.1002/chem.201002621.
[4] W. Yuan, Y. Zhou, Y. Li, C. Li, H. Peng, J. Zhang, Z. Liu, L. Dai, G. Shi, The edge- and basal-plane-specific electrochemistry of a single-layer graphene sheet, Sci. Rep. (3) (2013) 2248, doi:10.1038/srep02248.
[5] L. Wang, Z. Sofer, M. Pumera, Will any crap we put into graphene increase its electrocatalytic effect? ACS Nano 14 (1) (2020) 21–25, doi:10.1021/acsnano.9b00184.
[6] M. Pumera, Materials electrochemists' never-ending quest for efficient electrocatalysts: the devil is in the impurities, ACS Catal. 10 (13) (2020) 7087–7092, doi:10.1021/acscatal.0c02020.
[7] P. Marvan, Š. Huber, J. Luxa, V. Mazánek, D. Sedmidubský, Z. Sofer, M. Pumera, Edge vs. basal plane electrochemistry of layered pnictogens (As, Sb, Bi): does edge always offer faster electron transfer? Appl. Mater. Today 16 (2019) 179–184, doi:10.1016/j.apmt.2019.05.009.
[8] Z. Sofer, D. Sedmidubský, Š. Huber, J. Luxa, D. Bouša, C. Boothroyd, M. Pumera, Layered black phosphorus: strongly anisotropic magnetic, electronic, and electron-transfer properties, Angew. Chem. Int. Ed. 55 (10) (2016) 3382–3386, doi:10.1002/anie.201511309.
[9] J. Sturala, Z. Sofer, M. Pumera, Chemistry of layered pnictogens: phosphorus, arsenic, antimony, and bismuth, Angew. Chem. Int. Ed. 58 (23) (2019) 7551–7557, doi:10.1002/anie.201900811.
[10] S.M. Beladi-Mousavi, M. Pumera, 2D-Pnictogens: alloy-based anode battery materials with ultrahigh cycling stability, Chem. Soc. Rev. 47 (18) (2018) 6964–6989, doi:10.1039/C8CS00425K.
[11] M. Pumera, Z Sofer, 2D monoelemental arsenene, antimonene, and bismuthene: beyond black phosphorus, Adv. Mater. 29 (21) (2017) 1605299, doi:10.1002/adma.201605299.
[12] S.M. Tan, A. Ambrosi, Z. Sofer, Š. Huber, D. Sedmidubský, M. Pumera, Pristine basal- and edge-plane-oriented molybdenite MoS_2 Exhibiting Highly Anisotropic Properties, Chem. Eur. J. 21 (19) (2015) 7170–7178, doi:10.1002/chem.201500435.
[13] C. Tsai, K. Chan, F. Abild-Pedersen, J.K. Nørskov, Active edge sites in $MoSe_2$ and WSe_2 catalysts for the hydrogen evolution reaction: a density functional study, Phys. Chem. Chem. Phys. 16 (26) (2014) 13156–13164, doi:10.1039/c4cp01237b.
[14] A. Tuxen, J. Kibsgaard, H. Gøbel, E. Laegsgaard, H. Topsøe, J.V. Lauritsen, F. Besenbacher, Size threshold in the dibenzothiophene adsorption on MoS_2 nanoclusters, ACS Nano 4 (8) (2010) 4677–4682, doi:10.1021/nn1011013.
[15] T.F. Jaramillo, K.P. Jørgensen, J. Bonde, J.H. Nielsen, S. Horch, I. Chorkendorff, Identification of active edge sites for electrochemical H_2 evolution from MoS_2 Nanocatalysts, Science 317 (5834) (2007) 100–102, doi:10.1126/science.1141483.
[16] X. Chia, A.Y.S. Eng, A. Ambrosi, S.M. Tan, M. Pumera, Electrochemistry of nanostructured layered transition-metal dichalcogenides, Chem. Rev. 115 (21) (2015) 11941–11966, doi:10.1021/acs.chemrev.5b00287.
[17] K. Ghosh, M. Pumera, Free-standing electrochemically coated MoSx based 3D-printed nanocarbon electrode for solid-state supercapacitor application, Nanoscale 13 (11) (2021) 5744–5756, doi:10.1039/D0NR06479C.
[18] X. Chia, M. Pumera, Characteristics and performance of two-dimensional materials for electrocatalysis, Nat. Catal. 1 (12) (2018) 909–921, doi:10.1038/s41929-018-0181-7.
[19] S.M. Tan, M. Pumera, Two-dimensional materials on the rocks: positive and negative role of dopants and impurities in electrochemistry, ACS Nano 13 (3) (2019) 2681–2728, doi:10.1021/acsnano.8b07795.
[20] K.S. Novoselov, D. Jiang, F. Schedin, T.J. Booth, V.V. Khotkevich, S.V. Morozov, A.K. Geim, Two-dimensional atomic crystals, PNAS 102 (30) (2005) 10451–10453, doi:10.1073/pnas.0502848102.
[21] V. Nicolosi, M. Chhowalla, M.G. Kanatzidis, M.S. Strano, J.N. Coleman, Liquid exfoliation of layered materials, Science 340 (6139) (2013) 1226419, doi:10.1126/science.1226419.
[22] R. Gusmão, Z. Sofer, D. Bouša, M. Pumera, Pnictogen (As, Sb, Bi) nanosheets for electrochemical applications are produced by shear exfoliation using kitchen blenders, Angew. Chem. Int. Ed. 56 (46) (2017) 14417–14422, doi:10.1002/anie.201706389.
[23] G.A. Muller, J.B. Cook, H.S. Kim, S.H. Tolbert, B. Dunn, High performance pseudocapacitor based on 2D layered metal chalcogenide nanocrystals, Nano Lett. 15 (3) (2015) 1911–1917, doi:10.1021/nl504764m.
[24] D. Chen, G. Ji, B. Ding, Y. Ma, B. Qu, W. Chen, J.Y. Lee, *In situ* nitrogenated graphene-few-layer WS_2 composites for fast and reversible Li+ storage, Nanoscale 5 (17) (2013) 7890–7896, doi:10.1039/c3nr02920d.
[25] S. Wu, Z. Zeng, Q. He, Z. Wang, S.J. Wang, Y. Du, Z. Yin, X. Sun, W. Chen, H. Zhang, Electrochemically reduced single-layer MoS_2 nanosheets: characterization, properties, and sensing applications, Small 8 (14) (2012) 2264–2270, doi:10.1002/smll.201200044.

[26] X. Yu, K. Sivula, Toward large-area solar energy conversion with semiconducting 2D transition metal dichalcogenides, ACS Energy Lett. 1 (1) (2016) 315–322, doi:10.1021/acsenergylett.6b00114.
[27] D. Voiry, M. Salehi, R. Silva, T. Fujita, M. Chen, T. Asefa, V.B. Shenoy, G. Eda, M. Chhowalla, Conducting MoS_2 nanosheets as catalysts for hydrogen evolution reaction, Nano Lett. 13 (12) (2013) 6222–6227, doi:10.1021/nl403661s.
[28] M. Pumera, Z. Sofer, A. Ambrosi, Layered transition metal dichalcogenides for electrochemical energy generation and storage, J. Mater. Chem. A 2 (24) (2014) 8981–8987, doi:10.1039/C4TA00652F.
[29] W. Yuan, Y. Zhou, Y. Li, C. Li, H. Peng, J. Zhang, Z. Liu, L. Dai, G. Shi, The edge- and basal-plane-specific electrochemistry of a single-layer graphene sheet, Sci. Rep. (3) (2013) 2248, doi:10.1038/srep02248.
[30] C.L. Bentley, M. Kang, F.M. Maddar, F. Li, M. Walker, J. Zhang, P.R. Unwin, Electrochemical maps and movies of the hydrogen evolution reaction on natural crystals of molybdenite (MoS_2): basal vs. edge plane activity, Chem. Sci. 8 (9) (2017) 6583–6593, doi:10.1039/c7sc02545a.
[31] Y. Takahashi, Y. Kobayashi, Z. Wang, Y. Ito, M. Ota, H. Ida, A. Kumatani, K. Miyazawa, T. Fujita, H. Shiku, Y.E. Korchev, Y. Miyata, T. Fukuma, M. Chen, T. Matsue, High-resolution electrochemical mapping of the hydrogen evolution reaction on transition-metal dichalcogenide nanosheets, Angew. Chem. Int. Ed. 59 (9) (2020) 3601–3608, doi:10.1002/anie.201912863.
[32] B. Tao, P.R. Unwin, C.L. Bentley, Nanoscale variations in the electrocatalytic activity of layered transition-metal dichalcogenides, J. Phys. Chem. C 124 (1) (2020) 789–798, doi:10.1021/acs.jpcc.9b10279.
[33] C.L. Bentley, M. Kang, P.R. Unwin, Nanoscale surface structure-activity in electrochemistry and electrocatalysis, J. Am. Chem. Soc. 141 (6) (2019) 2179–2193, doi:10.1021/jacs.8b09828.
[34] C. Yan, C. Gong, P. Wangyang, J. Chu, K. Hu, C. Li, X. Wang, X. Du, T. Zhai, Y. Li, J. Xiong, 2D group IVB transition metal dichalcogenides, Adv. Funct. Mater. 28 (39) (2018) 1803305, doi:10.1002/adfm.201803305.
[35] R.J. Toh, Z. Sofer, M. Pumera, Catalytic properties of group 4 transition metal dichalcogenides (MX2 ; M = Ti, Zr, Hf; X = S, Se, Te), J. Mater. Chem. A 4 (47) (2016) 18322–18334, doi:10.1039/C6TA08089H.
[36] C. Wan, X. Gu, F. Dang, T. Itoh, Y. Wang, H. Sasaki, M. Kondo, K. Koga, K. Yabuki, G.J. Snyder, R. Yang, K. Koumoto, Flexible n-type thermoelectric materials by organic intercalation of layered transition metal dichalcogenide TiS_2, Nat. Mater. 14 (6) (2015) 622–627, doi:10.1038/nmat4251.
[37] W. Zhang, Z. Huang, W. Zhang, Y. Li, Two-dimensional semiconductors with possible high room temperature mobility, Nano Res. 7 (12) (2014) 1731–1737, doi:10.1007/s12274-014-0532-x.
[38] L. Sun, C. Chen, Q. Zhang, C. Sohrt, T. Zhao, G. Xu, J. Wang, D. Wang, K. Rossnagel, L. Gu, C. Tao, L. Jiao, Suppression of the charge density wave state in two-dimensional 1T-$TiSe_2$ by atmospheric oxidation, Angew. Chem. Int. Ed. 56 (31) (2017) 8981–8985, doi:10.1002/anie.201612605.
[39] H. Tao, M. Zhou, R. Wang, K. Wang, S. Cheng, K. Jiang, TiS_2 as an advanced conversion electrode for sodium-ion batteries with ultra-high capacity and long-cycle life, Adv. Sci. 5 (11) (2018) 1801021, doi:10.1002/advs.201801021.
[40] J. Tang, X. Huang, T. Lin, T. Qiu, H. Huang, X. Zhu, Q. Gu, B. Luo, L. Wang, MXene derived TiS_2 nanosheets for high-rate and long-life sodium-ion capacitors, Energy Storage Mater. 26 (2020) 550–559, doi:10.1016/j.ensm.2019.11.028.
[41] P. Li, X. Zheng, H. Yu, G. Zhao, J. Shu, X. Xu, W. Sun, S.X. Dou, Electrochemical potassium/lithium-ion intercalation into $TiSe_2$: kinetics and mechanism, Energy Storage Mater. 16 (2019) 512–518, doi:10.1016/j.ensm.2018.09.014.
[42] K.S. Novoselov, A.K. Geim, S.V. Morozov, D. Jiang, Y. Zhang, S.V. Dubonos, I.V. Grigorieva, A.A. Firsov, Electric field effect in atomically thin carbon films, Science 306 (5696) (2004) 666–669, doi:10.1126/science.1102896.
[43] A.Y.S. Eng, A. Ambrosi, Z. Sofer, P. Šimek, M. Pumera, Electrochemistry of transition metal dichalcogenides: strong dependence on the metal-to-chalcogen composition and exfoliation method, ACS Nano 8 (12) (2014) 12185–12198, doi:10.1021/nn503832j.
[44] H.L. Chia, C.C. Mayorga-Martinez, N. Antonatos, Z. Sofer, J.J. Gonzalez-Julian, R. Webster, M. Pumera, MXene Titanium Carbide-based Biosensors: Strong Dependence of Exfoliation Method on Performance, Anal. Chem. 92 (3) (2020) 2452–2459, doi:10.1021/acs.analchem.9b03634.

Chapter 8. Corrosion Study of the Layered Transition Metal Dichalcogenide Crystals

Published paper included in this chapter:

S. Wert, C. Iffelesberger, **K. A. Novčić**, and M. Pumera, *Corrosion of Catalyst in High Resolution: Layered Transition Metal Dichalcogenides Electrocatalyse Water Splitting and Corrode During the Process,* **Journal of Catalysis (2022)**, 416, 85-91, doi.org/10.1016/j.jcat.2022.10.023.

8.1. Motivation for the Study

Transition metal dichalcogenides have been widely studied for energy conversion applications as they show promising electrochemical properties. However, the electrochemical processes that occur on the surfaces of these catalysts are followed by morphological and electrochemical changes on the catalytic surfaces. Therefore, this paper investigates these changes in the MoS_2, TiS_2 and $TiSe_2$ bulk crystals during the hydrogen evolution reaction. The microscopic changes are observed by SECM, while the morphological changes are monitored by scanning electron microscopy (SEM) and confocal laser scanning microscopy (CLSM).

8.2. Paper Conclusion

This study demonstrates the changes of different bulk crystals of transition metal dichalcogenides (MoS_2, TiS_2 and $TiSe_2$) when used as electrodes in hydrogen evolution reactions. The microscopic study of these crystals performed by SECM shows negligible changes in the morphology of the MoS_2 bulk crystal, which CLSM and SEM analysis also confirm. However, the bulk crystals of TiS_2 and $TiSe_2$ were significantly damaged during the electrochemical reaction, which resulted in their exfoliation and instability. Therefore, this

study demonstrates the limitations of bulk crystals of TiS_2 and $TiSe_2$ in electrochemical water-splitting reactions.

8.3. Student Contribution

The student is the third author of this paper who contributed to the study by being involved in the sample preparation and the characterization of the elemental composition of the investigated crystals. The student was also involved in writing the manuscript and preparing figures.

Journal of Catalysis 416 (2022) 85–91

Contents lists available at ScienceDirect

Journal of Catalysis

journal homepage: www.elsevier.com/locate/jcat

Corrosion of catalyst in high resolution: Layered transition metal dichalcogenides electrocatalyse water splitting and corrode during the process

Stefan Wert [a], Christian Iffelsberger [a], Katarina A. Novčić [a], Martin Pumera [a,b,c,*]

[a] Future Energy and Innovation Laboratory, Central European Institute of Technology, Brno University of Technology, Purkyňova 123, 61200 Brno, Czech Republic
[b] Faculty of Electrical Engineering and Computer Science, VSB - Technical University of Ostrava, 17. listopadu 2172/15, 70800 Ostrava, Czech Republic
[c] Department of Medical Research, China Medical University Hospital, China Medical University, No. 91 Hsueh-Shih Road, Taichung 40402, Taiwan

ARTICLE INFO

Article history:
Received 7 July 2022
Revised 17 October 2022
Accepted 26 October 2022
Available online 30 October 2022

Keywords:
Transition metal dichalcogenides
Scanning electrochemical microscopy
2D materials
Titanium disulfide
Titanium diselenide
Molybdenum disulfide
Hydrogen
Corrosion

ABSTRACT

Among the vast field of 2D materials, transition metal dichalcogenides (TMDs) have emerged as promising materials for electrocatalysis. Many of them, such as MoS_2, were found to be potent electrocatalysts for the hydrogen evolution reaction (HER), which is vital for making electrochemical water splitting, a green route for obtaining hydrogen, economically feasible. In this work, we investigated the morphological and (electro)chemical changes undergoing in synthetic bulk crystals of MoS_2, TiS_2, and $TiSe_2$ during HER. Local electrochemical changes were observed using scanning electrochemical microscopy (SECM). Scanning electron microscopy (SEM) and confocal laser scanning microscopy (CLSM) were utilized to monitor morphological changes. Furthermore, the chemical composition of the materials was analyzed using X-ray photoelectron spectroscopy (XPS) and electron dispersive X-ray spectroscopy (EDS). Changes in the atomic structure were studied using X-ray diffraction (XRD). Our experiments showed different degrees of corrosion occurring in these materials, with the magnitude of corrosion decreasing in the order $TiSe_2$ > TiS_2 > MoS_2. These findings are of tremendous importance for the development of transition metal dichalcogenide electrocatalysts, which are touted to replace platinum for hydrogen evolution reaction.

1. Introduction

Alternative energy storage solutions are widely sought to reduce the energy sector's carbon footprint. A promising option is converting excess electrical energy into chemical energy in the form of hydrogen. An environmentally friendly approach to achieve this is electrochemical water splitting [1], where water is split into hydrogen and oxygen by applying an external current. The main drawback of this approach is that catalysts are required to decrease the energy needed to drive this process, thus reducing its costs to become economically feasible. To date, the most capable catalysts are based on rare metals like platinum, but their high cost and limited availability leave them unsuitable for widespread industrial application [2].

There is an intensive search for alternative, earth-abundant materials. The so-called 2D materials are a large group of earth-abundant compounds that are promising candidates for energy-related applications such as (photo)electrocatalysis and energy storage [3,4]. The group of 2D materials includes, but is not limited to, layered pnictogens[5–10] and transition metal selenophosphites [11–14], MXenes [15–17], and transition metal dichalcogenides (TMDs) [18–22]. The latter have the chemical formula MX_2, with M being a transition metal (e.g., Ti, Mo, W) and X representing the chalcogenide (e.g., S, Se, Te). Among TMDs, MoS_2 is most extensively studied compound because it is one of the best candidates for supporting the hydrogen evolution reaction (HER) [21,23], one of the half-reactions involved in electrochemical water splitting. The capability of TiS_2 and $TiSe_2$ to support the HER was

Abbreviations: CLSM, confocal laser scanning microscopy; EDS, energy dispersive X-ray spectroscopy; HER, hydrogen evolution reaction; PAC, probe approach curve; PDMS, polydimethylsiloxane; SECM, scanning electrochemical microscopy; SEM, scanning electron microscope; SG/TC, substrate generation/tip collection; TMD, transition metal dichalcogenide.

* Corresponding author at: Future Energy and Innovation Laboratory, Central European Institute of Technology, Brno University of Technology, Purkyňova 123, 61200 Brno, Czech Republic.
E-mail address: pumera.research@gmail.com (M. Pumera).

https://doi.org/10.1016/j.jcat.2022.10.023
0021-9517/

proven in previous studies [24–27], but experiments with bulk crystals are missing so far.

In order to replace platinum as a catalyst in hydrogen evolution reaction, what is an important parameter is not only catalytic activity but also the stability of the catalyst. Here we show both, the catalytic activity and corrosion of layered crystals of TiS_2, $TiSe_2$ and MoS_2 during HER, with micrometer resolution (Fig. 1). MoS_2 was reported to be stable in acidic solutions (similar to Pt) [28]. In addition, it was shown to be stable during hydrogen evolution [29]. Group IV TMD like TiS_2 and $TiSe_2$ were not investigated in this regard yet. Thus, this work aims to analyze the degree of corrosion inflicted by the HER, and its impact on the materials' morphology, chemical structure, and electrochemical activity on a microscopic level. We included MoS_2 as a reference TMD in our study due to its high catalytic activity and stability [29].

2. Experimental

2.1. Materials and chemicals

Bulk crystals of TMDs were acquired from 2d-age.com. The crystal samples were prepared according to a previously reported protocol [30], using the following materials. For establishing electrical contact to the crystal samples, a 1:1 (m:m) mixture of two-component epoxy resin (Struers Aps, Denmark) and graphite powder (<20 µm, synthetic, Sigma-Aldrich) was used. The carbon SEM stubs utilized as sample holders were purchased from Micro to Nano, Netherlands. Polydimethylsiloxane (PDMS, SYLGARD™ 184) was obtained from Dow Inc., Michigan, USA. A solution containing 1.5 mM ferrocene methanol (FcMeOH, 99 %, ABCR GmbH, Germany) and 0.2 M potassium nitrate (KNO_3, analytical grade, Merck KGaA, Germany) served as a mediator during SECM measurements. 0.5 M sulfuric acid (H_2SO_4, 96 %, analytical grade, Penta, Czech Republic) was used for experiments involving the HER. Solutions were prepared with deionized water with a resistivity > 18.2 MΩ cm (Milli-Q Advantage A10 system, Merck Millipore, Germany).

2.2. Instrumentation

A commercially available SECM (Sensolytics, Germany) was used for localized electrochemical characterization and connected to a bipotentiostat (PGSTAT302N, Autolab, Netherlands). SECM images and probe approach curves (PACs) were recorded with a 25 µm diameter Pt disk ultramicroelectrode (UME, RG = 11, Sensolytics, Germany). A graphite rod served as a counter electrode and a Ag/AgCl (3 M KCl) reference electrode was used for all experiments. All potentials refer to this reference system. Electrical contact to samples was realized using conductive copper tape.

A MIRA 3 SEM (Tescan, Czech Republic) and a Bruker XFlash 5010 EDS were used to acquire SEM and EDS images, using accelerating voltages of either 5 kV or 20 kV. Changes in chemical composition of the samples was assessed using XPS (AXIS SupraTM, Kratos, United Kingdom). Spectra were recorded using a monochromatic Al Kα (1486.7 eV) excitation source, calibrated against the carbon 1 s signal at 284.8 eV, and evaluated with Casa XPS software. The XRD patterns were measured using an X-ray diffractometer (Rigaku SmartLab 3 kW) with Brag Brentano geometry using Cu Kα radiation (λ = 0.15418 nm). The operation current and voltage were 30 mA and 40 kV, respectively. Data evaluation of SECM experiments was performed using Gwyddion 2.55 and Origin 2020 software. Optical imaging and height profiling of the embedded MoS_2, TiS_2 and $TiSe_2$ crystals was done with confocal laser scanning microscopy (CLSM, Olympus Lext OLS4100).

Prior to imaging, the probe was positioned by performing PACs in the carbon epoxy region near the respective crystals (Fig. S1). The probes were approached until the probe current decreased by ~ 50 %. SECM images were acquired at that distance if not stated otherwise and recorded with a pixel size of 25 µm and a maximum probe velocity of 100 µm s^{-1}. For feedback mode images, the probe potential was set to E_{Probe} = 0.5 V while the substrate was kept at open circuit potential. Substrate generation/ tip collection (SG/TC) images in FcMeOH were recorded with probe and substrate potentials of E_{Probe} = − 0.2 and $E_{Substrate}$ = 0.5 V, respectively. After initial investigation of the local conductivity and electrochemical activity via SECM, the solution in the SECM measurement cell was exchanged from 1.5 mM FcMeOH to 0.5 M H_2SO_4. In that solution, the crystal samples underwent HER treatment. It consisted of a linear scan voltammogram recorded at the sample, scanning the potential from 0.0 V to − 0.8 V at a scan rate of 5 mV s^{-1} (given in Fig. S2). Following that, a potential of − 0.8 V was applied at the samples for 3 min. The corresponding chronoamperograms are shown in Fig. S3. Afterwards, the solution in the measurement cell was exchanged for FcMeOH again, and SECM characterization was repeated. For changing the solution, the cell and sample were rinsed multiple times with water and the electrolyte to be inserted.

3. Results and discussion

The electrocatalytic capability, the stability and changes of the crystals' surface was investigated *via* SEM and SECM before and after performing the HER treatment at the samples. To contain a widely studied benchmark material in our work, a bulk crystal of MoS_2 was investigated as well. Its SEM image (Fig. 2A) shows that the crystal surface contains numerous cracks, and some of the basal planes appear curved. In the EDS maps of the same area (Fig. S4), most of the crystal surface contains mainly Mo and S. A few smaller spots contain an increased amount of carbon, which was introduced by the sample preparation with the graphite/epoxy mixture. In the feedback mode SECM image in Fig. 2B, local differences in conductivity are observable. The SG/TC mode image (Fig. 2C) shows a similar pattern in current distribution, with the

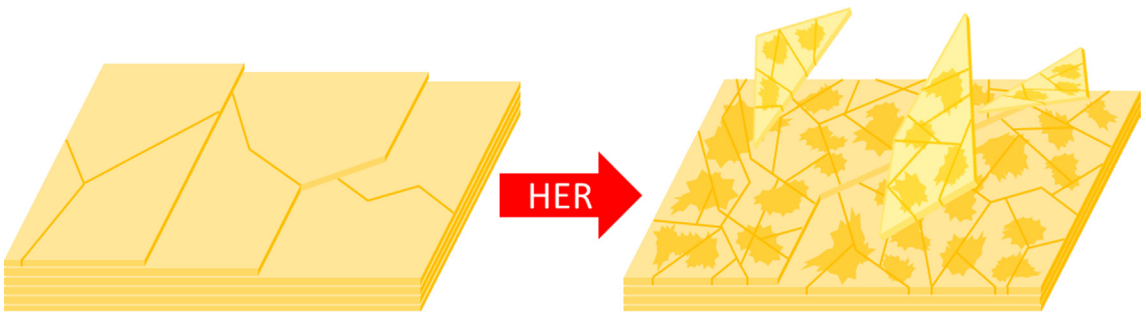

Fig. 1. Schematic structure of TMDs and the possible morphological changes occurring when the HER is triggered.

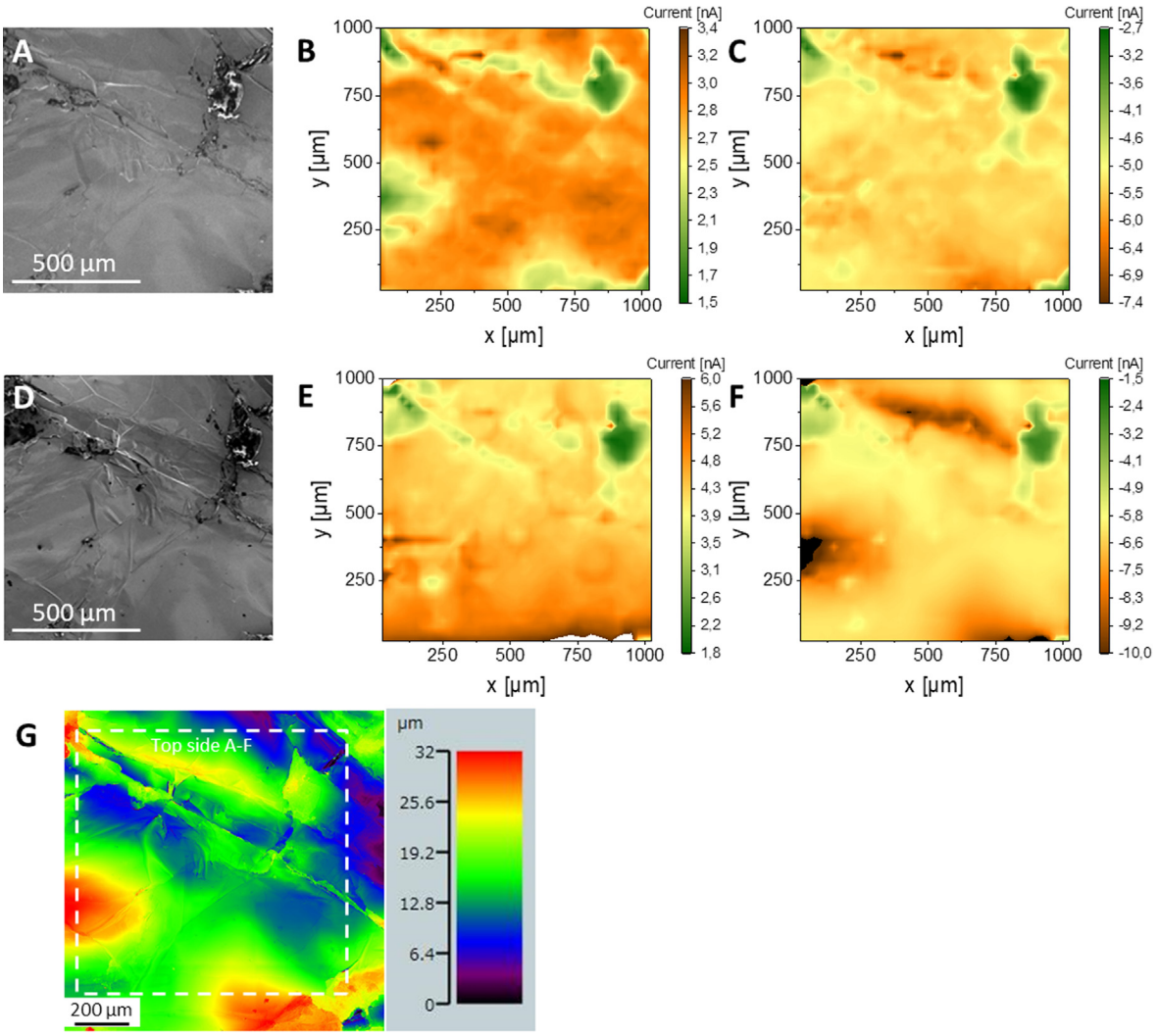

Fig. 2. SEM and SECM images of MoS_2 before (**A-C**) and after HER (**D-F**). **A/D:** SEM images before/after HER. **B/E:** Feedback SECM images recorded in 1.5 mM FcMeOH before/after HER. E_{Probe} = 0.5 V. **C/F:** SG/TC SECM images recorded in FcMeOH before/after HER. E_{Probe} = − 0.2 V, $E_{Substrate}$ = 0.5 V. **G:** CLSM image of MoS_2. The dashed box indicates the area investigated in **A-F**.

main difference at the poorly conductive spots in the bottom half of the feedback image, where higher currents were measured. These differences in the feedback and SG/TC images can be linked to topographical variations on the crystal surface shown by CLSM in Fig. 2G. The electrochemically inactive spots can be linked to coverage with epoxy, as can be seen in the corresponding EDS images as spots with high carbon content (Fig. S4).

The SEM image of MoS_2 recorded after the HER (Fig. 2D) does not show any significant structural changes in comparison to Fig. 2A. In addition, EDS maps obtained after HER (Fig. S4) show a similar local element distribution, and the carbon impurities remained. The SECM images of the same area appeared very similar to the ones recorded prior to the HER treatment. The main difference in the afterward recorded feedback mode image in Fig. 2E can be seen in its bottom half, where high currents were measured at two spots – in contrast to low currents measured in the previous image in Fig. 2B. The SG/TC mode image recorded after HER shows that the same spots are highly electrochemically active as well. The CLSM micrograph of the sample recorded after HER (Fig. 2G) shows a maximum height difference of 32 µm and correlates well with both SEM images in Fig. 2A and D. The major protrusions of the surface are located where a high electrochemical activity is present in Fig. 2F, thus the differences in conductivity and electrochemical activity are related to topographical variations. Overall, the changes in local surface structure, conductivity, and electrochemical activity of MoS_2 can be considered negligible. Thus, our observations are in line with previous stability studies of this material [29]. Regarding chemical changes in the surface of the MoS_2 crystal due to HER, XPS and EDS show that the ratio between Mo and S decreased slightly from 0.59 to 0.55 (XPS) and 0.51 to 0.49 (EDS, Table S1). The wide spectra of the samples show no significant changes in the material upon HER treatment (Fig. S5). Previous studies regarding the stability of the material suggest the formation of elemental Mo and H_2S for the conditions applied in our experiments [28]. Additionally, we performed XRD analysis of the MoS_2 sample, but no changes in the atomic structure of the material can be seen (Fig. S6). Thus, according to our observations, MoS_2 bulk crystals remain very stable under HER conditions and maintain their chemical composition, local electrochemical activity, and morphology.

As the first group IV TMD representative, TiS_2 was studied. In the SEM image (Fig. 3A), the pristine TiS_2 crystal appeared as a flat surface with a minor distribution of grains. To facilitate its comparison with the SECM images, the SEM image was tilted (the original image is given in Fig. S7A). In the corresponding EDS maps (Fig. S8), most of the crystal surface is comprised of Ti and S, with carbon

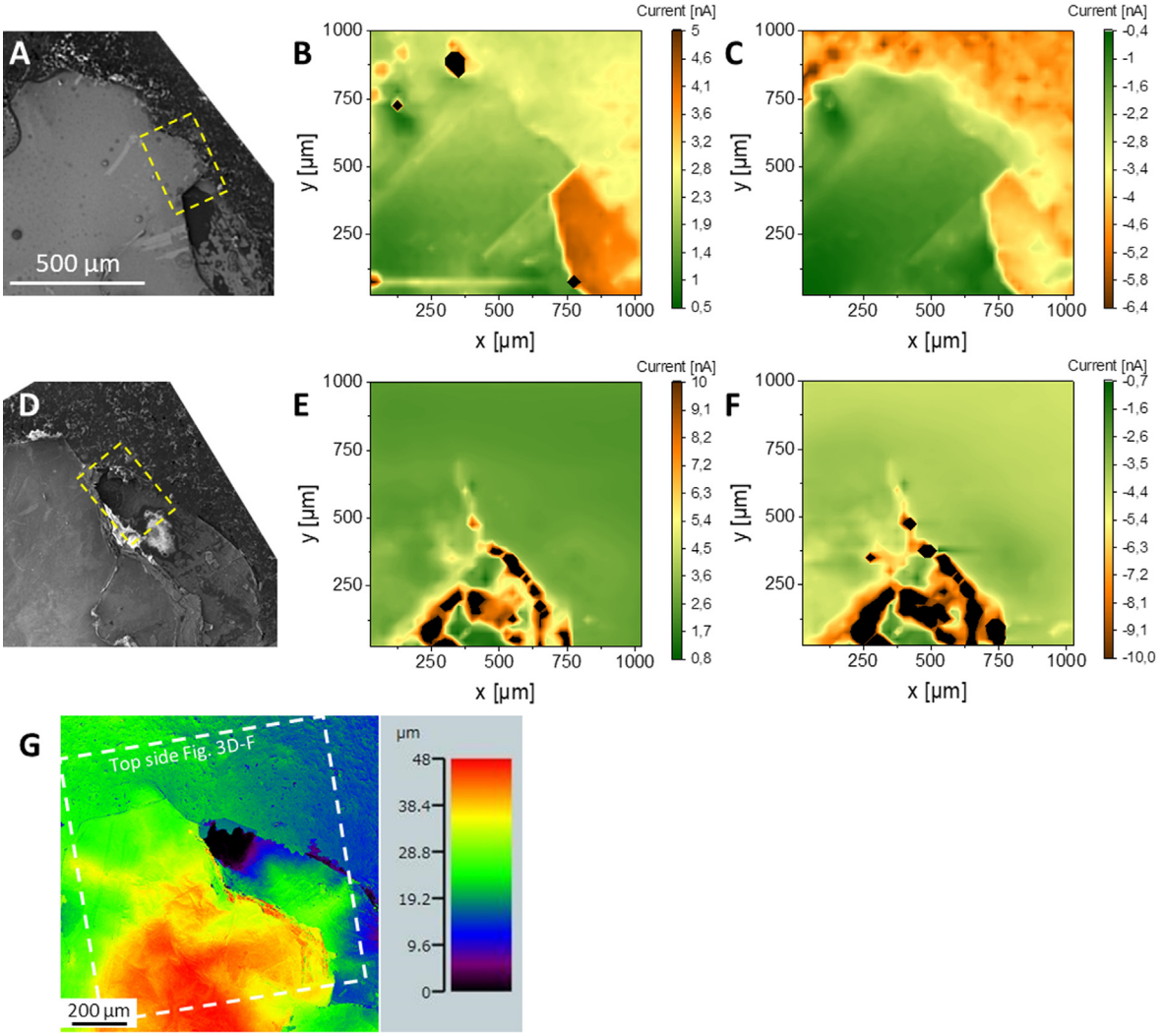

Fig. 3. SEM and SECM images of TiS_2 before (**A-C**) and after HER (**D-F**). The yellow dashed boxes highlight where a piece of the TiS_2 disappeared after HER. **A/D:** SEM images before/after HER. **B/E:** Feedback SECM images recorded in 1.5 mM FcMeOH before/after HER. E_{Probe} = 0.5 V. **C/F:** SG/TC SECM images recorded in FcMeOH before/after HER. E_{Probe} = − 0.2 V, $E_{Substrate}$ = 0.5 V. Substrate-to-tip distance in **E** and **F** was increased by 30 µm. **G:** CLSM image of MoS_2. The dashed box indicates the area investigated in **A-F**. (For interpretation of the references to colour in this figure legend, the reader is referred to the web version of this article.)

impurities present mainly in the top left and bottom right region of the crystal. Their origin is related to the graphite/epoxy matrix partly covering the TiS_2 surface. In the feedback mode SECM image of the pristine crystal (Fig. 3B), its surface appears mostly non-conductive, except for the yellow diagonal lines corresponding to cracks visible in the SEM image in Fig. S9. The horizontal yellow line in the bottom part is assumed to be an artifact caused by probe-sample contact. The bottom right region of the TiS_2 surface showed a very high conductivity. A possible reason for this is the spoilage by carbon residues from the surrounding matrix. In the SG/TC mode SECM image showing the local electrochemical activity (Fig. 3C), the more conductive spots from the feedback mode image also exhibit an increased electrochemical activity. This corresponds well to previous studies where an increased electrochemical activity was observed at TMD crystal edges [30].

The SEM image obtained after applying the HER protocol (Fig. 3D) showed staining of the crystal surface. Additionally, a piece of crystal disappeared (yellow highlighted area in Fig. 3A and D). Close-up SEM images of the surface before and after HER (Fig. S10) reveal that the crystal surface was damaged, resulting in cracks that created new edges. Furthermore, edges at the crystal border that existed prior to the HER treatment delaminated into single- or few-layer sheets. The feedback SECM image (Fig. 3E) covering the area of Fig. 3D showed a high conductivity in the bottom part of the crystal, together with frequent probe-substrate contact (occurring at the black spots). A similar observation can be made in the SG/TC SECM image in Fig. 3F. The highly electroactive spots correspond to conductive locations from the feedback image in Fig. 3E. The black spots in the SECM images correspond to locations where the probe current reached very high values due to probe-substrate contact. This indicates an expansion of the crystal, which was also observed using CLSM. The corresponding image (Fig. 3G) reveals that the HER resulted in height differences of 35 µm within the studied area, and probe-substrate contact occurred at the peak positions. In addition, this severe height difference led to high probe-to-substrate distances in the top half of the SECM images, thus low currents were measured and no details of the TiS_2 surface are visible in these regions. The chronoamperogram of the HER in Fig. S3B also indicates structural changes of the crystal over time, since the current response is very unsteady. Overall, these observations show that bulk crystals of TiS_2 take severe damage during HER.

The changes in the chemical composition of TiS_2 were investigated *via* XPS and EDS. Table S2 highlights the changes in atomic

percentage upon HER treatment, determined by both XPS (wide spectra in Fig. S11) and EDS. While XPS indicated a drastic decrease of the Ti:S ratio from 0.81 to 0.07, the ratio according to EDS remains constant at 0.53. The difference in values obtained by both techniques might be a result of their different surface sensitivity. Since XPS is more surface sensitive, it provides information about the top layers of the crystal, while EDS collects information from deeper layer of the crystal as well. Thus, the HER changes the surface composition of the TiS_2 crystal. XRD studies of TiS_2 before and after HER (Fig. S12) do not show significant changes in the peaks of TiS_2, nor the formation of peaks related to other species (apart from matrix peaks).

To study the impact of the chalcogenide atom on the severity of HER corrosion, $TiSe_2$ was included in the study. The SEM micrograph in Fig. 4A shows the pristine crystal before SECM studies and HER experiments. Similar to TiS_2, the crystal appears flat, with a few larger edges visible. The crystal borders and the top left region are covered by the graphite-epoxy matrix, which was confirmed by EDS maps of the same area (Fig. S13). In the feedback SECM image (Fig. 4B), the part of the crystal that is not covered by epoxy appears homogeneously conductive. The corresponding SG/TC SECM image (Fig. 4C) shows a generally high electrochemical activity of the $TiSe_2$ surface, albeit less homogenous and higher near the crystal borders compared to its center.

Upon application of the HER treatment, the $TiSe_2$ crystal underwent severe morphological changes visible in the SEM image in Fig. 4D. The crystal surface appears heavily exfoliated, and areas previously covered by epoxy resin/graphite composite expose parts of the material as well. EDS maps (Fig. S14) support this observation as the carbon content decreased in these regions of the crystal. Furthermore, the HER protocol led to crystal flakes floating in the electrolyte. In addition, the chronoamperogram in Fig. S3C shows an increase in current over time as hydrogen is generated. This happens due to the heavy exfoliation exposing more active areas over time. Both feedback and SG/TC mode images (Fig. 4E and F, respectively) show significant changes in both local conductivity and electrochemical activity, with frequent current spikes measured (black spots) due to tip-substrate contact. A possible reason for this is linked to the significant swelling of the crystal observed by CLSM in Fig. 4G. A maximum height difference of 143 µm was measured for the sample, thus it is very likely that

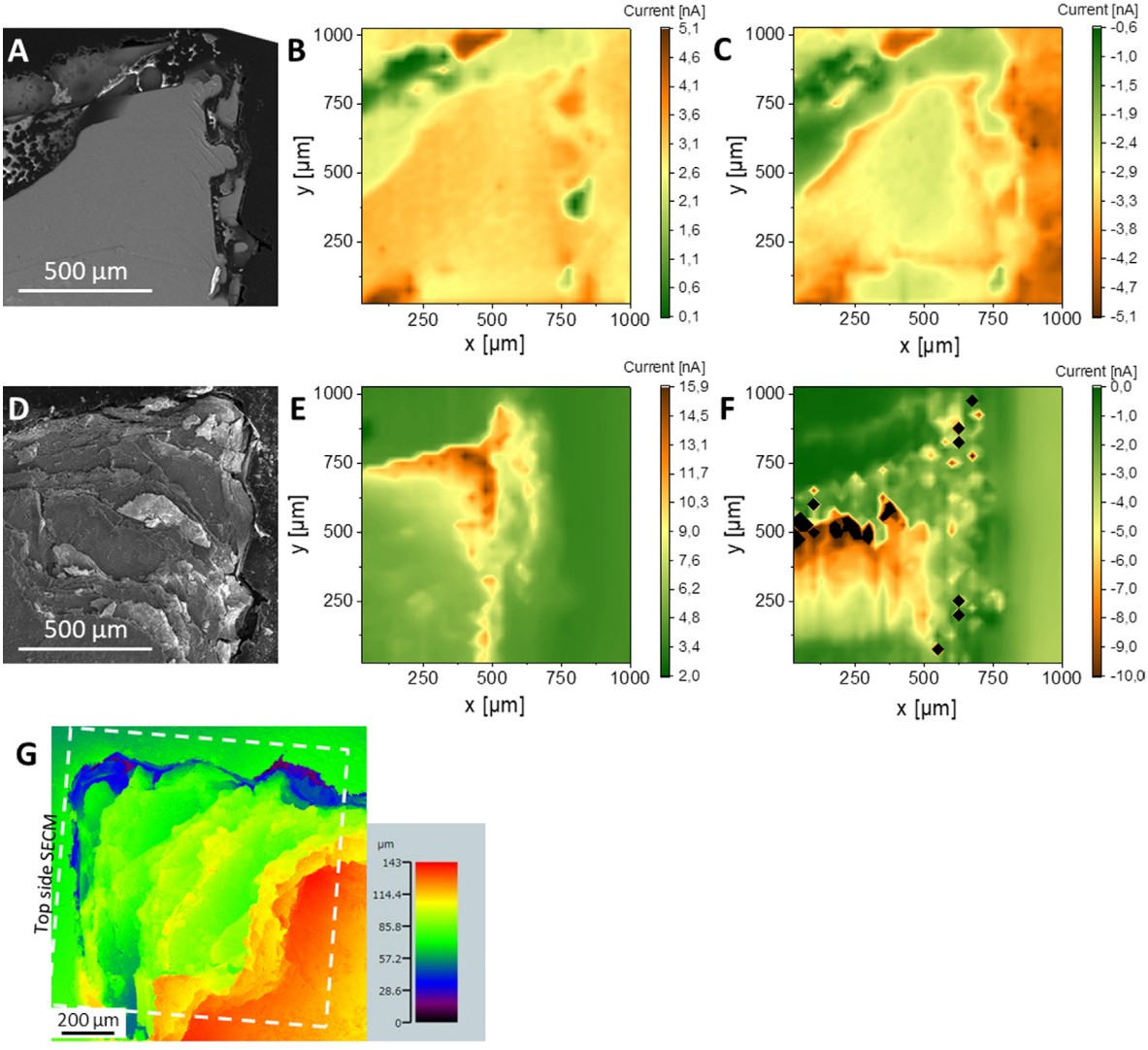

Fig. 4. SEM and SECM images of $TiSe_2$ before (**A-C**) and after HER (**D-F**). **A/D:** SEM images before/after HER. **B/E:** Feedback SECM images recorded in 1.5 mM FcMeOH before/after HER. E_{Probe} = 0.5 V. **C/F:** SG/TC SECM images recorded in FcMeOH before/after HER. E_{Probe} = − 0.2 V, $E_{Substrate}$ = 0.5 V. Substrate-to-tip distance in **E** and **F** was increased by 20 µm. **G:** CLSM image of MoS_2. The dashed box indicates the area investigated in **A-F**.

the SECM probe made surface contact during the scan and removed layers of the crystal.

Due to the drastic effects of the HER on the structure of $TiSe_2$, changes in chemical composition are expected as well. For this, XPS and EDS were employed both before and after the HER at the sample. The changes in atomic composition determined by both techniques are highlighted in Table S3. According to XPS, the Ti:Se ratio changes from initially 0.51 to 8.45 after the HER. In contrast, EDS only shows a minor increase of the ratio from 0.58 to 0.60. Again, the differences in results between both techniques are most likely related to a difference in surface sensitivity, as XPS is more surface sensitive and chemical changes are expected to occur at the $TiSe_2$ crystal surface. The significant increase of the Ti:Se ratio determined by XPS indicates a severe loss of Se at the crystal surface (wide spectra in Fig. S15). XRD analysis of the $TiSe_2$ sample (Fig. S16) did not show significant changes in the atomic structure of the material, apart from graphite peaks appearing in the measurement after HER treatment, which stem from the graphite/epoxy matrix used for sample preparation.

It is expected that the elemental variations shown by XPS for both TiS_2 and $TiSe_2$ impact their conductivity, since varying the chalcogen content can be used to tune the bandgap of TMDs, altering their (semi-)metallic nature [31]. Thus, it can be expected that the bandgaps of TiS_2 and $TiSe_2$ are altered during the HER as their chalcogen content changed. We are however not able to correlate local differences to the materials' activity to chalcogen content, since the SECM response is strongly impacted by topography. This would require a separate study of correlating local chalcogen content with material activity, performed without stressing the materials under corrosive conditions which change the topography. Consequently, the local influence of the chalcogen content of TMDs on electrochemical and electrocatalytic activity remains an open question that needs to be addressed in future studies.

4. Conclusions

In the work presented herein, we investigated the extent of changes that different TMDs undergo when used as an electrode for the HER. TiS_2, $TiSe_2$, and MoS_2 were studied, and noticeable differences were observable among these materials. MoS_2 showed no noticeable changes in morphology and minor changes in electrochemical activity shown by SECM. XPS and EDS only showed a minor decrease in Mo content. TiS_2 and $TiSe_2$ on the other hand showed significant exfoliation of the crystal surface and damage to the basal planes. The extent of damage resulting from HER was most severe for $TiSe_2$, as numerous crystal pieces detached from the main crystal, while TiS_2 mostly remained its shape. In both cases, the exfoliation led to exposure of novel edge sites visible as active spots in the SECM images. On the chemical side, TiS_2 showed a significant loss in Ti content at the crystal surface, which was proven by XPS. This process went alongside the reduction of Ti and oxidation of S. The surface of $TiSe_2$ drastically changed its chemical composition as well and the Se content heavily decreased. Consequently, the usability of TiS_2 and $TiSe_2$ bulk crystals for HER, and thus electrochemical water splitting, is limited due to their poor morphological and chemical stability.

CRediT authorship contribution statement

Stefan Wert: Writing – original draft, Investigation, Methodology. **Christian Iffelsberger:** Investigation, Writing – review & editing. **Katarina A. Novčić:** Investigation, Writing – review & editing. **Martin Pumera:** Funding acquisition, Supervision, Resources.

Declaration of Competing Interest

The authors declare that they have no known competing financial interests or personal relationships that could have appeared to influence the work reported in this paper.

Data availability

Data will be made available on request.

Acknowledgement

M.P. acknowledges the financial support of Grant Agency of the Czech Republic (EXPRO: 19-26896X). C.I. acknowledges the financial support by the European Union's Horizon 2020 research and innovation program under the Marie Skłodowska-Curie grant agreement No. 888797. K.A.N. acknowledges the financial support from Quality Internal Grants of BUT (KInG BUT) (Reg.No. CZ.02.2.69/0.0/0.0/19_073/0016948), financed from the OP RDE. The authors gratefully acknowledge the CzechNanoLab project LM2018110 funded by MEYS CR for the financial support of the measurements/sample fabrication at CEITEC Nano Research Infrastructure.

Appendix A. Supplementary material

The supporting information contains probe approach curves measurements with the LSV and chronoamperometry measurements of the crystals as well as the EDS and close-up SEM images of the samples before and after HER treatment, and CLSM images. In addition, XPS and XRD data of the samples is included.

Supplementary data to this article can be found online at https://doi.org/10.1016/j.jcat.2022.10.023.

References

[1] M. Wang, L. Zhang, Y. He, H. Zhu, Recent advances in transition-metal-sulfide-based bifunctional electrocatalysts for overall water splitting, J. Mater. Chem. A 9 (9) (2021) 5320–5363.
[2] C.G. Morales-Guio, L.-A. Stern, X. Hu, Nanostructured hydrotreating catalysts for electrochemical hydrogen evolution, Chem. Soc. Rev. 43 (18) (2014) 6555–6569, https://doi.org/10.1039/c3cs60468c.
[3] R. Tong, K.W. Ng, X. Wang, S. Wang, X. Wang, H. Pan, Two-dimensional materials as novel co-catalysts for efficient solar-driven hydrogen production, J. Mater. Chem. A 8 (44) (2020) 23202–23230, https://doi.org/10.1039/D0TA08045D.
[4] K. Sivula, R. van de Krol, Semiconducting materials for photoelectrochemical energy conversion, Nat. Rev. Mater. 1 (2) (2016), https://doi.org/10.1038/natrevmats.2015.10.
[5] P. Marvan, Š. Huber, J. Luxa, V. Mazánek, D. Sedmidubský, Z. Sofer, M. Pumera, Edge vs. basal plane electrochemistry of layered pnictogens (As, Sb, Bi): does edge always offer faster electron transfer?, Appl Mater. Today 16 (2019) 179–184, https://doi.org/10.1016/j.apmt.2019.05.009.
[6] M. Pumera, Z. Sofer, 2D monoelemental arsenene, antimonene, and bismuthene: beyond black phosphorus, Adv. Mater. 29 (21) (2017) 1605299, https://doi.org/10.1002/adma.201605299.
[7] S.M. Beladi-Mousavi, M. Pumera, 2D-pnictogens: alloy-based anode battery materials with ultrahigh cycling stability, Chem. Soc. Rev. 47 (18) (2018) 6964–6989, https://doi.org/10.1039/C8CS00425K.
[8] M. Pumera, Materials electrochemists' never-ending quest for efficient electrocatalysts: the devil is in the impurities, ACS Catal. 10 (13) (2020) 7087–7092, https://doi.org/10.1021/acscatal.0c02020.
[9] Z. Sofer, D. Sedmidubský, Š. Huber, J. Luxa, D. Bouša, C. Boothroyd, M. Pumera, Layered black phosphorus: strongly anisotropic magnetic, electronic, and electron-transfer properties, Angew. Chem. Int. Ed. 55 (10) (2016) 3382–3386, https://doi.org/10.1002/anie.201511309.
[10] J. Sturala, Z. Sofer, M. Pumera, Chemistry of layered pnictogens: phosphorus, arsenic, antimony, and bismuth, Angew. Chem. Int. Ed. 58 (23) (2019) 7551–7557, https://doi.org/10.1002/anie.201900811.
[11] C.C. Mayorga-Martinez, Z. Sofer, D. Sedmidubský, Š. Huber, A.Y.S. Eng, M. Pumera, Layered metal thiophosphite materials: magnetic, electrochemical, and electronic properties, ACS Appl. Mater. Interfaces 9 (14) (2017) 12563–12573, https://doi.org/10.1021/acsami.6b16553.

[12] R. Gusmão, Z. Sofer, D. Sedmidubský, Š. Huber, M. Pumera, The role of the metal element in layered metal phosphorus triselenides upon their electrochemical sensing and energy applications, ACS Catal. 7 (12) (2017) 8159–8170, https://doi.org/10.1021/acscatal.7b02134.
[13] R. Gusmão, Z. Sofer, M. Pumera, Exfoliated layered manganese trichalcogenide phosphite ($MnPX_3$, X = S, Se) as electrocatalytic van der waals materials for hydrogen evolution, Adv. Funct. Mater. 29 (2) (2019) 1805975, https://doi.org/10.1002/adfm.201805975.
[14] R. Samal, G. Sanyal, B. Chakraborty, C.S. Rout, Two-dimensional transition metal phosphorous trichalcogenides (MPX_3): a review on emerging trends, current state and future perspectives, J. Mater. Chem. A 9 (5) (2021) 2560–2591, https://doi.org/10.1039/D0TA09752G.
[15] Z.W. Seh, K.D. Fredrickson, B. Anasori, J. Kibsgaard, A.L. Strickler, M.R. Lukatskaya, Y. Gogotsi, T.F. Jaramillo, A. Vojvodic, Two-dimensional molybdenum carbide (MXene) as an efficient electrocatalyst for hydrogen evolution, ACS Energy Lett. 1 (3) (2016) 589–594, https://doi.org/10.1021/acsenergylett.6b00247.
[16] Z. Kang, M.A. Khan, Y. Gong, R. Javed, Y. Xu, D. Ye, H. Zhao, J. Zhang, Recent progress of MXenes and MXene-based nanomaterials for the electrocatalytic hydrogen evolution reaction, J. Mater. Chem. A 9 (10) (2021) 6089–6108, https://doi.org/10.1039/D0TA11735H.
[17] A. Vahid Mohammadi, J. Rosen, Y. Gogotsi, The world of two-dimensional carbides and nitrides (MXenes), Science 372 (6547) (2021), https://doi.org/10.1126/science.abf1581.
[18] X. Chia, M. Pumera, Characteristics and performance of two-dimensional materials for electrocatalysis, Nat. Catal. 1 (12) (2018) 909–921, https://doi.org/10.1038/s41929-018-0181-7.
[19] X. Chia, A.Y.S. Eng, A. Ambrosi, S.M. Tan, M. Pumera, Electrochemistry of nanostructured layered transition-metal dichalcogenides, Chem. Rev. 115 (21) (2015) 11941–11966, https://doi.org/10.1021/acs.chemrev.5b00287.
[20] T.F. Jaramillo, K.P. Jørgensen, J. Bonde, J.H. Nielsen, S. Horch, I. Chorkendorff, Identification of active edge sites for electrochemical H_2 evolution from MoS_2 nanocatalysts, Science 317 (5834) (2007) 100–102, https://doi.org/10.1126/science.1141483.
[21] M. Pumera, Z. Sofer, A. Ambrosi, Layered transition metal dichalcogenides for electrochemical energy generation and storage, J. Mater. Chem. A 2 (24) (2014) 8981–8987, https://doi.org/10.1039/C4TA00652F.
[22] A.Y.S. Eng, A. Ambrosi, Z. Sofer, P. Šimek, M. Pumera, Electrochemistry of transition metal dichalcogenides: strong dependence on the metal-to-chalcogen composition and exfoliation method, ACS Nano 8 (12) (2014) 12185–12198, https://doi.org/10.1021/nn503832j.
[23] D. Voiry, M. Salehi, R. Silva, T. Fujita, M. Chen, T. Asefa, V.B. Shenoy, G. Eda, M. Chhowalla, Conducting MoS_2 nanosheets as catalysts for hydrogen evolution reaction, Nano Lett. 13 (12) (2013) 6222–6227, https://doi.org/10.1021/nl403661s.
[24] T. Das, S. Chakraborty, R. Ahuja, G.P. Das, TiS_2 monolayer as an emerging ultrathin bifunctional catalyst: influence of defects and functionalization, ChemPhysChem 20 (4) (2019) 608–617, https://doi.org/10.1002/cphc.201801031.
[25] Z. Song, J. Yi, J. Qi, Q. Zheng, Z. Zhu, L. Tao, Y. Cao, Y. Li, Z. Gao, R. Zhang, L. Huang, G. Li, Z. Xu, X. Wu, Y. Wang, C. Shen, Y.-Y. Zhang, H. Lu, X. Lin, S. Du, H.-J. Gao, Line defects in monolayer $TiSe_2$ with adsorption of Pt atoms potentially enable excellent catalytic activity, Nano Res. 15 (5) (2022) 4687–4692.
[26] R.J. Toh, Z. Sofer, M. Pumera, Catalytic properties of group 4 transition metal dichalcogenides (MX_2; M = Ti, Zr, Hf; X = S, Se, Te), J. Mater. Chem. A 4 (47) (2016) 18322–18334, https://doi.org/10.1039/C6TA08089H.
[27] E. Rahmanian, C.C. Mayorga-Martinez, N. Rohaizad, J. Luxa, Z. Sofer, M. Pumera, Structural transition induced by niobium doping in layered titanium disulfide: the impact on electrocatalytic performance, Appl. Mater. Today 19 (2020), https://doi.org/10.1016/j.apmt.2020.100555.
[28] Z. Wang, Y.-R. Zheng, J. Montoya, D. Hochfilzer, A. Cao, J. Kibsgaard, I. Chorkendorff, J.K. Nørskov, Origins of the instability of nonprecious hydrogen evolution reaction catalysts at open-circuit potential, ACS Energy Lett. 6 (6) (2021) 2268–2274, https://doi.org/10.1021/acsenergylett.1c00876.
[29] M. Ledendecker, J.S. Mondschein, O. Kasian, S. Geiger, D. Göhl, M. Schalenbach, A. Zeradjanin, S. Cherevko, R.E. Schaak, K. Mayrhofer, Stability and activity of non-noble-metal-based catalysts toward the hydrogen evolution reaction, Angew. Chem. Int. Ed. 56 (33) (2017) 9767–9771, https://doi.org/10.1002/anie.201704021.
[30] S. Wert, C. Iffelsberger, K.A. Novčić, F.-M. Matysik, M. Pumera, Edges are more electroactive than basal planes in synthetic bulk crystals of TiS_2 and $TiSe_2$, Appl. Mater. Today 26 (2022), https://doi.org/10.1016/j.apmt.2021.101309.
[31] M.S. Shawkat, J. Gil, S.S. Han, T.-J. Ko, M. Wang, D. Dev, J. Kwon, G.-H. Lee, K.H. Oh, H.-S. Chung, T. Roy, Y. Jung, Y. Jung, Thickness-independent semiconducting-to-metallic conversion in wafer-scale two-dimensional $PtSe_2$ layers by plasma-driven chalcogen defect engineering, ACS Appl. Mater. Interfaces 12 (12) (2020) 14341–14351.

Chapter 9. Microscopic Electrochemical Activity of Double Transition Metal MAX phase Electrocatalyst

Published paper included in this chapter:

K. A. Novčić, C. Iffelesberger, and M. Pumera, *Layered MAX phase electrocatalyst activity is driven by only a few hot spots*, **Journal of Material Chemistry A (2022)**, 10, 3206-3215, doi.org/10.1039/D1TA06419C.

The results were presented at the conference: **18th International Conference on Electroanalysis (ESEAC 2022), 5th-9th June 2022, Vilnius, Lithuania**, where the student received the Analytical and Bioanalytical Chemistry Award for the best student oral presentation.

9.1. Motivation for the Study

The MAX phase particles have attracted much attention as electrocatalysts for the hydrogen evolution reaction (HER). However, their microscopic electrochemical activity remains largely unexplored. Due to the fact that the particles can have individual activity based on the differences in their orientation and size, it is interesting to investigate if such a trend is valid for the MAX phase microparticles. Therefore, in this paper, the macroscopic and microscopic electrochemical performance of double transition metal, Mo_2TiAlC_2, MAX phase microparticle-based sample is investigated in order to get insight into the distribution and uniformity of the HER activity of MAX phase microparticles over the particle-based sample.

9.2. Paper Conclusion

This study demonstrates the macroscopic and microscopic electrochemical performance for the HER of the double transition metal Mo_2TiAlC_2 MAX phase. The macroscopic electrochemical performance studied by traditional electrochemical techniques such as linear sweep

voltammetry shows the average electrochemical activity of the MAX phase electrocatalyst. Additionally, the microscopic electrochemical performance of the MAX phase, studied by SECM shows the non-uniform and individual activity of the MAX phase particles over the particle-based samples. This study provides relevant knowledge about the uniformity of the MAX phase active sites for hydrogen evolution reaction and has broad implications for our understanding of the electrocatalytic activity of MAX phases, which is of utmost importance for their future development as electrocatalysts.

9.3. Student Contribution

The student is the first author of this paper who contributed to the paper by performing the samples` preparation, optical characterization and elemental composition analysis of the samples as well as the macroscopic and microscopic electrochemical characterization of the samples via linear sweep voltammetry and scanning electrochemical microscopy. The student interpreted the data and wrote the manuscript.

Journal of Materials Chemistry A

ROYAL SOCIETY OF CHEMISTRY

PAPER

View Article Online
View Journal | View Issue

Cite this: J. Mater. Chem. A, 2022, 10, 3206

Layered MAX phase electrocatalyst activity is driven by only a few hot spots†

Katarina A. Novčić,[a] Christian Iffelsberger [a] and Martin Pumera *[abcd]

Received 29th July 2021
Accepted 27th December 2021

DOI: 10.1039/d1ta06419c

rsc.li/materials-a

Layered metal carbides, MAX phases, have gained significant interest in the scientific community due to their electrocatalytic and electrochemical properties. Among various MAX phases, Mo_2TiAlC_2 has driven much attention because of its enhanced electrochemical activity for the hydrogen evolution reaction (HER). So far, the macroscopic HER performance has been investigated by traditional electrochemical techniques such as voltammetry. However, the knowledge of the microscopic electrocatalytic behaviour, *i.e.*, distribution and location of highly active sites for HER is still limited. Herein, the microscopic analysis of the MAX phase microparticles shows that their electrocatalysis is driven by a few particles with an outstanding catalytic activity towards hydrogen evolution. Such observation is of high importance for design and applications of electrocatalysts in general.

Introduction

The constant rise in the global population has inevitably led to an increase in fossil fuel consumption, which is why turning to renewable energy sources and the green hydrogen cycle is becoming of crucial importance. Utilizing electrochemical water splitting *via* the hydrogen evolution reaction (HER) to produce clean hydrogen is a promising alternative to resolve the current energy and environmental crisis. Therefore, there is an urgent need to investigate catalysts for the hydrogen production.[1–5] The layered materials such as 2D transition metal dichalcogenides (TMDs), *i.e.* MoS_2 and WS_2, have been widely investigated as a promising electrocatalyst for the HER.[6–11] Their electrochemical HER activity has been reported to arise from catalytically active edge sites and strongly depends on the density of S-vacancies and defects on the catalytic surface.[12–19]

Beyond these, MAX phases, a family of layered ternary transition metal carbides and nitrides, have attracted significant attention because by etching the A element from the MAX phase structure, it is possible to synthesize the new group of materials called MXenes.[20–22] Besides, MAX phases themselves possess a unique combination of metallic and ceramic properties.[23,24] The general formula of MAX phases can be described as $M_{n+1}AX_n$, where M stands for an early transition metal, A is the element from III_A and IV_A group, X is C or N and $n = 1$, 2, or 3. Previously, the MAX phases have been reported to possess excellent properties *i.e.* good thermal and electrical conductivity,[25] oxidation resistance[26,27] and damage tolerance.[28] Moreover, recent studies of different MAX phases have demonstrated their electrochemical performance for energy-related applications such as HER, oxygen reduction reaction (ORR) and oxygen evolution reaction (OER).[29,30] Among various MAX phases, the Mo_2TiAlC_2 phase was reported to have the highest electrocatalytic activity for the HER.[29] Even though the macroscopic electrochemical activity of the MAX phases is known, there is a lack of deeper understanding and knowledge of the distribution and uniformity of the HER activity of the MAX phase particles.

Recently, the scanning probe techniques such as scanning electrochemical microscopy (SECM), have been employed to study the electrochemical activity of different electrocatalytic surfaces.[31–35] The SECM has been used for investigation of the catalytic surfaces by reflecting the surface morphology, conductivity and electrochemical activity as well as the location of the HER active sites on the electrocatalytic surfaces.[36–42]

Moreover, this technique has been employed to address the electrochemical activity of catalytic nanoparticles, such as Au, providing the information of the individual particle's activity, geometry and porosity.[43,44] Due to the fact that individual

[a]Future Energy and Innovation Laboratory, Central European Institute of Technology, Brno University of Technology, Purkyňova 656/123, 61200 Brno, Czech Republic. E-mail: pumera.research@gmail.com

[b]Energy Research Institute @ NTU (ERI@N), Research Techno Plaza, X-Frontier Block, Level 5, 50 Nanyang Drive, Singapore

[c]Department of Medical Research, China Medical University Hospital, China Medical University, No. 91 Hsueh-Shih Road, Taichung 40402, Taiwan

[d]Department of Chemical and Biomolecular Engineering, Yonsei University, 50 Yonsei-ro, Seodaemun-gu, Seoul 03722, Korea

† Electronic supplementary information (ESI) available: SEM micrograph of the Mo_2TiAlC_2 microparticles, XRD pattern of the Mo_2TiAlC_2 sample without Nafion, probe approach curves (PACs), the optical image of the Mo_2TiAlC_2 film, scanning electrochemical image recorded in the substrate generation/tip collection mode, CLSM images of the Mo_2TiAlC_2 film obtained with 100× lenses, table with the R_q values of the line roughness measurements of the Mo_2TiAlC_2 film, AFM image and line scan profile of the Mo_2TiAlC_2 microparticle, schematic illustration of the sample preparation process and cyclic voltammogram of the UME tip probe. See DOI: 10.1039/d1ta06419c

particle's activity could differ over particle-based sample, the investigation of the distribution of the particle activity for HER, uniformity of their conductivity and heterogeneity over the sample is of crucial importance. Even though the SECM has been employed in the investigation of the HER activity of different MXenes,[45] the microscopic study of the MAX phases has not been reported yet.

In this work, the macroscopic and microscopic performances for the HER of the Mo_2TiAlC_2 MAX phase microparticle films on a carbon electrode were investigated. The macroscopic electrochemical characterization of the Mo_2TiAlC_2 sample was performed *via* linear sweep voltammetry (LSV). Following, the microscopic electrochemical study of the Mo_2TiAlC_2 microparticles was done by SECM. The differences in the activity of the individual microparticles are visible by mapping the highly active spots for the HER performance over the Mo_2TiAlC_2 film. The surface catalytic ability for the ferrocene methanol (FcMeOH) regeneration as well as the electrochemical activity for the HER were carried out by SECM in feedback and substrate generation/tip collection (SG/TC) mode, respectively. Additionally, the confocal laser scanning microscopy (CLSM) and atomic force microscopy (AFM) were used to provide relevant information about the surface roughness. This study revealed that the overall catalytic activity of MAX phase film is only driven by a few localized hot spots of the highly catalytic microparticles, while the most of the MAX phase microparticles have lower catalytic activity. The individual catalytic behaviour of the MAX phase microparticles shows similarities with the behaviour of the $LiMn_2O_4$ particles that have been found to possess significant heterogeneous electrochemical behaviour for the (de) intercalation of the Li-ion at single particle level.[46] Additionally, this resembles the behaviour of the enzymes, where it was shown that some of the individual enzymes are much more active than the others.[47–50] This study revealed the general trend

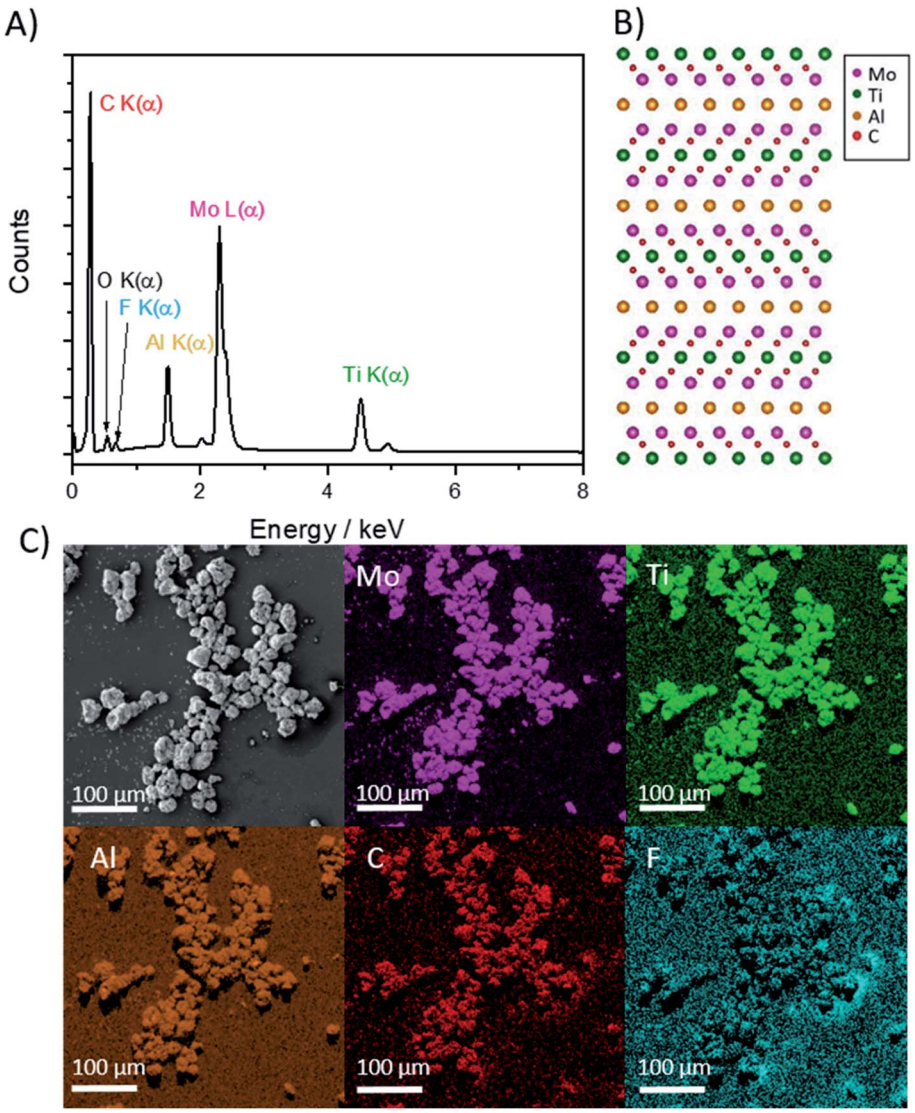

Fig. 1 Materials characterization of the Mo_2TiAlC_2 film. (A) Energy dispersive X-ray spectrum of the Mo_2TiAlC_2 film, (B) structure of the Mo_2TiAlC_2 MAX phase and (C) scanning electron micrograph (black & white) and EDS maps for the elemental distribution of Mo, Ti, Al, C and F on the Mo_2TiAlC_2 film.

in nature regarding the activity of smaller units that can differ from their average activity, making the knowledge of the individual characteristic more important. The presented work on highly active hot spots in MAX phase film will have a profound impact on the field of electrocatalysis in general.

Results and discussion

We studied macroscopic and microscopic electrochemical behaviour of MAX phase Mo_2TiAlC_2 film. The characterization of the morphology and the elemental composition of the Mo_2TiAlC_2 film was performed by scanning electron microscope (SEM) and energy-dispersive X-ray spectroscopy (EDS), respectively. The SEM micrograph of the Mo_2TiAlC_2 film visible in Fig. S1 (in ESI†) shows the structure of the round-shape MAX phase microparticles with the particle size ranging from 2 to 15 μm. The EDS spectrum, shown in Fig. 1A, confirms the presence of all elements of the Mo_2TiAlC_2 film with their atomic percentages of C 48.5%, Mo 21.8%, Ti 14.7%, Al 9.6% and O 3.4%. The sources of F (1.6%) and Si (0.4%) are the Nafion and the Si substrate used for the EDS analysis. The ratio between Mo, Ti and Al elements additionally confirms the presence of the Mo_2TiAlC_2 structure (as illustrated in Fig. 1B). The EDS maps with the corresponding SEM image of the Mo_2TiAlC_2 film (black & white) are presented in Fig. 1C. The EDS maps show the uniform distribution of Mo, Ti, Al, C and F elements over the Mo_2TiAlC_2 film. The X-ray diffraction (XRD) study of the Mo_2TiAlC_2 film without Nafion is shown in Fig. S2 in ESI.† The Mo_2TiAlC_2 film shows the intense characteristic peaks at 2θ of 9.4°, 19.2° and 39.7°, corresponding to the (002), (004) and (104) planes, respectively.[51,52]

Following that, the macroscopic and microscopic electrochemical performance for the HER of the Mo_2TiAlC_2 film was studied. The macroscopic HER performance was done by LSV in a 0.5 M H_2SO_4 solution. In LSV the potential is swept linearly, while the measured current allows the determination of the averaged macroscopic electrochemical performance of the catalytic material. Fig. 2A demonstrates the obtained LSV curves for the glassy carbon electrode covered with Nafion (Nafion@GC), pure glassy carbon electrode (GC), Mo_2TiAlC_2 film, and Pt/C. The GC, Nafion@GC and Pt/C served as a reference to evaluate the catalytic performance of the Mo_2TiAlC_2 film. The overpotential value of the Mo_2TiAlC_2 film obtained at the current density of -10 mA cm^{-2} is found to be -0.56 V (*vs.* RHE), which lies between the observed overpotential values of the GC and Pt/C and it is in good agreement with the reported value for the Mo_2TiAlC_2 phases of -0.57 V (*vs.* RHE).[29] The obtained overpotential value of the Mo_2TiAlC_2 film is comparable with the overpotential values of widely investigated TMDs, such as MoS_x (overpotential range 0.36–0.57 V) and WS_2 (overpotential range 0.42–0.8 V).[6,10,53]

The Mo_2TiAlC_2 film showed higher electrochemical performance for the HER compared to other MAX phases (such as Ti_2AlC, Ti_2SnC, Ti_3SiC_2, V_2AlC, Cr_2AlC, Ti_2AlN, Ti_3AlC_2, Cr_2AlB_2 and MoAlB), with overpotential value ranging from -0.63 V to -0.85 V (*vs.* RHE), as reported in the literature.[29,30]

Subsequently, the Tafel slopes were calculated from the obtained LSV results. The corresponding plots and calculated values of the slopes are presented in Fig. 2B and in the bar chart in Fig. 2C, respectively. The Tafel slopes of 32, 91, 115 and 126 mV dec^{-1} were found for the Pt/C, GC, Mo_2TiAlC_2 film and Nafion@GC, respectively. The obtained value of 115 mV dec^{-1} for the Mo_2TiAlC_2 film is slightly lower than the reported value of 127 mV dec^{-1}.[29] According to the Tafel analysis, the slope value is determined by the slow-rate step in the HER mechanism:

(1) Volmer step (hydrogen adsorption) ≈ 120 mV dec^{-1}

$$H^+ + e^- + (*) \rightarrow H_{ads}$$

(2) Tafel step (recombination of adsorbed hydrogen atoms) ≈ 30 mV dec^{-1}

$$H_{ads} + H_{ads} \rightarrow H_2 + 2(*)$$

(3) Heyrovský step (electrochemical hydrogen desorption) ≈ 40 mV dec^{-1}

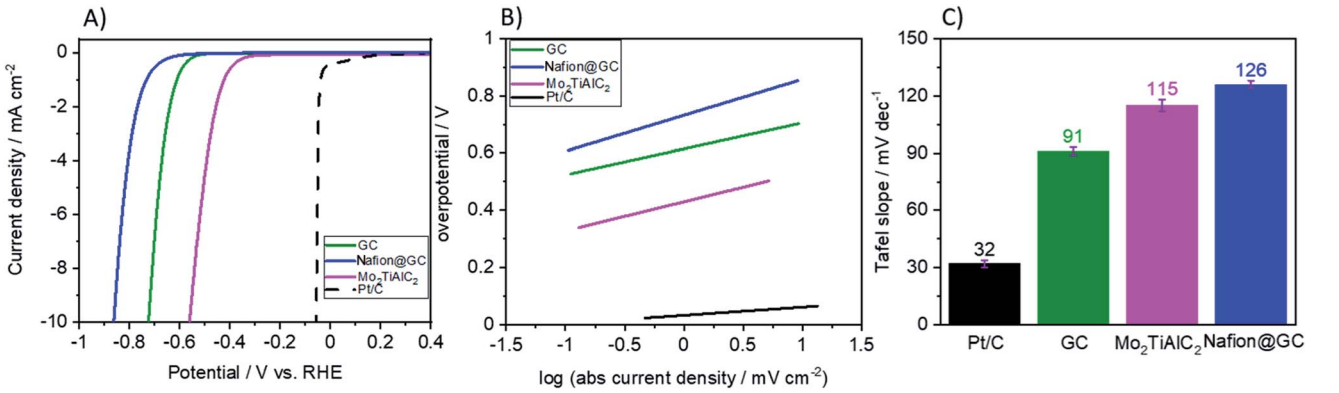

Fig. 2 Macroscopic electrochemical characterization of the Mo_2TiAlC_2 film. (A) Linear sweep voltammograms for the glassy carbon electrode covered with Nafion (Nafion@GC) (blue), pure glassy carbon (GC) (green), Mo_2TiAlC_2 film (magenta) and Pt/C (dash black) with (B) corresponding Tafel slopes and (C) bar charts showing the calculated values for the Tafel slopes. Measurements were performed in 0.5 M H_2SO_4 with a scan rate of 5 mV s^{-1}.

$$H^+ + H_{ads} + e^- \rightarrow H_2 + (*)$$

where (*) stands for the available active site on the catalytic surface. The obtained Tafel slope value for the Mo_2TiAlC_2 film indicates the slow-rate Volmer step of hydrogen adsorption in the HER mechanism.[29,30]

Even though the macroscopical electrochemical activity of the MAX phase is known from LSV measurements, there is a lack of deeper understanding and knowledge of the distribution and uniformity of the HER activity of the MAX phase microparticles. This is of crucial importance for particle-based samples, such as Mo_2TiAlC_2, where individual particles can have an individual contribution to the average or macroscopic activity. In order to gain a deeper understanding of the electrocatalytic activity at the micrometer level, SECM measurements of the Mo_2TiAlC_2 film was performed.

The most widely used operational modes of SECM are feedback and SG/TC mode, where material contrast and local differences in electrochemical activity of the substrate can be resolved, respectively.[54] The feedback mode operates in three-electrode system, where the ultra-microelectrode (UME) probe is scanned across the substrate of interest, providing the information about the local differences in conductivity.[55,56] Additionally, the SG/TC operational mode works in four-electrode system, where the substrate acts as a second working electrode. In this mode, the sufficient potential is applied to the substrate to initiate the reaction of interest and the adequate potential is applied to the UME probe to collect the generated species. By scanning the UME probe across the substrate in SG/TC mode, the local differences in HER activity of the substrate can be resolved due to the fact that a locally higher hydrogen concentration results in a higher anodic current response.[39,57]

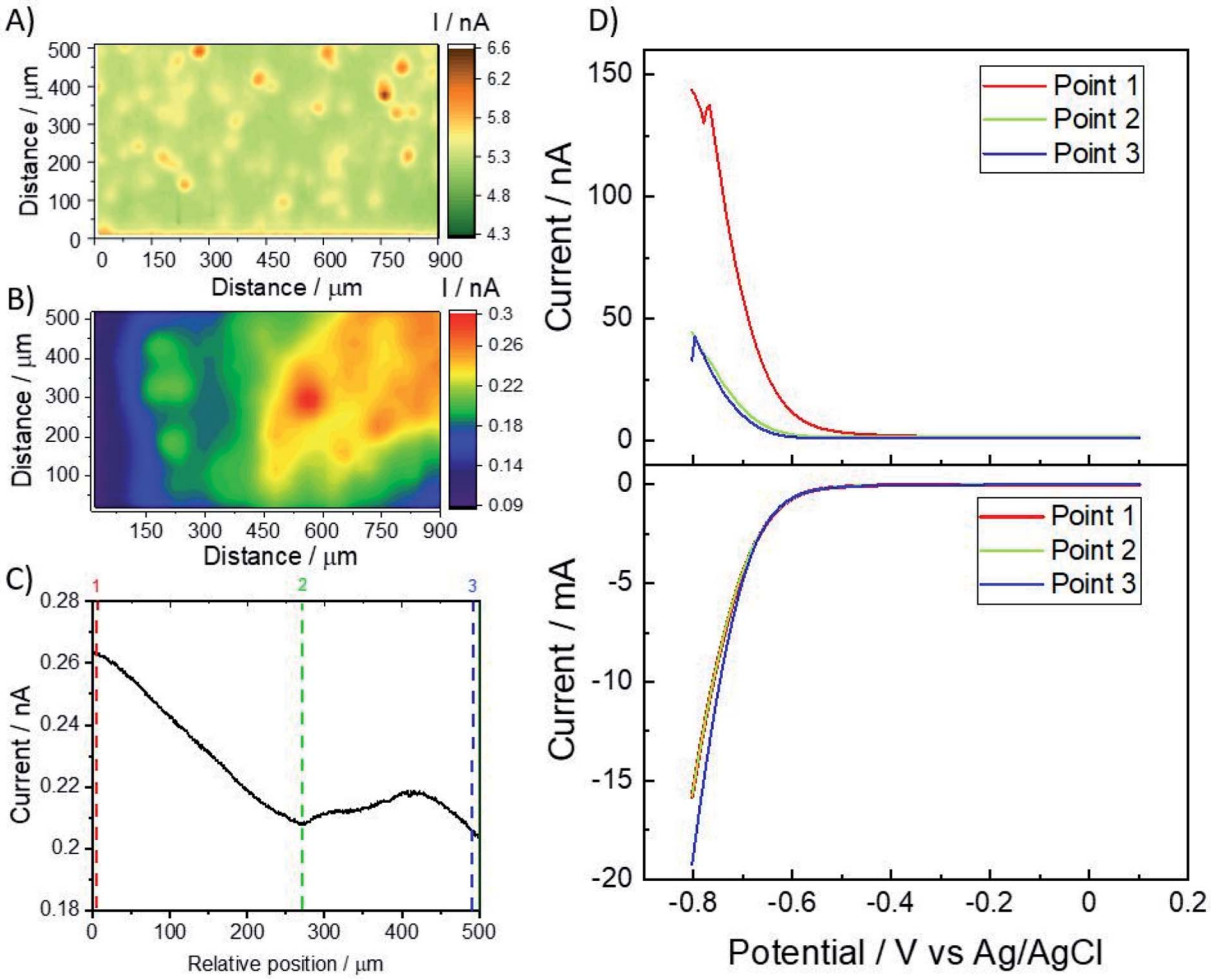

Fig. 3 Microscopic electrochemistry of the Mo_2TiAlC_2 microparticle film. (A) Scanning electrochemical image of the Mo_2TiAlC_2 film recorded in FcMeOH mediator solution in feedback mode with tip potential of 0.4 V (*vs.* Ag/AgCl). (B) SECM image recorded in the SG/TC mode in 0.5 M H_2SO_4 solution with the tip potential of 0.1 V and hydrogen generation potential of −0.55 V. For imaging, a maximum scan rate of 300 μm s^{-1}, pixel size of 10 × 10 μm and waiting time of 4 ms was used. (C) SECM line scan curve of the Mo_2TiAlC_2 film performed in 0.5 M H_2SO_4 solution with a max. speed of 50 μm s^{-1} and waiting time of 0 ms and (D) the corresponding local linear sweep voltammograms performed in 3 points of the sample with a scan rate of 50 mV s^{-1} showing the current response measured at the tip (up) and substrate (down). For all measurements a 25 μm diameter Pt disc UME was used.

Prior to SECM imaging, the electrochemical reactivity of the ferrocene methanol (FcMeOH) mediator species on the Mo_2TiAlC_2 microparticles was evaluated *via* probe approach curves (PACs) measurements. These curves were recorded for the Nafion@GC and Mo_2TiAlC_2 film in the mediator solution with the tip potential of 0.4 V (*vs.* Ag/AgCl), as shown in Fig. S3 (in ESI†). The obtained PACs were compared to the theoretically calculated curves for the pure positive[58] and pure negative[59] feedback as well as to the experimentally obtained curves for the glass, gold and pure GC substrates. The measured curves for the glass and gold substrates are in good agreement with the theoretically calculated curves, which confirms the diffusion controlled reaction of the FcMeOH mediator species on the investigated substrates. Furthermore, the regeneration of the FcMeOH mediator at the Nafion@GC substrate was found to be relatively slow compared to its regeneration on the Mo_2TiAlC_2 film. Following, the Mo_2TiAlC_2 film was characterized optically, as presented in Fig. S4 (in ESI†). The labelled area of the sample in this figure was scanned by SECM in feedback and SG/TC mode, respectively. The obtained SECM micrograph in feedback mode in FcMeOH mediator solution with the tip potential of 0.4 V (*vs.* Ag/AgCl) is shown in Fig. 3A. This figure demonstrates the material contrast between Mo_2TiAlC_2 microparticles (yellow and brown colour) and Nafion@GC surrounding (green colour), according to the obtained PACs (Fig. S3 in ESI†).

Subsequently, the microscopic electrochemical performance for the HER of the same area of the Mo_2TiAlC_2 film was studied in the SG/TC mode. The obtained SECM micrograph in 0.5 M H_2SO_4 with the hydrogen generation potential of −0.55 V and the tip collection potential of 0.1 V is presented in Fig. 3B. This figure shows the distribution of the electrochemically active sites for the HER. Compared to the corresponding SECM micrograph obtained in the feedback mode (Fig. 3A), it is found that not all microparticles visible in the feedback mode image equally contribute to the HER performance. Moreover, the SECM micrograph obtained in SG/TC mode (Fig. 3B) depicts relatively high (red), medium (yellow to green) and low (blue) active sites for HER. The blue colour corresponds to low HER activity correlated, according the obtained LSV data (Fig. 2A, blue curve), to the Nafion@GC substrate because the applied potential was not sufficient for the hydrogen generation. However, since the applied potential was high enough for the hydrogen generation on the Mo_2TiAlC_2 microparticles, green, yellow and red areas correspond to the particles of different HER activity.

Following, the line scan curve (as labeled in Fig. S5 in ESI†) was performed in order to study the change in the tip current measured along the *x*-axis. Fig. 3C shows the obtained line scan curve with the marked points of high (1), medium (2) and low (3) HER activity. Subsequently, the local LSV measurements in these 3 points were performed and the current responses at the UME tip and the substrate were measured, as shown in Fig. 3D. The differences in the tip current (Fig. 3D, up) indicate different local HER performance of the Mo_2TiAlC_2 microparticles. The point 1 which was assumed to have the highest HER activity also showed the highest tip current response. Moreover, at points 2 and 3 significantly lower tip current response were found because they correspond to the points with lower HER activity. As expected, the current measured at the substrate (Fig. 3D, down) was the same for all points. The high current response is caused by high particle activity as well as particles height. In order to study the surface height and morphology in detail, the optical characterization of the Mo_2TiAlC_2 film was performed by CLSM.

So far, the CLSM has been used in the study of different materials, providing the relevant information about the surface roughness.[60–62] In the contrast to the conventional light microscopy, a light source in the CLSM is made up of a laser beam.[62] The surface of the sample is scanned layer by layer, while the layers are composed into a three-dimensional (3D) microscopic image of the sample. The colour and height CLSM images of the Mo_2TiAlC_2 film are presented in Fig. 4A and B, respectively. Fig. 4A shows a colour CLSM image of the Mo_2TiAlC_2 film with the random distribution of the Mo_2TiAlC_2 microparticles over the Nafion@GC electrode substrate. Moreover, the CLSM height image (Fig. 4B) presents the microparticles of mostly equal height (green colour) and some slightly higher microparticles (red colour).

Observing the Mo_2TiAlC_2 film surface using the 100× lenses allow the accurate measurement of the surface roughness on

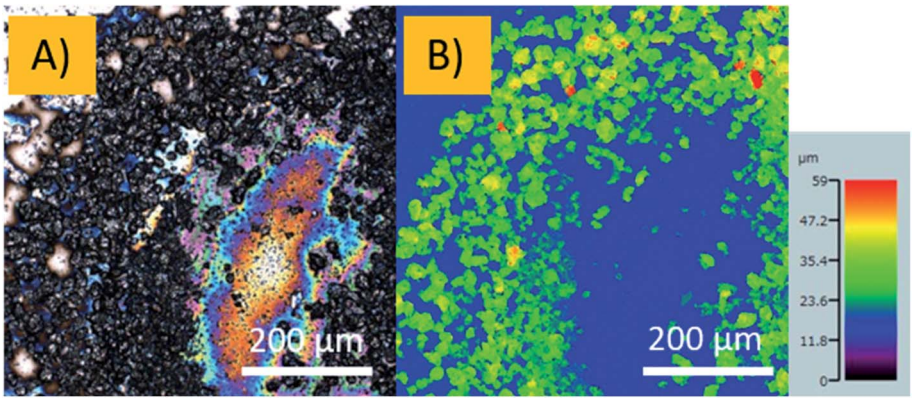

Fig. 4 Optical microscopic characterization of the Mo_2TiAlC_2 films performed by confocal laser scanning microscopy (CLSM). (A) Colour CLSM image and (B) corresponding false-colour image showing the height of the particles obtained with the 20× lenses.

a micron scale along cross-sectional lines of the surface.[60] Since the 100× lenses allow the observation of a 22 × 22 μm^2 surface area (as visible on the colour CLSM image in Fig. S6A in ESI†), the surface roughness was measured along the 10 cross-sectional lines: 5 horizontal and 5 vertical, as shown in Fig. S6B in ESI.† The roughness factor, R_q (root mean square deviation of the roughness profile) was calculated along the cross-sectional lines and the calculated values are summarized in the Table S1 in ESI.† The averaged R_q value for the Mo_2TiAlC_2 microparticles was found to be 0.145 ± 0.02 μm. Following, in order to do a more detail study of the roughness of the Mo_2TiAlC_2 microparticles, AFM imaging of a representative 2 × 2 μm^2 area of the Mo_2TiAlC_2 microparticles was performed. The obtained AFM image and the corresponding line scan profile are shown in the Fig. S7A and B in ESI,† respectively. The line scan profile is extracted from the labeled line in the AFM image (Fig. S7A in ESI†). The height differences in the line scan profile (Fig. S7B in ESI†) show the change in particle's height of 160 nm occurring at ≈0.2 μm (along *X* axis) that is followed by two consecutive changes of 5 nm each at ≈1 μm and ≈1.4 μm (along *X* axis), respectively.

However, the observed differences in the particle's height and surface roughness make negligible variations in the tip current. Therefore, the distribution of the HER activity shown in Fig. 3B, comes from the individual particle activity with highly active hot spots for the reaction. As shown in XRD study of the Mo_2TiAlC_2 film in Fig. S2 (in ESI†), the different particles' orientation are present which can cause differences in the individual particles' activity. This individual behaviour of the Mo_2TiAlC_2 microparticles is similar to the behaviour of the $LiMn_2O_4$ particles that have shown wide spectrum of activity for the Li-ion (de)intercalation at single particle level.[46] This additionally revealed the fact that individual particle's activity could differ over the particle-based sample, making the investigation of the distribution of the particle activity for HER of crucial importance.[43,44,46] Additionally, the individual behaviour of the MAX phase microparticles resembles the similar behaviour of the enzymes, since the enzymes are reported to be individually more active compared to their average activity.[47–50]

Conclusion

In summary, the electrochemical performance for the HER of the Mo_2TiAlC_2 films was investigated macroscopically and microscopically. The macroscopic electrochemical performance for the hydrogen evolution reaction (HER) of the film was studied by linear sweep voltammetry (LSV) and the obtained overpotential value was found to be −0.56 V (*vs.* RHE). The SECM image recorded in the feedback mode showed the random distribution of the Mo_2TiAlC_2 microparticles on the film. Following, the SG/TC mode imaging of the HER activity demonstrated the non-uniform distribution of the individual particle activity with highly active hot spots. Additionally, the optical study of the surface roughness done by confocal laser scanning microscopy (CLSM) and atomic force microscopy (AFM) showed the negligible differences in particle height over the film. Hence, the presented study demonstrates the Mo_2TiAlC_2 particles' individual microscopic electrochemical performance for the HER. The SECM imaging provides relevant knowledge regarding the uniformity of the particle' activity as well as the distribution of the HER active sites. Furthermore, this study gives insight into the surface electrochemical activity and provides the information regarding deeper understanding of the MAX phase HER activity which is relevant for its electrochemical application development. The conclusion that overall performance of random films of the electrocatalytic microparticles is driven by only few hotspots has broad implication on different materials and our understanding of electrocatalytic performance in general.

Experimental section

Chemicals & solutions

The MAX phase film was prepared from the Mo_2TiAlC_2 powder (Laizhou Kai Kai Ceramic Materials Co., Ltd., China). Isopropanol (2-propanol, 99.9%), platinum on graphite, (Pt/C, 20 wt% loading), and Nafion were purchased from Sigma-Aldrich, Germany. The PDMS film was prepared from polydimethylsiloxane (SYLGARD 184 Silicone, Elastomer Kit, Germany) following the producer instruction. As SECM mediator solution, a 1.5 mM FcMeOH (99%, ABCR GmbH, Germany) with 0.2 M KNO_3 (analytical grade, Merck KGaA, Germany) as the supporting electrolyte was used. For the hydrogen evolution reaction measurements, 0.5 M H_2SO_4 (96%, analytical grade, Penta, Czech Republic) was used. All solutions were prepared in deionized water with a resistivity greater than 18 MΩ cm.

Sample preparation

For the preparation of Mo_2TiAlC_2 suspension, 5 mg of the MAX phase powder was dispersed in 1 ml of water and isopropanol mixture (ratio 2 : 3). Afterwards, 40 μl of Nafion was added to this mixture, as described by Kumar *et al.*[29] Nafion is used as a standard binder for the preparation of the powder-based electrodes. For the preparation of Pt/C, 5 mg of the Pt/C was dispersed in 1 ml of water and after that 40 μl of Nafion was added. The mixtures were then sonicated for 30 min to obtain a well-dispersed suspension. For the macroscopic electrochemical characterization, 5 μl of the prepared suspension was drop-casted on the glassy carbon disk electrode (electrode radius: 1.5 mm) that was previously polished with 0.05 μm Al_2O_3 particles on a polishing pad and rinsed with ultrapure water. After drying, Mo_2TiAlC_2 film was ready for the macroscopic electrochemical characterization.

Following, the Mo_2TiAlC_2 film was prepared for the microscopic SECM measurements. In order to define the area for the SECM measurements, a PDMS film with a thickness of ∼0.5 mm and with a 1.5 mm diameter hole in the middle was placed on a glassy carbon plate (Sigradur® G, GmbH, Germany), as shown in Scheme S1A (in ESI†). The glassy carbon plate was previously polished with 0.05 μm Al_2O_3 particles on a polishing pad and rinsed with ultrapure water. Following, 1.2 μl of the prepared Mo_2TiAlC_2 suspension was drop-casted on the defined area on the glassy carbon electrode plate. After drying, the PDMS was

removed and the prepared Mo_2TiAlC_2 film, visible in the optical image in Scheme S1B (in ESI†), was ready for the SECM measurements.

Material characterization

Surface and elemental composition analysis of the Mo_2TiAlC_2 film were done by SEM and EDS with Mira 3 XMU SEM (Tescan) equipped with EDS (Oxford Instruments X-MAX^{20}) detector. The Mo_2TiAlC_2 sample was attached to the SEM holder using the Cu tape. For the measurement, an accelerating voltage of 20 kV was used. The XRD pattern of the Mo_2TiAlC_2 sample without Nafion was performed using an X-ray diffractometer (Rigaku SmartLab, 9 kW) using Cu $K_{\alpha1}$ radiation. The morphological and optical characterization of the prepared Mo_2TiAlC_2 film for the SECM measurements was done using the AFM (Dimension Icon with Airasyst cantilever, Bruker, USA) and CLSM (Olympus Lext OLS4100) with a 20× and 100× lenses as well as a stereomicroscope (Zeiss Stemi 508) with a colour camera (Axiocam 105) and Axio Vision Software. The roughness factor, R_q (root mean square deviation of the roughness profile) was calculated along the 10 cross-sectional lines (5 horizontal and 5 vertical) by OLYMPUS LEXT OLS4100 software.

Electrochemical characterization of the hydrogen evolution reaction performance

The macroscopic HER performance of the prepared Mo_2TiAlC_2 film was done by LSV using a potentiostat (Autolab, Metrohm, Netherlands), controlled by Nova 2.1 software. The measurements were performed in 0.5 M H_2SO_4 with a scan rate of 5 mV s^{-1}, starting from 0.2 V, with the Ag/AgCl 1 M KCl reference electrode and a graphite counter electrode. Unless stated otherwise, all potentials were converted and reported *versus* the reversible hydrogen electrode (RHE), calculated according to the literature.[63] The Tafel slopes were calculated from the obtained LSV measurements.

Following, the microscopic HER performance of the Mo_2TiAlC_2 film was investigated by SECM (Sensolytics, Germany). For the SECM measurements, a 25 μm diameter Pt disc UME (Sensolytics, Germany) was used. The characterization of the UME was done by cyclic voltammetry in 1.5 mM FcMeOH and 0.2 M KNO_3 mediator solution, with a scan rate of 50 mV s^{-1} and potential range from 0 V to 0.5 V (*vs.* Ag/AgCl). The cyclic voltammogram of the UME probe is shown in Fig. S8 (in ESI†). Before measurements, the UME was polished with 0.05 μm Al_2O_3 particles on a polishing pad and rinsed with ultrapure water. All SECM measurements were performed with Ag/AgCl 3 M KCl as a reference and Pt as a counter electrode. The reference electrode was calibrated by Metrohm following the standard procedure. The probe approach curve (PACs) measurements were performed in the mediator solution with a UME potential of 0.4 V (*vs.* Ag/AgCl), a max. approach speed of 1 μm s^{-1}, step width of 1 μm and waiting time of 0 ms. The PACs for theoretically positive and negative feedback were calculated, according to the literature.[58,59,64] The glass slide coated with the 30 nm thick gold film was used for the measurement of the positive feedback. The glass coating was done by a high vacuum coating system (Leica Microsystems EM ACE 600).

The SECM imaging of the Mo_2TiAlC_2 film was performed in the feedback and SG/TC mode. The SECM imaging in the feedback mode was done in 1.5 mM FcMeOH and 0.2 M KNO_3 mediator solution with the UME tip potential of 0.4 V (*vs.* Ag/AgCl). The SECM imaging in the SG/TC mode was performed in 0.5 M H_2SO_4 with the tip collection potential of 0.1 V and hydrogen generation potential of −0.55 V. For imaging a max. scan rate of 300 μm s^{-1}, pixel size of 10 × 10 μm and waiting time of 4 ms were used with a tip-to-substrate distance of ∼17 μm. The localized LSV measurements were performed in 0.5 M H_2SO_4 with a scan rate of 50 mV s^{-1}. The measurements were done in low, medium and high HER active spots with 3 repetitions in each point. All localized LSV measurements were done using a 25 μm Pt disc UME probe.

Funding sources

M. P. acknowledges the financial support by the Grant Agency of the Czech Republic (GACR EXPRO: 19-26896X). CzechNanoLab project LM2018110 funded by MEYS CR is gratefully acknowledged for the financial support of the measurements at CEITEC Nano Research Infrastructure. This project has received funding from the grant CEITEC-K-21-7063, realized within the project Quality Internal Grants of BUT (KInG BUT), Reg. No. CZ.02.2.69/0.0/0.0 19_073/0016948, which is financed from the OP RDE (Operational Program Research, Development and Education) and from the European Union's Horizon 2020 research and innovation program under the Marie Skłodowska-Curie grant agreement no. 888797.

Author contributions

K. A. N. performed the sample preparation, optical characterization of the sample with CLSM and electrochemical characterization *via* LSV and SECM and interpreted the data. C. I. performed the sample characterization *via* SEM, EDS and AFM measurements. M. P. supervised and conceptualized this work. The manuscript was written through contributions of all authors. All authors have given approval to the final version of the manuscript.

Conflicts of interest

There are no conflicts to declare.

Acknowledgements

M. P. acknowledge the financial support from the Grant Agency of Czech Republic (GACR EXPO: 19-26896X). K. A. N. acknowledges the grant CEITEC-K-21-7063, realized within the project Quality Internal Grants of BUT (KInG BUT), Reg. No. CZ.02.2.69/0.0/0.019_073/0016948, which is financed from the OP RDE (Operational Program Research, Development and Education). C. I. acknowledges the financial support by the European Union's Horizon 2020 Research and Innovation Program under

the Marie Skłodowska-Curie grant agreement no. 888797. K. A. N. and C. I. acknowledge the support from the CzechNanoLab Research Infrastructure (ID LM2018110, MEYS CR) for providing the sample characterization facilities. The authors thank Dr Pavla Roupcová from Central European Institute of Technology, Brno University of Technology, for providing XRD analysis of the sample.

References

1 J. Zhang, Y. Zhao, X. Guo, C. Chen, C. L. Dong, R. S. Liu, C. P. Han, Y. Li, Y. Gogotsi and G. Wang, Single Platinum Atoms Immobilized on an MXene as an Efficient Catalyst for the Hydrogen Evolution Reaction, *Nat. Catal.*, 2018, **1**, 985–992, DOI: 10.1038/s41929-018-0195-1.

2 J. Li, J. Hu, M. Zhang, W. Gou, S. Zhang, Z. Chen, Y. Qu and Y. Ma, A Fundamental Viewpoint on the Hydrogen Spillover Phenomenon of Electrocatalytic Hydrogen Evolution, *Nat. Commun.*, 2021, **12**, 3502, DOI: 10.1038/s41467-021-23750-4.

3 Y. Jiao, Y. Zheng, K. Davey and S. Z. Qiao, Activity Origin and Catalyst Design Principles for Electrocatalytic Hydrogen Evolution on Heteroatom-Doped Graphene, *Nat. Energy*, 2016, **1**, 16130, DOI: 10.1038/nenergy.2016.130.

4 K. L. Zhou, Z. Wang, C. B. Han, X. Ke, C. Wang, Y. Jin, Q. Zhang, J. Liu, H. Wang and H. Yan, Platinum Single-Atom Catalyst Coupled with Transition Metal/Metal Oxide Heterostructure for Accelerating Alkaline Hydrogen Evolution Reaction, *Nat. Commun.*, 2021, **12**, 3783, DOI: 10.1038/s41467-021-24079-8.

5 F. Li, X. V. Medvedeva, J. J. Medvedev, E. Khairullina, H. Engelhardt, S. Chandrasekar, Y. Guo, J. Jin, A. Lee, H. Thérien-Aubin, A. Ahmed, Y. Pang and A. Klinkova, Interplay of Electrochemical and Electrical Effects Induces Structural Transformations in Electrocatalysts, *Nat. Catal.*, 2021, **4**, 479–487, DOI: 10.1038/s41929-021-00624-y.

6 X. Chia and M. Pumera, Layered Transition Metal Dichalcogenide Electrochemistry: Journey across the Periodic Table, *Chem. Soc. Rev.*, 2018, **47**, 5602–5613, DOI: 10.1039/c7cs00846e.

7 Y. Li, S. Zuo, Q. H. Li, X. Wu, J. Zhang, H. Zhang and J. Zhang, Vertically Aligned MoS_2 with In-Plane Selectively Cleaved Mo−S Bond for Hydrogen Production, *Nano Lett.*, 2021, **12**(4), 1848–1855, DOI: 10.1021/acs.nanolett.0c04978.

8 Q. Lu, Y. Yu, Q. Ma, B. Chen and H. Zhang, 2D Transition-Metal-Dichalcogenide-Nanosheet-Based Composites for Photocatalytic and Electrocatalytic Hydrogen Evolution Reactions, *Adv. Mater.*, 2016, **28**, 1917–1933, DOI: 10.1002/adma.201503270.

9 M. Pumera, Z. Sofer and A. Ambrosi, Layered Transition Metal Dichalcogenides for Electrochemical Energy Generation and Storage, *J. Mater. Chem. A*, 2014, **2**, 8981–8987, DOI: 10.1039/c4ta00652f.

10 X. Chia and M. Pumera, Characteristics and Performance of Two-Dimensional Materials for Electrocatalysis, *Nat. Catal.*, 2018, **1**, 909–921, DOI: 10.1038/s41929-018-0181-7.

11 C. Tan, X. Cao, X. J. Wu, Q. He, J. Yang, X. Zhang, J. Chen, W. Zhao, S. Han, G. H. Nam, M. Sindoro and H. Zhang, Recent Advances in Ultrathin Two-Dimensional Nanomaterials, *Chem. Rev.*, 2017, **117**(9), 6225–6331, DOI: 10.1021/acs.chemrev.6b00558.

12 Y. Yan, B. Xia, X. Ge, Z. Liu, J. Y. Wang and X. Wang, Ultrathin MoS_2 Nanoplates with Rich Active Sites as Highly Efficient Catalyst for Hydrogen Evolution, *ACS Appl. Mater. Interfaces*, 2013, **5**, 12794–12798, DOI: 10.1021/am404843b.

13 T. F. Jaramillo, K. P. Jørgensen, J. Bonde, J. H. Nielsen, S. Horch and I. Chorkendorff, Identification of Active Edge Sites for Electrochemical H_2 Evolution from MoS_2 Nanocatalysts, *Science*, 2007, **317**, 100–102, DOI: 10.1126/science.1141483.

14 G. Li, D. Zhang, Q. Qiao, Y. Yu, D. Peterson, A. Zafar, R. Kumar, S. Curtarolo, F. Hunte, S. Shannon, Y. Zhu, W. Yang and L. Cao, All the Catalytic Active Sites of MoS_2 for Hydrogen Evolution, *J. Am. Chem. Soc.*, 2016, **51**, 16632–16638, DOI: 10.1021/jacs.6b05940.

15 J. Xie, H. Zhang, S. Li, R. Wang, X. Sun, M. Zhou, J. Zhou, X. W. Lou and Y. Xie, Defect-Rich MoS_2 Ultrathin Nanosheets with Additional Active Edge Sites for Enhanced Electrocatalytic Hydrogen Evolution, *Adv. Mater.*, 2013, **25**, 5807–5813, DOI: 10.1002/adma.201302685.

16 J. Zhang, J. Wu, H. Guo, W. Chen, J. Yuan, U. Martinez, G. Gupta, A. Mohite, P. M. Ajayan and J. Lou, Unveiling Active Sites for the Hydrogen Evolution Reaction on Monolayer MoS_2, *Adv. Mater.*, 2017, **29**, 1701955, DOI: 10.1002/adma.201701955.

17 S. Balasubramanyam, M. Shirazi, M. A. Bloodgood, L. Wu, M. A. Verheijen, V. Vandalon, W. M. M. Kessels, J. P. Hofmann and A. A. Bol, Edge-Site Nanoengineering of WS_2 by Low-Temperature Plasma-Enhanced Atomic Layer Deposition for Electrocatalytic Hydrogen Evolution, *Chem. Mater.*, 2019, **31**, 5104–5115, DOI: 10.1021/acs.chemmater.9b01008.

18 Q. Zhu, W. Chen, H. Cheng, Z. Lu and H. Pan, WS_2 Nanosheets with Highly-Enhanced Electrochemical Activity by Facile Control of Sulfur Vacancies, *ChemCatChem*, 2019, **11**, 2667–2675, DOI: 10.1002/cctc.201900341.

19 L. Li, Z. Qin, L. Ries, S. Hong, T. Michel, J. Yang, C. Salameh, M. Bechelany, P. Miele, D. Kaplan, M. Chhowalla and D. Voiry, Role of Sulfur Vacancies and Undercoordinated Mo Regions in MoS_2 Nanosheets toward the Evolution of Hydrogen, *ACS Nano*, 2019, **13**, 6824–6834, DOI: 10.1021/acsnano.9b01583.

20 M. Naguib, O. Mashtalir, J. Carle, V. Presser, J. Lu, L. Hultman, Y. Gogotsi and M. W. Barsoum, Two-Dimensional Transition Metal Carbides, *ACS Nano*, 2012, **6**, 1322–1331, DOI: 10.1021/nn204153h.

21 Y. Gogotsi and B. Anasori, The Rise of MXenes, *ACS Nano*, 2019, **13**, 8491–8494, DOI: 10.1021/acsnano.9b06394.

22 B. Anasori, M. R. Lukatskaya and Y. Gogotsi, 2D Metal Carbides and Nitrides (MXenes) for Energy Storage, *Nat. Rev. Mater.*, 2017, **2**, 16098, DOI: 10.1038/natrevmats.2016.98.

23 M. Radovic and M. W. Barsoum, MAX Phases: Bridging the Gap between Metals and Ceramics, *Am. Ceram. Soc. Bull.*, 2013, **92**, 20.

24 M. Barsoum and T. El-Raghy, The MAX Phases: Unique New Carbide and Nitride Materials, *Am. Sci.*, 2001, **89**, 334–343, DOI: 10.1511/2001.28.736.

25 Z. M. Sun, Progress in Research and Development on MAX Phases: A Family of Layered Ternary Compounds, *Int. Mater. Rev.*, 2011, **3**, 143–166, DOI: 10.1179/1743280410Y.0000000001.

26 D. Sauceda, P. Singh, A. R. Falkowski, Y. Chen, T. Doung, G. Vazquez, M. Radovic and R. Arroyave, High-Throughput Reaction Engineering to Assess the Oxidation Stability of MAX Phases, *npj Comput. Mater.*, 2021, **7**, 6, DOI: 10.1038/s41524-020-00464-7.

27 E. Drouelle, V. Brunet, J. Cormier, P. Villechaise, P. Sallot, F. Naimi, F. Bernard and S. Dubois, Oxidation Resistance of Ti_3AlC_2 and $Ti_3Al_{0.8}Sn_{0.2}C_2$ MAX Phases: A Comparison, *J. Am. Ceram. Soc.*, 2020, **103**, 1270–1280, DOI: 10.1111/jace.16780.

28 M. Sokol, V. Natu, S. Kota and M. W. Barsoum, On the Chemical Diversity of the MAX Phases, *Trends Chem.*, 2019, **1**, 210–223, DOI: 10.1016/j.trechm.2019.02.016.

29 (*a*) K. P. A. Kumar, O. Alduhaish and M. Pumera, Electrocatalytic Activity of Layered MAX Phases for the Hydrogen Evolution Reaction, *Electrochem. Commun.*, 2021, **125**, 106977, DOI: 10.1016/j.elecom.2021.106977; (*b*) H. L. Chia, C. C. Mayorga-Martinez, N. Antonatos, Z. Sofer, J. J. Gonzalez-Julian, R. D. Webster and M. Pumera, MXene Titanium Carbide-based Biosensors: Strong Dependence of Exfoliation Method on Performance, *Anal. Chem.*, 2020, **92**(3), 2452–2459, DOI: 10.1021/acs.analchem.9b03634.

30 N. F. Rosli, M. Z. M. Nasir, N. Antonatos, Z. Sofer, A. Dash, J. Gonzalez-Julian, A. C. Fisher, R. D. Webster and M. Pumera, MAX and MAB Phases: Two-Dimensional Layered Carbide and Boride Nanomaterials for Electrochemical Applications, *ACS Appl. Nano Mater.*, 2019, **2**, 6010–6021, DOI: 10.1021/acsanm.9b01526.

31 N. L. Ritzert, V. A. Szalai and T. P. Moffat, Mapping Electron Transfer at MoS_2 Using Scanning Electrochemical Microscopy, *Langmuir*, 2018, **34**, 13864–13870, DOI: 10.1021/acs.langmuir.8b02731.

32 H. S. Ahn and A. J. Bard, Electrochemical Surface Interrogation of a MoS_2 Hydrogen-Evolving Catalyst: In Situ Determination of the Surface Hydride Coverage and the Hydrogen Evolution Kinetics, *J. Phys. Chem. Lett.*, 2016, **7**, 2749–2752, DOI: 10.1021/acs.jpclett.6b01276.

33 S. Kumar, P. K. Sahoo and A. K. Satpati, Electrochemical and SECM Investigation of MoS_2/GO and MoS_2/RGO Nanocomposite Materials for HER Electrocatalysis, *ACS Omega*, 2017, **2**, 7532–7545, DOI: 10.1021/acsomega.7b00678.

34 A. Preet and T. E. Lin, A Review: Scanning Electrochemical Microscopy (Secm) for Visualizing the Real-Time Local Catalytic Activity, *Catalysts*, 2021, **11**, 594, DOI: 10.3390/catal11050594.

35 Y. Takahashi, Y. Kobayashi, Z. Wang, Y. Ito, M. Ota, H. Ida, A. Kumatani, K. Miyazawa, T. Fujita, H. Shiku, Y. E. Korchev, Y. Miyata, T. Fukuma, M. Chen and T. Matsue, High-Resolution Electrochemical Mapping of the Hydrogen Evolution Reaction on Transition-Metal Dichalcogenide Nanosheets, *Angew. Chem., Int. Ed.*, 2020, **59**, 3601–3608, DOI: 10.1002/anie.201912863.

36 H. Li, M. Du, M. J. Mleczko, A. L. Koh, Y. Nishi, E. Pop, A. J. Bard and X. Zheng, Kinetic Study of Hydrogen Evolution Reaction over Strained MoS_2 with Sulfur Vacancies Using Scanning Electrochemical Microscopy, *J. Am. Chem. Soc.*, 2016, **138**, 5123–5129, DOI: 10.1021/jacs.6b01377.

37 K. Jaouen, O. Henrotte, S. Campidelli, B. Jousselme, V. Derycke and R. Cornut, Localized Electrochemistry for the Investigation and the Modification of 2D Materials, *Appl. Mater. Today*, 2017, **8**, 116–124, DOI: 10.1016/j.apmt.2017.05.001.

38 C. Iffelsberger, S. Ng and M. Pumera, Catalyst Coating of 3D Printed Structures via Electrochemical Deposition: Case of the Transition Metal Chalcogenide MoS_x for Hydrogen Evolution Reaction, *Appl. Mater. Today*, 2020, **20**, 100654, DOI: 10.1016/j.apmt.2020.100654.

39 K. A. Novčić, C. Iffelsberger, S. Ng and M. Pumera, Local Electrochemical Activity of Transition Metal Dichalcogenides and Their Heterojunctions on 3D-Printed Nanocarbon Surfaces, *Nanoscale*, 2021, **13**, 5324–5332, DOI: 10.1039/d0nr06679f.

40 F. Podjaski, D. Weber, S. Zhang, L. Diehl, R. Eger, V. Duppel, E. Alarcón-Lladó, G. Richter, F. Haase, A. Fontcuberta i Morral, C. Scheu and B. V. Lotsch, Rational Strain Engineering in Delafossite Oxides for Highly Efficient Hydrogen Evolution Catalysis in Acidic Media, *Nat. Catal.*, 2020, **3**, 55–63, DOI: 10.1038/s41929-019-0400-x.

41 S. Xin, Z. Liu, L. Ma, Y. Sun, C. Xiao, F. Li and Y. Du, Visualization of the Electrocatalytic Activity of Three-Dimensional $MoSe_2$@reduced Graphene Oxide Hybrid Nanostructures for Oxygen Reduction Reaction, *Nano Res.*, 2016, **9**, 3795–3811, DOI: 10.1007/s12274-016-1249-9.

42 P. Hanekamp, T. Raith, C. Iffelsberger, T. Zankl, W. Robl and F. M. Matysik, Material Contrast Studies of Conductive Thin Films on Semiconductor Substrates Using Scanning Electrochemical Microscopy, *J. Appl. Electrochem.*, 2019, **49**, 455–463, DOI: 10.1007/s10800-019-01294-2.

43 Y. Yu, T. Sun and M. V. Mirkin, Scanning Electrochemical Microscopy of Single Spherical Nanoparticles: Theory and Particle Size Evaluation, *Anal. Chem.*, 2015, **87**, 7446–7453, DOI: 10.1021/acs.analchem.5b01690.

44 J. H. Bae, Y. Yu and M. V. Mirkin, Scanning Electrochemical Microscopy Study of Electron-Transfer Kinetics and Catalysis at Nanoporous Electrodes, *J. Phys. Chem. C*, 2016, **120**, 20651–20658, DOI: 10.1021/acs.jpcc.6b01620.

45 A. Djire, X. Wang, C. Xiao, O. C. Nwamba, M. V. Mirkin and N. R. Neale, Basal Plane Hydrogen Evolution Activity from Mixed Metal Nitride MXenes Measured by Scanning Electrochemical Microscopy, *Adv. Funct. Mater.*, 2020, **30**, 2001136, DOI: 10.1002/adfm.202001136.

46 B. Tao, L. C. Yule, E. Daviddi, C. L. Bentley and P. R. Unwin, Correlative Electrochemical Microscopy of Li-Ion (De) Intercalation at a Series of Individual $LiMn_2O_4$ Particles,

Angew. Chem., Int. Ed., 2019, **14**, 4606–4611, DOI: 10.1002/anie.201814505.

47 D. M. Rissin, H. H. Gorris and D. R. Walt, Distinct and Long-Lived Activity States of Single Enzyme Molecules, *J. Am. Chem. Soc.*, 2008, **130**, 5349–5353, DOI: 10.1021/ja711414f.

48 Q. Xue and E. S. Yeung, Differences in the Chemical Reactivity of Individual Molecules of an Enzyme, *Nature*, 1995, **373**, 681–683, DOI: 10.1038/373681a0.

49 B. P. English, W. Min, A. M. Van Oijen, T. L. Kang, G. Luo, H. Sun, B. J. Cherayil, S. C. Kou and X. S. Xie, Ever-Fluctuating Single Enzyme Molecules: Michaelis-Menten Equation Revisited, *Nat. Chem. Biol.*, 2006, **2**, 87–94, DOI: 10.1038/nchembio759.

50 W. Min, I. V. Gopich, B. P. English, S. C. Kou, X. S. Xie and A. Szabo, When Does the Michaelis-Menten Equation Hold for Fluctuating Enzymes?, *J. Phys. Chem. B*, 2006, **110**, 20093–20097, DOI: 10.1021/jp065187g.

51 Y. Niu, S. Fu, K. Zhang, B. Dai, H. Zhang, S. Grasso and C. Hu, Synthesis, Microstructure, and Properties of High Purity Mo_2TiAlC_2 Ceramics Fabricated by Spark Plasma Sintering, *J. Adv. Ceram.*, 2020, **9**(6), 759–768, DOI: 10.1007/s40145-020-0412-7.

52 B. Anasori, M. Dahlqvist, J. Halim, E. J. Moon, J. Lu, B. C. Hosler, E. N. Caspi, S. J. May, L. Hultman, P. Eklund, J. Rosén and M. W. Barsoum, Experimental and Theoretical Characterization of Ordered MAX Phases Mo_2TiAlC_2 and $Mo_2Ti_2AlC_3$, *J. Appl. Phys.*, 2015, **118**, 094304, DOI: 10.1063/1.4929640.

53 L. Tang, X. Meng, D. Deng and X. Bao, Confinement Catalysis with 2D Materials for Energy Conversion, *Adv. Mater.*, 2019, **31**, 1901996, DOI: 10.1002/adma.201901996.

54 D. Polcari, P. Dauphin-Ducharme and J. Mauzeroll, Scanning Electrochemical Microscopy: A Comprehensive Review of Experimental Parameters from 1989 to 2015, *Chem. Rev.*, 2016, **116**, 13234–13278, DOI: 10.1021/acs.chemrev.6b00067.

55 J. Molina, J. Fernández and F. Cases, Scanning Electrochemical Microscopy for the Analysis and Patterning of Graphene Materials: A Review, *Synth. Met.*, 2016, **222**, 145–161, DOI: 10.1016/j.synthmet.2016.10.019.

56 R. D. Martin and P. R. Unwin, Theory and Experiment for the Substrate Generation/Tip Collection Mode of the Scanning Electrochemical Microscope: Application as an Approach for Measuring the Diffusion Coefficient Ratio of a Redox Couple, *Anal. Chem.*, 1998, **70**, 276–284, DOI: 10.1021/ac970681p.

57 U. M. Tefashe, M. E. Snowden, P. D. Ducharme, M. Danaie, G. A. Botton and J. Mauzeroll, Local Flux of Hydrogen from Magnesium Alloy Corrosion Investigated by Scanning Electrochemical Microscopy, *J. Electroanal. Chem.*, 2014, **720–721**, 121–127, DOI: 10.1016/j.jelechem.2014.03.002.

58 J. L. Amphlett and G. Denuault, Scanning Electrochemical Microscopy (SECM): An Investigation of the Effects of Tip Geometry on Amperometric Tip Response, *J. Phys. Chem. B*, 1998, **49**, 9946–9951, DOI: 10.1021/jp982829u.

59 R. Cornut and C. Lefrou, A Unified New Analytical Approximation for Negative Feedback Currents with a Microdisk SECM Tip, *J. Electroanal. Chem.*, 2007, **1**, 59–66, DOI: 10.1016/j.jelechem.2007.05.007.

60 H. Kim, J. Choi, B. Chae and G. Kim, CLSM [Confocal Laser Scanning Microscope] Observation of the Surface Roughness of Pressurized Rock Samples During Freeze/Thaw Cycling, *J. Eng. Geol.*, 2015, **25**, 165–178, DOI: 10.9720/kseg.2015.2.165.

61 Y. Hou, L. Yu, W. Xie, L. C. Camacho, M. Zhang, Z. Chu, Q. Wei and R. Haag, Surface Roughness and Substrate Stiffness Synergize to Drive Cellular Mechanoresponse, *Nano Lett.*, 2020, **20**, 748–757, DOI: 10.1021/acs.nanolett.9b04761.

62 X. Teng, F. Li and C. Lu, Visualization of Materials Using the Confocal Laser Scanning Microscopy Technique, *Chem. Soc. Rev.*, 2020, **49**, 2408–2425, DOI: 10.1039/c8cs00061a.

63 R. Van de Krol and M. Gratzel, Electronic Materials: Science & Technology, in *Photoelectrochemical Hydrogen Production*, 2012, DOI: 10.1007/978-1-4614-1380-6.

64 A. J. Bard and M. V. Mirkin, *Scanning Electrochemical Microscopy*, 2nd edn, 2001, DOI: 10.1201/9780203910771.

Chapter 10. Solvent Effects on the Electrochemical Activity of $Ti_3C_2T_x$ MXenes

Published paper included in this chapter:

K. A. Novčić, C. Iffelesberger, M. Palacios Corella, and M. Pumera, *Solvents dramatically influence the atomic composition and catalytic properties of $Ti_3C_2T_x$ MXenes*, **Journal of Material Chemistry A (2023)**, 11, 13419-13431, DOI: 10.1039/D3TA01441J.

10.1. Motivation for the Study

The electrochemical study of powder-based samples, such as MXenes, usually requires special electrode preparation, i.e., drop-casting of the powder dispersed in the solvent media. Moreover, the solvents used in the sample preparation can affect the macroscopic HER performance of the prepared MXene samples. Therefore, in this paper, the effects on the electrochemical performance, surface chemistry, and roughness of MXenes of four different solvents (water, ethanol, isopropanol, and dimethylformamide (DMF)) used in the preparation of the MXenes are investigated.

10.2. Paper Conclusion

This study demonstrates different solvent effects on the electrochemical activity of the $Ti_3C_2T_x$ MXene for hydrogen evolution reaction. It shows that the choice of solvent media used in the MXene sample preparation plays a vital role in the electrochemical activity, stability and long-term usage of MXenes. Among the investigated solvents, the long-term stability was the most promising when isopropanol and ethanol were used to make MXene suspensions. In contrast, water and DMF solvents caused MXene oxidation and changes in the elemental composition. The obtained results broadly impact on the choice of solvent media used in the sample preparation of MXenes, especially when comparing the electrochemical activity of the same

type of MXenes prepared from different solvents. This paper gives an insight into the long-term storage of MXenes, which is crucial in their energy conversion application.

10.3. Student Contribution

The student is the first author of this paper who contributed to the paper by performing the samples` preparation, optical characterization and elemental composition analysis of the samples, with their electrochemical characterization. The student interpreted the data and wrote the manuscript.

Journal of Materials Chemistry A

ROYAL SOCIETY OF CHEMISTRY

PAPER

View Article Online
View Journal | View Issue

Cite this: *J. Mater. Chem. A*, 2023, **11**, 13419

Solvents dramatically influence the atomic composition and catalytic properties of $Ti_3C_2T_x$ MXenes†

Katarina A. Novčić, [a] Christian Iffelsberger, [a] Mario Palacios-Corella [a] and Martin Pumera *[abc]

Received 8th March 2023
Accepted 10th April 2023

DOI: 10.1039/d3ta01441j

rsc.li/materials-a

A fast-growing family of two-dimensional materials, MXenes, has drawn much attention due to their excellent catalytic properties and wide range of applications. One of the most common ways to work with powder-based materials, such as $Ti_3C_2T_x$ MXenes, consists in the dispersion of the catalytic materials in various solvents followed by drop-casting of the prepared suspensions onto desired surfaces. However, the solvent employed to prepare the powder dispersions can have noticeable effects on the electrochemical performance of the drop-cast samples. Herein, four different solvents (water, ethanol, isopropanol, and *N*,*N*′-dimethylformamide), used as dispersion media in the preparation of the $Ti_3C_2T_x$ MXene samples, and their effects on the electrocatalytic activity of $Ti_3C_2T_x$ MXenes towards the hydrogen evolution reaction (HER) were studied by linear sweep voltammetry. As shown in this work, the different solvents provoke changes in the roughness and dispersibility of the material, as well as a partial oxidation of the $Ti_3C_2T_x$ microparticles which leads to dissimilar surface coverages, resulting in different overpotential values for the catalytic HER. The findings of this research are of crucial importance for knowledge about the electrocatalytic performance of MXene samples, and their storage and long-term usage.

Introduction

Hydrogen has been proposed as a clean and promising energy carrier that supports the development of renewable energy sources in order to overcome the global warming crisis. Therefore, the focus is on the generation of "green" hydrogen *via* the electrolysis of water. As a one-half reaction in the water-splitting process, the hydrogen evolution reaction (HER) is considered a promising approach for clean hydrogen production.[1–3] Platinum-based electrocatalysts are found to be the most efficient for the HER.[4–7] However, their scarcity and high cost represent the biggest obstacles in their large-scale use. Thus, developing non-noble metal-based catalysts for the HER has attracted a lot of attention.

Two dimensional (2D) materials have been widely studied as promising catalytic materials in energy conversion application. Among them, transition metal phosphides (especially bimetallic phosphides)[8,9] and transition metal dichalcogenides (TMDs)[10] have received great attention due to their catalytic properties and enhanced activity towards the HER.

Recent development in 2D materials gave rise to the family of MXenes, a large group of ternary transition metal carbides and nitrides with the general formula of $M_{n+1}X_nT_x$, where M represents an early transition metal (such as Sc, Ti, Zr, V, Nb, Mo or Cr), X is carbon and/or nitrogen, and T_x stands for the surface termination (*e.g.*, oxygen, hydroxyl, or fluorine). Mxenes are synthesized by selective etching of certain atomic layers from their MAX phase precursors.[11–15] The distinctive properties of MXenes include high electrical conductivity,[16] electrochemical activity,[17,18] high-temperature stability,[19] optical properties,[20–22] and unique layered structure with rich chemistry. Moreover, due to their excellent mechanical properties with metallic conductivity and chemical stability,[23] MXenes can be blended with polymers to improve the conductivity and mechanical properties of polymers in energy-related applications.[18,24,25] Their hydrophilic nature[26] allows their dispersion in different solvents, and thus, MXenes can be applied on the substrate or used as conductive inks.[27] Additionally, they have been studied as catalysts in energy storage and conversion processes,[18–22] and found application as chemical sensors, electromagnetic interference shielding and biomedicine.[27–40] In contrast to other widely studied 2D materials, such as TMDs (*e.g.*, MoS_2 and WS_2), featuring catalytically active edges for the HER,[41–47] MXenes are

[a]*Future Energy and Innovation Laboratory, Central European Institute of Technology, Brno University of Technology, Purkyňova 656/123, 61200 Brno, Czech Republic. E-mail: pumera.research@gmail.com*

[b]*Faculty of Electrical Engineering and Computer Science, VSB – Technical University of Ostrava, 17. listopadu 2172/15, 70800 Ostrava, Czech Republic*

[c]*Department of Medical Research, China Medical University Hospital, China Medical University, No. 91 Hsueh-Shih Road, Taichung 40402, Taiwan*

† Electronic supplementary information (ESI) available. See DOI: https://doi.org/10.1039/d3ta01441j

reported to have a catalytically active basal plane.[17,48,49] A study by Djire *et al.*[50] demonstrated the basal plane of a single M–$Ti_4N_3T_x$ MXene nanoflake to be strongly active compared to the edge side due to the largely exposed metallic sites for proton adsorption, thus providing experimental evidence of the catalytic activity of the MXene basal plane.

Recent studies that focused on MXene synthesis have reported the high importance of their surface termination (T_x) regarding their tuning properties and, hence, their application in energy conversion and storage.[14,17,48,51] Density functional theory (DFT) calculations of the MXenes predict a strong influence of the surface termination type on MXenes' work function and electronic band.[52] Moreover, the surface termination depends on the etching and delamination conditions during MXene synthesis, the type of M element in the MXene structure, and their post-synthesis treatments.[16,53]

As a part of their post-synthesis treatment, the utilization of powder-based materials, like MXenes, for catalytic purposes including electrocatalysis, typically involves dispersing MXene powder in solvent media and then applying the suspension on the desired surface. These techniques include spray-coating, drop-casting, dip-coating, or other deposition techniques among which drop-casting has been widely used.[54–59]

The influence of different solvents used in the preparation of particle-based samples can alter the distribution of the drop-cast particles, thus affecting the electrochemical activity of the samples. For example, the effects of different solvents on surface termination were previously reported for carbon nanotubes, $MoSe_2$, and MoS_2, where the impact of dispersion media used in film preparation on their catalytic performance for the HER and oxygen evolution reaction (OER) was demonstrated.[60–62] Moreover, the solvent media can have a different effect on the ageing of the particle-based suspensions and changes in the chemical composition of the dispersed particles over time. This additionally affects the surface termination of the drop-cast particles and can tune their electrochemical activity. Due to the fact that the polar surface of MXenes allows their dispersion in different solvent media,[63] it is of crucial importance to investigate the influence of the solvents used in the preparation of MXene suspensions on their HER performance. Recent studies demonstrated water,[64] ethanol,[40] isopropanol[40] and DMF[56] to be commonly used in the MXene post-synthesis treatment due to their low cost and affordability. Therefore, this study aims to investigate the electrochemical activity of MXenes treated with different solvents over time.

Herein, four different and commonly used solvent media (water, ethanol, isopropanol and *N*,*N*′-dimethylformamide) were employed in the preparation of fresh and one-month-old (aged) $Ti_3C_2T_x$ MXene suspensions. The HER electrochemical performance of the fresh and aged drop-cast $Ti_3C_2T_x$ MXene samples was studied. The electrochemical characterization of the samples was performed by linear sweep voltammetry (LSV) while analysis of their morphology and elemental composition was performed by scanning electron microscopy (SEM), energy-dispersive X-ray spectroscopy (EDS), and X-ray photoelectron spectroscopy (XPS). Additionally, the surface roughness analysis of the MXene samples was performed by confocal laser scanning microscopy (CLSM). This study reveals the importance of the solvent effects in surface coverage and elemental composition of the MXenes, which is relevant to their electrochemical performance. The results obtained in this study are of crucial importance for general knowledge about the catalysts prepared using the solvent-based method, the choice of the used solvents as well as an understanding of their surface chemistry.

Experimental section

Chemicals and solutions

MXene dispersions were prepared from $Ti_3C_2T_x$ powder (Y-carbon, Ukraine). *N*,*N*′-dimethylformamide, DMF (99.9%, analytical grade), ethanol, EtOH (96%, analytical grade), and sulfuric acid (H_2SO_4, 96%, analytical grade), which were purchased from Penta, Czech Republic. Isopropanol, IPA (2-propanol, 99.9%, analytical grade) and titanium(IV) oxide (TiO_2, rutile) powder were purchased from Sigma-Aldrich, Germany. Deionized water with a resistivity greater than 18 MΩ cm was used for the preparation of the 0.5 M H_2SO_4 solution and water-based MXene suspension.

Preparation of the $Ti_3C_2T_x$ MXene samples

For the preparation of the $Ti_3C_2T_x$ MXene suspensions, 5 mg of $Ti_3C_2T_x$ MXene powder was separately dispersed in 1 mL of water, EtOH, IPA and DMF, respectively. The mixtures were then sonicated for 30 min and well shaken to ensure the obtention of homogenous suspensions, as illustrated in Scheme 1A. Following this, immediately after mixing, 5 μL of the freshly prepared suspension were taken and drop-cast separately onto a glassy carbon electrode (GCE) (electrode radius: 1.5 mm), as shown in Scheme 1B. Prior to this, the GCE was polished with 0.05 μm Al_2O_3 particles on a polishing pad and rinsed with ultrapure water. After that, the samples were dried at room temperature and the freshly prepared $Ti_3C_2T_x$ MXene samples (with final MXene loading ~1.11 mg cm^{-2}) were ready for electrochemical characterization. For the control experiments, an aqueous dispersion of TiO_2 with the same concentrations employed for MXenes was prepared and sonicated for 30 min, and finally 5 μL of the dispersion was drop-cast on the GCE, followed by drying. To understand the effect of ageing on the MXenes' properties, the as-prepared suspensions were kept in closed glass vials at room temperature for one month. After that, the suspensions were shaken and 5 μL of each was drop-cast onto the polished GCEs. After drying, the $Ti_3C_2T_x$ MXene samples were ready for electrochemical characterization (Scheme 1C).

Electrochemical characterization of $Ti_3C_2T_x$ MXene samples

Electrochemical characterization of the prepared MXene samples was performed by linear sweep voltammetry (LSV) using a potentiostat (Autolab, Metrohm, The Netherlands), and controlled by Nova 2.1 software. The measurements were performed in 0.5 M H_2SO_4, with a scan rate of 5 mV s^{-1} starting from 0.2 V with a Ag/AgCl 1 M KCl reference electrode and graphite counter electrode.

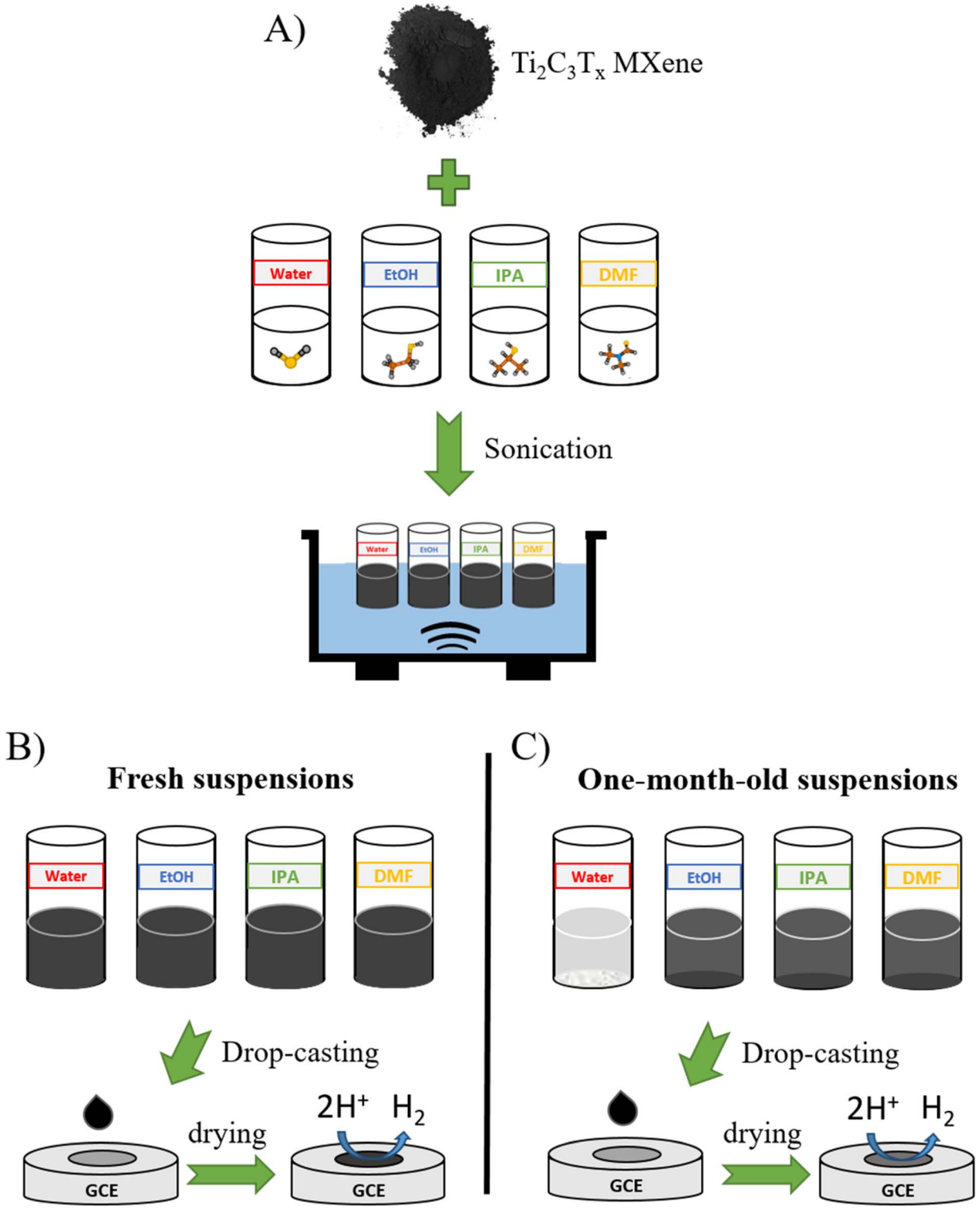

Scheme 1 (A) Schematic illustration of $Ti_3C_2T_x$ MXene treatment using water, EtOH, IPA, and DMF solvents. The $Ti_3C_2T_x$ MXene samples are prepared from (B) fresh and (C) one-month-old (aged) suspensions on glassy carbon electrode (GCE) surfaces *via* drop-casting.

Unless stated otherwise, all potentials were converted and reported according to the literature.[65] The Tafel slopes were calculated from the obtained LSV measurements.

Materials characterization of $Ti_3C_2T_x$ MXene samples

The morphology of the MXene samples was examined by using a Mira3 XMU SEM (Tescan, Czech Republic) with an electron accelerating voltage of 5 kV. Elemental mapping and EDS

spectra were obtained with an EDX detector (Oxford Instruments X-MAX[20]) integrated into the Mira3 XMU with an accelerating voltage of 20 kV. The MXene samples were prepared on a Si wafer attached to the SEM specimen holder. The chemical composition analysis of the MXene powder and films was performed by XPS (Kratos, AXIS Supra, Manchester, UK) using a monochromatic Al Kα (1486.7 eV) excitation source. The XPS spectra were calibrated against the carbon 1s signal at 284.8 eV. Casa XPS software and Origin Pro 2019 were used for data fitting and plotting. Optical characterization of the sample was performed by confocal laser scanning microscopy (CLSM) (Olympus LEXT-OLS 4100) with 20× lenses.

Results and discussion

Catalytic properties of $Ti_3C_2T_x$ MXene samples dispersed in various solvents, such as water, ethanol (EtOH), isopropanol (IPA), and *N*,*N*′-dimethylformamide (DMF) from fresh and one-month-old (aged) suspensions on glassy carbon surfaces were investigated by linear sweep voltammetry (LSV). A relationship between changes in the electrochemical properties of the MXenes exposed to the solvents and their morphology and elemental composition is made through a side-by-side comparison using scanning electron microscopy (SEM) and confocal laser scanning microscopy (CLSM), as well as energy dispersive X-ray spectroscopy (EDS) and X-ray photoelectron spectroscopy (XPS) analysis.

First, the electrochemical performance for the HER of the $Ti_3C_2T_x$ MXene samples prepared from fresh suspensions was tested as shown in Fig. 1A–D. For easier identification, MXene samples were named after the solvent used in the suspension, *i.e.*, MXene–water, MXene–EtOH, MXene–IPA, and MXene–DMF. The overpotential values obtained at a current density of -10 mA cm^{-2} of the fresh MXene samples range from -0.64 V (MXene–DMF) to -0.72 V (MXene–EtOH) and are summarized in the bar chart in Fig. 1E. Moreover, a TiO_2 film served as a reference due to the known tendency of $Ti_3C_2T_x$ MXenes to oxidize and form TiO_2.[64,66,67] Interestingly, the overpotential values obtained for the MXene samples are comparable with those of the widely investigated TMDs, such as bulk WS_2.[68,69] Additionally, it is worth mentioning that the effect of pure solvents drop-cast on the glassy carbon electrode (GCE) without any material support (*i.e.*, bare electrodes) was also investigated by LSV, as shown in Fig. S1 in the ESI.† This figure reveals negligible differences in the overpotential values between the bare electrodes and demonstrates no interactions between the GCE substrate and investigated solvents. Compared to the electrochemical performance of the bare electrodes, an overpotential shift in the electrochemical activity of the MXene samples was observed, ranging from 80 mV (MXene–EtOH) to 140 mV (MXene–water and MXene–DMF).

The influence of sample ageing of MXenes on their electrocatalytic performance was investigated using the common practice of suspending MXene powder in a solvent as a stock solution. After one month, the electrochemical performance of the MXene samples prepared from aged suspensions was studied. The dashed lines in Fig. 1A–D represent the measurements carried out on MXene–water-old, MXene–EtOH-old, MXene–IPA-old, and MXene–DMF-old samples. The obtained overpotential values for the MXene-old samples were found to be in a range from -0.79 V (MXene–EtOH-old) to more than -0.93 V (MXene–water-old), as shown in Fig. 1E (dashed bars). Following that, a side-by-side comparison between the fresh and aged MXene samples led to the conclusion that the overpotential shift gradually decreased following the trend water- > DMF- > IPA- > EtOH-based MXene samples.

Subsequently, Tafel analysis of the investigated MXene samples was carried out and the obtained Tafel plots are presented in Fig. S2 in the ESI.† The calculated Tafel slope values are summarized in the bar chart in Fig. 1F. According to the Tafel slope analysis, which provides insight into the rate-limiting step in the HER mechanism,[70,71] the reaction starts with protons being reduced and adsorbed on the catalyst surface (Volmer step) (i), followed by recombination of the adsorbed hydrogen atoms (Tafel step) (ii) or by electrochemical hydrogen desorption (Heyrovský step) (iii). The HER mechanism in the acid media can be described as:

$$\text{(i) } H^+ + e^- + (*) \rightarrow H(ads)$$

$$\text{(ii) } H(ads) + H(ads) \rightarrow H_2 + 2(*)$$

$$\text{(iii) } H^+ + H(ads) + e^- \rightarrow H_2 + (*)$$

The (*) refers to the active site on the catalytic surface.

Tafel slopes above 120 mV dec^{-1} are found for all investigated MXene samples, indicating that the Volmer step is the rate-determining step in the HER mechanism.[56] Variations in the Tafel slope values between the MXene samples prepared from fresh and aged suspensions are found to be in a range from 31 mV dec^{-1} (IPA) to 75 mV dec^{-1} (DMF), which follows the changes in their overpotentials.

Following that, the morphological changes in the drop-cast $Ti_3C_2T_x$ MXene microparticles were studied by scanning electron microscopy (SEM), and the obtained micrographs are presented in Fig. 2. The low-magnification SEM images obtained from the fresh MXene samples pointed to the influence of solvents on the $Ti_3C_2T_x$ MXene microparticle distribution as shown in Fig. 2A. This figure showed that the distribution of the microparticles over the GCE substrate depends on the type of solvent used in suspension preparation and its boiling temperature. Some of the main properties of the investigated solvent media are summarized in Table S1 in the ESI†. Solvents with a higher boiling point show a much more even distribution of the material on the surface as compared to volatile solvents.[54,62] Therefore, the drying effect has a similar impact on the MXene–EtOH and MXene–IPA samples, which showed a uniform but clustered distribution of microparticles. The slower drying rate of DMF and water allows the material to settle slowly on the substrate with the closely packed particles.[54] This additionally provides more homogeneous coverage of the electrode surface and thus, can affect

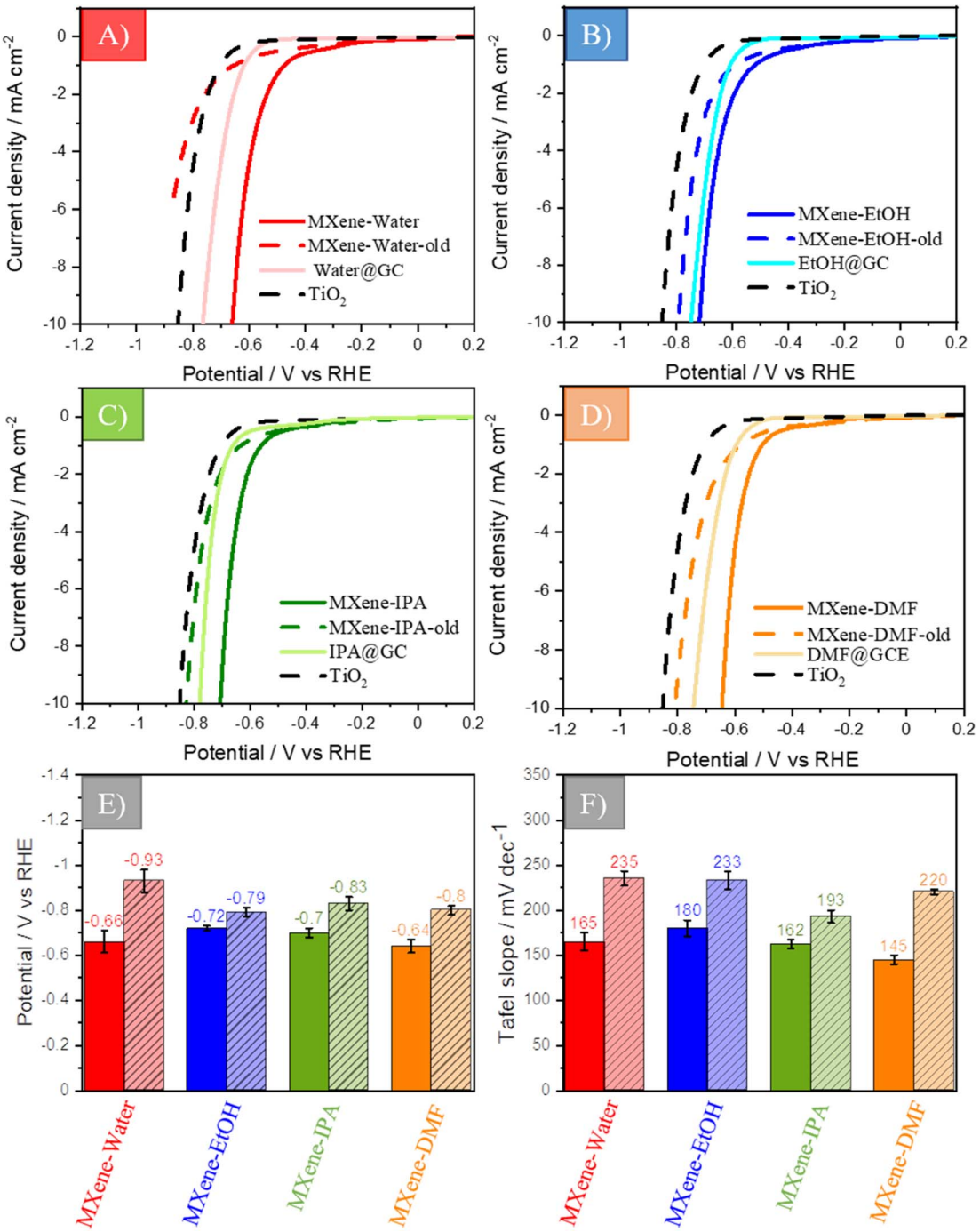

Fig. 1 Electrochemical characterization of the $Ti_3C_2T_x$ MXene samples. Linear sweep voltammograms for $Ti_3C_2T_x$ MXenes prepared from (A) water, (B) EtOH, (C) IPA, and (D) DMF suspensions, respectively. The bare electrode (solvents drop-cast on the GCE without any material support) and TiO_2 sample (dashed black line) served as the reference. (E) Bar chart showing the summarized overpotential values obtained at a current density of -10 mA cm^{-2} for the MXenes prepared from fresh and aged (dashed bars) suspensions. (F) Bar chart showing the corresponding Tafel slope values of the MXene samples. Measurements were performed in 0.5 M H_2SO_4 with a scan rate of 5 mV s^{-1}.

the HER measurements (Fig. 1) since smaller particles give rise to a bigger surface area. A similar drying effect is also reported on the MoS_2 catalytic particles when the same solvents are used for material dispersion.[62]

Additionally, the morphology of the investigated MXene samples treated from fresh and aged suspensions was examined at high magnification as shown in the SEM micrographs in Fig. 2B and C, respectively, finding the $Ti_3C_2T_x$ microparticles with a size of 5–10 μm. The SEM micrographs of the $Ti_3C_2T_x$ MXene microparticles obtained from the fresh suspensions (Fig. 2B) show insignificant morphological differences between them. However, the SEM images of the

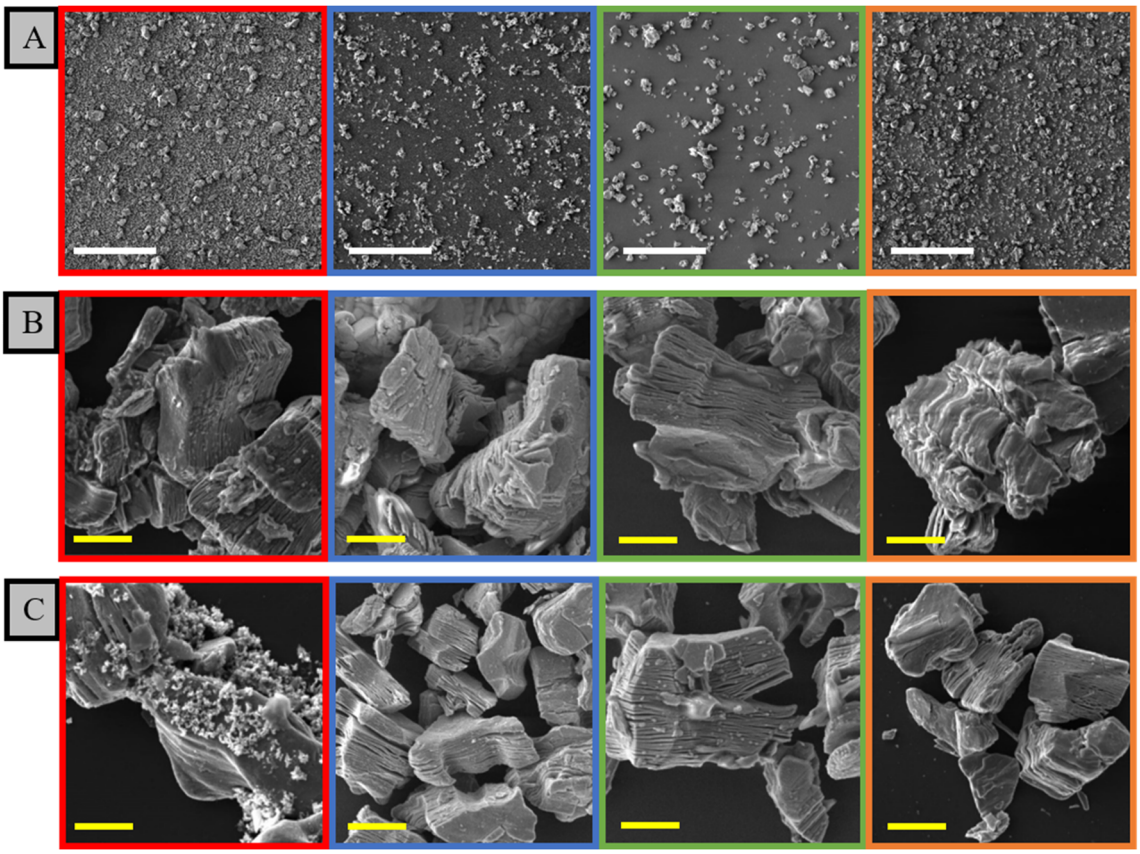

Fig. 2 Scanning electron micrographs of the $Ti_3C_2T_x$ MXene samples prepared from water (red), EtOH (blue), IPA (green), and DMF (orange) suspensions. (A) SEM micrograph of the wide area of the MXene samples; the scale is 100 μm. MXene samples prepared from the (B) fresh and (C) aged suspensions. The scale in micrographs (B) and (C) is 5 μm.

$Ti_3C_2T_x$ MXene microparticles captured from the aged suspensions (Fig. 2C) reveal clear changes in the surface morphology of the MXene–water-old $Ti_3C_2T_x$ microparticles. This is caused by the degradation of the original $Ti_3C_2T_x$ microparticles and it is followed by the formation of new and smaller particles. On the other hand, the $Ti_3C_2T_x$ MXene microparticles suspended in DMF, EtOH, or IPA for a month did not show any remarkable changes in compared with the $Ti_3C_2T_x$ microparticles prepared from fresh suspensions.

Subsequently, the differences in the surface roughness of the $Ti_3C_2T_x$ MXene samples caused by variation in their particle distribution over the GCE substrate were examined optically by confocal laser scanning microscopy (CLSM), as shown in Fig. 3. The color CLSM images of the MXene–EtOH and MXene–IPA samples shown in Fig. 3B and C, respectively, pointed to the random distribution of the $Ti_3C_2T_x$ microparticles over the GCE substrate, showing a similar pattern in particle distribution as visible in the SEM images in Fig. 2A. However, the color CLSM images of the MXene–water and MXene–DMF samples (Fig. 3A and D, respectively) showed uniform coverage of the substrate with closely packed $Ti_3C_2T_x$ microparticles. The CLSM height images of the $Ti_3C_2T_x$ MXene samples presented in Fig. 3a–d showed negligible differences in the particle height and thus, a similar thickness of the drop-cast material over the GCE substrate.

Following this, in order to study the surface roughness of the MXene samples, the $Ti_3C_2T_x$ MXene surfaces were observed using 20× lenses, which allowed the measurement of the surface roughness on a micron scale along the 8 cross-sectional lines: 4 horizontal and 4 vertical[72] as shown in Fig. S3 in the ESI.† The roughness factor R_g (root mean square of the roughness profile) was calculated along the indicated cross-sectional lines, and the calculated average values were found to be 5.39 and 6.21 for MXene–water and MXene–DMF samples, respectively, while this value was lower (4.18 and 3.18) for MXene–EtOH and MXene–IPA samples, respectively. The observed differences in the surface roughness of the investigated $Ti_3C_2T_x$ MXene samples caused the differences in their electrochemical performance and could be responsible for the small overpotential shift measured between the fresh MXene samples, as shown in Fig. 1.

Subsequently, the elemental composition analysis of the investigated MXene samples was performed by energy-dispersive X-ray spectroscopy (EDS) in order to get better insight into the effects of the solvents on the changes in the $Ti_3C_2T_x$ microparticle composition. The EDS maps of the $Ti_3C_2T_x$ MXene microparticles (Fig. S4 in the ESI†) showed the uniform distribution of Ti, C, and O over the MXene samples.

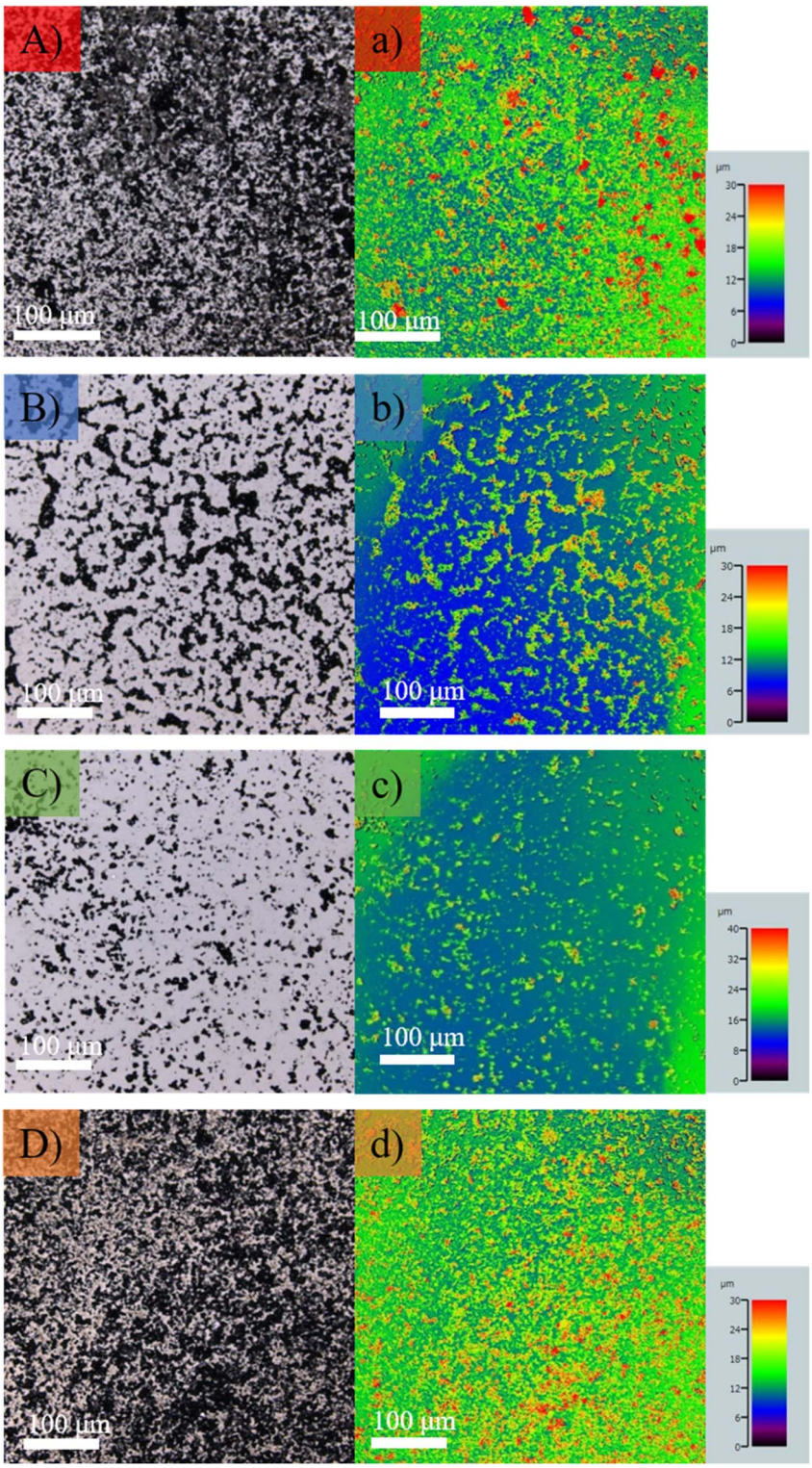

Fig. 3 Optical characterization of the $Ti_3C_2T_x$ MXene samples performed by confocal laser scanning microscopy (CLSM). (A–D) Color CLSM images and (a–d) corresponding false-color CLSM images showing the height of the $Ti_3C_2T_x$ MXene microparticles obtained with 20× lenses. MXene samples were prepared from fresh water (red), EtOH (blue), IPA (green), and DMF (orange) suspensions.

The corresponding EDS spectra (Fig. 4) further confirmed the presence of all constructed elements (Ti, C, O, and F) on the $Ti_3C_2T_x$ MXene samples, and their atomic percentages are represented in Table S2 in the ESI.†

Moreover, a side-by-side comparison of the MXene samples prepared from fresh and aged suspensions allows the identification of the different levels of MXene microparticle oxidation, as measured by using the Ti : O ratio. In general, MXene

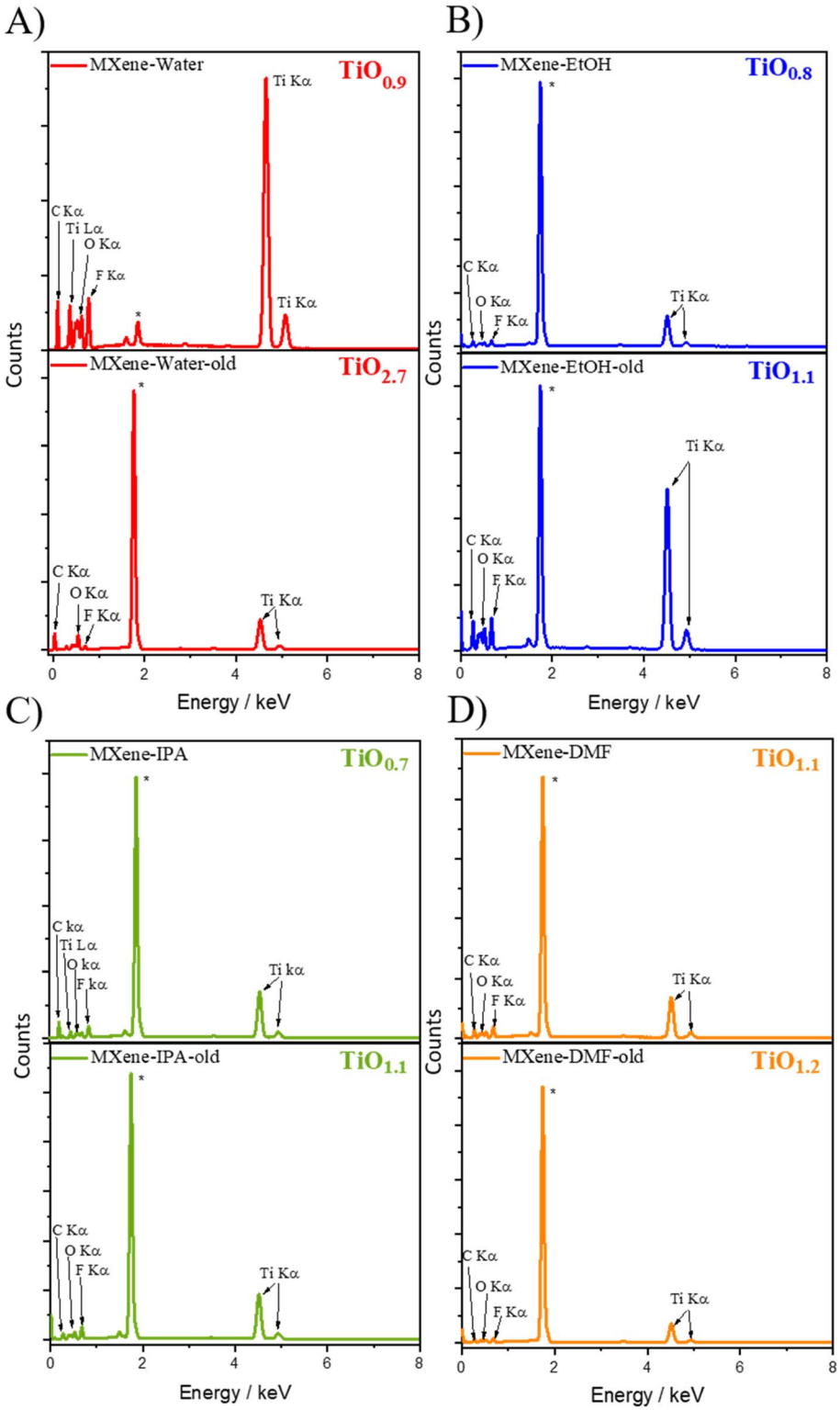

Fig. 4 Energy-dispersive X-ray (EDS) spectra of the $Ti_3C_2T_x$ MXene samples prepared from the (A) water, (B) EtOH, (C) IPA, and (D) DMF fresh suspensions (up) and aged suspensions (down), respectively, with different ratios of Ti and O. "*" refers to the Si (Kα) peak that originates from the Si wafer used as a substrate.

samples prepared from fresh suspensions showed almost the same level of oxidation (Ti : O ~1). In the case of the MXene samples prepared from aged suspensions, the Ti : O ratio was found to be ~1.2, except for the MXene–water-old sample where this value increased drastically to ~2.7. Additional comparison of MXene samples prepared from fresh and aged suspensions revealed that the Ti to O ratio did not change significantly for IPA-, EtOH-, and DMF-based MXene samples.

Following this, the compositional changes of the $Ti_3C_2T_x$ MXene samples were further analyzed by a surface-sensitive technique, such as X-ray photoelectron spectroscopy (XPS). A control XPS survey spectrum of non-treated $Ti_3C_2T_x$ MXene powder (Fig. S5 in the ESI†) confirmed the presence of the constituent elements in the MXene powder with the atomic percentages of Ti (12.32%), C (17.95%), O (17.86%), and F (54.87%). Additionally, the XPS spectra of the MXene samples prepared from fresh and aged suspensions were recorded, as shown in Fig. 5. The spectra confirmed the presence of Ti, O, C, and F on the catalyst surface of all of the investigated MXene samples and their calculated atomic percentages are summarized in Table S3 in the ESI.† As expected, these values are found to be different compared to the obtained atomic percentages of the same elements acquired by EDS (Table S2 in the ESI†), owing to different penetration depths of the techniques.

Moreover, the MXene samples prepared from fresh suspensions showed a higher oxygen content and thus, a lower Ti to O ratio compared to the MXene powder (Ti : O ~0.68), which indicated a different level of $Ti_3C_2T_x$ particles' oxidation after their dispersion in the investigated solvent media. However, a comparison between the $Ti_3C_2T_x$ MXene samples treated with fresh suspensions showed small variations in particle surface oxidation, causing negligible differences in their HER performance (Fig. 1).

Considering the MXene samples prepared from the aged suspensions, the highest oxygen content was found for the MXene–water-old sample, which is in line with the EDS results of the same sample. The Ti to O ratio of ~2.4 additionally confirmed TiO_2 formation on the catalytic surface of the MXene–water-old sample (visible in Fig. 2), which was caused by the degradation and instability of $Ti_3C_2T_x$ particles in water. On the other hand, the negligible changes in the surface chemistry between samples treated with EtOH and IPA separately indicated the high stability of the $Ti_3C_2T_x$ particles in these solvent media and, thus, a low change in their overpotential shift for the HER (Fig. 1).

Additionally, an increase in C content was observed between the MXene–EtOH/MXene–EtOH-old and MXene–IPA/MXene–IPA-old samples. This indicated the possible adsorption of the solvents on these MXene catalytic surfaces due to their lower surface tension,[63,73,74] thus preventing oxidative degradation of the $Ti_3C_2T_x$ MXene microparticles. Moreover, the O content slightly increased in the case of MXene–DMF-based samples, which demonstrated a low oxidation state of the $Ti_3C_2T_x$ microparticles in DMF solvent. However, the relatively high difference in C and noticed change in N content between the MXene–DMF/MXene–DMF-old samples pointed to the possible adsorption and intercalation of DMF on the $Ti_3C_2T_x$ catalytic particles.[34] The observed changes in the surface chemistry of the dispersed $Ti_3C_2T_x$ microparticles in DMF solvent caused the second largest overpotential shift as measured by LSV, as shown in Fig. 1.

Therefore, the different solvents used in the preparation of the $Ti_3C_2T_x$ MXene samples caused different changes in the distribution, morphology, and surface chemistry of the dispersed $Ti_3C_2T_x$ microparticles. This study reveals the importance of the post-synthesis treatment of $Ti_3C_2T_x$ MXene microparticles, their storage, and the choice of the solvent used for particle dispersion since this has an impact on the surface chemistry of the $Ti_3C_2T_x$ microparticles, which can further affect their electrochemical performance for the HER.

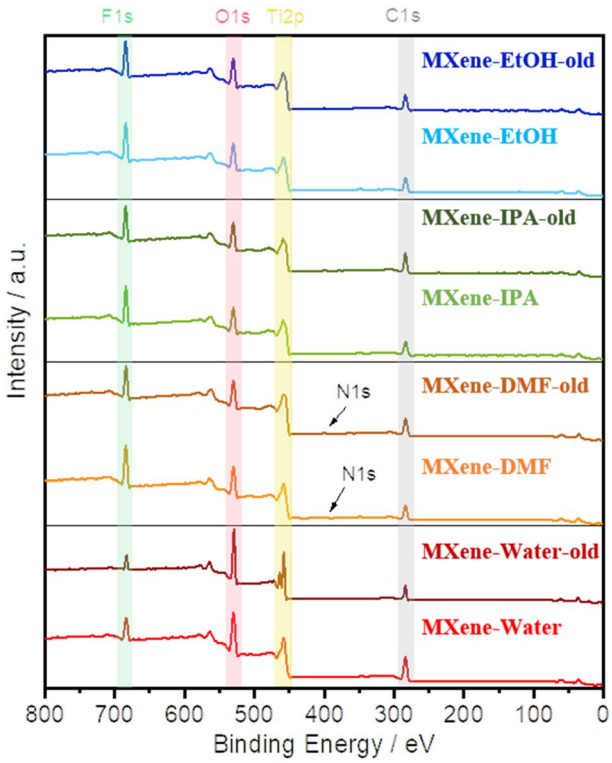

Fig. 5 X-ray photoelectron spectroscopy (XPS) study of the $Ti_3C_2T_x$ MXene samples. Survey spectra of MXene samples prepared from fresh and aged suspensions of water, EtOH, IPA, and DMF.

Conclusion

In this systematic study, the effects of four solvents (water, ethanol, isopropanol, and DMF) used in $Ti_3C_2T_x$ MXene treatment on their electrocatalytic performance for the hydrogen evolution reaction (HER) were investigated. The overpotential range of MXene samples prepared from fresh suspensions was found to be from −0.64 V (MXene–DMF) to −0.72 V (MXene–EtOH), while for MXene samples treated with aged suspensions, the range was from −0.79 V (MXene–EtOH-old) to −0.93 V (MXene–water-old). The largest overpotential shift was noticed in MXene–water-based samples while the smallest was in the MXene–EtOH-based samples. Changes in the HER activity of the $Ti_3C_2T_x$ MXene samples were followed by changes in their surface coverage, particle distribution, and elemental surface composition. Scanning electron microscopy (SEM) analysis showed morphological changes in the MXene–water-old sample, with TiO_2 particle formation on the catalyst surface. Following this, confocal laser scanning microscopy (CLSM) demonstrated the differences in the surface roughness of the $Ti_3C_2T_x$ MXene samples caused by variations in their particle distribution and surface coverage. Energy-dispersive X-ray spectroscopy (EDS) and X-ray photoelectron spectroscopy

(XPS) analysis of the $Ti_3C_2T_x$ MXene samples showed a different level of particle oxidation. The $Ti_3C_2T_x$ MXene microparticles were found to be unstable in water media, which was followed by TiO_2 formation and, hence, a large overpotential shift in the HER activity of MXene–water-based samples. On the other hand, EtOH and IPA were found to be appropriate solvents for the preparation and storage of the $Ti_3C_2T_x$ MXene microparticles because the drop-cast $Ti_3C_2T_x$ microparticles were prevented from oxidative degradation, which accounts for the negligible changes in their HER activity. Moreover, DMF media caused small changes in the surface chemistry of the $Ti_3C_2T_x$ MXene microparticles, and thus, variations in the overpotential shift of the MXene–DMF-based samples.

The results obtained in this study have a profound impact on the preparation of $Ti_3C_2T_x$ MXene samples because different solvents have different impacts on their HER performance. Therefore, the choice of solvent used in MXene electrode preparation plays an important role in the study of their electrocatalytic activity, which is of utmost importance when comparing the electrochemical activity of the same type of MXenes prepared using different solvent media. Additionally, this study provides knowledge about the electrocatalytic performance of differently treated MXene samples and their storage and long-term usage, which is important for their application in the hydrogen evolution reaction.

Author contributions

K. A. N. performed the sample preparation and sample characterization *via* SEM, EDS, XPS, and CLSM, and electrochemical characterization *via* LSV. C. I. and M. P.-C. were involved in data interpretation and reviewing the manuscript. M. P. supervised and conceptualized this work. The manuscript was written through the contributions of all authors. All authors have given approval to the final version of the manuscript.

Conflicts of interest

There are no conflicts to declare.

Acknowledgements

M. P. acknowledges financial support from the Grant Agency of the Czech Republic (EXPO: 19-26896X). K. A. N. acknowledges grant CEITEC-VUT-J-23-8341, realized within the Specific CEITEC Junior Project. C. I. acknowledges financial support by the European Union's Horizon 2020 Research and Innovation Program under Marie Skłodowska-Curie grant agreement no. 888797. K. A. N., C. I. and M. P.-C. acknowledge support from the CzechNanoLab Research Infrastructure (ID LM2018110, MEYS CR) for providing the sample characterization facilities.

References

1 J. K. Nørskov, T. Bligaard, A. Logadottir, J. R. Kitchin, J. G. Chen, S. Pandelov and U. Stimming, Trends in the Exchange Current for Hydrogen Evolution, *J. Electrochem. Soc.*, 2005, **152**(3), J23–J26, DOI: 10.1149/1.1856988.

2 S. J. Gutić, A. S. Dobrota, E. Fako, N. V. Skorodumova, N. López and I. A. Pašti, Hydrogen Evolution Reaction-from Single Crystal to Single Atom Catalysts, *Catalysts*, 2020, **10**(3), 290, DOI: 10.3390/catal10030290.

3 G. Zhao, K. Rui, S. X. Dou and W. Sun, Heterostructures for Electrochemical Hydrogen Evolution Reaction: A Review, *Adv. Funct. Mater.*, 2018, **28**(43), 1803291, DOI: 10.1002/adfm.201803291.

4 T. He, W. Wang, F. Shi, X. Yang, X. Li, J. Wu, Y. Yin and M. Jin, Mastering the Surface Strain of Platinum Catalysts for Efficient Electrocatalysis, *Nature*, 2021, **598**, 76–81, DOI: 10.1038/s41586-021-03870-z.

5 D. V. Esposito, S. T. Hunt, A. L. Stottlemyer, K. D. Dobson, B. E. McCandless, R. W. Birkmire and J. G. Chen, Low-Cost Hydrogen-Evolution Catalysts Based on Monolayer Platinum on Tungsten Monocarbide Substrates, *Angew. Chem., Int. Ed.*, 2010, **49**(51), 9859–9862, DOI: 10.1002/anie.201004718.

6 Y. Shi, Z. R. Ma, Y. Y. Xiao, Y. C. Yin, W. M. Huang, Z. C. Huang, Y. Z. Zheng, F. Y. Mu, R. Huang, G. Y. Shi, Y. Y. Sun, X. H. Xia and W. Chen, Electronic Metal–Support Interaction Modulates Single-Atom Platinum Catalysis for Hydrogen Evolution Reaction, *Nat. Commun.*, 2021, **12**, 3021, DOI: 10.1038/s41467-021-23306-6.

7 J. Zhang, Y. Zhao, X. Guo, C. Chen, C. L. Dong, R. S. Liu, C. P. Han, Y. Li, Y. Gogotsi and G. Wang, Single Platinum Atoms Immobilized on an MXene as an Efficient Catalyst for the Hydrogen Evolution Reaction, *Nat. Catal.*, 2018, **1**, 985–992, DOI: 10.1038/s41929-018-0195-1.

8 J. Zhu, E. Jiang, X. Wang, Z. Pan, X. Xu, S. Ma, P. Kang Shen, L. Pan, M. Eguchi, A. K. Nanjundan, J. Shapter and Y. Yamauchi, Gram-Scale Production of Cu_3P-Cu_2O Janus Nanoparticles into Nitrogen and Phosphorous Doped Porous Carbon Framework as Bifunctional Electrocatalysts for Overall Water Splitting, *Chem. Eng. J.*, 2022, **427**, 130946, DOI: 10.1016/j.cej.2021.130946.

9 Z. Ding, H. Yu, X. Liu, N. He, X. Chen, H. Li, M. Wang, Y. Yamauchi, X. Xu, M. A. Amin, T. Lu and L. Pan, Prussian Blue Analogu e Derived Cobalt–Nickel Phosphide/Carbon Nanotube Composite as Electrocatalyst for Efficient and Stable Hydrogen Evolution Reaction in Wide-PH Environment, *J. Colloid Interface Sci.*, 2022, **616**, 210–220, DOI: 10.1016/j.jcis.2022.02.039.

10 X. Chia and M. Pumera, Characteristics and Performance of Two-Dimensional Materials for Electrocatalysis, *Nat. Catal.*, 2018, **1**(12), 909–921, DOI: 10.1038/s41929-018-0181-7.

11 M. Naguib, M. Kurtoglu, V. Presser, J. Lu, J. Niu, M. Heon, L. Hultman, Y. Gogotsi and M. W. Barsoum, Two-Dimensional Nanocrystals: Two-Dimensional Nanocrystals Produced by Exfoliation of Ti_3AlC_2, *Adv. Mater.*, 2011, **23**(37), 4248–4253, DOI: 10.1002/adma.201190147.

12 M. Naguib, O. Mashtalir, J. Carle, V. Presser, J. Lu, L. Hultman, Y. Gogotsi and M. W. Barsoum, Two-Dimensional Transition Metal Carbides, *ACS Nano*, 2012, **6**(2), 1322–1331, DOI: 10.1021/nn204153h.

13 Y. Gogotsi and B. Anasori, The Rise of MXenes, *ACS Nano*, 2019, **13**(8), 8491–8494, DOI: 10.1021/acsnano.9b06394.
14 B. Anasori, M. R. Lukatskaya and Y. Gogotsi, 2D Metal Carbides and Nitrides (MXenes) for Energy Storage, *Nat. Rev. Mater.*, 2017, **2**, 16098, DOI: 10.1038/natrevmats.2016.98.
15 K. A. Novčić, C. Iffelsberger and M. Pumera, Layered MAX Phase Electrocatalyst Activity Is Driven by Only a Few Hot Spots, *J. Mater. Chem. A*, 2022, **10**(6), 3206–3215, DOI: 10.1039/d1ta06419c.
16 J. L. Hart, K. Hantanasirisakul, A. C. Lang, B. Anasori, D. Pinto, Y. Pivak, J. T. van Omme, S. J. May, Y. Gogotsi and M. L. Taheri, Control of MXenes' Electronic Properties through Termination and Intercalation, *Nat. Commun.*, 2019, **10**, 522, DOI: 10.1038/s41467-018-08169-8.
17 Z. W. Seh, K. D. Fredrickson, B. Anasori, J. Kibsgaard, A. L. Strickler, M. R. Lukatskaya, Y. Gogotsi, T. F. Jaramillo and A. Vojvodic, Two-Dimensional Molybdenum Carbide (MXene) as an Efficient Electrocatalyst for Hydrogen Evolution, *ACS Energy Lett.*, 2016, **1**(3), 589–594, DOI: 10.1021/acsenergylett.6b00247.
18 H. Wang and J. M. Lee, Recent Advances in Structural Engineering of MXene Electrocatalysts, *J. Mater. Chem. A*, 2020, **8**, 10604–10624, DOI: 10.1039/d0ta03271a.
19 M. Seredych, C. E. Shuck, D. Pinto, M. Alhabeb, E. Precetti, G. Deysher, B. Anasori, N. Kurra and Y. Gogotsi, High-Temperature Behavior and Surface Chemistry of Carbide MXenes Studied by Thermal Analysis, *Chem. Mater.*, 2019, **31**(9), 3324–3332, DOI: 10.1021/acs.chemmater.9b00397.
20 L. Gao, H. Chen, A. V. Kuklin, S. Wageh, A. A. Al-Ghamdi, H. Ågren and H. Zhang, Optical Properties of Few-Layer Ti_3CN MXene: From Experimental Observations to Theoretical Calculations, *ACS Nano*, 2022, **16**(2), 3059–3069, DOI: 10.1021/acsnano.1c10577.
21 K. Hantanasirisakul and Y. Gogotsi, Electronic and Optical Properties of 2D Transition Metal Carbides and Nitrides (MXenes), *Adv. Mater.*, 2018, **30**(52), 1804779, DOI: 10.1002/adma.201804779.
22 J. Muñoz, M. Palacios-Corella and M. Pumera, Electrically Reading a Light-Driven Molecular Switch on 2D-$Ti_3C_2T_x$ MXene via Molecular Engineering: Towards Responsive MXetronics, *J. Mater. Chem. A*, 2022, **10**(32), 17001–17008, DOI: 10.1039/d2ta03349f.
23 Y. J. Wan, K. Rajavel, X. M. Li, X. Y. Wang, S. Y. Liao, Z. Q. Lin, P. L. Zhu, R. Sun and C. P. Wong, Electromagnetic Interference Shielding of $Ti_3C_2T_x$ MXene Modified by Ionic Liquid for High Chemical Stability and Excellent Mechanical Strength, *Chem. Eng. J.*, 2021, **15**(408), 127303, DOI: 10.1016/j.cej.2020.127303.
24 K. Ghosh and M. Pumera, MXene and MoS_{3-x} Coated 3D-Printed Hybrid Electrode for Solid-State Asymmetric Supercapacitor, *Small Methods*, 2021, **5**(8), 2100451, DOI: 10.1002/smtd.202100451.
25 J. V. Vaghasiya, C. C. Mayorga-Martinez, Z. Sofer and M. Pumera, MXene-Based Flexible Supercapacitors: Influence of an Organic Ionic Conductor Electrolyte on the Performance, *ACS Appl. Mater. Interfaces*, 2020, **12**(47), 53039–53048, DOI: 10.1021/acsami.0c12879.
26 Y. Zhang, L. Wang, N. Zhang and Z. Zhou, Adsorptive Environmental Applications of MXene Nanomaterials: A Review, *RSC Adv.*, 2018, **8**, 19895–19905, DOI: 10.1039/c8ra03077d.
27 C. Zhang, L. McKeon, M. P. Kremer, S. H. Park, O. Ronan, A. Seral-Ascaso, S. Barwich, C. Coileáin, N. McEvoy, H. C. Nerl, B. Anasori, J. N. Coleman, Y. Gogotsi and V. Nicolosi, Additive-Free MXene Inks and Direct Printing of Micro-Supercapacitors, *Nat. Commun.*, 2019, **10**, 1795, DOI: 10.1038/s41467-019-09398-1.
28 M. R. Lukatskaya, O. Mashtalir, C. E. Ren, Y. Dall'Agnese, P. Rozier, P. L. Taberna, M. Naguib, P. Simon, M. W. Barsoum and Y. Gogotsi, Cation Intercalation and High Volumetric Capacitance of Two-Dimensional Titanium Carbide, *Science*, 2013, **341**(6153), 1502–1505, DOI: 10.1126/science.1241488.
29 Y. Xia, T. S. Mathis, M. Q. Zhao, B. Anasori, A. Dang, Z. Zhou, H. Cho, Y. Gogotsi and S. Yang, Thickness-Independent Capacitance of Vertically Aligned Liquid-Crystalline MXenes, *Nature*, 2018, **557**, 409–412, DOI: 10.1038/s41586-018-0109-z.
30 Y. Wei, R. A. Soomro, X. Xie and B. Xu, Design of Efficient Electrocatalysts for Hydrogen Evolution Reaction Based on 2D MXenes, *J. Energy Chem.*, 2021, **55**, 244–255, DOI: 10.1016/j.jechem.2020.06.069.
31 E. Redondo and M. Pumera, MXene-Functionalised 3D-Printed Electrodes for Electrochemical Capacitors, *Electrochem. Commun.*, 2021, **124**, 106920, DOI: 10.1016/j.elecom.2021.106920.
32 Y. Z. Zhang, K. H. Lee, D. H. Anjum, R. Sougrat, Q. Jiang, H. Kim and H. N. Alshareef, MXenes Stretch Hydrogel Sensor Performance to New Limits, *Sci. Adv.*, 2018, **4**, 6, DOI: 10.1126/sciadv.aat0098.
33 P. Mayorga-Burrezo, J. Muñoz, D. Zaoralová, M. Otyepka and M. Pumera, Multiresponsive 2D $Ti_3C_2T_x$ MXene via Implanting Molecular Properties, *ACS Nano*, 2021, **15**(6), 10067–10075, DOI: 10.1021/acsnano.1c01742.
34 M. S. Cao, Y. Z. Cai, P. He, J. C. Shu, W. Q. Cao and J. Yuan, 2D MXenes: Electromagnetic Property for Microwave Absorption and Electromagnetic Interference Shielding, *Chem. Eng. J.*, 2019, **359**(1), 1265–1302, DOI: 10.1016/j.cej.2018.11.051.
35 J. Liu, L. Mckeon, J. Garcia, S. Pinilla, S. Barwich, M. Möbius, P. Stamenov, J. N. Coleman and V. Nicolosi, Additive Manufacturing of Ti_3C_2-MXene-Functionalized Conductive Polymer Hydrogels for Electromagnetic-Interference Shielding, *Adv. Mater.*, 2022, **34**(5), 2106253, DOI: 10.1002/adma.202106253.
36 M. Soleymaniha, M. A. Shahbazi, A. R. Rafieerad, A. Maleki and A. Amiri, Promoting Role of MXene Nanosheets in Biomedical Sciences: Therapeutic and Biosensing Innovations, *Adv. Healthcare Mater.*, 2019, **8**(1), 1801137, DOI: 10.1002/adhm.201801137.
37 L. Li, X. Fu, S. Chen, S. Uzun, A. S. Levitt, C. E. Shuck, W. Han and Y. Gogotsi, Hydrophobic and Stable MXene-Polymer

Pressure Sensors for Wearable Electronics, *ACS Appl. Mater. Interfaces*, 2020, **12**(13), 15362–15369, DOI: 10.1021/acsami.0c00255.

38 C. C. Mayorga-Martinez, J. Vyskočil, F. Novotný and M. Pumera, Light-Driven Ti_3C_2 MXene Micromotors: Self-Propelled Autonomous Machines for Photodegradation of Nitroaromatic Explosives, *J. Mater. Chem. A*, 2021, **9**(26), 14904–14910, DOI: 10.1039/d1ta02256c.

39 J. V. Vaghasiya, C. C. Mayorga-Martinez, J. Vyskočil and M. Pumera, Flexible Wearable MXene Ti_3C_2-Based Power Patch Running on Sweat, *Biosens. Bioelectron.*, 2022, **1**(205), 114092, DOI: 10.1016/j.bios.2022.114092.

40 H. L. Chia, C. C. Mayorga-Martinez, N. Antonatos, Z. Sofer, J. J. Gonzalez-Julian, R. D. Webster and M. Pumera, MXene Titanium Carbide-Based Biosensor: Strong Dependence of Exfoliation Method on Performance, *Anal. Chem.*, 2020, **92**(3), 2452–2459, DOI: 10.1021/acs.analchem.9b03634.

41 Y. Yan, B. Xia, X. Ge, Z. Liu, J. Y. Wang and X. Wang, Ultrathin MoS_2 Nanoplates with Rich Active Sites as Highly Efficient Catalyst for Hydrogen Evolution, *ACS Appl. Mater. Interfaces*, 2013, **5**(24), 12794–12798, DOI: 10.1021/am404843b.

42 T. F. Jaramillo, K. P. Jørgensen, J. Bonde, J. H. Nielsen, S. Horch and I. Chorkendorff, Identification of Active Edge Sites for Electrochemical H_2 Evolution from MoS_2 Nanocatalysts, *Science*, 2007, **317**(5834), 100–102, DOI: 10.1126/science.1141483.

43 G. Li, D. Zhang, Q. Qiao, Y. Yu, D. Peterson, A. Zafar, R. Kumar, S. Curtarolo, F. Hunte, S. Shannon, Y. Zhu, W. Yang and L. Cao, All the Catalytic Active Sites of MoS_2 for Hydrogen Evolution, *J. Am. Chem. Soc.*, 2016, **138**(51), 16632–16638, DOI: 10.1021/jacs.6b05940.

44 J. Xie, H. Zhang, S. Li, R. Wang, X. Sun, M. Zhou, J. Zhou, X. W. Lou and Y. Xie, Defect-Rich MoS_2 Ultrathin Nanosheets with Additional Active Edge Sites for Enhanced Electrocatalytic Hydrogen Evolution, *Adv. Mater.*, 2013, **25**(40), 5807–5813, DOI: 10.1002/adma.201302685.

45 S. Balasubramanyam, M. Shirazi, M. A. Bloodgood, L. Wu, M. A. Verheijen, V. Vandalon, W. M. M. Kessels, J. P. Hofmann and A. A. Bol, Edge-Site Nanoengineering of WS_2 by Low-Temperature Plasma-Enhanced Atomic Layer Deposition for Electrocatalytic Hydrogen Evolution, *Chem. Mater.*, 2019, **31**(14), 5104–5115, DOI: 10.1021/acs.chemmater.9b01008.

46 S. Wert, C. Iffelsberger, K. A. Novčić, F. M. Matysik and M. Pumera, Edges Are More Electroactive than Basal Planes in Synthetic Bulk Crystals of TiS_2 and $TiSe_2$, *Appl. Mater. Today*, 2022, **26**, 101309, DOI: 10.1016/j.apmt.2021.101309.

47 K. A. Novčić, C. Iffelsberger, S. Ng and M. Pumera, Local Electrochemical Activity of Transition Metal Dichalcogenides and Their Heterojunctions on 3D-Printed Nanocarbon Surfaces, *Nanoscale*, 2021, **13**, 5324–5332, DOI: 10.1039/d0nr06679f.

48 A. D. Handoko, K. D. Fredrickson, B. Anasori, K. W. Convey, L. R. Johnson, Y. Gogotsi, A. Vojvodic and Z. W. Seh, Tuning the Basal Plane Functionalization of Two-Dimensional Metal Carbides (MXenes) to Control Hydrogen Evolution Activity, *ACS Appl. Energy Mater.*, 2018, **1**(1), 173–180, DOI: 10.1021/acsaem.7b00054.

49 Y. Jiang, T. Sun, X. Xie, W. Jiang, J. Li, B. Tian and C. Su, Oxygen-Functionalized Ultrathin $Ti_3C_2T_x$ MXene for Enhanced Electrocatalytic Hydrogen Evolution, *ChemSusChem*, 2019, **12**(7), 1368–1373, DOI: 10.1002/cssc.201803032.

50 A. Djire, X. Wang, C. Xiao, O. C. Nwamba, M. V. Mirkin and N. R. Neale, Basal Plane Hydrogen Evolution Activity from Mixed Metal Nitride MXenes Measured by Scanning Electrochemical Microscopy, *Adv. Funct. Mater.*, 2020, **30**(47), 2001136, DOI: 10.1002/adfm.202001136.

51 B. Anasori, C. Shi, E. J. Moon, Y. Xie, C. A. Voigt, P. R. C. Kent, S. J. May, S. J. L. Billinge, M. W. Barsoum and Y. Gogotsi, Control of Electronic Properties of 2D Carbides (MXenes) by Manipulating Their Transition Metal Layers, *Nanoscale Horiz.*, 2016, **1**, 227–234, DOI: 10.1039/c5nh00125k.

52 T. Schultz, N. C. Frey, K. Hantanasirisakul, S. Park, S. J. May, V. B. Shenoy, Y. Gogotsi and N. Koch, Surface Termination Dependent Work Function and Electronic Properties of $Ti_3C_2T_x$ MXene, *Chem. Mater.*, 2019, **31**(17), 6590–6597, DOI: 10.1021/acs.chemmater.9b00414.

53 M. Malaki, A. Maleki and R. S. Varma, MXenes and Ultrasonication, *J. Mater. Chem. A*, 2019, **7**, 10843–10857, DOI: 10.1039/c9ta01850f.

54 A. Kaliyaraj Selva Kumar, Y. Zhang, D. Li and R. G. Compton, A Mini-Review: How Reliable Is the Drop Casting Technique?, *Electrochem. Commun.*, 2020, **121**, 106867, DOI: 10.1016/j.elecom.2020.106867.

55 L. Yin, K. N. Kim, J. Lv, F. Tehrani, M. Lin, Z. Lin, J. M. Moon, J. Ma, J. Yu, S. Xu and J. Wang, A Self-Sustainable Wearable Multi-Modular E-Textile Bioenergy Microgrid System, *Nat. Commun.*, 2021, **12**(1), 1–12, DOI: 10.1038/s41467-021-21701-7.

56 K. P. Akshay Kumar, K. Ghosh, O. Alduhaish and M. Pumera, Dip-Coating of MXene and Transition Metal Dichalcogenides on 3D-Printed Nanocarbon Electrodes for the Hydrogen Evolution Reaction, *Electrochem. Commun.*, 2021, **122**, 106890, DOI: 10.1016/j.elecom.2020.106890.

57 T. R. Bartlett, S. V. Sokolov and R. G. Compton, Electrochemical Nanoparticle Sizing Via Nano-Impacts: How Large a Nanoparticle Can Be Measured?, *ChemistryOpen*, 2015, **4**(5), 600–605, DOI: 10.1002/open.201500061.

58 Y. Zhang, A. K. Selva Kumar, D. Li, M. Yang and R. G. Compton, Nanoparticle- and Nanotube-Modified Electrodes: Response of Drop-Cast Surfaces, *ChemElectroChem*, 2020, **7**(22), 4614–4624, DOI: 10.1002/celc.202001295.

59 J. Lv, L. Yin, X. Chen, I. Jeerapan, C. A. Silva, Y. Li, M. Le, Z. Lin, L. Wang, A. Trifonov, S. Xu, S. Cosnier and J. Wang, Wearable Biosupercapacitor: Harvesting and Storing Energy from Sweat, *Adv. Funct. Mater.*, 2021, 2102915, DOI: 10.1002/adfm.202102915.

60 A. C. Â. Dorim, H. Aleixo, E. de Souza Barcellos and L. L. Okumura, Influence of the Solvent on the "Casting"

Methodology for MWCNT-Modified Glassy Carbon and Platinum Electrodes, *Electroanalysis*, 2015, **27**(11), 2663–2669, DOI: **10.1002/elan.201500265**.

61 C. L. Manzanares Palenzuela, J. Luxa, Z. Sofer and M. Pumera, $MoSe_2$ Dispersed in Stabilizing Surfactant Media: Effect of the Surfactant Type and Concentration on Electron Transfer and Catalytic Properties, *ACS Appl. Mater. Interfaces*, 2018, **10**(21), 17820–17826, DOI: **10.1021/acsami.7b19744**.

62 X. J. Chua and M. Pumera, The Effect of Varying Solvents for MoS_2 Treatment on Its Catalytic Efficiencies for HER and ORR, *Phys. Chem. Chem. Phys.*, 2017, **19**, 6610–6619, DOI: **10.1039/c6cp08205j**.

63 K. Maleski, V. N. Mochalin and Y. Gogotsi, Dispersions of Two-Dimensional Titanium Carbide MXene in Organic Solvents, *Chem. Mater.*, 2017, **29**(4), 1632–1640, DOI: **10.1021/acs.chemmater.6b04830**.

64 M. Urso, M. Ussia, F. Novotný and M. Pumera, Trapping and Detecting Nanoplastics by MXene-Derived Oxide Microrobots, *Nat. Commun.*, 2022, **13**(1), 1–14, DOI: **10.1038/s41467-022-31161-2**.

65 R. V. d. Krol and M. Gratzel, Electronic Materials: Science & Technology, in *Photoelectrochemical Hydrogen Production*, 2012, DOI: **10.1007/978-1-4614-1380-6**.

66 C. Zhou, X. Wang, H. Luo, L. Deng, S. Wei, Y. Zheng, Q. Jia and J. Liu, Rapid and Direct Growth of Bipyramid TiO_2 from $Ti_3C_2T_x$ MXene to Prepare Ni/TiO_2/C Heterogeneous Composites for High-Performance Microwave Absorption, *Chem. Eng. J.*, 2020, **383**, 123095, DOI: **10.1016/j.cej.2019.123095**.

67 T. Habib, X. Zhao, S. A. Shah, Y. Chen, W. Sun, H. An, J. L. Lutkenhaus, M. Radovic and M. J. Green, Oxidation Stability of $Ti_3C_2T_x$ MXene Nanosheets in Solvents and Composite Films, *npj 2D Mater. Appl.*, 2019, **3**, 8, DOI: **10.1038/s41699-019-0089-3**.

68 X. Chia and M. Pumera, Layered Transition Metal Dichalcogenide Electrochemistry: Journey across the Periodic Table, *Chem. Soc. Rev.*, 2018, **47**, 5602–5613, DOI: **10.1039/c7cs00846e**.

69 S. M. Tan and M. Pumera, Bottom-up Electrosynthesis of Highly Active Tungsten Sulfide (WS_{3-x}) Films for Hydrogen Evolution, *ACS Appl. Mater. Interfaces*, 2016, **8**(6), 3948–3957, DOI: **10.1021/acsami.5b11109**.

70 B. E. Conway and L. Bai, Determination of Adsorption of OPD H Species in the Cathodic Hydrogen Evolution Reaction at Pt in Relation to Electrocatalysis, *J. Electroanal. Chem.*, 1986, **198**(1), 149–175, DOI: **10.1016/0022-0728(86)90033-1**.

71 B. E. Conway and B. V. Tilak, Interfacial Processes Involving Electrocatalytic Evolution and Oxidation of H_2, and the Role of Chemisorbed H, *Electrochim. Acta*, 2002, **47**(22–23), 3571–3594, DOI: **10.1016/S0013-4686(02)00329-8**.

72 H. Kim, J. Choi, B. Chae and G. Kim, CLSM [Confocal Laser Scanning Microscope] Observation of the Surface Roughness of Pressurized Rock Samples During Freeze/Thaw Cycling, *J. Eng. Geol.*, 2015, **25**(2), 165–178, DOI: **10.9720/kseg.2015.2.165**.

73 A. N. Enyashin and A. L. Ivanovskii, Structural and Electronic Properties and Stability of MXenes Ti_2C and Ti_3C_2 Functionalized by Methoxy Groups, *J. Phys. Chem. C*, 2013, **117**(26), 13637–13643, DOI: **10.1021/jp401820b**.

74 A. Iqbal, J. Hong, T. Y. Ko and C. M. Koo, Improving Oxidation Stability of 2D MXenes: Synthesis, Storage Media, and Conditions, *Nano Convergence*, 2021, **8**, 9, DOI: **10.1186/s40580-021-00259-6**.

Chapter 11. Conclusion and Future Perspective

This Thesis represents a comprehensive study of the layered two-dimensional (2D) catalysts and their application in clean hydrogen production. The research output achieved in this Thesis provides knowledge about the preparation, characterization and electrocatalytic activity of 2D materials. A significant advancement in the field was made by investigating the microscopic hydrogen evolution reaction (HER) activity using an innovative electrochemical tool, such as scanning electrochemical microscopy (SECM). The main results are divided into four areas of study and follow the Thesis' main objectives (defined in **Chapter 1**).

Firstly, the study on the transition metal dichalcogenide (TMD) modified thermally activated 3D-printed nanocarbon electrodes (**Chapter 6**) provided information about the material contrast based on the differences in their HER activity and gave a profound understanding of the electrocatalytic activity of TMDs as well as their heterojunctions on the 3D-printed nanocarbon electrodes. The microscopic HER performance of the activated TMD-deposited 3D-printed electrodes studied on the cross sections of the nanocarbon electrodes by using SECM demonstrated that the HER active sites are not solely located at the outer surface, but also in the interior of the nanocarbon structure with different thicknesses of the HER active sites. As a result, this methodological study provides a deeper understanding of the electrochemical activity of TMD-modified 3D-printed nanocarbon-based materials, which is important for their future development as electrochemical devices.

Exploring the bulk TMD crystals (**Chapters 7** and **8**), the electrochemical analysis of the MoS_2, TiS_2 and $TiSe_2$ crystals demonstrated that their activity for the HER is derived from the catalytically active edges, compared to the less active basal plane. Additionally, the study of their stability during this reaction shows that the MoS_2 crystal does not go through morphological changes. In contrast, TiS_2 and $TiSe_2$ bulk crystals get damaged and exfoliated

during the HER, which limits their application for electrochemical water splitting. The obtained results are relevant for the future utilization and development of the group IV B TMDs.

Expanding the research to the MAX phases (**Chapter 9**), the macroscopic and microscopic electrochemical performance for the HER of the double transition metal MAX phases, Mo_2TiAlC_2, microparticles were investigated. The microscopic SECM study of the MAX phase microparticles demonstrated the non-uniform distribution of the individual particle activity with highly active hot spots for the HER. This study provides relevant knowledge about the uniformity of the overall HER performance of the MAX phase microparticles, which has broad implications on the general understanding of the electrocatalytic performance of these materials.

Furthermore, this Thesis focuses on the macroscopic HER performance of the MXene electrocatalysts and the effects of the four solvents (water, ethanol, isopropanol and dimethylformamide) typically used in the preparation of the $Ti_3C_2T_x$ MXene samples (**Chapter 10**). The macroscopic electrochemical performance of the MXenes prepared from the fresh and one-month-old suspensions was investigated. It provides an insight into the effects solvent media have on the surface chemistry and elemental composition of the MXenes, which is of utmost importance when comparing the electrochemical activity of the same type of MXenes prepared using different solvent media.

This Thesis presents the methodological study of the macroscopic and microscopic electrochemical activity of different layered 2D materials. The obtained results have broad implications on our general understanding of the electrocatalytic surfaces, uniformity, and distribution of their electrochemical active sites. Additionally, they present a solid foundation for the future exploration of the electrochemical activity of these materials on micro- to nano-scale, which leads to a deeper understanding of their surface chemistry.

Therefore, to be closer to the practical application of 2D materials as electrocatalysts, the future steps should consider the electrochemical nature of these materials on a smaller scale. Investigation of the materials' electrochemical properties at a microscopic level provides vital information for the improvement of their macroscopic electrochemical activity, resultsing in their enhanced applicability as electrocatalysts in clean hydrogen production.

Finally, in order to apply these materials on large-scale clean hydrogen production, it is necessary to keep up with the technological development and advancement which can rely on and support the fossil fuel-free energy system and combine them with other economic measures, including international cooperation and fundamental research.

ii. List of Abbreviations:

Abbreviation	Explanation	Unit
A	Electrode area	[m^2]
a	Electrode radius	[m]
a_i	Activity of species *i*	
AFM	Atomic force microscopy	
C_{dl}	Double layer capacity	[F]
C	Concentration	[mol dm^{-3}]
CE	Counter electrode	
CLSM	Confocal laser scanning microscopy	
CV	Cyclic voltammetry	
d	Tip-to-substrate-distance	[m]
D	Diffusion coefficient	[cm^2 s^{-1}]
E	Potential	[V]
E^0	Standard electrode potential	[V]
$E^{0`}$	Formal electrode potential	[V]
e^-	Electron	
e	Elementary charge	[1.60218 $\cdot 10^{-19}$ C]
EDS	Energy dispersive X-ray spectroscopy	
E_1	Starting potential	[V]
E_2	Vertex potential	[V]
EtOH	Ethanol	
F	Faraday constant	[9.64853 $\cdot 10^{-4}$ C mol^{-1}]
	Farad	
FcMeOH	Ferrocene methanol	
I	Current	[A]
I_M	Measured current	[A]
I_∞	Current measured in bulk	[A]
I_C	Non-Faradaic current	[A]
I_D	Mass transport limited current	[A]
I_F	Faradaic current	[A]
IPA	Isopropanol	
J_x	Flux	[mol cm^{-2} s^{-1}]
L	Normalized tip-to-substrate distance	[m]

LSV	Linear sweep voltammetry	
n	Amount of substance	[mol]
	Number of transferred electrons	
O	Oxidized species	
PAC	Probe approach curve	
Q	Charge	[C]
R	Universal gas constant	[8.31447 J mol^{-1} K^{-1}]
	Reduced species	
Rc	Ohmic resistance	[Ω]
RE	Reference electrode	
r_g	Radius of UME	
SECM	Scanning electrochemical microscopy	
SEM	Scanning electron microscopy	
SG/TC	Substrate generation/tip collection	
T	Temperature	[K]
t	Time	[s]
TMDs	Transition metal dichalcogenides	
UME	Ultramicroelectrode	
WE	Working electrode	
XPS	X-ray photoelectron spectroscopy	
XRD	X-ray diffraction	
2D	Two-dimensional	
3D	Three-dimensional	
z	Stoichiometric number of transferred electrons	
γ_i	Activity coefficient	
δ	Thickness of diffusion layer	

Appendix

Published paper: M. Sanna, **K. A. Novčić**, S. Ng, M. Černý, and M. Pumera, *The unexpected photoelectrochemical activity of MAX phases: the role of oxide impurities,* **Journal of Material Chemistry A (2023)**, DOI: 10.1039/d2ta06929f.

This paper is not a part to be evaluated since it is used in the thesis of PhD student Michela Sanna, MSc, and it is presented here as the appendix.

Student contribution:

The student (Katarina Novčić. MSc) is the second author of the paper who contributed to the paper by performing the theoretical calculation of the investigated MAX phases by density functional calculations as well as material characterization and was involved in data analysis and writing the original draft of the manuscript.

Journal of Materials Chemistry A

ROYAL SOCIETY OF CHEMISTRY

PAPER

View Article Online
View Journal | View Issue

Cite this: J. Mater. Chem. A, 2023, 11, 3080

The unexpected photoelectrochemical activity of MAX phases: the role of oxide impurities†

Michela Sanna, [a] Katarina A. Novčić, [a] Siowwoon Ng, [a] Miroslav Černý[bc] and Martin Pumera *[ade]

Received 1st September 2022
Accepted 6th January 2023

DOI: 10.1039/d2ta06929f

rsc.li/materials-a

MAX phases are layered ternary compounds that are mainly studied for their physical properties and their use in the synthesis of MXenes. Their application in energy generation has been investigated and recently, the unexpected photoactivity of MAX phases under the influence of a visible light source has been reported. To investigate the origin of this photoactivity, theoretical calculations and experimental characterisation of the structural and optical properties of three MAX phases, Nb_2AlC, Ta_2AlC and Ti_3AlC_2, were performed. Although the theoretical calculations confirmed that the phases presented no band gap in the vicinity of the Fermi level, the experimental evaluation showed two main absorptions for Nb_2AlC and Ta_2AlC (2.2 eV, 3.1 eV, and 2.2 eV, 3.3 eV, respectively) and one for Ti_3AlC_2 (2.4 eV). To confirm the observations from the optical characterisation, the phases were applied as photoelectrocatalysts for hydrogen generation under the influence of light of different wavelengths. Nb_2AlC and Ta_2AlC performed better when exposed to UV light, while Ti_3AlC_2 showed the lowest overpotential under the influence of visible light, in accordance with the experimentally estimated band gaps. The materials were extensively characterised and the photoactivity of MAX phases was attributed to the presence of photoactive oxide impurities on the surface of the material, which are naturally formed from contact with air and solvents. In this work, we show how these impurities can lead to better performances thanks to their intrinsic photoactivity, indicating the prospects for the use of MAX phases in other photoelectrochemical processes.

Introduction

The dramatic increase in energy demand in the past decades and the consequent overexploitation of fossil fuels have contributed to the great need to find alternative energy sources. Among the environmentally friendly energy sources, one of the most interesting alternatives to fossil fuels to alleviate environmental and energy issues is solar energy, combined with electrochemical reactions to store energy in chemical bonds.[1,2] In 2007, it was estimated that in the so-called "solar belt", which referred to the abundant solar radiation region of the Earth between latitudes of 40°N and 40°S, the yearly average input of solar energy is 18.48 MJ (m^2 day^{-1}).[3] This is a remarkable amount of free energy that can be harvested and implemented in future energy production technology to achieve long-term sustainable and renewable energy sources. For this reason, the scientific community has long focused on the solar production of clean hydrogen fuels with high energy density through photoelectrochemical reactions.[4–6] Various (photo) electrocatalytic materials from TiO_2,[7,8] $BiVO_4$,[9,10] CdS,[11,12] and MoS_2,[13,14] to more recent work on Xenes[15,16] and MXenes,[17,18] have been investigated for hydrogen production, and new catalysts are continuously being studied and tested for application in this field.

MAX phases (MAX) are a class of layered ternary compounds with the general formula $M_{n+1}AX_n$ (M = early transition metal, A = IIIA and IVA group element, X = C or N, and n = 1, 2, or 3), which possess hexagonal crystal structures with $P6_3/mmc$ symmetry.[19–22] MAX are known for possessing properties typical of metals and ceramics, such as thermal and electrical conductivity, chemical and oxidation resistance, and damage tolerance.[19,22,23] Lately, MAX have been the centre of attention because they are the parent materials in the creation of two-dimensional (2D) MXenes. The A layer of MAX can be selectively etched to form MXenes.[24–26] These 2D materials have attracted attention for electrochemical applications since they

[a]Future Energy and Innovation Laboratory, Central European Institute of Technology, Brno University of Technology, Purkyňova 123, 61200 Brno, Czech Republic. E-mail: pumera.research@gmail.com

[b]Central European Institute of Technology, Brno University of Technology, Technická 2, CZ-616 69 Brno, Czech Republic

[c]Faculty of Mechanical Engineering, Brno University of Technology, Technická 2, CZ-616 69 Brno, Czech Republic

[d]Faculty of Electrical Engineering and Computer Science, VSB–Technical University of Ostrava, 17. Listopadu 2172/15, 70800 Ostrava, Czech Republic

[e]Department of Medical Research, China Medical University Hospital, China Medical University, No. 91 Hsueh-Shih Road, Taichung 40402, Taiwan

† Electronic supplementary information (ESI) available. See DOI: https://doi.org/10.1039/d2ta06929f

are characterised by high metallic conductivity, high negative zeta potential, and fast charge transfer kinetics.[27–30] The interest of the scientific community is concentrated on the application of MXenes in different fields, although MAX and their properties have not been fully investigated. Recent studies have taken one step back, looking into the fundamental electrochemical properties of MAX phases and the possible application of these compounds as (photo)electrocatalysts for energy conversion.[22,31,32]

In previous studies,[33,34] MAX showed better catalytic performances when exposed to different light sources. Ta_2AlC, Cr_2AlC, Ti_2AlC and Ti_3AlC_2 demonstrated improved photoelectrocatalytic H_2 production when illuminated by a 660 nm light source.[33] In addition, Cr_2AlC demonstrated huge potential in the photodegradation of various cationic and anionic dyes under the influence of visible and UV light, showing an optical band gap of 1.28 eV.[34] These studies provided evidence that in contrast to the metallic nature of MAX,[35,36] some of them, if not all, possess band gaps and absorb light, as shown in Scheme 1, so they can be applied in solar-driven applications.

Here, we aim to understand the origin of the photoactivity of these compounds. We report a theoretical and experimental study on three MAX, namely Nb_2AlC, Ta_2AlC, and Ti_3AlC_2. A theoretical study on the total and partial density of states and band structure was carried out based on Density Functional Theory (DFT). The morphology, surface composition, and optical properties of MAX were analysed in detail by SEM, EDS and XPS. Finally, the phases were applied as a photoelectrocatalyst for hydrogen generation under the influence of different sources of light. Trace amounts of impurities (in ppm or even in ppb levels) have been reported to influence traditional synthetic chemistry catalysis,[37–40] electrocatalysis[41–47] and photocatalysis.[48,49] This is true about metals,[37] metal oxides[45] and phase impurities[50] because in catalysis (chemical, electrochemical or photochemical) the small active sites can overwhelmingly dominate the much more sluggish performance of the "host" material.[41,42,51] We show that oxide impurities within the MAX are the driving force of the photoelectrochemistry, like impurities are the driving force of the electrochemistry in research on carbon nanotubes,[41,42] graphene[43,44] and transition metal dichalcogenides.[45–47]

Experimental

Materials

MAX phases (Nb_2AlC, Ta_2AlC, and Ti_3AlC_2) were obtained from Laizhou Kai Kai Ceramic Material Co. Ltd. and were used without additional treatment. Screen-printed carbon electrodes (SPCE, SE 101) were purchased from CH instruments, and sulfuric acid (H_2SO_4, 96%) from Penta, Czech Republic. All solutions were prepared using deionised water with a resistivity of 18 MΩ cm.

Theoretical calculations

The first principles DFT calculations were performed using the Vienna *Ab initio* Simulation Package (VASP) and the generalised gradient approximation (GGA) in parametrisation by Perdew, Burke and Ernzerhof (PBE). The cut-off energy of 500 eV and a Monkhorst–Pack Γ-centered 19 × 19 × 4 k-point mesh were used. For the study of MAX, a 2 × 2 × 1 supercell was created. VESTA code[52] and Origin-Pro 2020 were used for the structure visualisation. Analysis of the electronic properties was

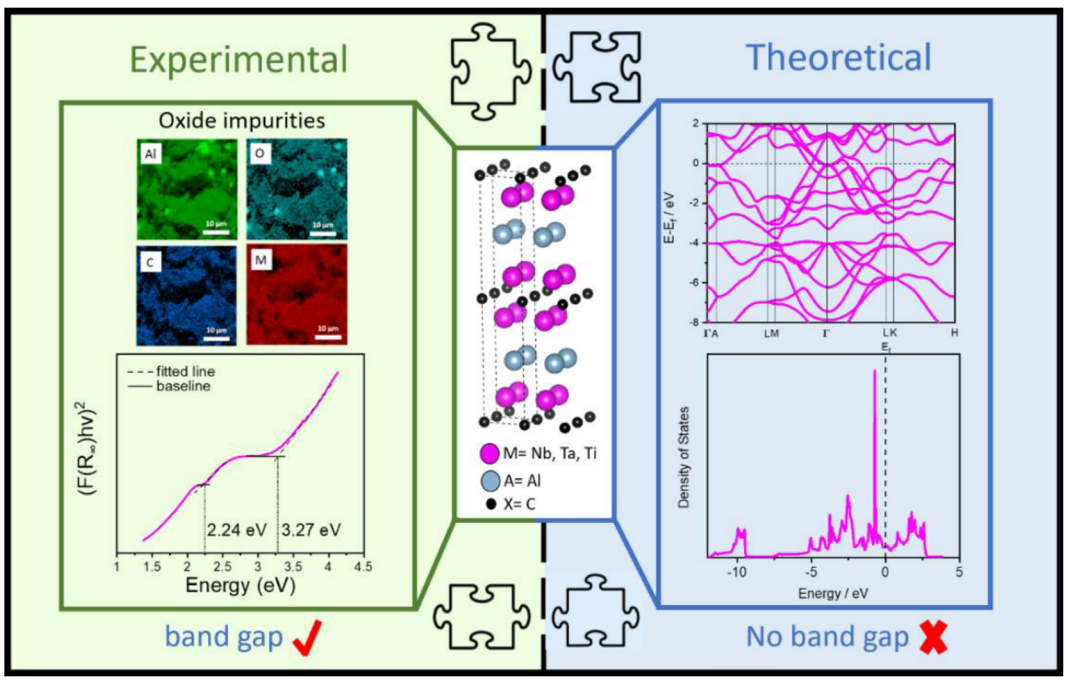

Scheme 1 Schematic representation of the motivation and the approach used in this work for the investigation of the photoactivity of MAX phases.

performed through calculations of the band structure and total and partial density of states (DOS).

Materials characterisations

The morphology of the MAX phase powders was analysed using a scanning electron microscope (SEM, Mira 3 XMU Tescan) equipped with an energy-dispersive X-ray spectroscopy (EDS) detector X-MAX20 (Oxford Instruments) for elemental mapping. An accelerating voltage of 20 kV was used for the analysis of the elemental composition. Further information about the chemical composition was obtained using X-ray photoelectron spectroscopy (XPS, Kratos Analytical Axis Supra). All the obtained spectra were analysed using the CasaXPS software and calibrated against the C 1s peak at 285 eV. The high-resolution spectra of the major elements were fitted using a Shirley-type background. The X-ray diffraction (XRD) patterns were obtained using an X-ray diffractometer (Rigaku SmartLab 3 kW) with Cu Kα source of wavelength 0.1789 nm. The optical images of the prepared electrodes were acquired by Stereomicroscope Zeiss Stemi 508 (STEMI) and the thickness determination was done by confocal laser scanning microscopy (CLSM, Olympus LEXT-OLS 4100) with 10× lenses. The reflectance spectra of MAX phases were measured by mounting an integrating sphere in a UV-vis spectrophotometer (JASCO V-750) operated by JASCO software. The measurements were performed within the range of 300–900 nm, using a scan speed of 400 nm min^{-1}. The Kubelka–Munk (K–M) function was employed to estimate the band gap of MAX phases. In particular, the reflectance measurements can be converted into the corresponding absorption spectra, applying the K–M function $F(R_\infty)$,[53] as defined in eqn (1):

$$F(R_\infty) = \frac{K}{S} = \frac{1 - R_\infty}{2R_\infty} \text{ where } R_\infty = \frac{R_{sample}}{R_{standard}} \quad (1)$$

$F(R_\infty)$ can substitute for the absorption coefficient α defined in the Tauc method[54] by eqn (2):

$$(\alpha h\nu)^{\frac{1}{n}} = B(h\nu - E_g) \quad (2)$$

where h = Planck constant, υ = frequency, E_g = band gap energy, B = constant. The factor n depends on the nature of the transition, and it is equal to 2 for indirect transition band gaps and equal to $\frac{1}{2}$ for direct transition band gaps. Eqn (2) can be finally written in the form of eqn (3) and (4):

$$(F(R_\infty) \times h\nu)^2 = B(h\nu - E_g) \text{ for direct transition band gap} \quad (3)$$

$$(F(R_\infty) * h\nu)^{\frac{1}{2}} = B(h\nu - E_g) \text{ for indirect transition gap} \quad (4)$$

Tauc plots were obtained by plotting $(F(R_\infty)\ h\nu)^2$ *versus* photon energy and the baseline approach was used for the graphic extrapolation of the values.[55] In this approach, the linear fit is applied to the fundamental peak, similar to the Tauc method, and to the slope below the fundamental peak, which can be identified as the "baseline". The estimation of the band gap energy is given by the intersection of the two fitting lines. The absorbance spectra were converted from the reflectance measurement using the spectral analysis tool of the JASCO software.

Electrode preparation

Aqueous solutions of MAX phases (5 mg mL^{-1}) were sonicated for 30 minutes, and 5 μL of the obtained suspensions were drop-casted on SPCE and dried using a heat lamp. The same procedure was used to prepare the glassy carbon (GC) electrodes used for the chronoamperometry measurements. The loading of material on the electrodes was 0.35 mg cm^{-2}. The distribution of the particles on the SPCE was studied using the back-scattered electron detector mounted on the SEM, while the height of the deposition was analysed using CLSM. The obtained data, reported in Fig. S1,† showed that the size of the MAX particles varied in the range from 2 to 15 μm with a typical distribution of materials by the drop-casting technique.[56] Moreover, CLSM analysis showed that the thickness of the deposited MAX varied by up to 36.9 μm for Nb_2AlC, 19.2 μm for Ta_2AlC, and 38.6 μm for Ti_3AlC_2.

Photoelectrochemical measurements

All the measurements were carried out in a three-electrode configuration, using the prepared MAX on SPCE as the working electrode, a graphite rod as the counter electrode, and Ag/AgCl (1 M KCl) as the reference electrode. The electrodes were immersed in a quartz cell containing 0.5 M H_2SO_4 solution, and a potentiostat (PGSTAT204, Metrohm Autolab, The Netherlands) operated by NOVA software (version 2.1) was used to perform linear sweep voltammetry with a scan rate of 5 mV s^{-1}. The measured potentials were converted to the Reversible Hydrogen Electrode (RHE). A customised LED setup (LZ4-44UV00, LZ4-40B208, and LZ4-40R208, LedEngin Inc.) with interchangeable wavelengths (365 nm, 460 nm, and 660 nm) was used as the illumination source. The LSV of the bare SPCE was measured in the dark as a reference, while MAX phases were tested with and without illumination. For chronoamperometry measurements, GC electrodes were used as the working electrode and a fixed potential of −0.56 V *vs.* RHE was applied. The light source (660 nm) was switched on/off at regular intervals.

Results & discussion

We first performed a theoretical investigation of the properties of three MAX, specifically Nb_2AlC, Ta_2AlC, and Ti_3AlC_2 (Scheme 2), using the first principle calculations based on DFT. The plots of the total density of states (DOS) of Nb_2AlC, Ta_2AlC and Ti_3AlC_2 are presented in Fig. 1A–C. The DOS calculations show the metallic nature of all investigated MAX with no band gap. The continuous DOS across the Fermi level (E_f) indicates that the material is electrically conductive. Subsequently, partial DOS of Nb_2AlC, Ta_2AlC and Ti_3AlC_2 was used to study the nature of the chemical bonding. Fig. S2† shows the element and orbital resolved DOS of the MAX. From this Figure, the Fermi level is dominantly occupied by the transition metals of Nb, Ta and Ti,

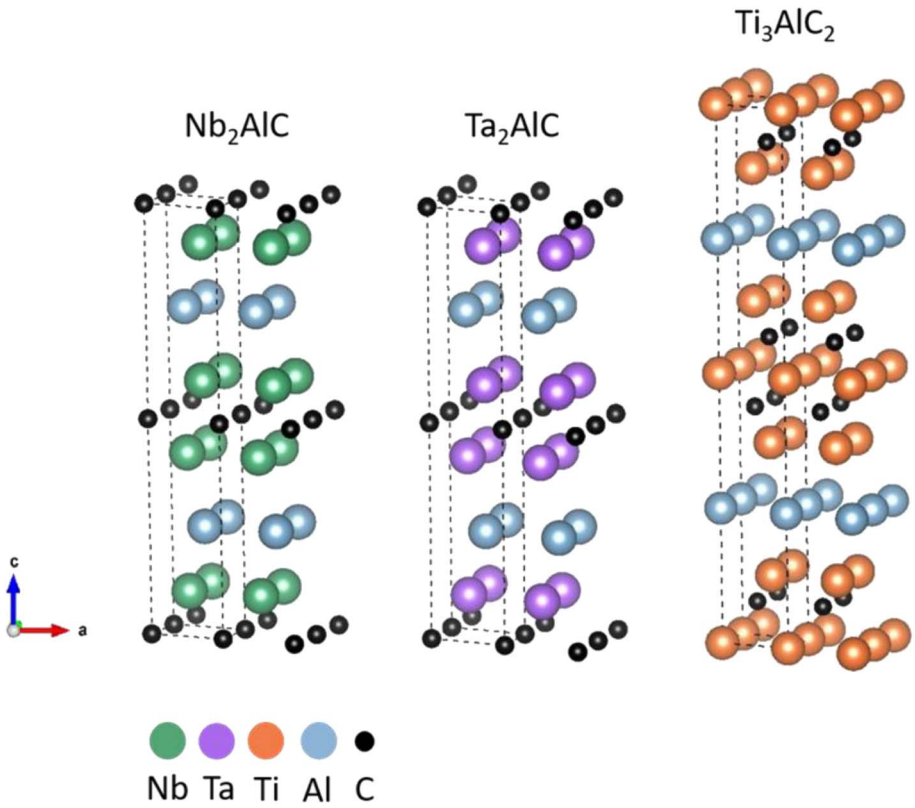

Scheme 2 Schematic illustration of the structure of MAX phases. The dashed lines show the edges of the unit cell.

respectively, which is also visible in the total DOS (Fig. 1A–C) that follows the pattern of the Nb (d), Ta (d) and Ti (d) orbitals. There is hybridisation between the transition metals Nb (d), Ta (d) and Ti (d) and C (p) at around −5 eV, −3 eV and −10 eV, respectively. The transition metals also showed hybridisation with the Al (p) at around −2 eV, −5 eV and −2.5 eV, respectively.

The *ab initio* electronic structure calculations of the investigated MAX predicted the band structure with numerous bands crossing the Fermi level, as shown in Fig. 1a–c. There is no gap in the vicinity of the Fermi level, which additionally confirmed the metallic nature of the MAX. The DOS and band structure results agree with previous works on theoretical studies of Nb_2AlC,[57,58] Ta_2AlC[36] and Ti_3AlC_2.[35,59]

Having a basic understanding of the MAX, we proceeded with extensive experimental material characterisations. SEM was used to study the morphology of the three phases and the obtained micrographs are shown in Fig. 2A–C. All the MAX presented the tight layered structure typical of these non-exfoliated materials and no additional structures were seen.

A detailed study of the surface elemental composition by employing EDS confirmed the presence of the composing elements of the MAX (transition metal, aluminium, and carbon), but also detected a considerable amount of oxygen. In particular, the elemental mapping reported in Fig. 3A–C shows that oxygen is uniformly distributed on the MAX, indicating the possible presence of metal oxides. Comparing the mapping of oxygen with the other elements, we observed the correspondence of the high-intensity spots between aluminium and oxygen, suggesting the presence of aluminium oxide. The elemental quantification from the EDS spectra (Fig. S3†) shows that Ta_2AlC is the MAX with the largest amount of oxygen (22.9 At%), followed by Nb_2AlC (10.8 At%), and Ti_3AlC_2 (4.8 At%). For all of them, the sum of the elements deviated from the expected stoichiometry, supporting the presence of other elements or different metal oxides.

XPS was utilised to study in more detail the surface chemical compositions of the three MAX (Fig. 4A–C). The survey spectra of the phases confirmed the observation by EDS, showing the presence of the corresponding transition metals, aluminium, carbon, and oxygen. No additional elements were detected. Only the main peaks for each element were labelled in the survey spectra in Fig. 4. The high-resolution spectra of all the main peaks were recorded to further analyse the oxidation state of the transition metals and the chemical bonding with carbon and oxygen. The deconvolution of the transition metal region confirmed the presence of metal-carbide and metal–oxygen bonds. In particular, the Nb 3d region revealed the doublet peaks for the metallic state Nb^0 (202.9 eV, 205.6 eV),[60] the doublet relative to the bond with carbon (203.7 eV, 206.4 eV),[61] and the one for the oxidation state Nb^{5+} (207.3 eV, 210.0 eV),[62] denoting the presence of Nb_2O_5. The deconvolution of the Ta 4f region showed the Ta–C doublets (22.4 eV, 24.2 eV),[63] and the peaks related to the oxidation state Ta^{5+} (26.1 eV, 28.0 eV),[64] which can be attributed to Ta_2O_5. The high-resolution spectrum of the Ti 2p region of Ti_3AlC_2 revealed the Ti–C doublets (455.0 eV, 461.2 eV),[65] the peaks related to the metallic state Ti^0

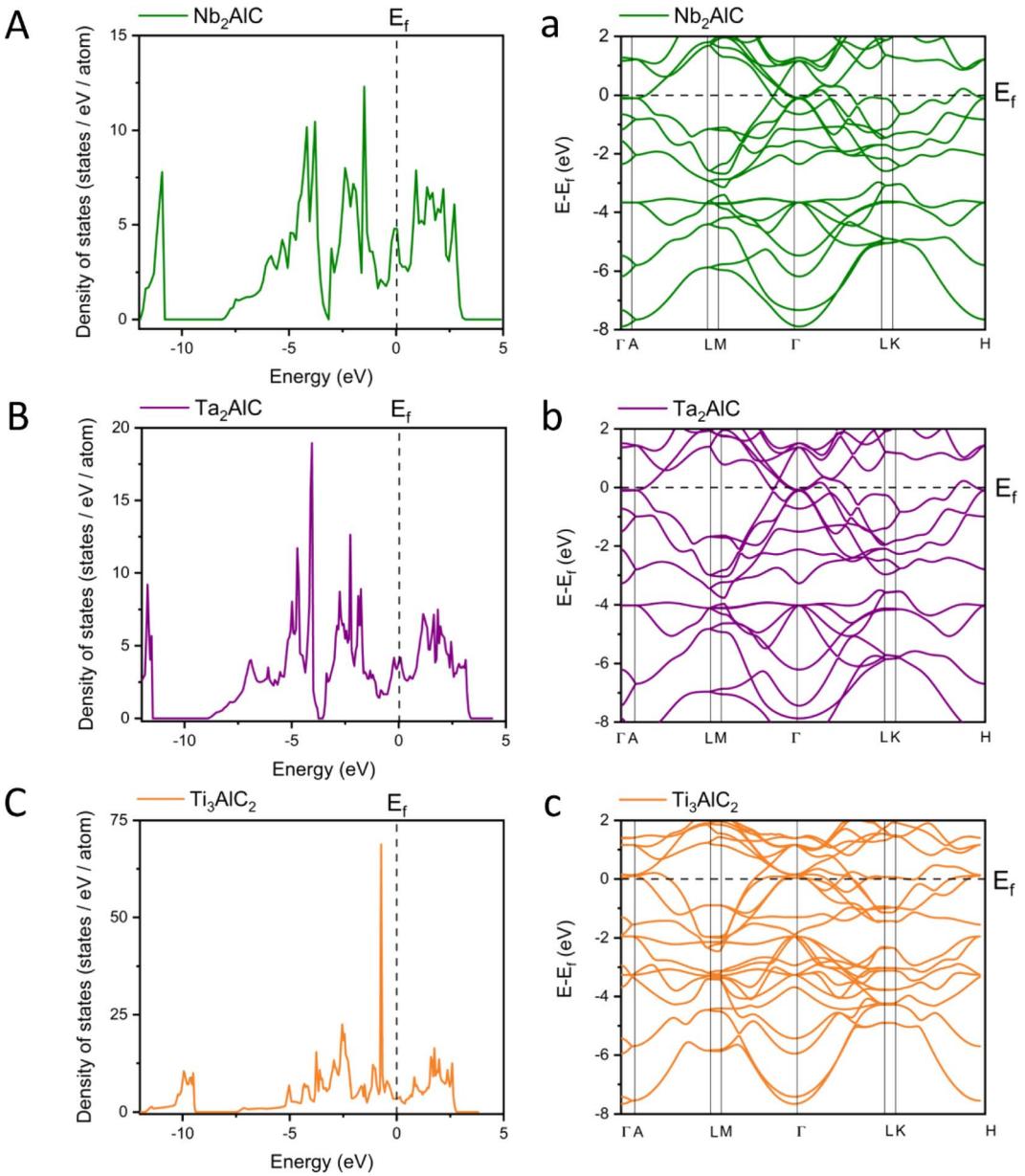

Fig. 1 Total density of states (DOS) and band structure of Nb_2AlC (A, a), Ta_2AlC (B, b) and Ti_3AlC_2 (C, c). The Fermi level, E_f is shown by the black dashed line.

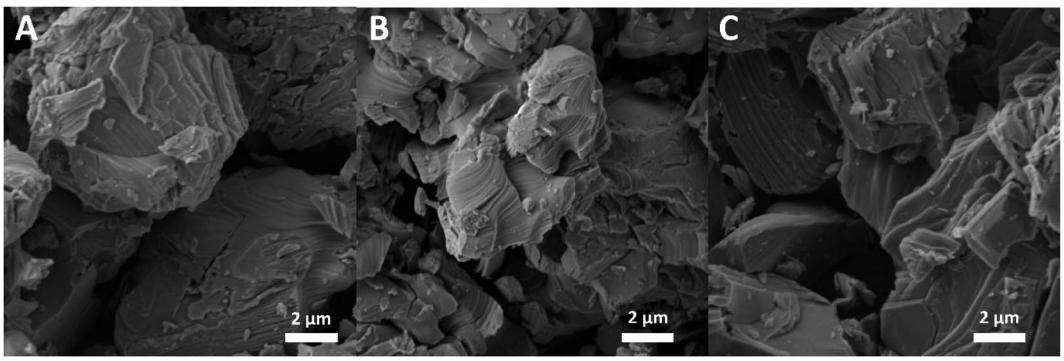

Fig. 2 SEM micrographs of MAX phases, Nb_2AlC (A), Ta_2AlC (B), and Ti_3AlC_2 (C). The scale bars are 2 μm.

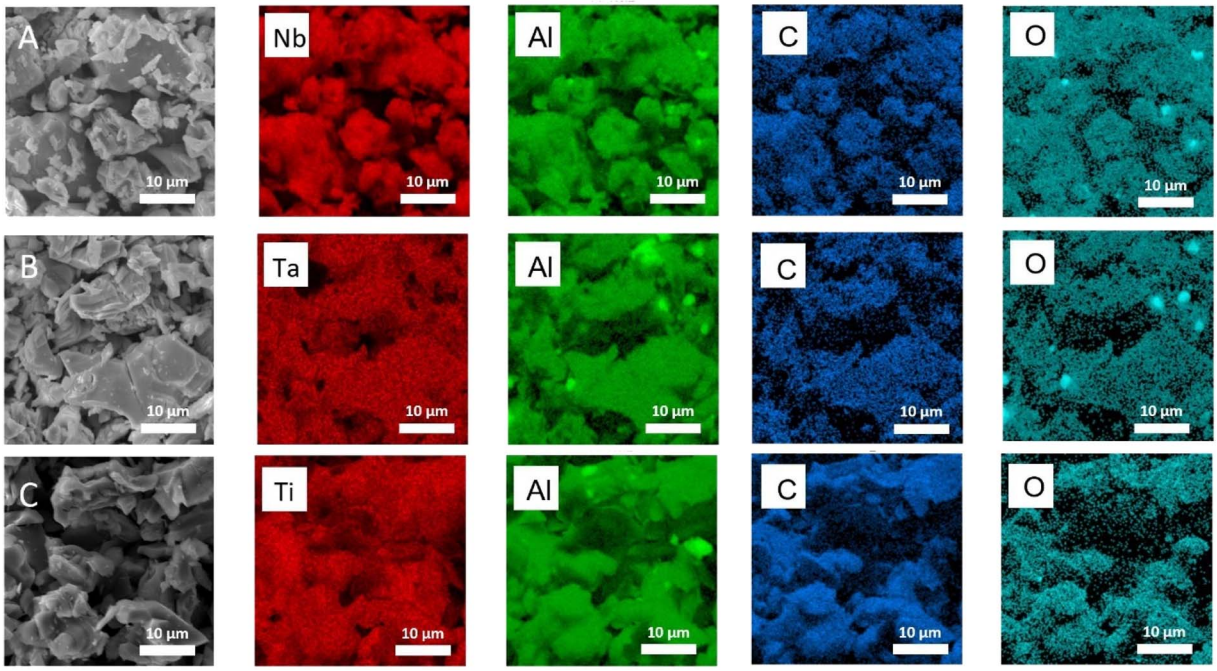

Fig. 3 EDS mapping of MAX phases, Nb_2AlC (A), Ta_2AlC (B), and Ti_3AlC_2 (C), showing the corresponding metal (Nb, Ta or Ti), Al, C, and O. The scale bars are 10 μm.

(453.7 eV, 459.8 eV),[66] and those of the oxidation state Ti^{4+} (458.6 eV, 464.2 eV),[67] which indicated the existence of TiO_2. The deconvolution of the Al 2p region of all the MAX validated what was deducted from EDS mapping. The wide peak at 74.4 eV indicated the presence of Al_2O_3, Al–O and Al–OH in the three MAX.[68] The detailed analysis of the C 1s region presented similar characteristics for all MAX, with the peak correlated to the adventitious carbon (285.0 eV), and the metal carbide peak of the analysed material (Nb–C 282.8 eV,[69] Ta–C 282.5 eV,[69] and Ti–C 281.3 eV[65]). The deconvolution of the O 1s region confirmed the presence of the corresponding transition metal oxides detected from the high-resolution spectrum of the transition metals of the MAX, in particular the Nb_2O_5 peak at 530.3 eV,[62] Ta_2O_5 at 530.2 eV,[64] and TiO_2 at 529.7 eV.[67] Similarly, the peak in the O 1s region related to Al_2O_3 (531.3 eV)[68] was detected in all the MAX.

Except for a few aluminium oxide particles detected from the EDS mapping in Fig. 3, in general, no visibly different structures were noticed from the SEM images in Fig. 2. It is apparent from the EDX and XPS analyses that all MAX contain a certain amount of their respective transition metal oxides and aluminium oxides (and hydroxides) in the bulk and on the surface. Moreover, the XRD patterns of MAX phases, reported in Fig. S4,† confirmed the presence of MAX phases[70–72] and traces of Al_2O_3,[72] but without the corresponding metal oxides. On the other hand, the metal oxides detected with the surface-sensitive XPS analysis were not found with XRD measurements. The observations suggest the low concentration of the metal (Nb, Ta, Ti) oxides relative to the MAX and the poor crystallinity of these compounds. In general, the presence of the additional metal oxides that are not expected from the pure MAX would likely influence the properties and the electrochemical performances of the MAX, since metal oxides such as Nb_2O_5, Ta_2O_5, TiO_2 and Al_2O_3 are either photoactive or catalytically active, or both.[73–77]

The estimation of the optical band gap of the MAX was obtained based on diffuse reflectance measurements. The Kubelka–Munk (K–M) model[53] was applied in the calculation of the absorption coefficient of thick powder samples and subsequently led to the band gap extrapolation from the Tauc plot, through graphical methods. Assuming direct transition for the MAX, Fig. 5A–C show the Tauc plots transformed from the reflectance measurement (eqn (3)). Details of the optical bandgap estimation are given in the Experimental section. The estimation of the band gap value is usually obtained using the Tauc plot graphical method for semiconductor materials but, in this work, materials characterisations showed the co-existence of more than a single semiconductor compound in the MAX. For this reason, the "baseline method" was adopted, also applying a linear fit to the slope right below the fundamental absorption (baseline, solid line) and the band gap was extrapolated from the intersection of the two fitted lines.[55] Nb_2AlC and Ta_2AlC showed two different steep regions, indicating the presence of two different photoactive semiconductors, thus, two band gap values were obtained, 2.2 eV and 3.1 eV for Nb_2AlC, and 2.2 eV and 3.3 eV for Ta_2AlC. Ti_3AlC_2 presented only one fundamental absorption with a band gap of 2.4 eV. The estimation of the band gap was also performed assuming indirect transitions, as shown in Fig. S5.† The calculated values agreed with the ones previously discussed, differing by about 0.1 eV. Considering what was observed from the materials characterisation, the different band gaps can be related to the different metal oxides detected with XPS analyses. It was reported that

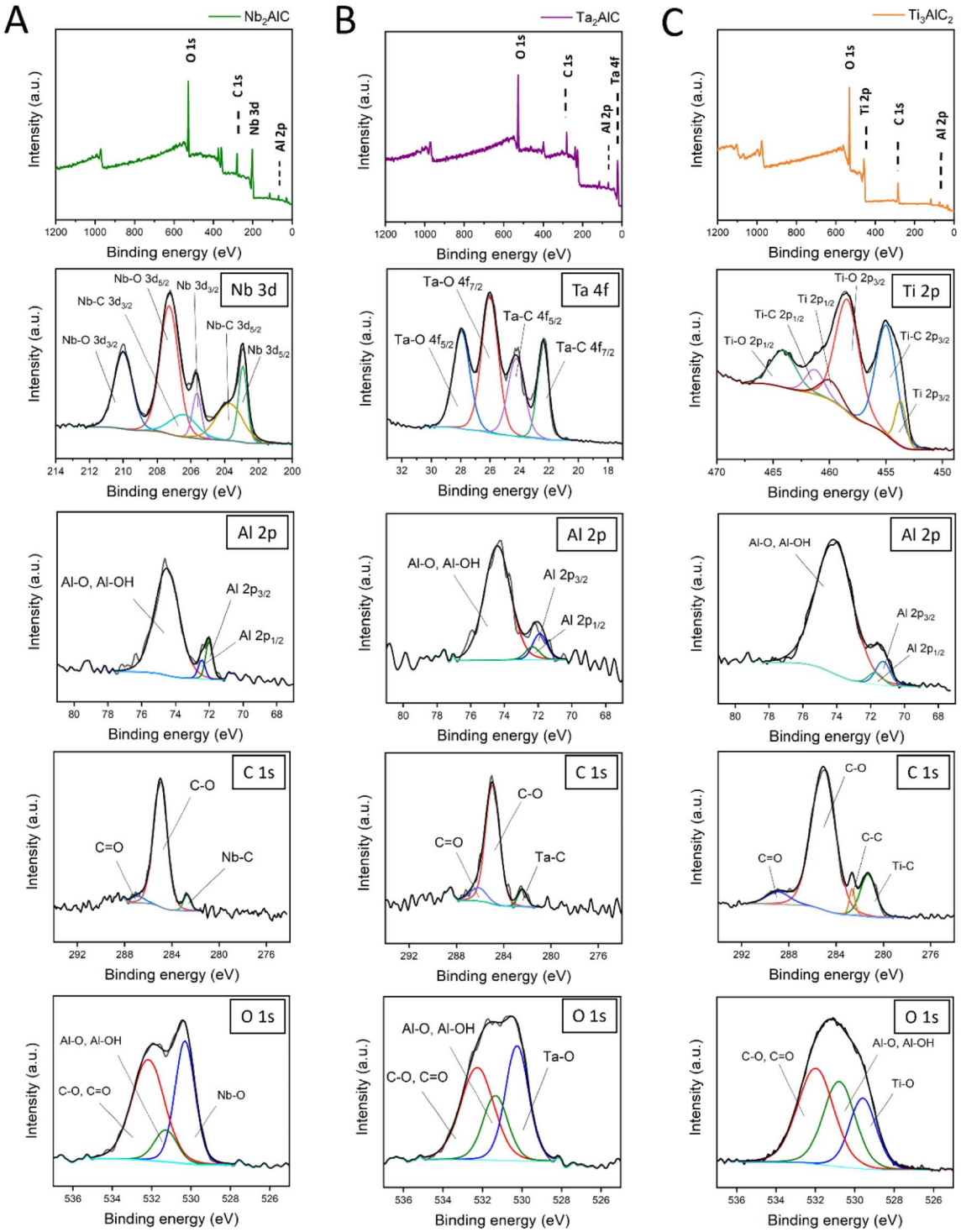

Fig. 4 XPS spectra of MAX phases, Nb_2AlC (A), Ta_2AlC (B), and Ti_3AlC_2 (C) with high-resolution analysis of metal (Nb 3d, Ta 4f or Ti 2p), Al 2p, C 1s, and O 1s. The main XPS peak for each element is labelled in the survey spectrum.

the band gap of Nb_2O_5 can vary between 3.1 eV and 5.3 eV,[78] while for Ta_2O_5 it was reported that the experimental band gap is between 3.6 eV and 4.0 eV.[79–81] The latter differs from the calculated value but it is also important to highlight that the equation developed by Tauc referred to amorphous materials, therefore the presence of crystalline phases can lead to the underestimation of the band gap.[82,83] Moreover, the absorption spectra of Nb_2AlC, Ta_2AlC, and Ti_3AlC_2 (Fig. S6†) confirmed that all the MAX showed absorptions in the visible and UV region.

The material characterisations highlighted two features that are common to all the MAX: the presence of Al_2O_3 detected by EDS and XPS, and the existence of a material that possesses

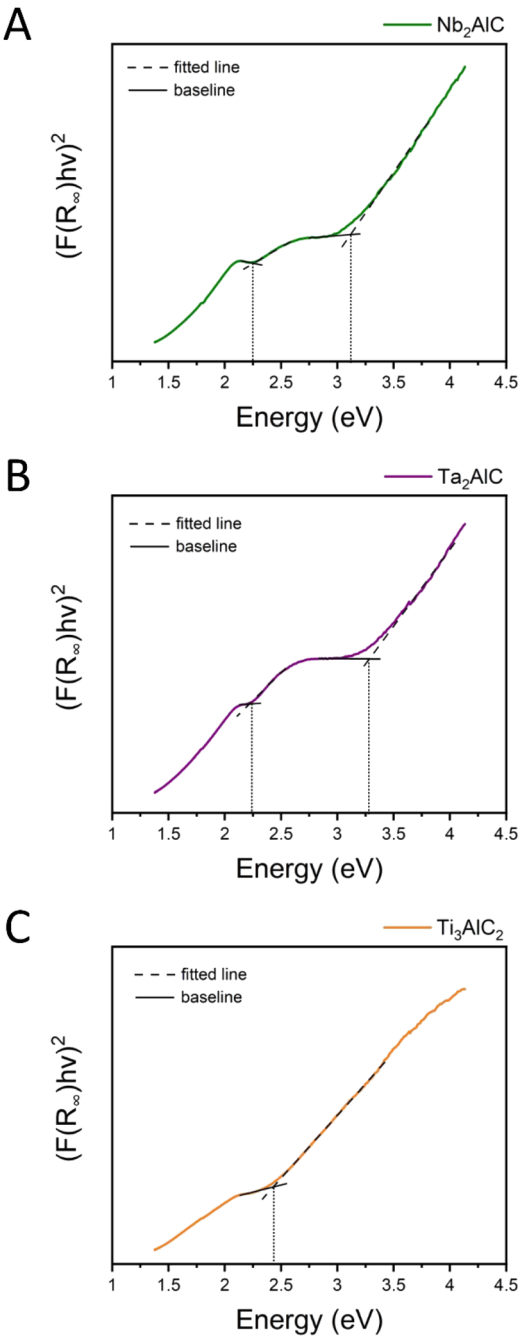

Fig. 5 Tauc plots of the Kubelka–Munk function calculated from the reflectance spectra of Nb_2AlC (A), Ta_2AlC (B), and Ti_3AlC_2 (C), assuming direct transitions. The dashed and solid black lines show the fitted line from the Tauc method and the baseline, respectively. The estimation of the band gap value corresponds to the abscissa of the intersection of the two lines, as shown by the dotted vertical line.

a band gap around 2.2–2.4 eV, extrapolated from the Tauc plots. Al_2O_3 is an insulator that is not supposed to absorb light, since it possesses a wide band gap between 5.1 eV and 7.6 eV, depending on the crystalline form and the synthesis method.[84] However, it was reported that Al_2O_3 can be applied in the photodegradation of phenolic compounds under the influence of UV light.[73,74] In particular, it was reported how the band gap of the Al_2O_3 synthesised by the sol–gel method changed dramatically based on the annealing temperature, ascribed to the hydroxyl groups of the material. These functionalities are responsible for the photoresponse since they allow the absorption of molecules that can form reactive oxygen species, involved in the degradation process.[73] The presence of Al–OH groups was detected in all MAX used in this work, as shown in Fig. 4. However, it is difficult to understand their role in the photocatalytic process since they are impurities that formed spontaneously due the exposure to air and they cannot easily be isolated to investigate in detail their exact composition and properties. In contrast to the theoretical calculation that all three MAX have continuous DOS and band structures without a gap, indicating a metallic behaviour, the experimental evaluation shows that the MAX with mixed metal oxides, as a whole, possess optical band gaps with semiconductor characteristics and potentially demonstrate photoresponses.

To verify the hypothesis, linear sweep voltammetry was used to test the photoelectrochemical activity of MAX for HER under the influence of illumination at different wavelengths. The wavelength of the light sources was chosen based on the estimated band gaps mentioned above, covering the region of the electromagnetic spectrum that goes from ultraviolet (UV, 365 nm), close to the start (blue, 460 nm) and the end (red, 660 nm) of the visible region. Fig. 6A–C show that considering the overpotential at -10 mA cm^{-2}, all MAX presented a lower overpotential compared to the bare screen-printed carbon electrodes (SPCE, dashed line), measured for reference. Generally, exposure to the light led to better performances for all MAX. Nb_2AlC showed the lowest overpotential under the influence of UV light (758 mV), followed by the red (814 mV), and the blue light sources (863 mV), as compared to non-illuminated (904 mV). Ta_2AlC also presented a decreased overpotential of 760 mV, 787 mV, and 811 mV when illuminated by 365 nm, 460 nm, and 660 nm light, respectively. The electrode measured without illumination again presented the highest overpotential (863 mV). As mentioned above, both MAX performed better after exposure to UV light, thanks to the presence of the respective transition metal oxides (Nb_2O_5 and Ta_2O_5) that are known to be active in the UV region. However, Ti_3AlC_2 exhibited an overpotential of 814 mV in the dark and showed the best photoactivity when exposed to visible light, presenting an overpotential of 680 mV with the blue source and 697 mV with the red one, but was less active when illuminated by UV light, with an overpotential of 736 mV. This trend agrees with the fundamental absorption in the visible region and the deduced band gap (2.4 eV) shown in Fig. 5C. The results agree with the photoactivity of MAX in the literature.[33,34]

Eventually, chronoamperometry measurements (Fig. S7†) were performed in the same electrolyte switching on/off the light source (660 nm) to confirm the photoelectrochemical response reported in Fig. 6. The results showed that all MAX exhibited a larger current increment during illumination as compared to the bare GC. In particular, Nb_2AlC showed the most prominent increase in current, followed by Ti_3AlC_2 and Ta_2AlC. The results obtained agree with the trend of the polarisation curves in Fig. 6.

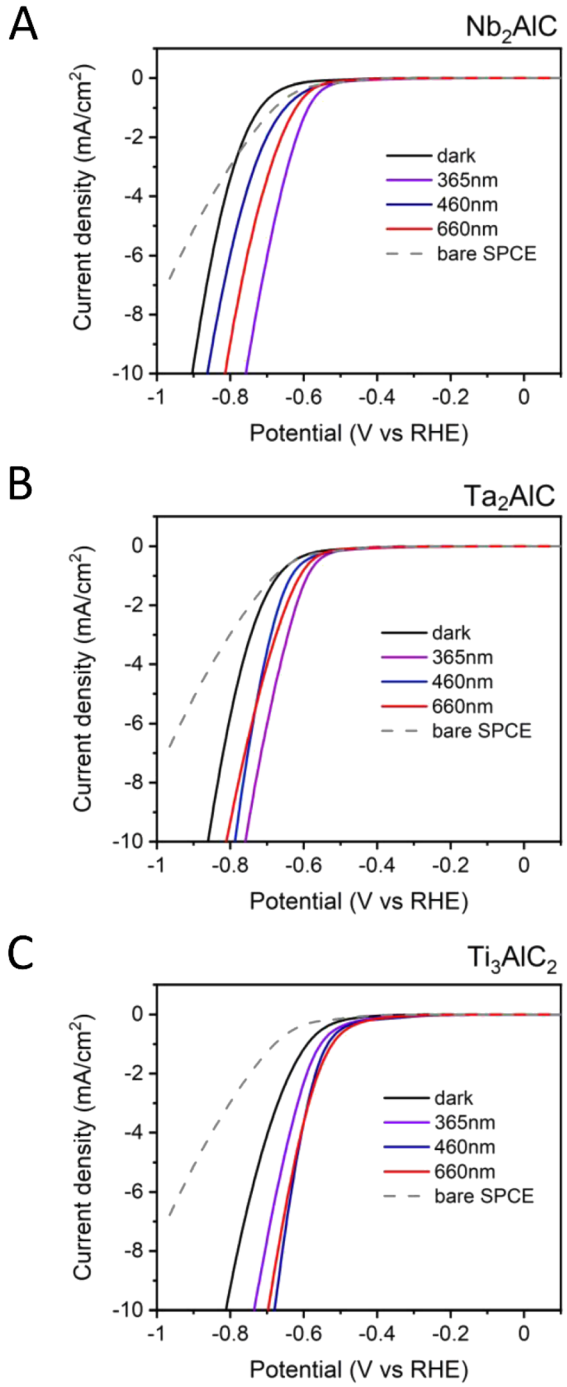

Fig. 6 Linear sweep voltammograms of MAX phases, Nb_2AlC (A), Ta_2AlC (B), and Ti_3AlC_2 (C) supported by SPCE measured in 0.5 M H_2SO_4 electrolyte; scan rate 5 mV s^{-1}. The measurements were carried out in the dark and then the sample was exposed to light sources of different wavelengths.

The application of the Nb_2AlC, Ta_2AlC and Ti_3AlC_2 as photoelectrocatalysts for hydrogen production reinforced the hypothesis that the detected metal oxide impurities contributed significantly to the photoactivity of these materials, as schematically shown in Scheme 3. Furthermore, surface engineering

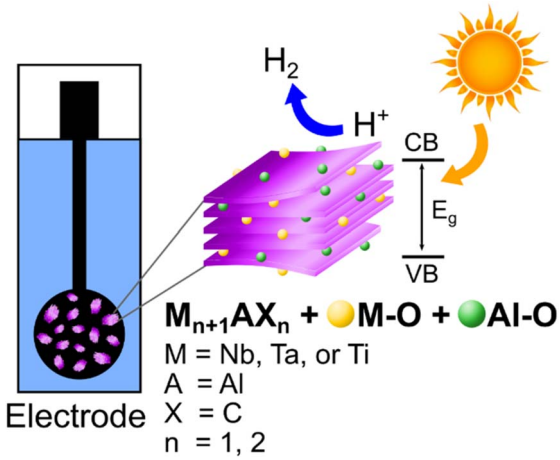

Scheme 3 Representation of the mechanism of the photoelectrochemical HER, where the oxide impurities take part in the photoelectrocatalytic process.

can be used to tune the properties of these materials and optimise their performance in energy-related applications.

Conclusion

In summary, we studied the properties of three MAX phases, Nb_2AlC, Ta_2AlC, and Ti_3AlC_2, using theoretical and experimental approaches to investigate the origin of their photoactivity. The theoretical calculations conclude that the metals contribute dominantly to the DOS around the Fermi level, confirming the metallic nature of these compounds, with no band gap in the vicinity of the Fermi level. XPS and EDS analyses detected not only the presence of the respective transition metal oxides but also a relevant amount of Al_2O_3. In contrast to the theoretical calculation, it was experimentally estimated that for Nb_2AlC and Ta_2AlC, there are two fundamental absorptions at 2.2 eV, 3.1 eV, and 2.2 eV, 3.3 eV, respectively. Moreover, the estimated band gap for Ti_3AlC_2 was 2.4 eV. As a confirmation of the presence of photoactive material, all MAX showed enhanced photocatalytic activity towards the HER when exposed to illumination by different light sources. In particular, Nb_2AlC and Ta_2AlC performed better (758 mV and 760 mV of overpotential, respectively) when exposed to UV light, and Ti_3AlC_2 showed the lowest overpotential (680 mV) when exposed to the 460 nm light source, in accordance with the estimated optical band gaps. In general, the formation of oxides on MAX phases has been already reported, since contamination is unavoidable if the material comes in contact with the air or with oxidising solvents.[85,86] In this work, we showed how these impurities can play a crucial role in photoelectrochemical hydrogen generation, leading to better performances thanks to their intrinsic photoactivity. These findings can open the door for further implementation of MAX phases as photoelectrocatalysts. In addition to the three MAX investigated in this work, more than 150 other MAX phases[87] synthesised to date might demonstrate similar photoactive properties, which are yet to be tested and possibly applied in this field.

Author contributions

M. S: material characterisation (SEM, EDS, XPS and optical measurements), electrochemical measurements, data analysis, original draft. K. N.: theoretical calculations (DOS, band structure), material characterisation (XRD, CLSM), data analysis, original draft. S. N.: conceptualisation, data analysis, editing and revision of the manuscript. M. C.: funding acquisition, supervision of theoretical part, editing and revision of the manuscript. M. P.: funding acquisition, supervision of the experimental part, conceptualisation, editing and revision of the manuscript.

Conflicts of interest

There are no conflicts to declare.

Acknowledgements

The authors acknowledge CzechNanoLab project at CEITEC Nano Research Infrastructure (LM2018110, MEYS CR) for the support in material characterisation. M. S. acknowledges the financial support from JCMM and all partners for the Brno PhD Talent scholarship, financed by the Brno City Municipality. M. S. and K. N. acknowledge the project Quality Internal Grants of BUT (KInG BUT), Reg. No. CZ.02.2.69/0.0/0.0/19_073/0016948, which is financed from the OP RDE. M. P. acknowledges the Grant Agency of the Czech Republic (GACR EXPRO: 19–26896X). M. Č. acknowledges the M-ERA.Net project No. TH71020004 (HYSUCAP).

References

1 J. Gong, C. Li and M. R. Wasielewski, *Chem. Soc. Rev.*, 2019, **48**, 1862–1864.
2 B. A. Pinaud, J. D. Benck, L. C. Seitz, A. J. Forman, Z. Chen, T. G. Deutsch, B. D. James, K. N. Baum, G. N. Baum, S. Ardo, H. Wang, E. Miller and T. F. Jaramillo, *Energy Environ. Sci.*, 2013, **6**, 1983–2002.
3 M. D. Islam, I. Kubo, M. Ohadi and A. A. Alili, *Appl. Energy*, 2009, **86**, 511–515.
4 T. Hisatomi, J. Kubota and K. Domen, *Chem. Soc. Rev.*, 2014, **43**, 7520–7535.
5 X. Yu, M. S. Prévot, N. Guijarro and K. Sivula, *Nat. Commun.*, 2015, **6**, 7596.
6 S. Koumi Ngoh and D. Njomo, *Renewable Sustainable Energy Rev.*, 2012, **16**, 6782–6792.
7 I. S. Cho, Z. Chen, A. J. Forman, D. R. Kim, P. M. Rao, T. F. Jaramillo and X. Zheng, *Nano Lett.*, 2011, **11**, 4978–4984.
8 R. Van De Krol, Y. Liang and J. Schoonman, *J. Mater. Chem.*, 2008, **18**, 2311–2320.
9 L. Wang, R. Liang, T. Zhou, J. Zheng, B. M. Liang, H. P. Zhang, F. M. Luo, P. G. Gibson and G. Wang, *Ann. Allergy, Asthma Immunol.*, 2017, **119**, 324–332.
10 O. Monfort, L. C. Pop, S. Sfaelou, T. Plecenik, T. Roch, V. Dracopoulos, E. Stathatos, G. Plesch and P. Lianos, *Chem. Eng. J.*, 2016, **286**, 91–97.
11 S. Han, Y. C. Pu, L. Zheng, L. Hu, J. Z. Zhang and X. Fang, *J. Mater. Chem. A*, 2016, **4**, 1078–1086.
12 S. Dolai, P. Maiti, A. Ghorai, R. Bhunia, P. K. Paul and D. Ghosh, *ACS Appl. Mater. Interfaces*, 2021, **13**, 438–448.
13 K. Ghosh, S. Ng, C. Iffelsberger and M. Pumera, *Appl. Mater. Today*, 2022, **26**, 101301.
14 S. Ng, R. Zazpe, J. Rodriguez-Pereira, J. Michalička, J. M. Macak and M. Pumera, *J. Mater. Chem. A*, 2021, **9**, 11405–11414.
15 S. Ng, J. Sturala, J. Vyskocil, P. Lazar, J. Martincova, J. Plutnar and M. Pumera, *ACS Nano*, 2021, **15**, 11681–11693.
16 K. N. Dinh, Y. Zhang, J. Zhu and W. Sun, *Chem. – A Eur. J.*, 2020, **26**, 6437–6446.
17 K. P. Akshay Kumar, K. Ghosh, O. Alduhaish and M. Pumera, *Electrochem. Commun.*, 2021, **122**, 106890.
18 Z. W. Seh, K. D. Fredrickson, B. Anasori, J. Kibsgaard, A. L. Strickler, M. R. Lukatskaya, Y. Gogotsi, T. F. Jaramillo and A. Vojvodic, *ACS Energy Lett.*, 2016, **1**, 589–594.
19 M. Sokol, V. Natu, S. Kota and M. W. Barsoum, *Trends Chem.*, 2019, **1**, 210–223.
20 M. W. Barsoum and M. Radovic, *Annu. Rev. Mater. Res.*, 2011, **41**, 195–227.
21 Z. M. Sun, *Int. Mater. Rev.*, 2011, **56**, 143–166.
22 N. F. Rosli, M. Z. M. Nasir, N. Antonatos, Z. Sofer, A. Dash, J. Gonzalez-Julian, A. C. Fisher, R. D. Webster and M. Pumera, *ACS Appl. Nano Mater.*, 2019, 6010–6021.
23 M. Radovic and M. W. Barsoum, *Am. Ceram. Soc. Bull.*, 2013, **92**, 20–27.
24 M. Malaki, A. Maleki and R. S. Varma, *J. Mater. Chem. A*, 2019, **7**, 10843–10857.
25 Y. Cheng, L. Wang, Y. Song and Y. Zhang, *J. Mater. Chem. A*, 2019, **7**, 15862–15870.
26 M. Khazaei, A. Ranjbar, K. Esfarjani, D. Bogdanovski, R. Dronskowski and S. Yunoki, *Phys. Chem. Chem. Phys.*, 2018, **20**, 8579–8592.
27 A. VahidMohammadi, J. Rosen and Y. Gogotsi, *Science*, 2021, **372**, eabf1581.
28 M. Naguib, O. Mashtalir, J. Carle, V. Presser, J. Lu, L. Hultman, Y. Gogotsi and M. W. Barsoum, *ACS Nano*, 2012, **6**, 1322–1331.
29 O. Mashtalir, M. Naguib, V. N. Mochalin, Y. Dall'Agnese, M. Heon, M. W. Barsoum and Y. Gogotsi, *Nat. Commun.*, 2013, **4**, 1–7.
30 J. C. Lei, X. Zhang and Z. Zhou, *Front. Phys.*, 2015, **10**, 276–286.
31 K. A. Novčić, C. Iffelsberger and M. Pumera, *J. Mater. Chem. A*, 2022, **10**, 3206–3215.
32 K. P. Akshay Kumar, O. Alduhaish and M. Pumera, *Electrochem. Commun.*, 2021, **125**, 106977.
33 M. Sanna, S. Ng, J. V. Vaghasiya and M. Pumera, *ACS Sustainable Chem. Eng.*, 2022, **10**, 2793–2801.
34 B. Shalini Reghunath, D. Davis and K. R. Sunaja Devi, *Chemosphere*, 2021, **283**, 131281.
35 J. Gertzen, P. Levecque, T. Rampai and T. van Heerden, *Mater. (Basel).*, 2021, **14**, 1–12.
36 X. Qian, Y. Li, X. He, H. Fan and S. Yun, *J. Phys. Chem. Solids*, 2011, **72**, 954–956.

37 I. Thomé, A. Nijs and C. Bolm, *Chem. Soc. Rev.*, 2012, **41**, 979–987.
38 S. L. Buchwald and C. Bolm, *Angew. Chem.*, 2009, **121**, 5694–5695.
39 P.-F. Larsson, A. Correa, M. Carril, P.-O. Norrby and C. Bolm, *Angew. Chem.*, 2009, **121**, 5801–5803.
40 N. E. Leadbeater and M. Marco, *J. Org. Chem.*, 2003, **68**, 5660–5667.
41 C. E. Banks, A. Crossley, C. Salter, S. J. Wilkins and R. G. Compton, *Angew. Chem., Int. Ed.*, 2006, **45**, 2533–2537.
42 B. Šljukić, C. E. Banks and R. G. Compton, *Nano Lett.*, 2006, **6**, 1556–1558.
43 C. H. An Wong, Z. Sofer, M. Kubešová, J. Kučera, S. Matějková and M. Pumera, *Proc. Natl. Acad. Sci. U. S. A.*, 2014, **111**, 13774–13779.
44 L. Wang, Z. Sofer and M. Pumera, *ACS Nano*, 2020, **14**, 21–25.
45 N. Mohamad Latiff, L. Wang, C. C. Mayorga-Martinez, Z. Sofer, A. C. Fisher and M. Pumera, *Nanoscale*, 2016, **8**, 16752–16760.
46 R. J. Toh, Z. Sofer, J. Luxa and M. Pumera, *ChemCatChem*, 2017, **9**, 1168–1171.
47 M. Pumera, *ACS Catal.*, 2020, **10**, 7087–7092.
48 M. P. Browne, V. Urbanova, J. Plutnar, F. Novotný and M. Pumera, *J. Mater. Chem. A*, 2020, **8**, 1120–1126.
49 S. M. Tan and M. Pumera, *ACS Nano*, 2019, **13**, 2681–2728.
50 X. J. Chua, S. M. Tan, X. Chia, Z. Sofer, J. Luxa and M. Pumera, *Chem. – A Eur. J.*, 2017, **23**, 3169–3177.
51 K. R. Ward, M. Gara, N. S. Lawrence, R. S. Hartshorne and R. G. Compton, *J. Electroanal. Chem.*, 2013, **695**, 1–9.
52 K. Momma and F. Izumi, *J. Appl. Crystallogr.*, 2011, **44**, 1272–1276.
53 P. Kubelka and F. Munk, *Z. Tech. Phys.*, 1931, **12**, 593–601.
54 J. Tauc, *Mat. Res. Bull.*, 1968, **3**, 37–46.
55 P. Makuła, M. Pacia and W. Macyk, *J. Phys. Chem. Lett.*, 2018, **9**, 6814–6817.
56 A. Kaliyaraj Selva Kumar, Y. Zhang, D. Li and R. G. Compton, *Electrochem. Commun.*, 2020, **121**, 106867.
57 Z. U. Din Babar, J. Fatheema, N. Arif, M. S. Anwar, S. Gul, M. Iqbal and S. Rizwan, *RSC Adv.*, 2020, **10**, 25669–25678.
58 A. J. Xu, W. W. Zhong and X. Zhang, *Comput. Condens. Matter*, 2016, **6**, 1–4.
59 X. H. Wang and Y. C. Zhou, *J. Mater. Sci. Technol.*, 2010, **26**, 385–416.
60 T. A. Sasaki and Y. Baba, *Phys. Rev. B: Condens. Matter Mater. Phys.*, 1985, **31**, 791–797.
61 A. Darlinski, *IEEE Trans. Magn.*, 1987, **23**, 1381–1384.
62 N. Özer, M. D. Rubin and C. M. Lampert, *Sol. Energy Mater. Sol. Cells*, 1996, **40**, 285–296.
63 T. Anazawa, S. Tokumitsu, R. Sekine, E. Miyazaki, K. Edamoto, H. Kato and S. Otani, *Surf. Sci.*, 1995, **328**, 263–268.
64 S. F. Ho, S. Contarini and J. W. Rabalais, *J. Phys. Chem.*, 1987, **91**, 4779–4788.
65 J. Luthin and C. Linsmeier, *Phys. Scr. T*, 2001, **91**, 134–137.
66 A. A. Galuska, J. C. Uht and N. Marquez, *J. Vac. Sci. Technol., A*, 1988, **6**, 110–122.
67 M. C. Biesinger, L. W. M. Lau, A. R. Gerson and R. S. C. Smart, *Appl. Surf. Sci.*, 2010, **257**, 887–898.
68 J. Van den Brand, W. G. Sloof, H. Terryn and J. H. W. De Wit, *Surf. Interface Anal.*, 2004, **36**, 81–88.
69 L. Ramqvist, K. Hamrin, G. Johansson, A. Fahlman and C. Nordling, *J. Phys. Chem. Solids*, 1969, **30**, 1835–1847.
70 A. Liu, Q. Yang, X. Ren, F. Meng, L. Gao, M. Gao, Y. Yang, T. Ma and G. Wu, *Ceram. Int.*, 2020, **46**, 6934–6939.
71 T. H. Scabarozi, J. Roche, A. Rosenfeld, S. H. Lim, L. Salamanca-Riba, G. Yong, I. Takeuchi, M. W. Barsoum, J. D. Hettinger and S. E. Lofland, *Thin Solid Films*, 2009, **517**, 2920–2923.
72 C. L. Yeh and Y. S. Chen, *Ceram. Int.*, 2017, **43**, 15659–15665.
73 F. Tzompantzi, Y. Piña, A. Mantilla, O. Aguilar-Martínez, F. Galindo-Hernández, X. Bokhimi and A. Barrera, *Catal. Today*, 2014, **220–222**, 49–55.
74 Y. Piña-Pérez, F. Tzompantzi-Morales, R. Pérez-Hernández, R. Arroyo-Murillo, P. Acevedo-Peña and R. Gómez-Romero, *Fuel*, 2017, **198**, 11–21.
75 M. Ni, M. K. H. Leung, D. Y. C. Leung and K. Sumathy, *Renewable Sustainable Energy Rev.*, 2007, **11**, 401–425.
76 S. Furukawa, Y. Ohno, T. Shishido, K. Teramura and T. Tanaka, *ACS Catal.*, 2011, **1**, 1150–1153.
77 V. Gurylev, *Mater. Today Sustain.*, 2022, **18**, 100131.
78 R. A. Rani, A. S. Zoolfakar, A. P. O'Mullane, M. W. Austin and K. Kalantar-Zadeh, *J. Mater. Chem. A*, 2014, **2**, 15683–15703.
79 R. M. Fleming, D. V. Lang, C. D. W. Jones, M. L. Steigerwald, D. W. Murphy, G. B. Alers, Y. H. Wong, R. B. Van Dover, J. R. Kwo and A. M. Sergent, *J. Appl. Phys.*, 2000, **88**, 850–862.
80 W. J. Chun, A. Ishikawa, H. Fujisawa, T. Takata, J. N. Kondo, M. Hara, M. Kawai, Y. Matsumoto and K. Domen, *J. Phys. Chem. B*, 2003, **107**, 1798–1803.
81 F. Z. Tepehan, F. E. Ghodsi, N. Ozer and G. G. Tepehan, *Sol. Energy Mater. Sol. Cells*, 1997, **46**, 311–321.
82 A. Dolgonos, T. O. Mason and K. R. Poeppelmeier, *J. Solid State Chem.*, 2016, **240**, 43–48.
83 G. Gal, Y. Mastai, G. Hodes and L. Kronik, *J. Appl. Phys.*, 1999, **86**, 5573–5577.
84 E. O. Filatova and A. S. Konashuk, *J. Phys. Chem. C*, 2015, **119**, 20755–20761.
85 K. Chen, N. Qiu, Q. Deng, M. H. Kang, H. Yang, J. U. Baek, Y. H. Koh, S. Du, Q. Huang and H. E. Kim, *ACS Biomater. Sci. Eng.*, 2017, **3**, 2293–2301.
86 S. Myhra, J. A. A. Crossley and M. W. Barsoum, *J. Phys. Chem. Solids*, 2001, **62**, 811–817.
87 R. Khaledialidusti, M. Khazaei, S. Khazaei and K. Ohno, *Nanoscale*, 2021, **13**, 7294–7307.

